



Colloids in random potentials: Optical realization and characterization of rough laser light fields

Inaugural-Dissertation

zur

Erlangung des Doktorgrades der
Mathematisch-Naturwissenschaftlichen Fakultät
der Heinrich-Heine-Universität Düsseldorf

vorgelegt von

Jörg Bewerunge

aus Düsseldorf

Düsseldorf, Mai 2016

Aus dem Institut für experimentelle Physik der kondensierten Materie,
Lehrstuhl für Physik der weichen Materie
der Heinrich-Heine-Universität Düsseldorf

Gedruckt mit der Genehmigung der
Mathematisch-Naturwissenschaftlichen Fakultät der
Heinrich-Heine-Universität Düsseldorf

Referent: Prof. Dr. Stefan U. Egelhaaf
Koreferent: Prof. Dr. Hartmut Löwen
Tag der mündlichen Prüfung: 04.07.2016

ABSTRACT

Random potential energy landscapes (rPELs) represent a facile and versatile tool of statistical physics to analyze various complex phenomena, e.g. diffusion in disordered media and biological cells as well as glass transitions and protein folding. A controlled experimental realization of rPELs is therefore highly desired. In this work, a novel optical set-up is designed, constructed and tested, based upon a specially designed diffuser. Furthermore, its application to the study of colloidal particles is presented.

When laser light impinges on the diffuser, a random intensity speckle pattern is created. Colloidal particles exposed to this speckle pattern experience a rPEL whose local properties depend on the light intensity and the particle volume. In particular, this set-up offers the unique option to freely tune the correlation length and the distribution of energy values of the rPEL from exponential to Gaussian. Moreover, the new set-up offers a much larger field of view compared to established methods, allowing for studies with significantly improved statistics.

The set-up has been used to induce a rPEL with a non-Gaussian distribution of energy values and systematically study the spatial arrangement and dynamics of colloidal particles as a function of the potential roughness, tuned by the laser power, and the particle concentration. The former is characterized by the local probability density of the particles, the disorder-averaged pair density correlation function and the Edwards-Anderson order parameter, which quantifies the correlation of the mean local density among disorder realizations. Made possible by the new set-up, such a correlation function has been determined for the first time in experiments. Analysis of the particle concentration reveals that collisions caused by particle-particle interactions increase the probability of trapped particles to cross energy barriers. Hence, an increase in the concentration leads to a decrease of the trapping strength. In particular, a critical concentration has been found, at which particle-particle and particle-potential interactions are balanced. This results in a re-entrant behaviour of the short-term diffusion coefficient and strongly heterogeneous dynamics.

ZUSAMMENFASSUNG

Raue Potentiallandschaften (rPEL) stellen ein vielseitiges Werkzeug der statistischen Physik dar, um komplexe Phänomene zu studieren, z.B. Diffusion in ungeordneten Medien, Glasübergänge und Protein-Faltung. Eine experimentelle Verwirklichung einer kontrollierbaren rPEL ist daher wünschenswert. In dieser Arbeit werden dazu das Design und die Konstruktion eines neuartigen optischen Aufbaus vorgestellt, der auf einem speziellen Diffusor basiert und zur Untersuchung kolloidaler Proben genutzt wird.

Wenn ein Laserstrahl auf einen Diffusor trifft, wird ein zufälliges Intensitäts-Flecken-Muster erzeugt. Kolloidale Teilchen, die diesem Flecken-Muster ausgesetzt werden, erfahren eine rPEL, deren lokalen Eigenschaften von der Lichtintensität und dem Teilchen-Volumen abhängen. Der optische Aufbau bietet die einzigartige Möglichkeit, die Korrelationslänge frei zu verändern und die Verteilung der Energiewerte der rPEL zu variieren. Im Vergleich zu etablierten Methoden liefert dieser Aufbau einen viel größeren Beobachtungsbereich und ermöglicht daher Untersuchungen mit signifikant besserer Statistik.

Der Aufbau wurde dazu benutzt, eine rPEL zu erzeugen, deren Energiewerte nicht Gauß-verteilt sind. Weiterhin wurden die räumliche Anordnung und Dynamik kolloidaler Teilchen in Abhängigkeit von der Rauigkeit des Potentials, welche durch die Laserstärke verändert wird, und der Teilchenkonzentration systematisch untersucht. Der erste Aspekt wird durch die lokale Wahrscheinlichkeitsdichte der Teilchen, die unordnungsgemittelte Dichte-Korrelationsfunktion und den Edwards-Anderson-Ordnungsparameter charakterisiert, der die Korrelation der mittleren lokalen Dichte zwischen verschiedenen Realisierungen der Unordnung quantifiziert. Solche Korrelationsfunktionen konnten mit Hilfe des neuen Aufbaus erstmals experimentell bestimmt werden. Eine Analyse der Teilchenkonzentration wiederum zeigt, dass Kollisionen, die durch Teilchen-Teilchen-Wechselwirkungen hervorgerufen werden, die Wahrscheinlichkeit dafür erhöhen, dass gefangene Teilchen Energiebarrieren überwinden. Eine Erhöhung der Konzentration führt also zu einer Verringerung der Fallenstärke. Insbesondere wurde eine kritische Konzentration festgestellt, bei der Teilchen-Teilchen- und Teilchen-Potential-Wechselwirkungen einander ausgleichen. Daher werden eine zu- und wieder abnehmende Kurzzeitdiffusion und eine sehr heterogene Teilchen-Dynamik beobachtet.

AUTHOR'S DECLARATION

I declare that the work in this dissertation was carried out autonomously, independently and without using any unauthorized help, and has not in the same or a similar form been submitted at a different institution. This is my first attempt at obtaining a doctoral degree.

Signature: Date:

DANKSAGUNG

Ich bedanke mich bei all denjenigen, die mich während meines Studiums und meiner Promotion unterstützt haben und diese Arbeit somit erst ermöglichten.

Zu allererst danke ich meinem Doktorvater Prof. Dr. Stefan U. Egelhaaf für die zur Verfügungstellung eines sehr spannenden Themas und der damit verbundenen Anstellung an seinem Institut. Er hat mich jederzeit unterstützt und gefördert und mich immer mit interessanten Fragen und Anregungen zu neuen Ideen und Lösungsansätzen inspiriert. Weiterhin danke ich meinem Co-Betreuer und Zweitgutachter Prof. Dr. Hartmut Löwen dafür, dass er für Fragen stets zur Verfügung stand und mir durch den SFB TR6 die Möglichkeit gegeben hat, mich auch in einem internationalen Umfeld weiterzuentwickeln.

Selbstverständlich gilt mein Dank auch all meinen Mitstudenten, -doktoranden und allen Kollegen an unserem Institut (und darüber hinaus), die mir jeder Zeit mit Rat und Tat zur Seite standen und mich bei der Veröffentlichung (der Resultate) dieser Arbeit und nicht enden wollenden Korrekturdurchgängen, bei der Lösung von (alltäglichen) experimentellen Problemen und beim Überspringen so mancher (theoretischer) Hürde unterstützt haben. Dazu gehört natürlich auch, dass ich mich an so manche 'fruitful discussion', die bekanntlich im Rheinland auch durchaus feucht-fröhlich enden kann, gerne zurück erinnern werde. Dankbar bin ich auch all meinen Freunden, die mich immer wieder aufgebaut, motiviert und (manchmal durchaus auf kreative Art und Weise) abgelenkt haben. Bitte entschuldigt, dass ich an dieser Stelle nicht jeden Einzelnen nennen kann.

Besonderer Dank gilt meiner Familie und meiner Freundin Maria, die mich mit sehr viel Geduld und Verständnis jederzeit bedingungslos unterstützt haben. Ihr wart immer ein Ansporn für mich, dieses Ziel zu erreichen, und ich danke euch, dass ihr gerade auch in stressigen Phasen immer an meiner Seite standet und auch in Zukunft stehen werdet. Solltet ihr einmal Hilfe benötigen, ihr könnt euch meiner Unterstützung gewiss sein!

CONTENTS

Contents	v
List of Figures	vii
1 Background	1
1.1 Colloidal Dispersions	1
1.2 Colloidal Interactions	2
1.3 Phase Behaviour in Colloidal Dispersions	3
1.4 Diffusion of Colloidal Particles: Brownian Motion	4
1.5 Light Forces Acting on Colloidal Particles	7
1.6 Rough Energy Landscapes	10
2 Overview	15
2.1 Experimental Set-up	15
2.2 Speckle Patterns: Optically Generated Random Potential Energy Landscapes	16
2.3 Colloids Probing a rPEL	18
2.3.1 Spatial Arrangement of Colloids in rPELs	21
2.4 Two-Dimensional Colloidal Dynamics in rPELs	24
2.4.1 Anomalous Diffusion in Correlated Potentials	24
2.4.2 Time- and Ensemble-Averages in Relaxing Systems: Evolution of Particle Dynamics in a rPEL	27
2.4.3 Anomalous Diffusion in Crowded Environments	31
3 Scientific Papers	39
3.1 Paper I: Experimental creation and characterization of random potential- energy landscapes exploiting speckle patterns	39
3.2 Paper II: Colloids Exposed to Random Potential Energy Landscapes: from Particle Number Density to Particle-Potential and Particle-Particle Interactions	55
3.3 Paper III: Particle dynamics in two-dimensional random-energy landscapes: Experiments and simulations	69
3.4 Paper IV: Particle Dynamics in Rough Potentials with Spatial Correlations .	83

3.5	Paper V: Time- and ensemble-averages in evolving systems: the case of Brownian particles in random potentials	91
3.6	Paper VI: Anomalous Colloidal Diffusion: Interplay of Crowding and an External Random Potential	103
3.7	Paper VII: Colloids in light fields: Particle dynamics in random and periodic energy landscapes	123

LIST OF FIGURES

1.1	The colloidal length scale	1
1.2	Hard sphere potential	3
1.3	Hard disc phase diagram	4
1.4	Trajectories and displacement distributions for normal and sub-diffusion	5
1.5	Geometric optics	8
1.6	Kilimanjaro mountain range	11
1.7	Examples for energy landscapes	11
2.1	The experimental set-up	15
2.2	Intensity and potential pattern	17
2.3	rPEL and its characteristics	17
2.4	Particle in a rough potential	18
2.5	'State diagram'	19
2.6	Particles sampling the landscape	20
2.7	Time-averaged particle density	21
2.8	$C(r)$, $g^{(1)}(r)$ and $g^{(2)}(r)$	22
2.9	TEAMSD, $D(t)$, $\mu(t)$ and $\alpha(t)$ as a function of laser power	24
2.10	Diffusion coefficient $D(t)$ as a function of the particle radius R	26
2.11	Diffusion coefficient $D(t)$ for different starting times t_{start}	28
2.12	Quenched vs relaxed system: $D(t)$ and EB	29
2.13	TAMSDs	31
2.14	Dense heterogeneous dynamics: Single particle trajectories	33
2.15	P_L - ϕ_A -diagram for short- and long-term dynamics	35

This page has been left intentionally blank.

BACKGROUND 1

1.1 Colloidal Dispersions

Colloids are particles which have a size between ≈ 1 nm to $10 \mu\text{m}$ in at least one of their dimensions, i.e. they are bigger than atoms and molecules but smaller than macroscopic objects which can be resolved by the human eye [1]. The typical colloidal length scale, which includes e.g. proteins and bacteria, is shown in Fig. 1.1 alongside a recorded image of our model system and some examples of objects with other length scales.

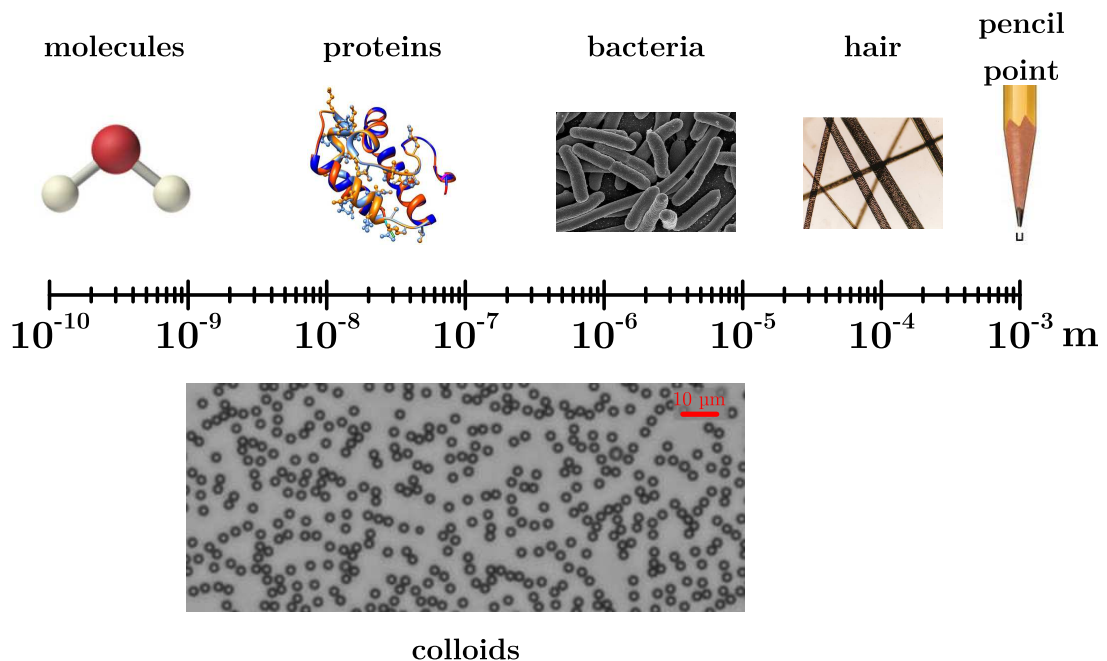


Figure 1.1: The colloidal length scale ($10^{-9} - 10^{-5}$ m) in comparison to other systems. At the bottom a recorded image of a colloidal sample with particles of radius $R = 1.4 \mu\text{m}$ is shown.

1.2 Colloidal Interactions

A colloidal dispersion usually consists of at least two phases, i.e. the colloids (dispersed phase) are dispersed in a continuous dispersion medium (dispersing phase), whereby either phase can be gaseous, liquid or solid; the exception is a gas phase dispersed in a gas, which is not a colloidal dispersion. Typical examples for the variety of these heterogeneous systems from everyday life are paint, ink, blood (all solid-liquid), fog (liquid-gas), and milk (liquid-liquid). In this work, a dispersion of solid particles in water is used (Fig. 1.1 bottom).

The lower boundary of the length scale is defined such that the dispersion medium can be seen as a continuum compared to the dispersed particles and hence quantum mechanical effects can be neglected. The upper limit is given by the internal thermal energy of the colloidal system, which has to be either in the range of or greater than the gravitational potential energy of the particles, such that thermal fluctuations in the system are still apparent and random motion of the particles is relevant (Sec. 1.4). Therefore, colloidal systems, driven by thermal energy and entropic forces, tend to move towards equilibrium and thus show, depending on inter-particle forces and the concentration of the dispersed phase, a rich phase behaviour.

1.2 Colloidal Interactions

Although each individual particle in a colloidal dispersion may have a small size and hence a low surface area, the large number of particles (of the order 10^{12} - 10^{14} /litre for $1\ \mu\text{m}$ particles) means the total surface area can be very large; hence the interface between the colloid and the dispersion medium is hugely important. Moreover, particles tend to build large agglomerates hence minimizing their free surface energy. An omnipresent attractive force between atoms, molecules or colloidal particles is the so called van der Waals force. If two particles approach each other, fluctuations in the surface charges induce dipole moments which leads to an attractive net force between the particles and favours aggregation. Thus, unwanted aggregation has to be prevented by modification of particle-particle interactions and stabilization of the particles in the dispersion. In this work, a repulsive force component was added in order to exploit charge stabilization. Dispersing charged particles in water results in an interplay between the attractive van der Waals force and the screened repulsive electrostatic forces between like-charged particles, which can be described by the so called Derjaguin-Landau-Verwey-Overbeek theory. The screening of the electrostatic repulsion is

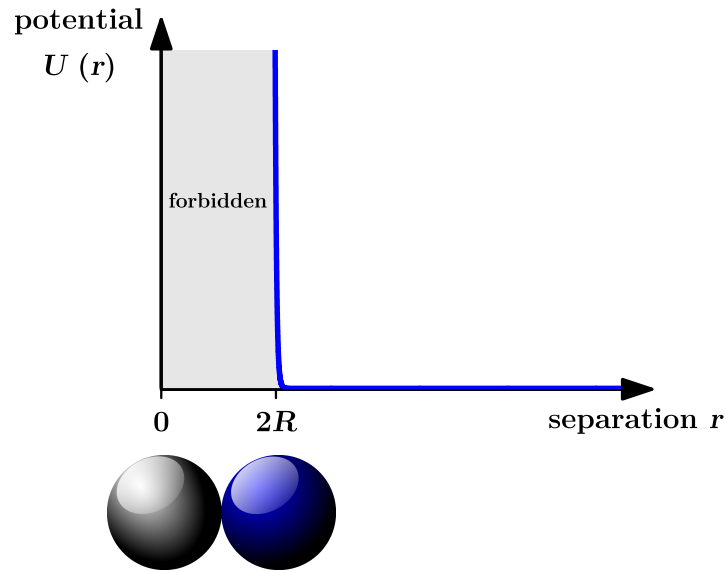


Figure 1.2: Illustration of the separation (r) dependent pair-potential $U(r)$ for hard sphere systems. The potential is infinitely large up to particle contact at $2R$ and zero at larger separations.

caused by dissolved ions in the solution, which build a layer of counterions around the particle and hence maintain overall charge neutrality. The thickness of this layer and thus the screening length strongly depends on the (number of) ions in the water and thus the range of the repulsion can be tuned via the salt concentration. If the range of the forces is very short in comparison to particle size, the interparticle forces can be approximated by the well-known hard-sphere interaction [2]. The resulting hard-sphere pair potential, which is infinitely large up to particle contact and zero at larger separations, is shown schematically in Fig. 1.2.

1.3 Phase Behaviour in Colloidal Dispersions

Fig. 1.3 schematically shows the phase behaviour of a two-dimensional colloidal dispersion with interparticle forces, which can be described by the hard-sphere model, as a function of the particle concentration $\phi_A = N\pi R^2/A$, where N is the number of particles, R is the average particle radius and A is the area of the field of observation; ϕ_A is hence the normalized two-dimensional particle density. In a monodisperse mixture and at low concentrations the system represents a heterogeneous liquid. An increase of the particle concentration does not change the disordered arrangement of the particles. However, the

1.4 Diffusion of Colloidal Particles: Brownian Motion

excluded volume increases and thus at $\phi_A \approx 0.7$, an entropy driven transition to an ordered crystalline phase sets in [2]. Unlike in three dimensions, in two dimensions an additional hexatic phase seemingly occurs in between the dense liquid and the solid ($0.7 \lesssim \phi_A \lesssim 0.72$) [3–7]. The origin and order of this transition are still under debate [3, 8–10] and depend on external influences on the system. The closed packing in a two-dimensional hard-sphere system corresponds to a geometrically possible regular triangular particle arrangement with $\phi_{A,cp} = \pi/\sqrt{12} \approx 0.907$ [11]. In non-equilibrium systems, such as those with high polydispersity, an amorphous glass phase can occur at $\phi_A \gtrsim 0.8$ [12–14].

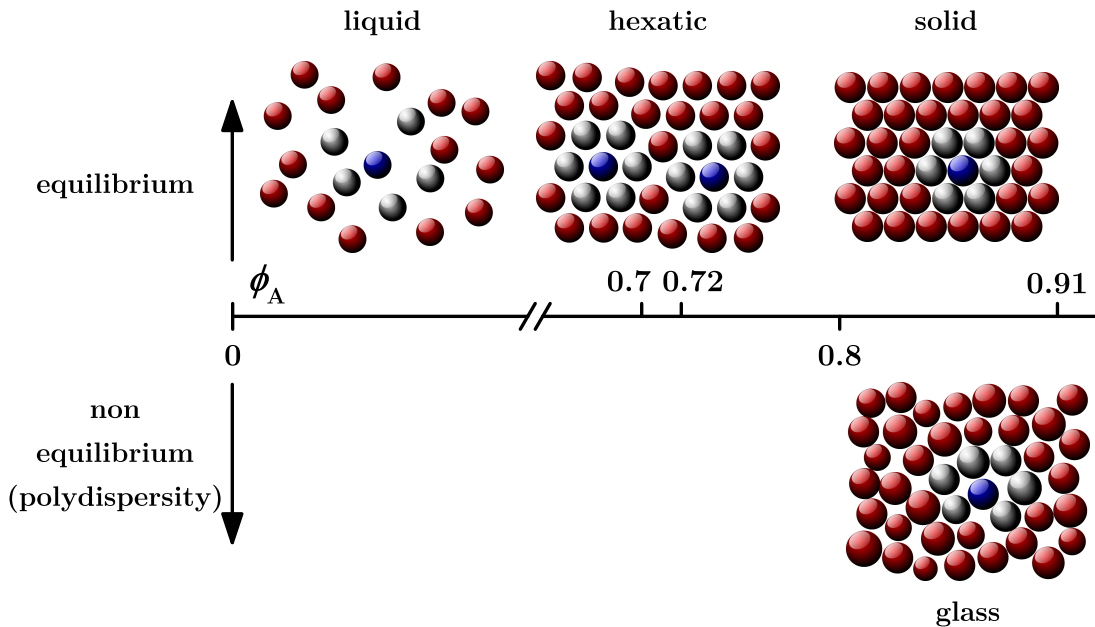


Figure 1.3: Schematic phase diagram for hard sphere systems in two-dimensions. Schematic showing the liquid (top left), the hexatic phase ($0.7 \lesssim \phi_A \lesssim 0.72$, top centre), the ordered solid ($\phi_A \gtrsim 0.72$, top right) and the amorphous glass phase (only in polydisperse samples, $\phi_A \gtrsim 0.8$, bottom). One particle and its next nearest neighbours are highlighted in blue and grey respectively, illustrating the local spatial arrangement.

1.4 Diffusion of Colloidal Particles: Brownian Motion

Colloidal particles dispersed in a liquid undergo random motion, which is driven by thermal energy. Due to collisions with solvent molecules a randomly fluctuating force acts on the particles. The resulting dynamic response, the so called Brownian motion (BM), can be

described by a random walk. Fig. 1.4 (a) shows a typical trajectory of a particle undergoing BM (black line) in two dimensions. Since motion in the x - and y -directions are statistically independent and a separate analysis of the diffusion in each of the directions is admissible, a one-dimensional analysis of the dynamical behaviour was performed. Thus, looking at the particle's position along one direction as a function of time, t (Fig. 1.4 (b), black line) reveals the typical dynamical behaviour of free diffusion.

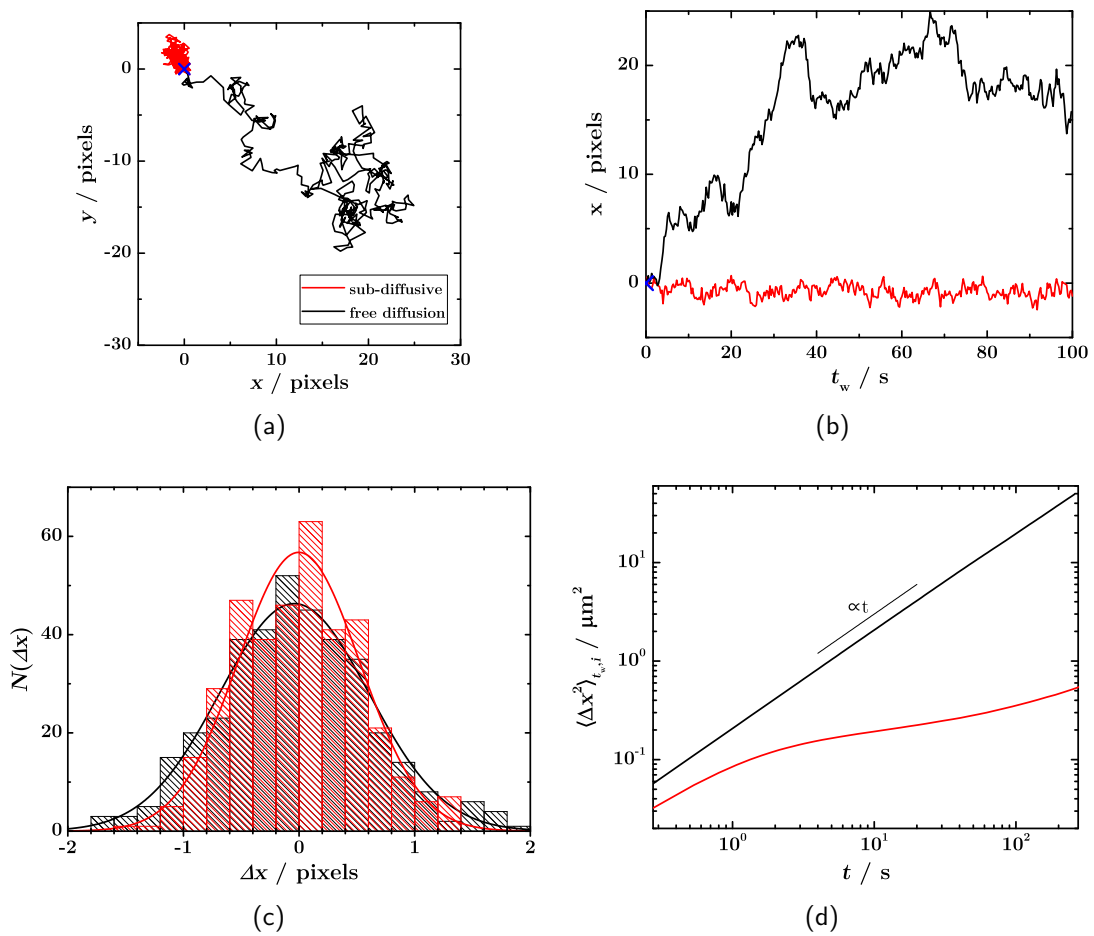


Figure 1.4: (a) Typical two-dimensional trajectories of a particle following normal diffusion (black) and one with sub-diffusive behavior (red); (b) The particles' positions in the x -direction as a function of waiting time, t_w ; (c) The number distribution of particle displacements $N(\Delta x)$ at lag time $t = 100$ s and a Gaussian fit to the data; (d) The time- and ensemble-averaged mean-squared displacement $\langle \Delta x^2 \rangle_{t_w, i}$.

To quantify the time-dependent dynamic behaviour of the particle ensemble, the analysis of the probability distribution of particle displacements, the so called van Hove self

1.4 Diffusion of Colloidal Particles: Brownian Motion

correlation function, has to be analysed. This is defined as [15–17]:

$$G_s(\Delta x, t) = \langle \delta [\Delta x + \mathbf{x}_i(t_w) - \mathbf{x}_i(t_w + t)] \rangle_{t_w, i} \quad (1.1)$$

$$= \frac{1}{N} \left\langle \sum_{i=1}^N \delta [\Delta x + \mathbf{x}_i(t_w) - \mathbf{x}_i(t_w + t)] \right\rangle_{t_w} \quad (1.2)$$

$$= \frac{N(\Delta x, t)}{2\pi w \Delta x \left(\sum_{i=1}^N N(\Delta x, t) \right)} \quad (1.3)$$

with the number of particles N , the Dirac delta function $\delta[\dots]$, the displacement counter $N(\Delta x, t)$, and the histogram bin width w . Furthermore, averaging over the particle ensemble i and/or waiting time t_w is indicated by angle brackets. The distribution G_s describes the probability that a particle moves a distance Δx in a time lag t and displays Gaussian behaviour for Brownian motion. Fig. 1.4 (c) shows the displacement counter $N(\Delta x, t)$ for a lag time of 100 s and the corresponding Gaussian fit (indicated by a black line for normal BM). In the absence of an external potential, the total net force on a particle for long times is zero and the first moment of the particle displacement distribution, i.e. its mean $\langle \Delta x \rangle$, is also zero, as can be seen in Fig. 1.4 (c). Therefore, the second moment of the distribution, i.e. the variance $\langle \Delta x^2 \rangle$, must be considered in order to analyse the dynamic behaviour of the particles. The time- and ensemble-averaged mean-squared displacement (MSD) for normal BM is given by

$$\langle \Delta x^2(t) \rangle = \left\langle [\mathbf{x}_i(t_w + t) - \mathbf{x}_i(t_w)]^2 \right\rangle \quad (1.4)$$

$$= 2D_0 t \quad (1.5)$$

where the proportionality constant D_0 is called the self-diffusion coefficient. Einstein showed in 1905 that the MSD is proportional to time (Eq. (1.5)) for freely diffusing particles [18], as can also be seen in Fig. 1.4 (d). If the particle motion is influenced by the particle concentration or an external potential, ‘anomalous’ diffusion emerges, and the MSD is represented by:

$$\langle \Delta x^2(t) \rangle \propto t^\mu \quad (1.6)$$

with the diffusive exponent μ . The lag time dependence of μ can be calculated from

$$\mu(t) = \frac{\partial}{\partial \log(t)} \log(\langle \Delta x^2(t) \rangle) . \quad (1.7)$$

If particles are hindered in their motion, they exhibit sub-diffusion, which is given by $\mu(t) < 1$. A typical trajectory, the resulting displacement distribution and the time- and ensemble-averaged MSD for a particle undergoing such sub-diffusive behaviour is shown in Fig. 1.4, indicated by the red line. In comparison with the freely diffusing particle, the sub-diffusive trajectory shows strongly hindered motion for all lag times, i.e. only small displacements (Fig. 1.4(b)). Hence the variance of the displacement distribution (Fig. 1.4(c)), i.e. its MSD, is smaller than for free diffusion (Fig. 1.4(d)). Furthermore, the lag time-dependent diffusion coefficient $D(t)$ is given by

$$D(t) = \frac{1}{2} \frac{\partial}{\partial(t)} \langle \Delta x^2(t) \rangle . \quad (1.8)$$

In the absence of drift, one can take the next higher non-zero moment of the displacement distribution into account $\langle \Delta x^4 \rangle$ and can calculate the so called non-Gaussian parameter (NGP), α_2 :

$$\alpha_2(t) = \frac{\langle \Delta x^4(t) \rangle}{3 \langle \Delta x^2(t) \rangle^2} - 1 . \quad (1.9)$$

The non-Gaussian parameter is the excess kurtosis of the displacement distribution and thus indicates deviations of the shape of the measured distribution from a Gaussian.

1.5 Light Forces Acting on Colloidal Particles

When exposed to a light field colloidal particles are subjected to optical forces; these have been described extensively [19–26].

For illustration, consider a transparent dielectric particle with radius R and a refractive index, n_p , which is higher than that of the surrounding medium, n_m , interacting with a collimated light beam. The refractive index mismatch causes the incident light to be scattered, reflected and absorbed by the particle (Fig. 1.5). The transferred momentum of the photons induces a reaction force on the particle, the so called radiation pressure, which

1.5 Light Forces Acting on Colloidal Particles

acts in the beam direction and is given by

$$F_{\text{rad}} = q \frac{n P_L}{c} \quad (1.10)$$

with the refractive index ratio $n = n_p/n_m$, the power of the photon source, i.e. laser power, P_L , and speed of light in a vacuum c . In the case of almost transparent dielectric spherical particles, the photons are scattered rather than reflected or absorbed and the quality factor q can be assumed to be in the order of 10^{-1} [24].

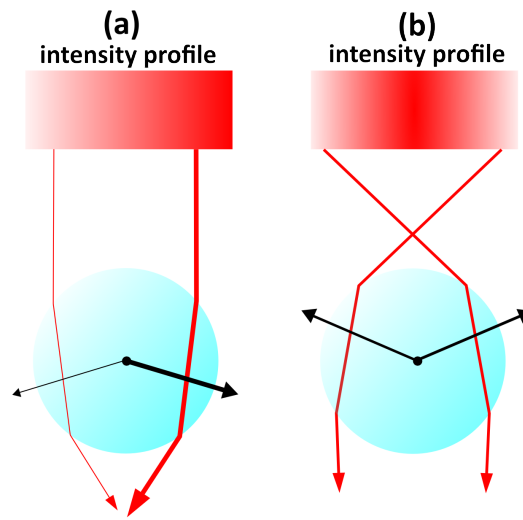


Figure 1.5: Optical gradient forces in the ray optics regime: (a) A spherical particle with $n_p > n_m$ is exposed to a collimated laser beam with a linear intensity gradient from left to right. The restoring force acts in the direction of the highest intensity, (b) The same particle exposed to a strongly focussed Gaussian beam. The axial light gradient forces the particle to the beam centre, while the gradient in the beam direction generates a restoring force, pulling the particle into the beam focus. Adapted from Ref. [25].

When calculating the optical forces that act on the spherical particles, two limiting cases typically are considered; the optical forces for these can be calculated exactly. If the particle is much larger than the wavelength of the trapping laser, i.e. $R \gg \lambda$, the light-induced forces can be described with geometrical (ray) optics. In this regime, refraction of light rays at the spherical surface of the particles is important, since it leads to a momentum transfer from photon to particle and therefore is the origin of a restoring force that acts in the direction of the light gradient. Fig. 1.5 schematically shows the forces on a particle for a light field with a linear gradient (a) and for the case of a strongly focussed laser with a Gaussian TEM₀₀ mode (b), i.e. highest intensity in the beam centre [25]. If a spherical

particle with $n_p > n_m$ is exposed to a collimated laser beam, the light rays are refracted towards the centre of the sphere. Thus, a linearly increasing intensity gradient leads to a restoring force that acts in the direction of the highest intensity (Fig. 1.5(a)). Furthermore, a particle exposed to a strongly focussed Gaussian beam will be forced by the axial light gradient to stay at the beam centre, whilst the gradient in the beam direction generates a restoring force, pulling the particle against the radiation pressure into the focal plane (Fig. 1.5(b)). Therefore, a spherical dielectric particle can be trapped in three dimensions with a single laser, an arrangement, first described by A. Ashkin and co-workers in 1986 [27] and commonly called optical tweezers.

If the particle is much smaller than the wavelength of the laser, i.e. $R \ll \lambda$, Rayleigh scattering becomes apparent. The electromagnetic field induces a dipole moment in the polarizable particle, which itself then acts as a point dipole. In the Rayleigh regime, the optical forces can be separated into two components: the scattering and gradient forces. On the one hand, the absorption and reemittance of light by the induced dipole can be summarized in the scattering force F_{scat} , which is given by [27]:

$$F_{\text{scat}} = \frac{128\pi^5 R^6 n_m}{3\lambda^4 c} \left(\frac{n^2 - 1}{n^2 + 2} \right)^2 I(\mathbf{r}) . \quad (1.11)$$

F_{scat} is proportional to the intensity of the incident laser beam $I(\mathbf{r})$, strongly depends on the particle size ($\propto R^6$) and, due to its origin, acts along the beam direction. On the other hand, an inhomogeneous light field permanently interacts with the induced dipole via the gradient force, which can be calculated in the time-averaged form as [22]:

$$F_{\text{grad}} = \frac{2\pi R^3 n_m}{c} \left(\frac{n^2 - 1}{n^2 + 2} \right) \nabla I(\mathbf{r}) . \quad (1.12)$$

F_{grad} is proportional to the intensity gradient $\nabla I(\mathbf{r})$ and for $n_p > n_m$ points into the direction of the highest intensity. If the gradient force exceeds the scattering force, i.e. $F_{\text{grad}} > F_{\text{scat}}$, as is the case with a strongly focussed Gaussian beam, the particle is pulled towards the focal spot, the region of highest intensity.

The case of a particle with a size similar to the wavelength of the trapping beam is more complex [23, 25, 26, 28, 29]; this is not well described by either of the two above introduced forces. Analytical solutions for this size regime are only known for some specific cases. For example, the generalized Lorentz-Mie theory provides a solution for the scattering of a plane

1.6 Rough Energy Landscapes

wave at a spherical dielectric particle. Since it includes the coherence of the laser light as well as the curvature of the particle, it is valid in a large size range, from very small particles (as usually described by the Rayleigh model) up to the ray optics regime [26]. Due to the complexity and computational costs, this theory is beyond the scope of this work and is not described here in detail.

Single beam optical gradient traps, i.e. optical tweezers, are used in many different scientific fields, such as physics, biology and medicine. Due to the ability to measure and apply forces with optical tweezers in the pico-Newton range and length scales in the nanometre to micron range, they have become a sophisticated tool to study biological and molecular phenomena, such as the observation of single-molecule motor movements [30, 31] and the stretching of DNA molecules [32]. Furthermore, the manipulation and investigation of colloidal systems is possible, since the applied optical forces and thus the potential energy of the light traps is of the order of the thermal energy of colloidal particles. Instead of optical tweezers, i.e. zero-dimensional optical traps, more complex higher dimensional optical intensity landscapes, such as multiple optical tweezers [33] (in three dimensions) or sinusoidal [34] and random interference patterns [35, 36] (both in two dimensions) can be realized by carefully manipulating the light field. Thus the influence of complex, modifiable energy landscapes on particle arrangement and dynamics can be studied.

1.6 Rough Energy Landscapes

Energy landscapes represent the energy of a system as a function of its (configurational) coordinates and/or other parameters of the system [37]. Fig. 1.6 shows a hiker on a mountain range as an example for a potential energy landscape (PEL). The walker follows a certain track on the (two-dimensional) spatial landscape, while his current potential energy is determined by the altitude. Thus the walker's potential energy can approximately be described by a distance to altitude diagram, i.e. a one-dimensional PEL (inlet). In fact, all movements can be examined as a function of an underlying potential landscape and thus a model system, as presented in this thesis, can be used to mimic the (anomalous) dynamics.

The concept of energy landscapes is used in many scientific fields to determine properties of systems ranging from small molecules, proteins and other biomolecules to large clusters, glasses and even biological cells [37]. Applications include transport in materials with defects

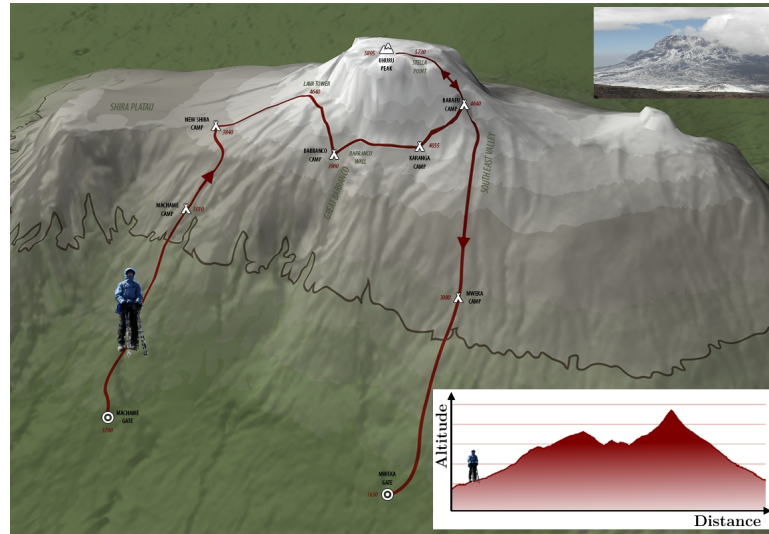


Figure 1.6: Kilimanjaro mountain range, an example for a potential energy landscape. When climbing the mountain a walker follows a certain track on a two-dimensional spatial landscape, while the third coordinate here is the altitude. Thus the walker’s potential energy can approximately be described by a distance to altitude diagram, i.e. a one-dimensional potential energy landscape (inlet). Adapted from Ref. [38].

or impurities [39], in inhomogeneous media [40, 41] such as biological cells [42–44], and in the presence of fixed obstacles, e.g. in a Lorentz gas [45]. Recently, energy landscapes have also been used to describe particle dynamics in glasses [13, 46–49] (Fig. 1.7 (a)), as well as to determine (bio)chemical reactions [50], and the folding of proteins and DNA [51, 52] (Fig. 1.7 (b)).

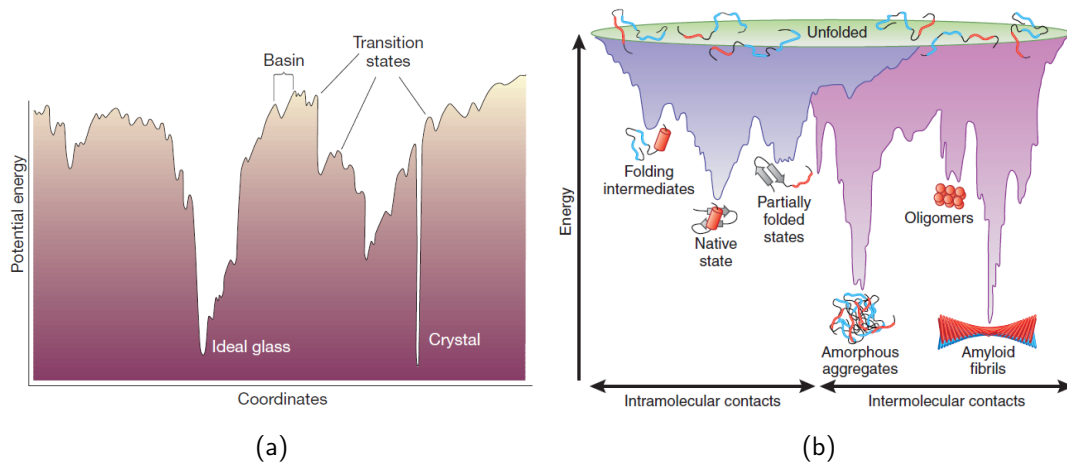


Figure 1.7: Schematic examples for rough energy landscapes: (a) potential energy landscape of a dense colloidal system as a function of configurational coordinates [46] and (b) folding energy landscape describing states of protein folding and aggregation [52].

Bibliography

The focus of this thesis is rough energy landscapes, which have been used in the interpretation of several experimental observations, such as the behavior of RNA, proteins and transmembrane helices [53, 54]. Furthermore, random potential energy landscapes (rPEL) often provide a very useful description of the effect of disorder on the dynamics [49, 55, 56]. Recent experiments in which single-molecule and -particle tracking methods were applied to biological samples such as cells and their membranes [41, 42], biofilms [57] or prototypical crowded fluids, e.g. dextran [58], revealed anomalous dynamics in such systems. Thus anomalous diffusion of particles or molecules in crowded environments, as investigated in this work, can be seen as a general scenario, encountered for example by a single species diffusing through a biological cell in the presence of other species. Furthermore, the dynamics are not only influenced by the concentration of the species under investigation, i.e. the tracer particles, or the overall concentration within the cell, but also by the presence of osmotic gradients or adsorption sites [41–43, 57, 58]. Although it seems counter-intuitive to consider sub-diffusion as a good strategy for a tracer particle to more quickly find its target in such an environment compared with the case of free diffusion, it has been proven that sub-diffusive dynamics can decrease the time until a biological species reaches a favourable spot or target as seen in special adsorption or reaction sites in cells, on cell membranes or DNA [59]. The various interactions of the species with its (micro-)environment result in an underlying potential energy landscape, which influences the (anomalous) diffusion process. The diffusion phenomena occurring from the intersection of both high concentrations, i.e. an crowded environment, and the amplitude of an underlying random potential has been analysed in this work with the help of a model system, which was experimentally realized by exploiting the interaction of light with spherical colloidal particles. In contrast to the biological examples described above, both the mobile obstacles and the diffusing tracer species have been mimicked with identical colloidal particles.

Bibliography

- [1] Hamley, I. W. *Introduction to Soft Matter*; John Wiley & Sons, Ltd, 2007.
- [2] Jones, R. *Soft Condensed Matter*; Oxford Master Series in Physics; OUP: Oxford, England, 2002.
- [3] Bernard, E. P.; Krauth, W. *Phys. Rev. Lett.* **2011**, *107*, 155704.
- [4] Kim, J.; Kim, C.; Sung, B. J. *Phys. Rev. Lett.* **2013**, *110*, 047801.
- [5] Marcus, A. H.; Schofield, J.; Rice, S. A. *Phys. Rev. E* **1999**, *60*, 5725.
- [6] Cui, B.; Lin, B.; Rice, S. A. *J. Chem. Phys.* **2001**, *114*, 9142.

- [7] Zangi, R.; Rice, S. A. *Phys. Rev. Lett.* **2004**, *92*, 035502.
- [8] Löwen, H. *Phys. Rev. E* **1996**, *53*, 53.
- [9] Wang, Z.; Alsayed, A. M.; Yodh, A. G.; Han, Y. *J. Chem. Phys.* **2010**, *132*, 154501.
- [10] Dillmann, P.; Maret, G.; Keim, P. *J. Phys.: Condens. Matter* **2012**, *24*, 464118.
- [11] Bayer, M.; Brader, J. M.; Ebert, F.; Fuchs, M.; Lange, E.; Maret, G.; Schilling, R.; Sperl, M.; Wittmer, J. P. *Phys. Rev. E* **2007**, *76*, 011508.
- [12] Roux, J. N.; Barrat, J. L.; Hansen, J.-P. *J. Phys.: Condens. Matter* **1989**, *1*, 7171.
- [13] Heuer, A. *J. Phys.: Condens. Matter* **2008**, *20*, 373101.
- [14] Bonales, L. J.; Martinez-Pedrero, F.; Rubio, M. A.; Ortega, F. *Langmuir* **2012**, *28*, 16555.
- [15] Van Hove, L. *Phys. Rev.* **1954**, *95*, 249.
- [16] Hansen, J.-P.; McDonald, I. R. *Theory of Simple Liquids*, 3rd ed.; Academic: London, England, 2006.
- [17] Hopkins, P.; Fortini, A.; Archer, A. J.; Schmidt, M. *J. Chem. Phys.* **2010**, *133*, 224505.
- [18] Einstein, A. *Ann. Phys.* **1905**, *322*, 549.
- [19] Ashkin, A. *Phys. Rev. Lett.* **1970**, *24*, 156.
- [20] Gordon, J. P. *Phys. Rev. A* **1973**, *8*, 14.
- [21] Ashkin, A. *Biophys. J.* **1992**, *61*, 569.
- [22] Harada, Y.; Asakura, T. *Opt. Commun.* **1996**, *124*, 529.
- [23] Tlusty, T.; Meller, A.; Bar-Ziv, R. *Phys. Rev. Lett.* **1998**, *81*, 1738.
- [24] Molloy, J. E.; Padgett, M. J. *Contemp. Phys.* **2002**, *43*, 241.
- [25] Neuman, K. C.; Block, S. M. *Rev. Sci. Instrum.* **2004**, *75*, 2787.
- [26] Bowman, R. W.; Padgett, M. J. *Rep. Prog. Phys.* **2013**, *76*, 28.
- [27] Ashkin, A.; Dziedzic, J. M.; Bjorkholm, J. E.; Chu, S. *Opt. Lett.* **1986**, *11*, 288.
- [28] Bonessi, D.; Bonin, K.; Walker, T. *J. Opt. A: Pure Appl. Opt.* **2007**, *9*, 228.
- [29] Stilgoe, A. B.; Nieminen, T. A.; Knöner, G.; Heckenberg, N. R.; Rubinsztein-Dunlop, H. *Opt. Express* **2008**, *16*, 15039.
- [30] Svoboda, K.; Schmidt, C. F.; Schnapp, B. J.; Block, S. M. *Nature* **1993**, *365*, 721.
- [31] Molloy, J.; Burns, J.; Kendrick-Jones, J.; Tregear, R.; White, D. *Nature* **1995**, *378*, 209.
- [32] Wang, M. D.; Yin, H.; Landick, R.; Gelles, J.; Block, S. M. *Biophys. J.* **1997**, *72*, 13351346.
- [33] Grier, D. G. *Nature* **2003**, *424*, 810.
- [34] Jenkins, M. C.; Egelhaaf, S. U. *J. Phys.: Condens. Matter* **2008**, *20*, 404220.
- [35] Evers, F.; Hanes, R. D. L.; Zunke, C.; Capellmann, R. F.; Beverunge, J.; Dalle-Ferrier, C.; Jenkins, M. C.; Ladadwa, I.; Heuer, A.; Castañeda-Priego, R.; Egelhaaf, S. U. *Eur. Phys. J. Special Topics* **2013**, *222*, 2995.
- [36] Evers, F.; Zunke, C.; Hanes, R. D. L.; Beverunge, J.; Ladadwa, I.; Heuer, A.; Egelhaaf, S. U. *Phys. Rev. E* **2013**, *88*, 022125.
- [37] Wales, D. J. *Energy Landscapes*; Cambridge University Press: Cambridge, England, 2004.

Bibliography

- [38] Kilimanjaro Mountain Range. http://www.tanzania-experience.com/de/wp-content/uploads/2014/08/kilimanjaro_machame_web-big.png.
- [39] Heuer, A.; Murugavel, S.; Roling, B. *Phys. Rev. B* **2005**, *72*, 174304.
- [40] Isichenko, M. B. *Rev. Mod. Phys.* **1992**, *64*, 961.
- [41] Hsieh, C.-L.; Spindler, S.; Ehring, J.; Sandoghdar, V. *J. Phys. Chem. B* **2014**, *118*, 1545.
- [42] Weiss, M.; Elsner, M.; Kartberg, F.; Nilsson, T. *Biophys. J.* **2004**, *87*, 3518.
- [43] Höfling, F.; Franosch, T. *Rep. Prog. Phys.* **2013**, *76*, 046602.
- [44] Tolić-Nørrelykke, I. M.; Munteanu, E.-L.; Thon, G.; Oddershede, L.; Berg-Sørensen, K. *Phys. Rev. Lett.* **2004**, *93*, 078102.
- [45] Höfling, F.; Franosch, T.; Frey, E. *Phys. Rev. Lett.* **2006**, *96*, 165901.
- [46] Debenedetti, P. G.; Stillinger, F. H. *Nature* **2001**, *410*, 259.
- [47] Nguyen, D.; Mallek, J.; Cloud, A. N.; Abelson, J. R.; Girolami, G. S.; Lyding, J.; Gruebele, M. *J. Chem. Phys.* **2014**, *141*, 204501.
- [48] Charbonneau, P.; Kurchan, J.; Parisi, G.; Urbani, P.; Zamponi, F. *Nat. Comm.* **2014**, *5*, 3725.
- [49] Royall, C. P.; Williams, S. R. *Phys. Rep.* **2015**, *560*, 1.
- [50] Min, W.; Xie, X. S.; Bagchi, B. *J. Chem. Phys.* **2009**, *131*, 065104.
- [51] Arcella, A.; Portelly, G.; Collepardo-Guevara, R.; Chakraborty, D.; Wales, D. J.; Orozco, M. *J. Phys. Chem. B* **2014**, *118*, 8540.
- [52] Hartl, F. U.; Hayer-Hartl, M. *Nat. Struct. Mol. Biol.* **2009**, *16*, 574.
- [53] Hyeon, C.; Thirumalai, D. *Proc. Natl. Acad. Sci. USA* **2003**, *100*, 10249.
- [54] Janovjak, H.; Knaus, H.; Muller, D. J. *J. Am. Chem. Soc.* **2007**, *129*, 246.
- [55] Chen, L.; Falcioni, M.; Deem, M. W. *J. Phys. Chem. B* **2000**, *104*, 6033.
- [56] Wolynes, P. G. *Acc. Chem. Res.* **1992**, *25*, 513.
- [57] Birjiniuk, A.; Billings, N.; Nance, E.; Hanes, J.; Ribbeck, K.; Doyle, P. S. *New J. Phys.* **2014**, *16*, 085014.
- [58] Ernst, D.; Hellmann, M.; Köhler, J.; Weiss, M. *Soft Matter* **2012**, *8*, 4886.
- [59] Guigas, G.; Weiss, M. *Biophys. J.* **2008**, *94*, 90.

2.1 Experimental Set-up

The main part of this work was the design and construction of a novel optical set-up with which a random potential energy landscape (rPEL) could be generated and to which colloids were exposed. A full description of the optical set-up and the characterization of the resulting rPEL can be found in paper I (published in [1]); a schematic and photograph of the set-up are shown in Fig. 2.1 and a short summary follows.

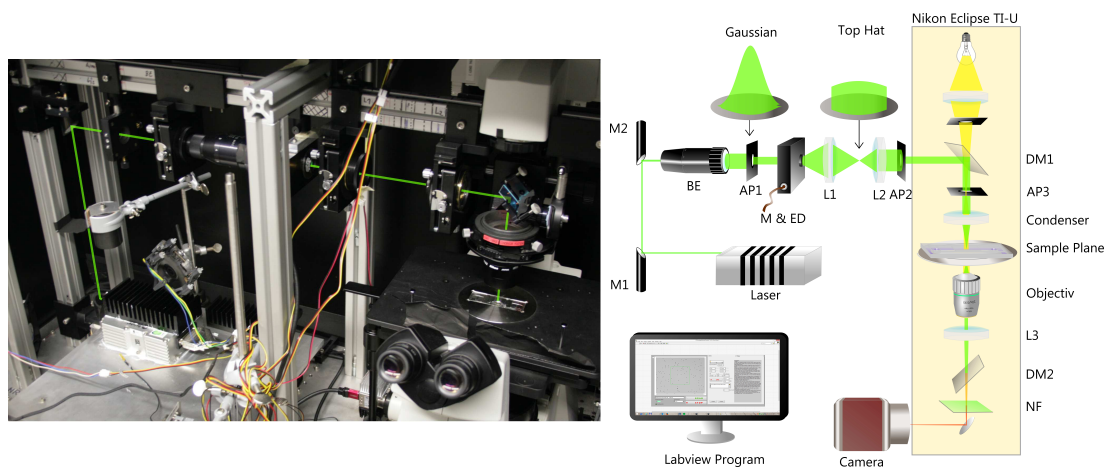


Figure 2.1: A photograph and schematic [2] of the experimental set-up used to generate random light fields to which colloidal samples were exposed. The beam path is highlighted in green.

The laser beam is steered into the sample plane of an inverted microscope (Nikon Eclipse Ti-U) with the help of three mirrors (M1, M2 and DM1 in Fig. 2.1), where the dichroic mirror is almost totally reflective for the laser wavelength but transmits most of the visible light of the microscope illumination. Colloidal samples that were sedimented into a quasi two-dimensional plane could be exposed to a light field and their motion simultaneously observed on the microscope and via a CMOS camera. Subsequently, these images

2.2 Speckle Patterns: Optically Generated Random Potential Energy Landscapes

were analysed, particle positions were obtained for each image and two-dimensional particle trajectories from time stacks of images were formed using standard particle tracking routines [3]. Furthermore, particle positions and trajectories were used to calculate statistical measures which characterize the arrangement and dynamics of the colloids in the presence of the rPEL, such as the time-averaged local particle density $\langle \rho(x, y, t) \rangle_t$ (Sec. 2.3) or the MSD $\langle \Delta r^2(t) \rangle$ (Sec. 2.4).

The central optical element of this set-up used to modify the laser beam, or more precisely its intensity distribution, is the so called Engineered Diffuser (ED, RPC Photonics) [4–6]. It consists of a random microlens array, which creates a macroscopically uniform intensity pattern with a so called top-hat intensity distribution when illuminated with a Gaussian laser beam. Nonetheless, interference between wavefronts coming from different microlenses leads to laser speckles, i.e. intensity fluctuations on the microscopic length scale of the particles. The size of the speckles can be modified with a beam expander (BE); by changing the diameter of the beam incident on the diffuser the number of illuminated microlenses, i.e. independent scattering centres, is changed. Furthermore, a motorized rotation stage to which the diffuser is mounted can be used to rotate the rough intensity pattern. This leads to a time-averaged flat intensity field and hence particles can solely be exposed to radiation pressure.

2.2 Speckle Patterns: Optically Generated Random Potential Energy Landscapes

This section describes the experimentally realized speckle patterns which represent random potential energy landscapes (rPELs) for colloidal particles. A detailed and quantitative characterization can be found in paper I and Ref. [1].

A recorded intensity pattern with randomly distributed intensities, i.e. laser speckles, is shown in Fig. 2.2. It can be rationalized as a superposition of many independent optical traps, which are randomly distributed. Therefore, colloidal particles exposed to the speckle pattern and with a refractive index larger than that of the dispersion medium, i.e. $n_p > n_m$, are pulled to regions of high intensity due to gradient forces (see Sec. 1.5). Such a particle experiences a rPEL with local properties determined by the light intensity ‘detected’ by the colloid, i.e. the intensity distribution over the whole particle volume. Thus integrating

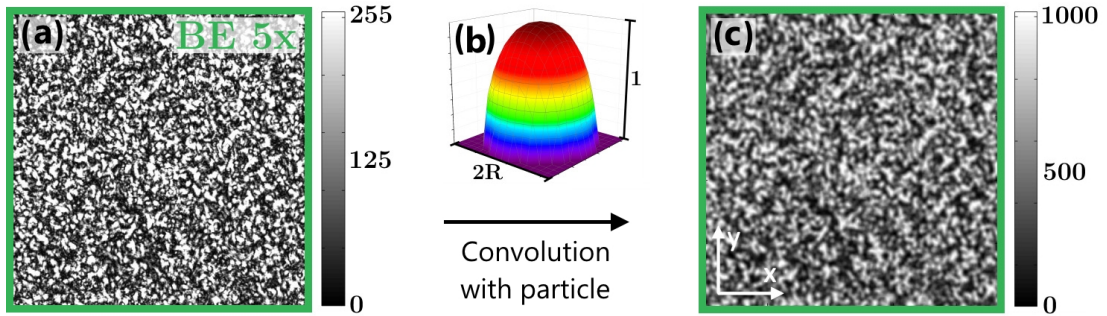


Figure 2.2: Convoluting the recorded image of the random intensity speckle pattern (a) with the volume of a test particle with radius $R = 1.4 \mu\text{m}$ (b) results in the random potential energy landscape experienced by the colloidal particle (c). The 8-bit values of the intensity and the values of the potential in arbitrary units are represented as grey levels. Adapted from Ref. [1].

the local intensity pattern $I(x, y)$ (Fig. 2.2(a)) over the particle volume (Fig. 2.2(b)) results in a local potential energy landscape $U(x, y)$ (Fig. 2.2(c)). Although the particle's polarizability and thus the exact amplitude are unknown, this method can be used to calculate the typical characteristics of the rPEL (Fig. 2.3), which are a Gaussian-shaped spatial correlation function C_U with a $1/e$ -width of about the particle size (Fig. 2.3(b)) and a Gamma-distributed potential probability density $p(U)$ (Fig. 2.3(c)).

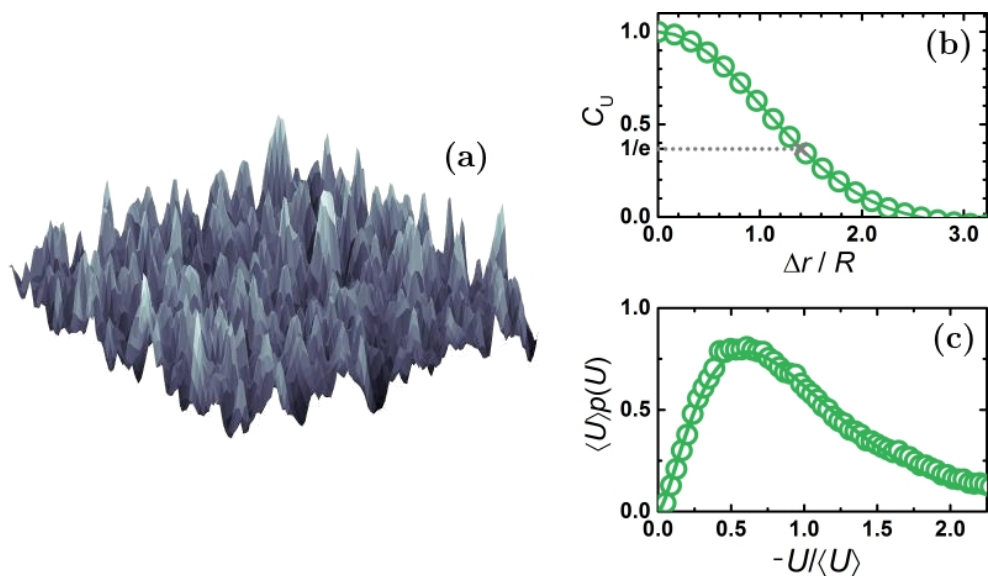


Figure 2.3: (a) Sketch of the two-dimensional rPEL used in experiments. Characteristic for the potential landscape are a Gaussian-shaped spatial correlation function C_U with $1/e$ -width $1.9 \mu\text{m}$ (b) and a Gamma-distributed potential probability density $p(U)$ (c).

2.3 Colloids Probing a rPEL

Besides the experimental realization of an optical random potential energy landscape, the systematic investigation of the modified spatial arrangement and dynamics of individual particles as well as particle ensembles exposed to such rPELs formed the main part of this thesis, as described in papers II-VI.

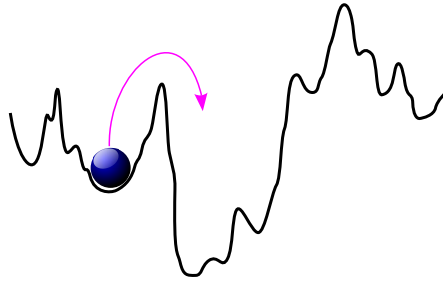


Figure 2.4: Sketch of a particle exploring a rough potential energy landscape.

An understanding of the influence of a random potential on the arrangement and dynamics of colloidal particles can be gained through examining individual particles in a one-dimensional rPEL (Fig. 2.4). Particles, which are initially quenched in a non-equilibrium state, move via BM and explore the potential landscape with all its valleys, saddles and peaks and hence their distribution evolves towards equilibrium. Since this is a one-dimensional problem, the diffusing particles have to overcome every single barrier, i.e. the local potential maxima, to mainly populate the deepest minima. They can however also get trapped for a long time in metastable states before equilibrium is reached. Particle dynamics are thus strongly sub-diffusive in the presence of a rPEL.

Compared to the one-dimensional picture, the particle diffusion in a two-dimensional rPEL is slightly different. In two dimensions, particles can circumvent potential hills by crossing adjacent saddles and can thus move around the maxima. Hence, the diffusivity of the particles is increased in contrast to the one-dimensional case even though dynamics are still sub-diffusive [7]. The time a particle needs to overcome the barriers in order to sample the whole landscape depends on the potential roughness, i.e. its spatial correlation function, $C(U)$, and the potential energy distribution, $p(U)$. Particle dynamics can therefore be adjusted from a normal diffusive to a strongly sub-diffusive state by changing these parameters. In most of the experiments described here, this was done by adjusting the laser power, P_L , which is proportional to the width of the potential and hence the distribution

of energy barriers [8], while the spatial correlation function was held constant. The particle concentration, ϕ_A , was also modified so that particle arrangement and dynamics could be studied as a function of both laser power and concentration. Fig. 2.5 shows sketches characterizing the different regimes investigated in this thesis in the P_L - ϕ_A -diagram. The effects of either increasing particle concentration at fixed laser power (horizontal lines) or increasing laser power at a range of concentrations (vertical lines) were analysed separately (see Sec. 2.4.1 and Sec. 2.4.3, respectively). Terms and colors used to indicate the laser power and particle concentration regimes focused on are outlined in Tab. 2.1.

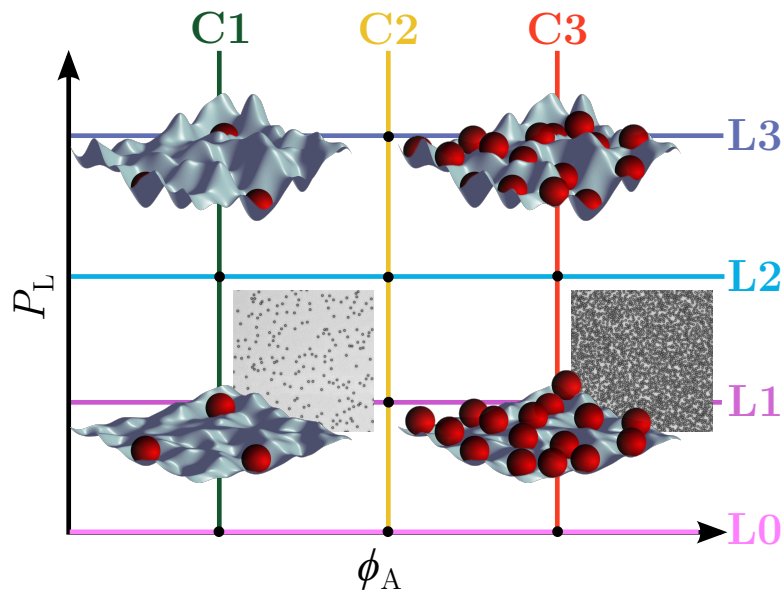


Figure 2.5: The explored range of laser power P_L and particle concentration ϕ_A includes different scenarios. The effects of either increasing particle concentration at different values of the laser power (horizontal lines) or increasing laser power at a range of concentrations (three vertical lines are shown exemplarily) were analysed. Sketches illustrating different values of concentration and potential roughness (laser power) are shown for four selected situations in the diagram. For two of them, recorded images of the colloidal samples interacting with the rPEL are also shown.

All experimental results, whether they describe static spatial measures or time-dependent dynamics, are based on exact detection of particle positions for all measurement times. Either particle trajectories can be subsequently calculated or the number of particles $N(x, y, t)$ in each region of size $\Delta x \Delta y$ at position $\mathbf{r}_i = (x_i, y_i)$ at each time t can be used to calculate the local particle density $\rho(x, y, t) = N(x, y, t) / \Delta x \Delta y$. The necessary discretization and resolution of the measured data as well as the whole calculation procedure are further described in paper II.

2.3 Colloids Probing a rPEL

Table 2.1: Terms and colors used to indicate different laser power and particle concentration regimes (cf. Fig. 2.5).

term	laser power P_L (mW)	area fraction ϕ_A	line/symbol color
L0	0		pink
L1	917		purple
L2	1640		light blue
L3	2600		dark blue
C1		0.05	green
C2		0.25	orange
C3		0.45	red

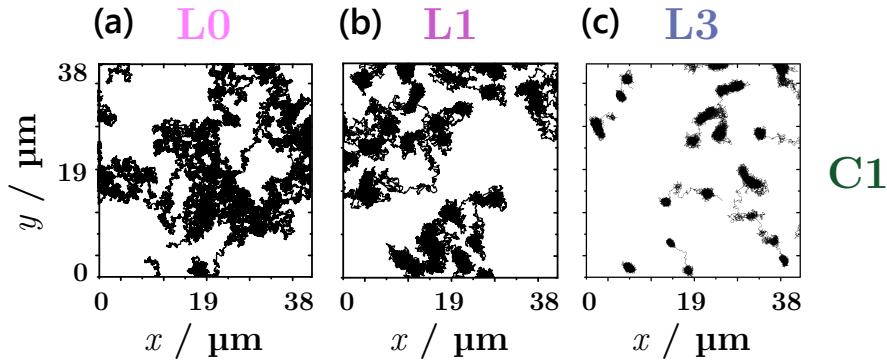


Figure 2.6: Colloidal particles interacting with the light field sample the rPEL. Trajectories in a central region of the colloidal sample for a measurement time $t_{\max} = 7200$ s are shown for low concentration C1 and increasing laser power L0 (a), L1 (b), and L3 (c). Trapping of particles in small regions becomes apparent for high laser power. Thus, only a small part of the sample is visited by particles within the time of the measurement t_{\max} .

The first step in understanding how particles interact with a two-dimensional rPEL in experiments is to investigate the sampling behaviour of the colloids in such a situation by analysing their trajectories as a function of the potential roughness. Fig. 2.6 shows the particle trajectories in a centred region of a dilute colloidal sample, C1, for measurement time $t_{\max} = 7200$ s, as a function of the laser power, when sub-diffusive behaviour in the presence of a rPEL becomes apparent comparing the picture in the absence of a rough potential L0 (a) with the ones recorded with laser power L1 (b) and L3 (c). Trapping of particles in small regions occurs for high laser powers and is stronger with higher laser powers, which equates to deeper mean potential depths. The particles thus visit only a part of the sample and at high laser power, L3, their movements are strongly restricted

to the sites of highest intensity, i.e. lowest potential (Fig. 2.6 (c)). A rough potential in combination with low particle concentration thus leads to an ‘undersampling’ of regions with high potential energies. In terms of the landscape picture, this is equivalent to particles moving around instead of over the hills. As a result, the time-averaged local particle density $\langle \rho(\mathbf{r}, t) \rangle_t$, which holds spatial information about the underlying potential, becomes a discretized particle density landscape where density maxima correspond to minima in the potential (Fig. 2.7 (a)). For high concentrations, particle-potential as well as particle-particle interactions have to be considered and hence $\langle \rho(\mathbf{r}, t) \rangle_t$ does not represent the rPEL any more, but a landscape smoothed by inter-particle collisions and diffusive particles (Fig. 2.7 (b)). A more detailed study of the high concentration regime, i.e. the influence of a crowded environment on the particle dynamics, is described in Sec. 2.4.3 and paper VI.

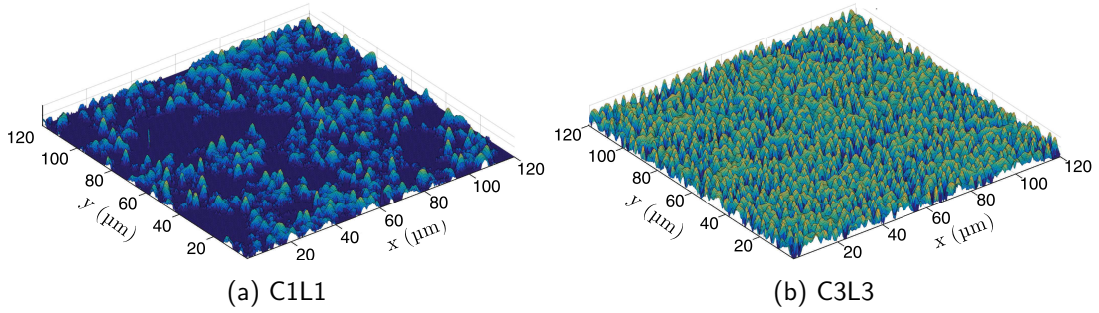


Figure 2.7: Time-averaged particle density landscape, $\langle \rho(\mathbf{r}, t) \rangle_t$, (a) for low laser power (L1) and low concentration (C1), and (b) for high laser power (L3) and high concentration (C3).

2.3.1 Spatial Arrangement of Colloids in rPELs

We determine the density autocovariance function, $C(r)$, the off-diagonal density correlation function, $g^{(2)}(r)$, and the pair density correlation function, $g^{(1)}(r)$, to characterize the local time-averaged particle density $\langle \rho(\mathbf{r}, t) \rangle_t$ and thus the particle-potential and particle-particle interactions.

The two-dimensional density autocovariance function, $C(\mathbf{r})$, is defined by [9]:

$$\begin{aligned} C(\mathbf{r}) &= \langle \langle \rho(\mathbf{r}', t) \rangle_t \langle \rho(\mathbf{r}' + \mathbf{r}, t) \rangle_t \rangle_{\mathbf{r}'} - \rho_0^2 \\ &= \mathcal{F}^{-1} \left(\mathcal{F} \left\{ \langle \rho(\mathbf{r}, t) \rangle_t - \rho_0 \right\} \mathcal{F} \left\{ \overline{\langle \rho(\mathbf{r}, t) \rangle_t - \rho_0} \right\} \right) \end{aligned} \quad (2.1)$$

2.3 Colloids Probing a rPEL

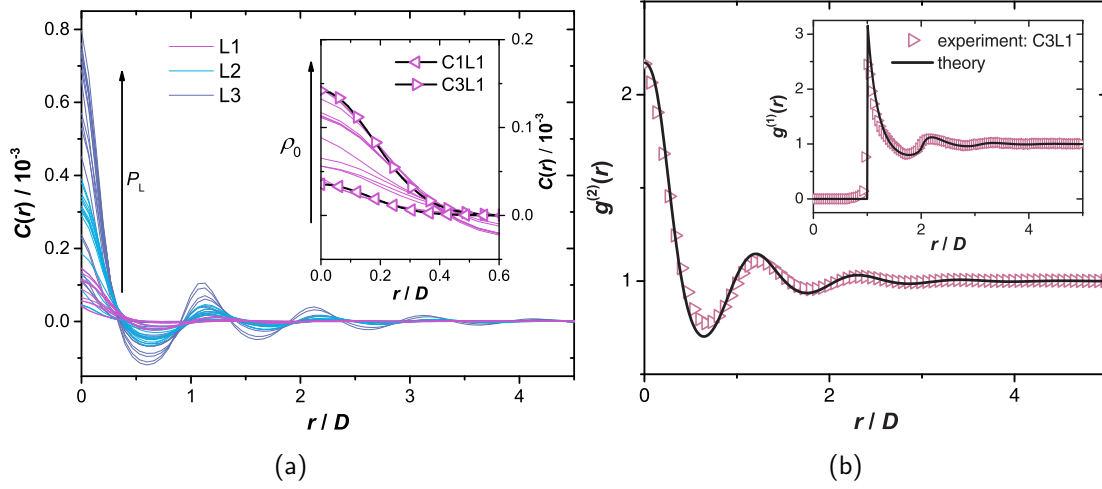


Figure 2.8: (a) Azimuthally averaged autocovariance function, $C(r)$, as a function of normalized distance r/D , for different laser powers, P_L (L1-L3, indicated by colours) and increasing mean particle density ρ_0 . The inset shows all data for L1 together with Gaussian fits to data corresponding to conditions C1L1 and C3L1 as black lines. (b) The experimentally determined azimuthally averaged off-diagonal density correlation function $g^{(2)}(r)$ and the pair density correlation function $g^{(1)}(r)$ (inset) compared with results obtained from the disorder-corrected liquid state theory, as a function of normalized distance, r/D , for high mean particle density (C3) and low laser power (L1).

with the Fourier transformation, inverse Fourier transformation and complex conjugation indicated by \mathcal{F} , \mathcal{F}^{-1} and $\overline{(\dots)}$, respectively. Here, an isotropic sample is considered and thus an azimuthal average is carried out; $C(r) = (1/2\pi) \int_0^{2\pi} C(r, \Theta) d\Theta$. It is shown in Fig. 2.8 (a) for different laser powers and mean particle densities. A pronounced peak is located at the origin of $C(r)$ independent of P_L and ρ_0 . It is well described by a Gaussian distribution $C(r) = \sigma^2 \exp(-r/l_c)^2$ with the amplitude $\sigma^2 = C(0) = \langle \langle \rho(\mathbf{r}, t) \rangle_t^2 \rangle_{\mathbf{r}} - \rho_0^2$ and correlation length l_c (Fig. 2.8 (a) inset). The amplitude, σ^2 , describes the probability to find a particle in a specific region for the entire measurement time and hence characterizes the mean depth of the potential minima as sampled by the particles. It increases with P_L as well as ρ_0 . The correlation length, l_c , characterizes the width of the potential minima as sampled by the particles and decreases with laser power P_L due to the tighter pinning of the particles. A minimum follows on the primary peak of $C(r)$ (Fig. 2.8 (a)). It becomes more pronounced with P_L and ρ_0 and occurs at a distance comparable to the correlation length of the potential. In potential minima trapped particles induce excluded volumes in their vicinities and thus cause a minimum in $C(r)$. Higher order minima and maxima are caused by particle-potential and multiple-particle interactions and reflect spatial arrangements of

neighbouring particles. Furthermore, $C(r) = 1$ in the absence of a rPEL and for low enough ρ_0 , where particle-particle interactions are not important.

The off-diagonal density correlation function, $g^{(2)}(\mathbf{r})$, is given by:

$$g^{(2)}(\mathbf{r}) = \frac{1}{\rho_0^2} \left[\langle \langle \rho(\mathbf{r}', t, l) \rangle_t \langle \rho(\mathbf{r}' + \mathbf{r}, t, l) \rangle_t \rangle_{\mathbf{r}'} \right] . \quad (2.2)$$

It is the density-normalized and disorder-averaged spatial correlation function and hence $g^{(2)}(\mathbf{r}) = C(\mathbf{r})/\rho_0^2 + 1$ for a large field of view, i.e. disorder averaging in one single realisation of the rPEL. $g^{(2)}(\mathbf{r})$ quantifies the probability for a particular location being occupied by a particle after an arbitrarily long time period [10]. Thus, it characterizes the coupling between positional ordering of the particles and the spatial disorder of the rPEL.

Furthermore, the disorder-averaged analogue of the pair density correlation function $g^{(1)}(\mathbf{r})$ is defined by [11]:

$$g^{(1)}(\mathbf{r}) = \frac{1}{\rho_0^2} \left[\langle \rho(\mathbf{r}', t, l) \rho(\mathbf{r}' + \mathbf{r}, t, l) \rangle_{t, \mathbf{r}'} \right] - \frac{1}{\rho_0} \delta(\mathbf{r}, l) . \quad (2.3)$$

where the time average for the disordered system has to be taken prior to the disorder average, $\delta(\mathbf{r}, l)$ is the Dirac delta function and the last term vanishes in the canonical ensemble. The pair distribution function, $g^{(1)}(\mathbf{r})$, describes the variance in $\langle \rho(\mathbf{r}, t) \rangle_t$ as a function of the distance. [12]

The azimuthal averages, $g^{(2)}(r)$ and $g^{(1)}(r)$, are shown in Fig. 2.8 (b) for low laser power (L1) and high mean particle density (C3), where the experimental results are compared to predictions of liquid state theory [12] generalised to include the effects of quenched disorder [11, 13]. (The reader is referred to paper II for details of the calculations.) The $g^{(2)}(r)$ agree very well, whereas the primary peak in $g^{(1)}(r)$ is overestimated in the theory. Fitting yields $\langle U^2 \rangle^{1/2} \approx 2k_B T$ for the strength of the disorder potential, which is consistent with experimental expectations.

The time-averaged local particle density, $\langle \rho(\mathbf{r}, t) \rangle_t$, was determined. It was analysed as a function of laser power, P_L , and mean particle density, ρ_0 (Fig. 2.7). Affected by the rPEL, local in time and/or space correlated particle density variations occur, which are characterized by the density correlation functions $C(r)$ (Fig. 2.8(a)), $g^{(2)}(r)$ (Fig. 2.8(b)) and $g^{(1)}(r)$ (Fig. 2.8(b) inset). The off-diagonal density correlation function reflects particle-potential interactions, namely the potential roughness and spatial correlations in the local

2.4 Two-Dimensional Colloidal Dynamics in rPELs

density, which are caused by trapped particles. This is the first time these correlation functions have experimentally been determined in the presence of quenched disorder.

2.4 Two-Dimensional Colloidal Dynamics in rPELs

2.4.1 Anomalous Diffusion in Correlated Potentials

As a model system for the project outlined in this thesis, colloidal particles were sedimented into a quasi two-dimensional layer and were then exposed to a rPEL. Both the spatial arrangement of the particles and their time-dependent dynamics were studied in relation to the particle concentration and the mean potential depth of the applied field, and its correlations, as controlled by the laser power. Papers IV and VI provide further details.

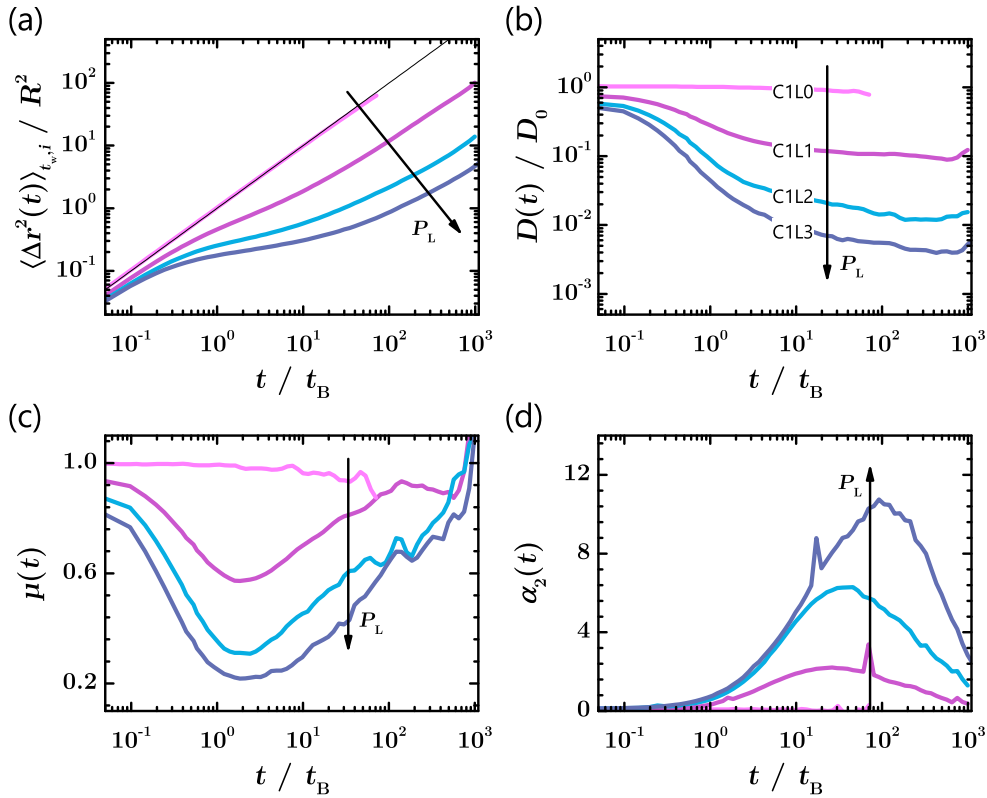


Figure 2.9: Experimental results illustrating the time-dependent dynamics in the dilute regime for normal diffusion in the absence of an external potential (L0, pink line) and anomalous diffusion in the presence of a rPEL as a function of laser power P_L (L1-3, see Tab. 2.1 for colors). The (anomalous) dynamics are represented by the time- and ensemble-averaged MSD (TEAMSD) (a), diffusion coefficient $D(t)$ (b), diffusive exponent $\mu(t)$ (c) and non-Gaussian parameter $\alpha_2(t)$ (d).

Fig. 2.9 shows the time-dependent particle dynamics in the dilute regime C1 in the absence of a laser field L0 and in the presence of a rPEL with three different laser powers L1-3. These are represented by the time- and ensemble-averaged mean-squared displacement (TEAMSD) $\langle \Delta r^2(t) \rangle_{t_w, i}$ (a), the normalized diffusion coefficient $D(t)/D_0$ (b), the diffusive exponent $\mu(t)$ (c), and the non-Gaussian parameter α_2 (d) (Eqs. (1.4) - (1.9)) all as a function of the normalized time t/t_B with the Brownian time $t_B = R^2/(4D_0)$ correcting for influences of the particle radius. As expected for normal diffusion, the TEAMSD is proportional to the time (Eq. (1.5)), whilst the diffusion coefficient and the diffusive exponent take constant values of one, and the NGP is equal to zero in the case of L0 and for all investigated times (pink lines). In the presence of a rPEL (L1-3) all four quantities indicate diffusive behaviour at very short and very long times and sub-diffusive behaviour at intermediate times, where an increase in the laser power leads to slower dynamics of the particles. Although exposed to a rPEL, particles can still freely diffuse within potential minima at short times if the particle size is less than the average speckle size. The influence of the rough potential landscape is strongest at intermediate times, since particles have to overcome potential barriers to move away from their initial position within potential traps. Dynamics at long times are again mostly determined by the particles, which were hindered from freely diffusing through the sample, but were able to overcome the potential barriers. The long-term diffusive exponent $D_L = \lim_{t \rightarrow \infty} D(t)$ thus becomes proportional to time, in the presence of a rough potential, with a value smaller than the initial one at short times, i.e. the short-term diffusion coefficient $D_S = \lim_{t \rightarrow 0} D(t)$ (Fig. 2.9 (b)).

The particles are sedimented to a quasi two-dimensional layer at the bottom of the sample cell and hence particle-wall interactions have to be considered with respect to their influence on particle dynamics at short times [14–16]. The radius dependent Stokes-Einstein diffusion coefficient D_0^{SE} , which describes free, two-dimensional particle diffusion in the absence of a boundary, is given by [17]:

$$D_0^{SE}(R) = \frac{k_B T}{6\pi\eta R}, \quad (2.4)$$

where k_B is the Boltzmann constant, T is temperature, and η the viscosity of the dispersion medium ($\eta = 1.002 \times 10^{-3}$ Pa s for water at $T = 20^\circ\text{C}$). The lateral motion of a particle adjacent to a wall depends on the particle center-wall separation, h , and is slowed down

2.4 Two-Dimensional Colloidal Dynamics in rPELs

due to hydrodynamic interactions (HIs). Faxen suggested a correction term for Eq. (2.4) including the dependence of h on the dynamics near the surface and thus the corrected short-term diffusion coefficient D_0^F becomes [14, 18]:

$$D_0^F(h, R) = \left(1 - \frac{9}{16} \frac{R}{h} + \mathcal{O}\left(\frac{R^3}{h^3}\right)\right) D_0^{\text{SE}}(R) \quad (2.5)$$

which was shown to correctly describe lateral diffusion results within an error of $\pm 5\%$ within this first order of the approximation [14].

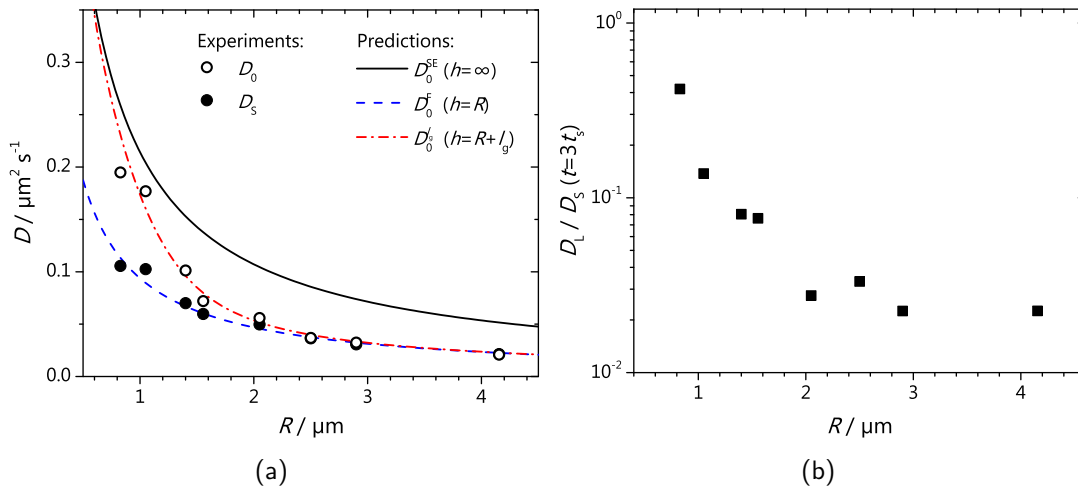


Figure 2.10: Examination of the particle dynamics considering radiation pressure, hydrodynamic interactions and potential correlations: (a) Measured short-term diffusion coefficient as a function of the particle radius, R , in the absence of an external potential, D_0 (L0, open symbols) and in the presence of a strong rPEL, D_S (L3, filled symbols) compared to the predictions of Stokes-Einstein (Eq. (2.4), solid black line), of Faxen with $h = R$ (Eq. (2.5), dashed blue line) and Faxen with $h = R + l_g$ (dash-dotted red line); (b) Long-term diffusion coefficient, D_L (solid symbols) as a function of the particle radius, R . While the long-term diffusion coefficient is rapidly decreasing with increasing R for small particles ($R < 2 \mu\text{m}$), it displays asymptotic behaviour for bigger particles.

Fig. 2.10 (a) shows the measured short-term diffusion coefficient as a function of the particle radius in the absence of an external potential (L0), D_0 , and in the presence of a strong rPEL (L3), D_S , compared to the predictions of Stokes-Einstein (Eq. (2.4)), and of Faxen (Eq. (2.5)) with $h = R$ and $h = R + l_g$, where l_g is the gravitational length as given by [19, 20]:

$$l_g(R) = \frac{k_B T}{g \Delta \rho V_p} \quad (2.6)$$

with the standard acceleration due to gravity $g = 9.8 \text{ m/s}^2$, the difference between the density of the polystyrene particle $\rho_p = 1.05 \times 10^3 \text{ kg/m}^3$ and the dispersion medium

$\rho_m = 1.00 \times 10^3 \text{ kg/m}^3$ (water), $\Delta\rho$, and the particle volume $V_p = 4\pi R^3/3$. The short-term dynamics of sedimented particles, i.e. D_0 , are best described by the prediction of Faxen including the gravitational length l_g and thus $h = R + l_g$. On the other hand, radiation pressure pushes the particles towards the wall and hence leads to a decrease in the short-term diffusion coefficient, especially for small particles. This can be accounted for by including Faxen's hydrodynamic correction with the particle-wall separation $h = R$.

The long-term diffusion coefficient normalized by the short-term value, i.e. D_L/D_S , is independent of hydrodynamic interactions and particle-wall separation and is hence only influenced by potential-particle interactions and thus the potential roughness, i.e. its spatial correlations. Fig. 2.10(b) shows the long-term diffusion coefficient as a function of the particle radius. While D_L is rapidly decreasing with increasing R for small particles ($R < 2 \text{ }\mu\text{m}$), it displays an asymptote for larger particles. Large particles are less influenced by the rPEL roughness due to their experiencing a smoothed out potential landscape caused by the integration over several laser speckles.

2.4.2 Time- and Ensemble-Averages in Relaxing Systems: Evolution of Particle Dynamics in a rPEL

This section contains a brief discussion of the effects of the type of averaging, i.e. time- and/or ensemble-averaging, on quantities that characterize the particle dynamics in rPELs, as studied in detail in paper V.

Initially, the particle ensemble is distributed randomly in the rPEL and the occupancy of potential energy values is homogeneous. With increasing waiting times, t_w , i.e. in the course of the experiment, the system evolves towards its equilibrium distribution, which depends on the probability distribution of energy values of the rPEL, $p(U)$, and the laser power. The relaxation of the system can be studied by determination of the time evolution of time- and/or ensemble-averaged dynamical quantities such as the MSD.

In order to improve statistics, time- and ensemble-averaged measures are often considered, such as the TEAMSD, $\langle \Delta r^2(t) \rangle_{t_w, i}$, and the corresponding diffusion coefficient $D(t) = \langle \Delta r^2(t) \rangle_{t_w, i} / t$. The latter is shown in Fig. 2.11 for a system initially quenched in the rPEL, i.e. not equilibrated, and a relaxed system, both for C1L2. The observation of the relaxed system was started at least 2 hours after the experiment was started (and thus the rPEL turned on) such that the system had enough time to evolve towards equilibrium.

2.4 Two-Dimensional Colloidal Dynamics in rPELs

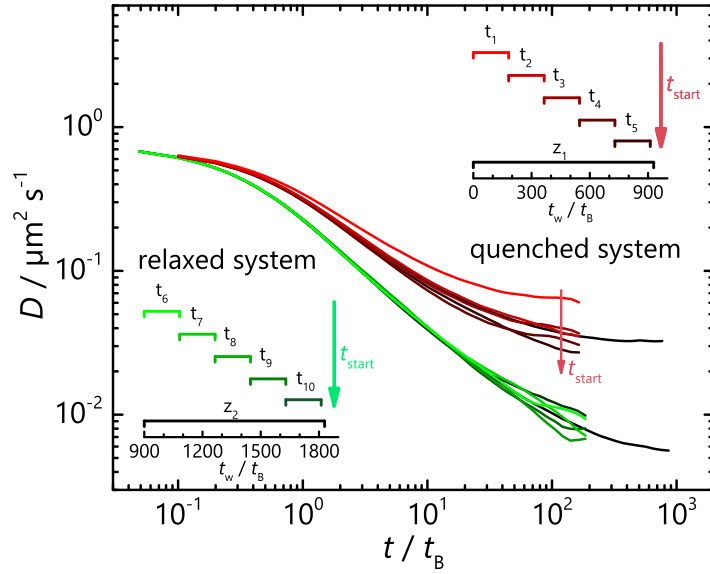


Figure 2.11: Time-dependent diffusion coefficient, $D(t)$, as calculated from the TEAMSD, for a system initially quenched in the rPEL, i.e. not equilibrated, and a relaxed system (as indicated). It was determined for conditions C1L2 and for a very long time interval (black lines) and several smaller time intervals, each of the same length but with different starting times, t_{start} (color gradient, see legend).

The diffusion coefficient was calculated for both systems for a very long time interval and several smaller time intervals, each of the same length but with different starting times, t_{start} (as indicated in the legend of Fig. 2.11). For all measurements independent of the starting time, t_{start} , the length of the measurement ($t_{\text{max}} - t_{\text{start}}$) or the state of relaxation of the system, $D(t)$ shows the expected behaviour. It initially displays normal diffusion followed by a decrease at intermediate times and a subsequent plateau at longer times. However, the relaxed system differs from the initially quenched system, as is apparent in two striking characteristics of the diffusion coefficients as calculated from TEAMSDs. Firstly, a comparison of $D(t)$ for the analysis of the longest time intervals (Fig. 2.11, black lines z_1 and z_2) reveals that the diffusion coefficient of the relaxed system is considerably smaller at intermediate and long time scales than that for the quenched system. Secondly, looking at smaller time intervals with increasing t_{start} (color gradient bright to dark lines) a clear dependence of the starting time on the long-term diffusion is observed for the quenched (t_1 to t_5) but not for the relaxed system (t_6 to t_{10}). This is caused by the average over waiting times t_w , which can depend on both the start time t_{start} and the total measurement time t_{max} and is thus related to the relaxation of the particle ensemble in ergodic systems, where

$$\lim_{t_{\max} \rightarrow \infty} \langle \Delta r^2(t) \rangle_{t_w} = \langle \Delta r^2(t) \rangle_i \quad (2.7)$$

is valid, as well as in non-ergodic systems [21, 22]. Therefore, it is necessary to separately study quantities that are either ensemble-averaged (EA) over all trajectories of the particle ensemble or time-averaged (TA) over a very long single trajectory, i.e. averaged over waiting times t_w . The ensemble-averaged mean-squared displacement (EAMSD), $\langle \Delta r^2(t) \rangle_i$, is given by

$$\langle \Delta r^2(t) \rangle_i = \frac{1}{N} \sum_{i=1}^N [r_i(t) - r_i(0)]^2, \quad (2.8)$$

while the time-averaged mean-squared displacement (TAMSD), $\langle \Delta r^2(t) \rangle_{t_w}$, can be calculated from

$$\langle \Delta r^2(t) \rangle_{t_w} = \frac{1}{t_{\max} - t} \int_{t_{\text{start}}}^{t_{\text{start}} + t_{\max} - t} [r_i(t_w + t) - r_i(t_w)]^2 dt_w. \quad (2.9)$$

In this case, the start time of the measurement does not necessarily have to coincide with the beginning of the experiment.

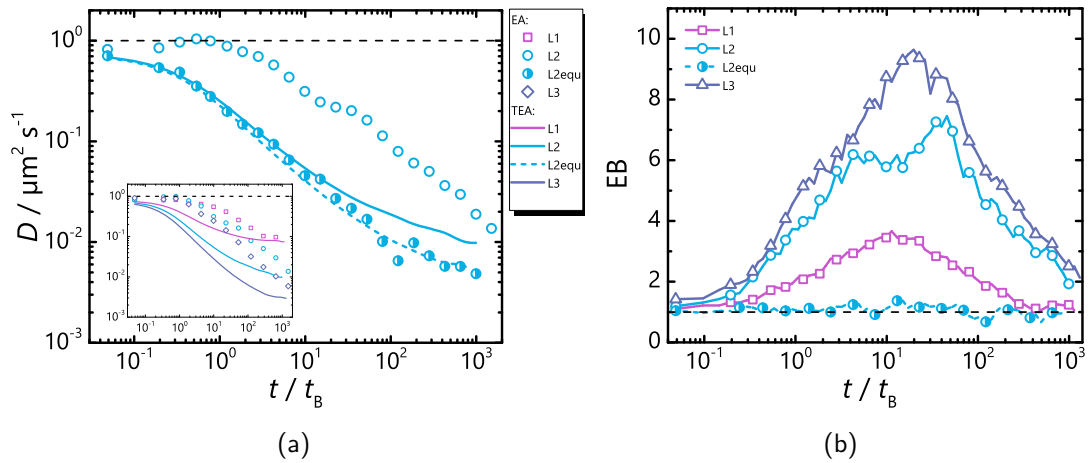


Figure 2.12: Comparison of an initially quenched system with a relaxed system: (a) Diffusion coefficient, $D(t)$, for C1L2 calculated for the quenched and the relaxed system from the EAMSD (open and half-filled circles, respectively) and the TEAMSD (blue solid and dashed line, respectively). The inset additionally shows results for quenched systems at laser powers L1 and L3. (b) Ergodicity (breaking) parameter, EB , as a function of the normalized time, t/t_B , for a quenched system and three different laser powers L1-3 (open symbols) and for a relaxed system and laser power L2 (half-filled circles).

The time-dependence of the diffusion coefficient as a measure for the anomalous dynamics of the system was calculated for a quenched and a relaxed system from their EAMSD as

2.4 Two-Dimensional Colloidal Dynamics in rPELs

well as TEAMSD and these are compared in Fig. 2.12 (a). The ensemble-averaged diffusion coefficient (open circles) for a quenched system is larger than the time- and ensemble-averaged one (blue solid line) at intermediate and long times as expected, although they almost coincide for very long times. The difference at finite times is caused by time-averaging and is independent of the potential strength (see inset of Fig. 2.12 (a)), whereas the crossing at late times is an indication of an ergodic system in which both the ensemble- and time-averages become equal for very long times. The relaxed system can easily be distinguished from the quenched system as both the ensemble-averaged (half-filled circles) and time- and ensemble-averaged diffusion coefficients (blue dashed line) coincide at all times. Indeed, the system is ergodic; if the waiting time after starting the experiment is long enough, the system evolves to equilibrium. Thus the (non-)ergodicity of a system can further be quantified by the so called auxiliary ergodicity parameter, $EB = \langle \Delta r^2 \rangle_i / \langle \Delta r^2 \rangle_{t_w, i}$, where $EB = 1$ indicates a necessary condition for ergodicity [23].

The analysis of the ergodicity (breaking) parameter, EB , which is shown in Fig. 2.12 (b) as a function of the normalized time, t/t_B , for a quenched system and three different laser powers L1-3 (open symbols) confirms the results from the analysis of the diffusion coefficients: $EB = 1$ for very small times whereby the particles do not interact with the potential, $EB > 1$ for intermediate times indicating temporal weakly non-ergodic behaviour induced by the rPEL and depending on the potential roughness and $EB \approx 1$ for long times, indicating ergodicity of the system. However, for a relaxed system and laser power L2 (Fig. 2.12 (b), half-filled circles) the auxiliary ergodicity parameter is equal to one for all times indicating the equilibrium state.

It has been shown that the evolution of the particle ensemble towards equilibrium is manifest in a reduction of the ensemble- and time-averaged diffusion coefficient with increasing waiting times since deeper minima are increasingly populated (Fig. 2.11). Time-averaged quantities reflect the relaxation of the particle ensemble towards equilibrium and hence can indicate when it is reached. Furthermore, differences between TAMSDs, EAMSDs and TEAMSDs as well as quantities based on these differences, such as the auxiliary ergodicity parameter EB , can be used to identify the mechanisms underlying anomalous diffusion in complex fluids and crowded environments [24–26].

2.4.3 Anomalous Diffusion in Crowded Environments

In this section, the main results of paper VI are briefly reviewed. The analysis of the mechanisms underlying the anomalous diffusion in rPELs in general is first shown, thus allowing the extension of the analysis to the influences of the particle concentration in crowded systems.

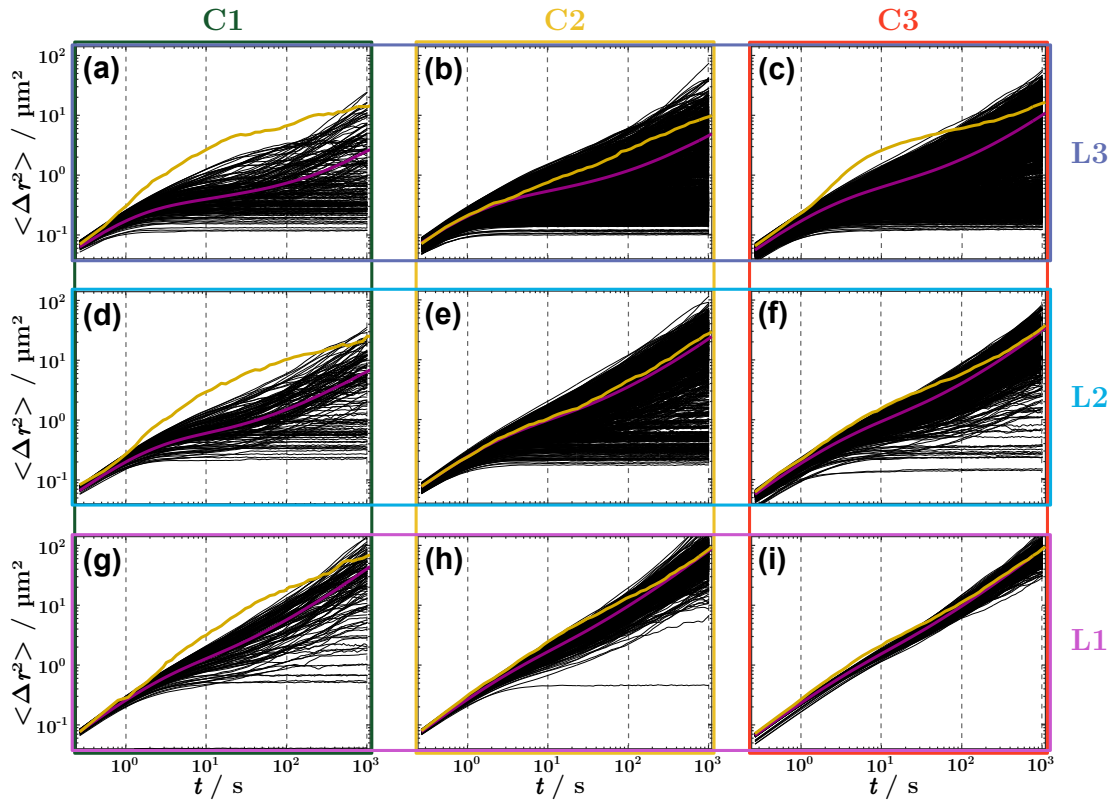


Figure 2.13: Single particle TAMSDs as well as TEAMSD (purple line) and EAMSD (yellow line) for different laser powers L1-3 (bottom to top) and concentrations C1-3 (left to right), respectively.

In order to understand the mechanisms underlying the anomalous diffusion in rPELs, the analysis of single trajectories and differences between the TAMSDs, EAMSD and TEAMSD have been studied. Differences are known to appear in systems exhibiting anomalous diffusion as well as in relaxing, i.e. temporarily non-ergodic, systems, as shown above. Fig. 2.13 shows the TAMSDs (black lines), EAMSD (yellow line) and TEAMSD (purple line) for different laser powers, i.e. potential strengths, L1-3 and concentrations C1-3. Single-trajectory measures such as the TAMSD can be analysed to characterize the heterogeneity of the particle dynamics. Normal free diffusion would be indicated by a linear slope with gradient one for all TAMSDs, no deviation between the TEAMSD and the EAMSD, and no differ-

2.4 Two-Dimensional Colloidal Dynamics in rPELs

ences between single trajectories at all times. However, small scatter between TAMSDs at the end of the measurement time can also be caused by time-averaging artefacts in the experimental data and is not necessarily a signature for heterogeneous dynamics.

Deviations to the freely diffusing case are observed for all concentrations and potential depths. In the presence of a rPEL with low laser power L1 and low concentration C1 (Fig. 2.13(g)) all TAMSDs show the typical sub-diffusive behaviour expected for diffusion in a rPEL, i.e. normal diffusion at short times and a plateau at intermediate times. The plateau of most of the TAMSDs is not very pronounced and hence they become diffusive again at long times. A few TAMSDs, however, show a plateau which extends over the whole time of the measurement, i.e. some particles are trapped at (or near) their initial position. Thus we can distinguish between two species, (fast) diffusing and trapped particles, i.e. obstacles, where a diffusing particle can become trapped and vice versa. The TAMSDs of the obstacles are up to two orders of magnitude lower than the ones of the diffusive particles and hence the TEAMSD is mainly determined by the diffusing species (Fig. 2.13(g), purple line). Time- and ensemble-averaged measures are biased in regard to fast moving particles and thus effects of the slower species are smoothed out. The heterogeneity of the dynamics can further be quantified by the difference between the TEAMSD and the EAMSD (yellow line). It is, as discussed above, an indicator for the ergodicity of the system and shows a system that still evolves towards equilibrium for intermediate times. For long times, however, the TEAMSD and the EAMSD almost fall on top of each other, pointing to an ergodic system.

Increasing the laser power to L3 at low concentrations C1 (Fig. 2.13(d) and (a)) leads to a majority of the particles being strongly confined in deep potential traps as indicated by more extended plateaus in the TAMSDs. Furthermore, the discrepancy between the TEAMSD and the EAMSD increases with the laser power and the system becomes non-ergodic for at least the time of the measurement, a signature for weak-ergodicity breaking. This has been observed in many systems with anomalous diffusion [23, 26].

One important question is the influence the particle concentration has on the anomalous diffusion as triggered by the rPEL? A first consideration of the case of low laser power L1 and increasing concentration C1-3 provides indications (Fig. 2.13(g-i)). An increase in the particle concentration leads to fewer and more weakly trapped particles and hence weaker sub-diffusive behaviour. At a high concentration C3, all TAMSDs as well as the

TEAMSD and the EAMSD almost coincide. Particle collisions lead to a higher probability for initially trapped particles to leave their potential well, lower the average trapping time and hence diffusion becomes more homogeneous. Thus, due to particle-particle interactions, all particles show the same slightly sub-diffusive dynamics at intermediate times, which is mostly determined by the volume occupied by the particles. In contrast, the case for high laser power L3 and the highest concentration C3 represents the most heterogeneous picture of the TAMSDs (Fig. 2.13(c)). On one hand, many TAMSDs show dynamical behaviour corresponding to normal diffusion or slight sub-diffusion; on the other hand, several TAMSDs form a plateau at long times indicating particles being trapped in the rPEL. Nevertheless, despite the heterogeneity, the difference of EAMSD and TEAMSD is smaller than at low concentrations and almost vanishing at long times, suggesting that the system is ergodic and almost at equilibrium at long times.

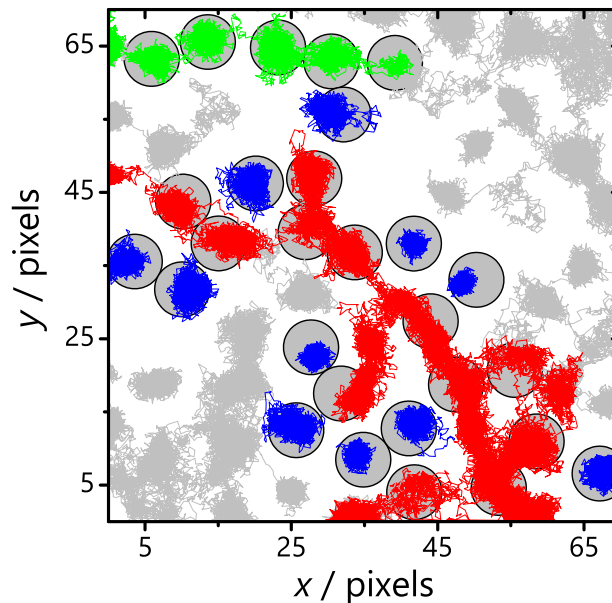


Figure 2.14: Schematic of the main diffusive processes. Trajectories at high concentration C3 and laser power L3 for a lag time of $t = 200 t_B$. Particles are drawn schematically as grey shaded areas in accordance with their radius $R = 1.4 \mu\text{m}$ at the last particle position, i.e. the end of the trajectories. Particle dynamics can be classified into three groups: Strongly hindered diffusion, i.e. trapping (blue), percolating diffusion (red), and hopping motions (green).

The heterogeneity of the diffusion for the case of high concentration C3 and laser power L3 can be recognized in Fig. 2.14, which shows a small section of the particle trajectories. Mechanisms underlying the anomalous diffusion in rPELs can be classified by three main

2.4 Two-Dimensional Colloidal Dynamics in rPELs

dynamical processes (indicated by differently colored trajectories in Fig. 2.14): strongly sub-diffusive, i.e. trapping (blue) and almost diffusive, i.e. percolating (red) behaviour, as well as nearest-neighbour rearrangements, i.e. hopping motion (green) are identified. The green trajectories (Fig. 2.14) form a connected line of five particles, where each is centred at a potential valley. Particles are trapped within their initial potential minima for most of the measurement time, but if one of the particles is randomly displaced by more than its own radius, the vacant potential valley is quickly occupied by an adjacent particle. Hence, string-like hopping motion occurs, where the step-size is discretized corresponding to the average distance between two adjacent potential minima. It is caused by the mean distance between potential minima almost matching the particle diameter and thus particles can only move if one of its nearest-neighbours rearranges. Furthermore, this effect depends on both the actual particle and potential minima arrangement and the particle concentration. Similar effects, namely spatially restricted and correlated dynamics, have been observed in experiments of very dense two-dimensional systems [27] but are also expected to occur in more complex systems such as the dense Lorentz gas, porous media and crowded (cellular) environments [28–34].

Thus far anomalous diffusion regarding ensemble-averaged measures such as the EAMSD and the TEAMSD as well as single particle measures, i.e. single trajectories and the TAMSDs, has been considered. Furthermore, the influences on the particle dynamics of both the strength of the rPEL, i.e. particle-potential interactions, and of the particle concentration, i.e. particle-particle interactions, were studied. One main result was that particle-potential interactions are most pronounced for low concentrations C1 and high laser power L3, whereas particle-particle interactions are more pronounced for high concentrations C3 and low laser power L1. However, the strongest heterogeneity in the dynamics was found for the case of both high concentration C3 and high laser power L3, indicating an intricate interplay of the interactions, which will be further characterized by a discussion of the short-term diffusion coefficient, D_s , and the long-term diffusion coefficient, D_L , which were calculated from TEAMSDs and are shown as a function of P_L and ϕ_A . Here, $D_s = D(t < 2.5 \text{ s})$ includes, in contrast to D_S as defined in Sec. 2.4.1, the influence of potential traps on the short-term dynamics.

The short-term diffusion coefficient is shown in Fig. 2.15 (a) in a schematic iso-diffusivity diagram as a function of laser power and particle concentration, where the measured D_s

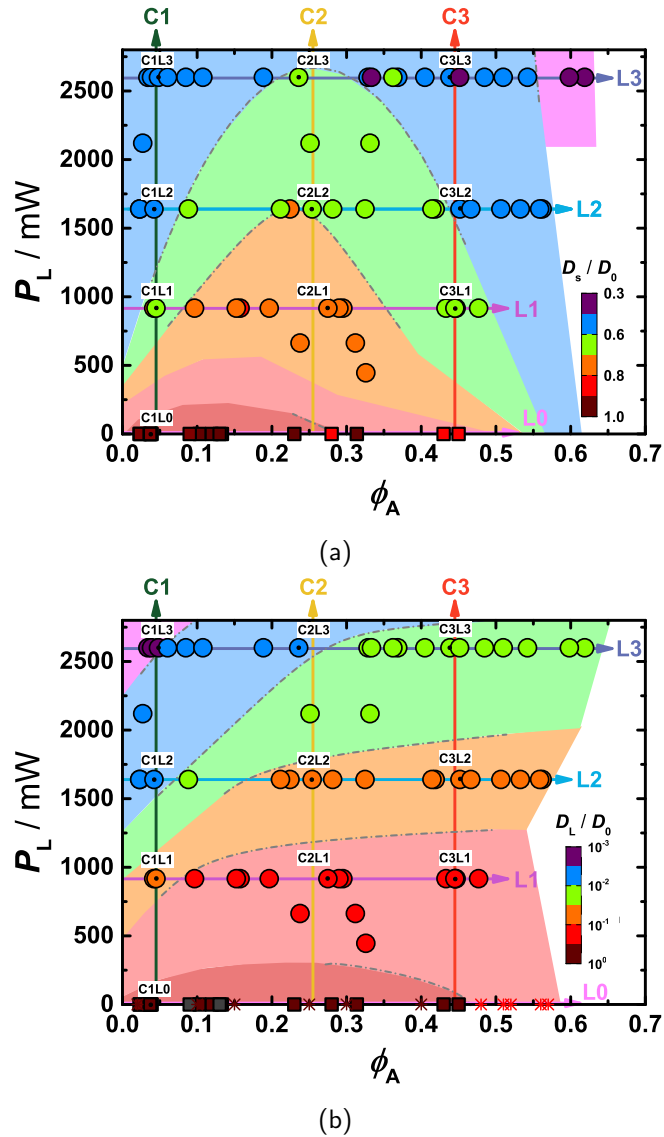


Figure 2.15: Short-term diffusion coefficient D_s (a) and long-term diffusion coefficient D_L (b) in the P_L - ϕ_A plane. Filled circles and squares are measured conditions in the presence and absence of a rPEL, respectively. The values of D_s and D_L are represented by a colour scale, where the gradient from purple to dark red indicates increasing values. Furthermore, extended experimental data, which were taken from Ref. [35] and also correspond to the absence of an external potential, are included in (b) as crosses. Grey dash-dotted lines indicate possible iso-diffusivity lines between suggested colored iso-diffusivity areas (see text for explanation).

values (symbols) appear as colour scale and the gradient from purple to dark red indicates increasing values. Additionally, regions with similar values of D_s , which are referred to as iso-diffusivity areas, are characterized by the same colors. However, these areas, which are an average over several iso-diffusivity lines with similar shape, can be seen as guides to

2.4 Two-Dimensional Colloidal Dynamics in rPELs

the eyes only, since D_s changes continuously and therefore no discrete transition between the indicated areas exists. As a main result, measurement points with a similar short-time diffusion coefficient form a dome-shaped area, i.e. D_s exhibits re-entrant behaviour with a maximum at $\phi_A \approx 0.1-0.3$, depending on the strength of the potential. This can best be seen by following the line L2 with constant laser power from low concentrations to high ones; D_s first increases until it reaches a maximum of $D_s \approx 0.06 \mu\text{m}^2\text{s}^{-1}$ at an area fraction of $\phi_A \approx 0.22$ and constantly decreases again afterwards. The width of the iso-diffusivity areas increases with increasing P_L due to counteracting influences of both the rPEL and the particle concentration. At low concentrations, particle-potential interactions predominate, whereas at high concentrations particle-particle interactions, i.e. excluded volume effects, prevail.

The long-term diffusion coefficient, D_L , is shown in Fig. 2.15 (b) as a function of P_L and ϕ_A , where the values are represented by a logarithmic color scale. Iso-diffusivity areas are again shown, this time for the long-term values. In contrast to their short-term equivalents, long-term iso-diffusivity lines increase at low concentrations with increasing laser power but saturate at high ϕ_A , independent of P_L . At even higher concentrations than the measured ones, the long-time diffusion coefficient is expected to decrease again, as previously found for the short-term iso-diffusivity lines (cf. Fig. 2.15 (a)), since particles become hindered in their motion by excluded volume effects [35, 36]. This argument is further strengthened by experimental results for the long-term diffusion coefficient in the absence of a rPEL (squares and asterisks [35] in Fig. 2.15 (b)), which shows a monotonic decrease of D_L with increasing concentration, where a limit of $D_L/D_0 \approx 0.1$ was suggested for the two-dimensional freezing transition in the absence of hydrodynamic interactions [37].

Single trajectory analysis, e.g. TAMSDs, have shown a very heterogeneous picture of the particle dynamics, which strongly depends on both the potential strength and the particle concentration. Particle-potential interactions are determined by the characteristics of the potential energy landscape, such as the spatial correlation function, $C(U)$, the potential probability distribution, $p(U)$, and the mean potential strength, $\langle U \rangle$, whereas particle-particle interactions are essentially determined by the particle concentration. As a result, trapped particles acting as obstacles hinder the motion of diffusing particles and hence a sub-diffusive regime emerges in the TEAMSD, while the TAMSDs show large scatter between different single trajectories. The probability of obstacles becoming diffusive or

particles becoming trapped is determined by both the potential strength and the particle concentration. An increase in the laser power leads to stronger trapping and therefore further immobilization of the particles, since the likelihood of a particle overcoming a potential energy barrier and thus becoming diffusive is decreased. Finally, the separately studied short- and long-term colloidal dynamics reveal a trend for the counteracting influences of particle concentration and potential strength and, at least for short times, a potential strength dependent critical concentration was identified. At this critical concentration these effects cancel each other out, resulting in a re-entrant regime of the short-term diffusion coefficient D_s (Fig. 2.15 (a)). A similar behaviour is also expected for the long-term diffusion coefficient D_L (Fig. 2.15 (b)).

Bibliography

- [1] Beverunge, J.; Egelhaaf, S. U. *Phys. Rev. A* **2016**, *93*, 013806.
- [2] Zunke, C. Driven Dynamics of Colloids in Random Potentials. Ph.D. thesis, Heinrich Heine University Düsseldorf, in preparation.
- [3] Crocker, J. C.; Grier, D. G. *J. Colloid. Interf. Sci.* **1996**, *179*, 298.
- [4] Sales, T. R. M. *Opt. Eng.* **2003**, *42*, 3084.
- [5] Ducharme, A. D. *Opt. Express* **2007**, *15*, 14573.
- [6] Sales, T. R. M. *Adv. Opt. Techn.* **2012**, *1*, 127.
- [7] Evers, F.; Hanes, R. D. L.; Zunke, C.; Capellmann, R. F.; Beverunge, J.; Dalle-Ferrier, C.; Jenkins, M. C.; Ladadwa, I.; Heuer, A.; Castañeda-Priego, R.; Egelhaaf, S. U. *Eur. Phys. J. Special Topics* **2013**, *222*, 2995.
- [8] Evers, F.; Zunke, C.; Hanes, R. D. L.; Beverunge, J.; Ladadwa, I.; Heuer, A.; Egelhaaf, S. U. *Phys. Rev. E* **2013**, *88*, 022125.
- [9] Steward, E. G. *Fourier Optics: An Introduction*; Courier Corporation, 2004.
- [10] Stein, D. L.; Newman, C. M. *Spin Glasses and Complexity*; Princeton University Press, 2013.
- [11] Sengupta, A.; Sengupta, S.; Menon, G. I. *Europhys. Lett.* **2005**, *70*, 635.
- [12] Hansen, J.-P.; McDonald, I. R. *Theory of Simple Liquids*, 3rd ed.; Academic: London, England, 2006.
- [13] Menon, G. I.; Dasgupta, C. *Phys. Rev. Lett.* **1994**, *73*, 1023.
- [14] Lin, B.; Yu, J.; Rice, S. *Phys. Rev. E* **2000**, *62*, 3909.
- [15] Sharma, P.; Ghosh, S.; Bhattacharya, S. *Appl. Phys. Lett.* **2010**, *97*, 104101.
- [16] Sonn-Segev, A.; Bawdziewicz, J.; Wajnryb, E.; Ekiel-Jeewska, M. L.; Diamant, H.; Roichman, Y. *J. Chem. Phys.* **2015**, *143*, 074704.
- [17] Einstein, A. *Ann. Phys.* **1905**, *322*, 549.
- [18] Faxén, H. *Arkiv. Mat. Astron. Fys.* **1923**, *17*, 27.
- [19] Perrin, J. *Atoms*; Constable: London, England, 1916.

Bibliography

- [20] Royall, C.; van Roij, R.; Van Blaaderen, A. *J. Phys.: Condens. Matter* **2005**, *17*, 2315.
- [21] Courtland, R. E.; Weeks, E. R. *J. Phys.: Condens. Matter* **2003**, *15*, S359.
- [22] Uneyama, T.; Miyaguchi, T.; Akimoto, T. *Phys. Rev. E* **2015**, *92*, 032140.
- [23] Metzler, R.; Jeon, J.-H.; Cherstvy, A. G.; Barkai, E. *Phys. Chem. Chem. Phys.* **2014**, *16*, 24128.
- [24] Ernst, D.; Hellmann, M.; Köhler, J.; Weiss, M. *Soft Matter* **2012**, *8*, 4886.
- [25] Ernst, D.; Köhler, J.; Weiss, M. *Phys. Chem. Chem. Phys.* **2014**, *16*, 7686.
- [26] Manzo, C.; A., T.-P. J.; Massignan, P.; Lapeyre Jr., G. J.; Lewenstein, M.; Garcia Parajo, F. G. *Phys. Rev. X* **2015**, *5*, 011021.
- [27] Marcus, A. H.; Schofield, J.; Rice, S. A. *Phys. Rev. E* **1999**, *60*, 5725.
- [28] Bouchaud, J.-P.; Georges, A. *Phys. Rep.* **1990**, *195*, 127.
- [29] Kärger, J.; Petzold, M.; Pfeifer, H.; Ernst, S.; Weitkamp, J. *J. Catal.* **1992**, *136*, 283.
- [30] Saxton, M. J. *Biophys. J.* **1994**, *66*, 394.
- [31] Höfling, F.; Franosch, T.; Frey, E. *Phys. Rev. Lett.* **2006**, *96*, 165901.
- [32] Kärger, J. In *Adsorption and Diffusion*; Karge, H. G., Weitkamp, J., Eds.; Springer: Berlin, Germany, 2008; Chapter Single-File Diffusion in Zeolites, pp 329–366.
- [33] Dix, J. A.; Verkman, A. S. *Annu. Rev. Biophys.* **2008**, *37*, 247.
- [34] Höfling, F.; Franosch, T. *Rep. Prog. Phys.* **2013**, *76*, 046602.
- [35] Ma, X.; Chen, W.; Wang, Z.; Peng, Y.; Han, Y.; Tong, P. *Phys. Rev. Lett.* **2013**, *110*, 078302.
- [36] Thorneywork, A. L.; Rozas, R. E.; Dullens, R. P. A.; Horbach, J. *Phys. Rev. Lett.* **2015**, *115*, 268301.
- [37] Löwen, H. *Phys. Rev. E* **1996**, *53*, 53.

3.1 Paper I: Experimental creation and characterization of random potential-energy landscapes exploiting speckle patterns

Journal: Physical Review A

Reference: *Phys. Rev. A* **98**, 013806 (2016)

Impact factor: 2.808

Authors: **Jörg Bewerunge** and Stefan U. Egelhaaf

1st author

JB designed and built the set-up, performed the measurements and analysed the data. JB and SUE conceived and discussed the project and SUE supervised the project. Both authors contributed to the writing of the manuscript.

90% contribution of JB

3.1 Paper I: Experimental creation and characterization of random potential-energy landscapes exploiting speckle patterns

This page has been left intentionally blank.

Experimental creation and characterization of random potential energy landscapes exploiting speckle patterns

Jörg Bewerunge¹ and Stefan U. Egelhaaf¹

¹*Condensed Matter Physics Laboratory, Heinrich Heine University, 40225 Düsseldorf, Germany*

(Dated: July 8, 2016)

The concept of potential energy landscapes is applied in many areas of science. We experimentally realize a random potential energy landscape (rPEL) to which colloids are exposed. This is achieved exploiting the interaction of matter with light. The optical set-up is based on a special diffuser, which creates a top-hat beam containing a speckle pattern. This is imposed on colloids. The effect of the speckle pattern on the colloids can be described by a rPEL. The speckle pattern as well as the rPEL are quantitatively characterized. The distributions of both, intensity and potential energy values, can be approximated by Gamma distributions. They can be tuned from exponential to approximately Gaussian with variable standard deviation, which determines the contrast of the speckles and the roughness of the rPEL. Moreover, the characteristic length scales, e.g. the speckle size, can be controlled. By rotating the diffuser, furthermore, a flat potential can be created and hence only radiation pressure exerted on the particles.

PACS numbers: 05.40.-a, 07.60.-j, 42.30.Ms, 42.60.Jf, 82.70.Dd

I. INTRODUCTION

A potential energy surface is a multi-dimensional surface that represents the potential energy of a system as a function of the coordinates and/or other parameters of its constituents, usually atoms, molecules or particles [1]. Since its topographical features resemble a landscape with mountain ranges, valleys and passes, frequently it is referred to as a potential energy landscape (PEL), despite typically being multi-dimensional. The PEL defines all the thermodynamic and kinetic properties of a system. The evolution of a system can pictorially be described by the motion of a point on the PEL.

The concept of a PEL is successfully used in many fields of science to determine the properties and behavior of systems ranging from small to polymeric (bio)molecules and from atomic clusters to biological cells [1]. They are used to describe, e.g., the particle dynamics in dense and crowded systems [2–5], on surfaces [6–8], between magnetic domains [9], and in inhomogeneous materials [10–13] as well as the effects of external potentials on the dynamics of ultracold atoms [14, 15], quantum gases [16], Bose-Einstein condensates [17–20], and their applications to atom cooling and trapping [21], and also include the investigation of the minimum energy conformations of molecules [1], and the folding and association of proteins and DNA [22–26].

Here we experimentally create a PEL to which colloidal particles are exposed and which changes, e.g., their arrangement and dynamics [1, 27–33]. As a model system, it can help to improve our understanding of the underlying principles governing the behavior in PELs and being common to different systems.

A PEL can experimentally be realized by exploiting the interaction of light with matter [34, 35]. We focus on large colloidal particles with a refractive index larger than the one of the dispersing liquid. Their interaction with

light is usually described by two forces [34, 35]: a scattering force or ‘radiation pressure’, which pushes the particles along the beam, and a gradient force, which pulls particles towards regions of high intensity. A classical application of this effect is optical tweezers which are used to trap and manipulate individual colloidal particles or groups of particles [34–37]. Rather than tightly focused beams, extended light fields can be used to create a PEL [38]. Light fields of almost any shape have been generated using spatial light modulators [38–43] or acousto-optic deflectors [44–46], while crossed laser beams [47–49] and other arrangements [50–52] have been used to create specific light fields.

Randomly-modulated intensity patterns, so-called laser speckles [53, 54], can be used to create a random potential energy landscape (rPEL). The landscape can be rationalized as a superposition of many independent randomly-distributed optical traps. They have been realized using various approaches: holographic methods to produce one [39–42] and two-dimensional [43, 55] patterns, optical fibers for two-dimensional patterns [56] as well as diffusers for one [18–20, 57], two [17, 21, 58] and three-dimensional [14, 59–61] patterns.

We use a special diffuser [62–65] to create a random light field, that is a fully developed speckle pattern. Due to the light-matter interactions, a colloidal particle exposed to the speckle pattern will experience a rPEL whose local value depends on the light intensity ‘detected’ by the particle. Since the particles are not point-like, the local potential value depends on the intensity distribution over the whole particle volume [48, 66–68]. We describe the interaction of a colloidal particle with the speckle pattern analogous to a detector that records the speckle intensity over a finite area. This allows us to quantitatively characterize the statistics of the rPEL. As will be shown, the distribution of energy values can be described by a Gamma distribution, and thus ranges from an exponential to an approximately Gaussian dis-

3.1 Paper I: Experimental creation and characterization of random potential-energy landscapes exploiting speckle patterns

2

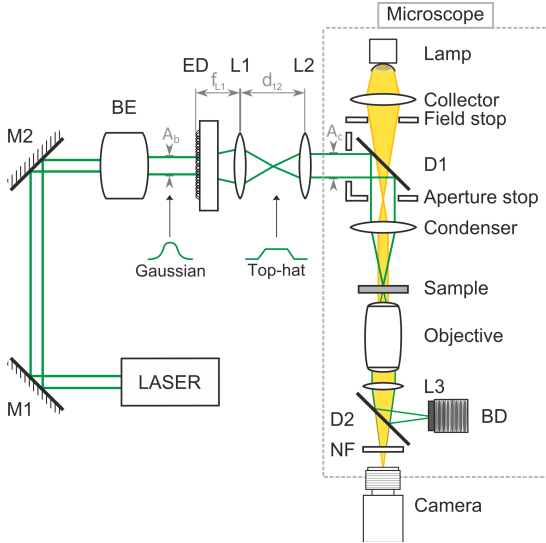


FIG. 1. (Color online) Schematic representation of the set-up used to create a speckle pattern, to which colloidal particles are exposed and simultaneously imaged with an optical microscope. The central optical element is a special diffuser (ED). It is illuminated by a parallel Gaussian beam and creates a top-hat beam including a speckle pattern, which is steered to the sample plane of an inverted microscope. See text for details.

tribution, and the correlation length is set by the particle and speckle sizes. The shape and width of the distribution and the correlation length hence can be tuned in a broad range. The obtained rPEL can be applied to study the spatial arrangement and dynamics of colloidal particles in an external potential [27, 28, 30–33, 38, 40–43]. The chosen diffuser allows the creation of a large light field and thus the simultaneous investigation of many particles, which typically results in excellent statistics. Furthermore, its small and compact design simplifies its alignment, movement and rotation.

II. CREATION OF SPECKLE PATTERNS

The set-up (Fig. 1) allows one to create a top-hat beam with a speckle pattern. Thus, there are intensity fluctuations on a small length scale, i.e. about the size of the colloidal particles. At the same time, the top-hat beam implies a constant intensity on a larger length scale, at least the field of view. This light field is used to impose a rPEL, without any underlying long-range variations, on colloidal particles. The particles are constrained to a quasi two-dimensional plane and can simultaneously be observed with an optical microscope.

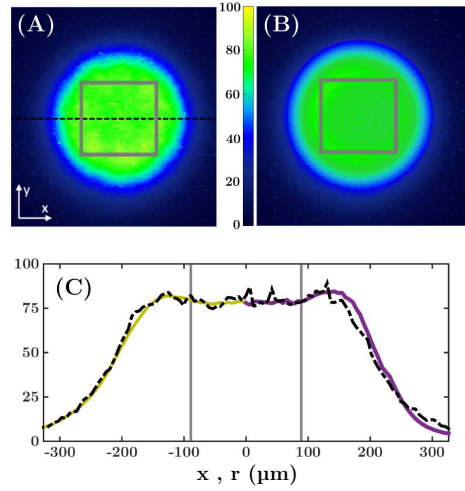


FIG. 2. (Color online) (A) Individual and (B) averaged intensity patterns in the sample plane. The average is taken over 120 images with an individual exposure time of 10 ms obtained with a rate of 10 fps while the diffuser is rotated with a constant angular velocity of $20^\circ/\text{s}$. The intensities in arbitrary units are represented by colors (as indicated). (C) Corresponding intensity profiles along the horizontal dashed line in (A) (dashed line) and azimuthal average of the pattern in (A) (yellow line on the left) and in (B) (purple line on the right). Experimental conditions BE $5\times$ (Tab. I). Measurements are performed with a beam profiler (Coherent Laser-Cam HR). Grey rectangles in (A) and (B) and grey lines in (C) indicate a field of view of $179 \times 179 \mu\text{m}^2$.

A. Diffuser

The central optical element of the set-up is a special diffuser (RPC Photonics, Engineered Diffuser™ EDC-1-A-1r, diameter 25.4 mm) [62, 64, 65]. It is a laser-written, randomly-arranged array of microlenses that vary in radius of curvature and size and cover on average an area $A_1 \approx 2000 \mu\text{m}^2$. When illuminated with an expanded Gaussian laser beam, individual wavefronts originate from each microlens whose characteristics are designed such that a macroscopically uniform intensity pattern with a small divergence is produced, reflecting a top-hat intensity distribution (Fig. 2) [65, 69]. Nonetheless, the random distribution as well as the individual variations of the microlenses and the interference of the corresponding wavefronts lead to microscopic intensity variations, i.e. laser speckles (Figs. 2A, 3A). The speckle pattern consists of three-dimensional cylindrical high-intensity regions [70]. Their orientation and position with respect to the beam axis determine the properties of the speckles in the two-dimensional sample plane [71, 72]. Thus the correct imaging of the modified beam into the sample plane of the microscope is important. Moreover,

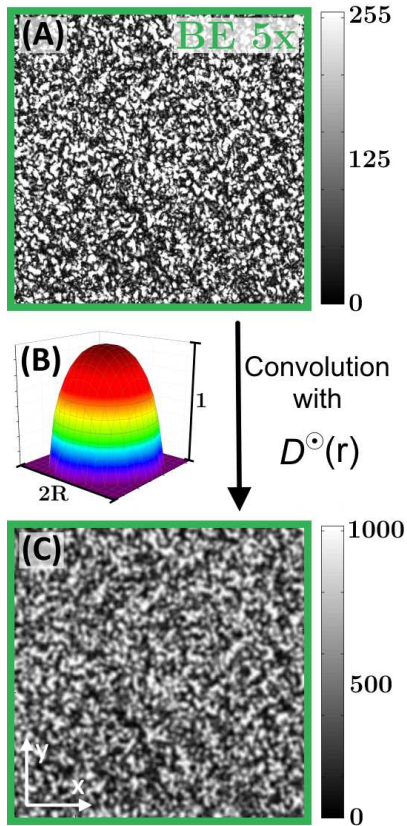


FIG. 3. (Color online) (A) Speckle pattern filling a field of view of $108 \times 108 \mu\text{m}^2$ corresponding to 480×480 pixels with intensities represented as grey levels (as indicated). Experimental conditions BE $5\times$ (Tab. I). (B) Weight function $D^\circ(r)$ (Eq. 8) representing the volume of a spherical colloidal particle with radius $R = 1.4 \mu\text{m}$. (C) Random potential energy landscape (rPEL) experienced by the particle in the speckle pattern shown in (A) and calculated by convolving the intensity in (A) with $D^\circ(r)$. The values of the potential in arbitrary units are represented as grey levels (as indicated).

the speckle size is controlled by the diameter of the illuminating laser beam, determining the number of illuminated microlenses. Their number is chosen large enough to ensure a statistically fully developed speckle pattern [53, 54]. By changing the position of the beam on the diffuser, statistically equivalent but independent realizations of the speckle pattern can be created.

B. Optical Set-up

The speckle pattern strongly depends on the properties of the beam incident on the diffuser. Fully devel-

oped speckles require the interference of many polarized monochromatic wavefronts with random phases and amplitudes and thus a large incident beam that illuminates many microlenses. Furthermore, the optics used to image the modified beam into the sample plane, especially their apertures, have to be designed carefully and, for imaging the speckle pattern, also the detector and its pixel size have to be considered.

A solid-state laser (Laser Quantum, Opus 532, wavelength $\lambda = 532 \text{ nm}$, maximum intensity $P_{L,\text{max}} = 2.6 \text{ W}$) provides a monochromatic linearly-polarized Gaussian beam which is slightly elliptical with an axial ratio of 1.12. The laser beam is steered by two mirrors (M1, M2, Fig. 1) to a beam expander (BE, Sill Optics, S6EXZ5076/121) with variable magnification ($1 - 8\times$) and divergence correction. Using the beam expander, the area A_b of the Gaussian beam hitting the diffuser can be controlled. The diffuser is mounted in a motorized rotation stage (Newport, PR50CC).

The beam leaving the diffuser is divergent (about 1°) and hence collimated by two lenses (L1, L2), where the first lens (L1, Edmund Optics, 1"DCX75, focal length $f_{L1} = 7.5 \text{ cm}$) is placed a distance f_{L1} behind the diffuser followed by the second lens (L2, Thorlabs, 2"PCX75, $f_{L2} = 7.5 \text{ cm}$) in a distance $d_{12} = 16 \text{ cm}$. This leads to a collimated beam with area A_c (about 1 cm^2 for a $5\times$ magnification of the beam expander, i.e. BE $5\times$, Tab. I) on the aperture stop, after the beam has been introduced into the light path of the inverted microscope by a dichroic mirror (D1, Edmund Optics, NT69-901). The condenser (Nikon, TI-C-LWD) then focuses the beam in the sample plane (Figs. 2A, 3A). The lenses (L1, L2) together with the condenser form a telecentric illumination system which collimates the beam and focuses it in the sample plane.

The laser beam is removed from the light path of the microscope by a dichroic mirror (D2, Edmund Optics, NT69-901) which deflects the beam into a beam dump (BD). Furthermore, a notch filter (NF, Edmund Optics NT67-119, optical density OD4 at $\lambda = 532 \text{ nm}$) is introduced in front of the camera.

The colloidal particles are observed using an inverted microscope (Nikon, Eclipse Ti-U) with usually a $20\times$ objective (Nikon, CFI S Plan Fluor ELWD, N.A. 0.45) and an optional additional magnification of $1.5\times$ resulting in a field of view of $431 \times 345 \mu\text{m}^2$ and $288 \times 230 \mu\text{m}^2$, respectively. The images are recorded using an 8-bit CMOS camera (PixeLINK, PL-B741F with 1280×1024 pixels, if not stated otherwise).

To image the speckle pattern at low laser intensities $P_L \approx 1 \text{ mW}$, the dichroic mirror (D2) and notch filter (NF) are removed. When examining the speckle pattern, a very dilute sample (less than five particles in the field of view) is used. The sedimented particles help to focus on the sample plane and hence record the relevant plane of the speckle pattern. The presence of a sample also leaves the light path unchanged. This ensures that the recorded speckle pattern represents the intensity distribution to

3.1 Paper I: Experimental creation and characterization of random potential-energy landscapes exploiting speckle patterns

4

which the particles are exposed.

III. CHARACTERISTICS OF SPECKLE PATTERNS

If wavefronts of the same wavelength but with random phases and amplitudes, as those created by the microlenses, interfere, speckle patterns occur. Speckles are characterized by intensity fluctuations on a small length scale but a uniform intensity on a larger length scale. The statistics of the intensity fluctuations, such as the intensity distribution and spatial correlation, have been investigated in the context of coherent light reflected from rough surfaces or transmitted through diffusers [53, 54, 73]. The same statistics are expected for the speckle pattern created by the present diffuser [62, 64, 65]. Thus below we follow [53, 54, 73].

A. Ideal Speckles

The interference of many monochromatic and linearly polarized wavefronts with random phasors results in a fully developed speckle pattern. In this case, the intensity distribution of the speckle pattern follows an exponential distribution

$$p(I) = \frac{1}{\langle I \rangle} \exp\left(-\frac{I}{\langle I \rangle}\right) \quad (1)$$

with the mean intensity $\langle I \rangle$ and standard deviation $\sigma = (\langle I^2 \rangle - \langle I \rangle^2)^{1/2} = \langle I \rangle$.

The normalized standard deviation represents the contrast of the speckle pattern,

$$c = \frac{\sigma}{\langle I \rangle} = \frac{\sqrt{\langle I^2 \rangle - \langle I \rangle^2}}{\langle I \rangle}. \quad (2)$$

The contrast c quantifies the magnitude of the intensity fluctuations. For an exponential distribution, i.e. a fully developed speckle pattern, it reaches its maximum value $c = 1$.

The spatial structure of the speckle pattern is characterized by the normalized spatial autocorrelation function of the intensity [53, 54, 70, 73]

$$C_I(\Delta\mathbf{r}) = \frac{\langle I(\mathbf{r})I(\mathbf{r} + \Delta\mathbf{r}) \rangle}{\langle I(\mathbf{r}) \rangle^2} - 1, \quad (3)$$

where $I(\mathbf{r})$ is the intensity at position \mathbf{r} and $\langle \rangle$ can represent both, an ensemble or a spatial average. A spatially infinite pattern without long-range correlations is self-averaging [74] and hence the spatial and ensemble averages coincide. To a good approximation this also holds for (finite) experimental speckle patterns, similar to the ones considered here [20]. The extent of $C_I(\Delta\mathbf{r})$ provides

a measure for the correlation area of the speckle pattern, that is the characteristic speckle area

$$A_S = \iint_{-\infty}^{\infty} C_I(\Delta\mathbf{r}) d^2\Delta\mathbf{r}. \quad (4)$$

B. Integrated Speckles

In an experimental situation, the optical elements and especially their apertures as well as the finite detector size have to be considered [53, 54, 73, 75]. The finite detector size can be taken into account through the weight function $D(\mathbf{r})$, which represents the spatial sensitivity of the detector. Accordingly, the effective detector area A_D can be calculated as

$$A_D = \iint_{-\infty}^{\infty} D(\mathbf{r}) d^2\mathbf{r}. \quad (5)$$

In the following also the (deterministic) autocorrelation function of the weight function $D(\mathbf{r})$ is required, which is given by

$$C_D(\Delta\mathbf{r}) = \frac{1}{A_D} \iint_{-\infty}^{\infty} D(\mathbf{r})D(\mathbf{r} - \Delta\mathbf{r}) d^2\mathbf{r}. \quad (6)$$

Based on $C_D(\Delta\mathbf{r})$, the effective measurement area is defined as

$$A_m = \frac{A_D}{C_D(\mathbf{0})} = \frac{A_D^2}{\iint_{-\infty}^{\infty} D^2(\mathbf{r}) d^2\mathbf{r}}. \quad (7)$$

A detector centered at position \mathbf{r} registers an intensity $I_D(\mathbf{r})$ that is the integrated intensity taking the weight function $D(\mathbf{r})$ into account, i.e. [53, 75]

$$I_D(\mathbf{r}) = \frac{1}{A_D} \iint_{-\infty}^{\infty} D(\Delta\mathbf{r})I(\mathbf{r} + \Delta\mathbf{r}) d^2\Delta\mathbf{r}. \quad (8)$$

The intensity distribution for a finite detector is described to a good approximation by a Gamma distribution

$$p(I_D) = \frac{1}{\Gamma(M)} \left(\frac{M}{\langle I_D \rangle}\right)^M I_D^{M-1} \exp\left(-\frac{M}{\langle I_D \rangle} I_D\right), \quad (9)$$

where Γ is the Gamma function and the mean of the detected intensity is identical with the mean of the ideal speckle pattern, i.e. $\langle I_D \rangle = \langle I \rangle$, and the normalized standard deviation or contrast is $c_D = 1/M^{1/2}$, if noise and correlations between neighboring pixels are absent. The parameter M is given by

$$M = \left(\frac{1}{A_D} \iint_{-\infty}^{\infty} C_I(\Delta\mathbf{r})C_D(\Delta\mathbf{r}) d^2\Delta\mathbf{r}\right)^{-1}, \quad (10)$$

which depends on the spatial characteristics of the speckle pattern and detector, i.e. the correlation functions of the intensity $C_I(\Delta\mathbf{r})$ (Eq. 3) and weight function $C_D(\Delta\mathbf{r})$ (Eq. 6), respectively.

If the effective measurement area A_m is large compared to the speckle area A_S , i.e. $A_m \gg A_S$, many speckles contribute to the detected intensity $I_D(\mathbf{r})$. Then M represents the (large) number of detected speckles, $M \approx A_m/A_S \gg 1$ [53, 54, 75], and $p(I_D)$ approaches a Gaussian distribution with mean $\langle I \rangle$ and normalized standard deviation c . In the opposite limit of a very small effective measurement area, $A_m \ll A_S$, only one speckle is detected. Thus $M \rightarrow 1$ and $p(I_D)$ approaches the exponential distribution (Eq. 1). In this case, neighboring detectors might no longer be independent. If, however, the effective measurement area and speckle area are similar ($A_m \approx A_S$), M can only be (numerically) calculated if $C_I(\Delta\mathbf{r})$ and $D(\mathbf{r})$ are known. Due to the complex effects of the optical components on the speckle pattern, this often is not the case and approximations must be used.

In the following we apply these relationships for different detectors and thus $D(\mathbf{r})$ (the different cases are indicated by superscripts); circular ($D^\bullet(\mathbf{r})$) and square ($D^\blacksquare(\mathbf{r})$) detector pixels, which are also subjected to smoothing ($D^\blacksquare(\mathbf{r})$) and binning ($D^\boxplus(\mathbf{r})$), as well as spherical ($D^\circ(\mathbf{r})$) and cubic ($D^\boxminus(\mathbf{r})$) particles acting as ‘detectors’.

1. Detector Pixel

In our experiments, the speckle patterns are detected by uniform square pixels. Their weight function is

$$D^\blacksquare(\mathbf{r}) = \begin{cases} 1 & \text{inside the pixel} \\ 0 & \text{outside the pixel} \end{cases} \quad (11)$$

and hence $A_m^\blacksquare = A_D^\blacksquare$ are equal to the pixel area. Based on this weight function, $C_D^\blacksquare(\Delta\mathbf{r})$ (Eq. 6) and $I_D^\blacksquare(\mathbf{r})$ (Eq. 8) can be calculated. Furthermore, it is expected that $p(I_D^\blacksquare)$ can be approximated by a Gamma distribution (Eq. 9). However, to calculate the parameter M^\blacksquare (Eq. 10), also $C_I^\blacksquare(\Delta\mathbf{r})$ (Eq. 3) is required.

If the top-hat beam is approximated by a Gaussian beam, the corresponding result for a Gaussian beam detected by uniform square pixels [54, 75],

$$C_I^\blacksquare(\Delta\mathbf{r}) = \exp\left(-\frac{\pi\Delta\mathbf{r}^2}{A_S}\right), \quad (12)$$

can be used. Then, M^\blacksquare is given by

$$M^\blacksquare = \left[\sqrt{\frac{A_S}{A_m^\blacksquare}} \operatorname{erf}\left(\sqrt{\frac{\pi A_m^\blacksquare}{A_S}}\right) - \left(\frac{A_S}{\pi A_m^\blacksquare}\right) \left\{ 1 - \exp\left(-\frac{\pi A_m^\blacksquare}{A_S}\right) \right\} \right]^{-2}. \quad (13)$$

For a Gaussian beam detected by uniform circular pixels

$$M^\bullet = \frac{A_m^\bullet}{A_S} \left[1 - \exp\left(-\frac{2A_m^\bullet}{A_S}\right) \times \left\{ I_0\left(\frac{2A_m^\bullet}{A_S}\right) + I_1\left(\frac{2A_m^\bullet}{A_S}\right) \right\} \right]^{-1}, \quad (14)$$

where I_0 and I_1 are modified Bessel functions of the first kind and orders zero and one, respectively. Further geometries have been considered [20, 53, 70, 75], but are less appropriate for the present situation.

To check the suitability of the above equations for our experimental situation, in particular the approximation of the top-hat beam by a Gaussian beam, these relations will be compared to our experimental results in Sec. IV A.

2. Colloidal Particle

Colloidal particles are susceptible to electromagnetic radiation if their refractive index is different from the one of the suspending liquid [34, 35]. Since the particles are not point-like, their response depends on the intensity integrated over their volume [48, 66–68]. This is analogous to the extended detector described above, except that the particle’s susceptibility (or polarizability) rather than the detector efficiency is relevant. It is proportional to the particle volume traversed by the beam. Since the speckles are oriented in beam direction and their extension in beam direction is much larger than in the sample plane [54, 70], the projection of the particle volume in beam direction is considered. The (projected) particle volume is taken into account through the weight function $D^\circ(r)$. For a homogeneous spherical particle the normalized weight function is

$$D^\circ(r) = \begin{cases} \frac{1}{R}\sqrt{R^2 - r^2} & \text{if } r \leq R \\ 0 & \text{if } r > R \end{cases}, \quad (15)$$

and shown in Fig. 3B. To obtain its absolute value, material specific parameters describing the light–particle interaction have to be considered [34, 35, 68] and summarized in a (r -independent) prefactor. Independent of this constant prefactor, the effective measurement area (Eq. 7), or rather effective particle area, becomes

$$A_m^\circ = \frac{8\pi}{9} R^2. \quad (16)$$

The (deterministic) autocorrelation function of the weight function $D^\circ(r)$, that is $C_D^\circ(\Delta\mathbf{r})$ (Eq. 6), can only be determined numerically [68]. Finally, taking into account the particle volume through $D^\circ(r)$, the integrated intensity $I_D^\circ(\mathbf{r})$ can be calculated (Eq. 8) [66–68].

Exploiting the analogy between a colloidal particle and a detector, we expect that the intensity distribution as experienced by the particle, i.e. the rPEL, can be approximated by a Gamma distribution, similar to Eqs. 9

3.1 Paper I: Experimental creation and characterization of random potential-energy landscapes exploiting speckle patterns

6

and 10, but its parameter M has to be determined. This analogy is explored and experimentally tested in Sec. IV B.

IV. RESULTS AND DISCUSSION

A. Speckle Pattern

Different speckle patterns are created by changing the size of the beam that illuminates the diffuser using the variable beam expander. Magnifications between $3\times$ and $7\times$ are possible yielding beam areas on the diffuser $0.3 \text{ cm}^2 \lesssim A_b \lesssim 1.7 \text{ cm}^2$ (Tab. I). Stationary speckle patterns as well as time-varying speckle patterns, created by rotating the diffuser, are investigated and the data compared to the relations presented above (Sec. III B 1) to test their applicability to the present experimental situation.

1. Stationary Speckle Pattern

The observed intensities $I_D^{\blacksquare}(\mathbf{r})$ (Figs. 3A, 4, left) resemble speckle patterns with their characteristic intensity fluctuations. A qualitative inspection indicates a decreasing speckle size with increasing beam size. The magnitude of the intensity fluctuations is quantified by the intensity distribution $p(I_D^{\blacksquare})$ (Fig. 5) and the contrast c (Tab. I). The observed $p(I_D^{\blacksquare})$ are well described by an exponential distribution (Eq. 1), which suggests fully developed speckles. This is consistent with the fact that all beam areas A_b are much larger than the microlens area A_l and hence many microlenses ($A_b/A_l > 10^4$) are illuminated and, in addition, the detector pixels are much smaller than the speckle area, i.e. $A_m \ll A_S^{\blacksquare}$. Only small deviations from an exponential distribution are observed. The smallest intensity occurs with a slightly larger probability. This is attributed to the finite exposure time and sensitivity of the camera, which limit the minimum detectable intensity. If, within the exposure time, too few photons are registered, the pixel will record zero intensity which thus occurs with a slightly too large probability. Also the highest intensities are recorded slightly too frequently due to noise together with the limited dynamic range of the 8-bit camera given the large range of intensity values. Still, the chosen exposure time and laser power provide the optimum compromise.

The normalized standard deviation of $p(I_D^{\blacksquare})$ or contrast c (Eq. 2) is found to be close to one (Tab. I), which is consistent with fully developed speckles. However, the contrast is slightly larger than one. This might be due to the flat-top instead of a Gaussian beam [76] and additional noise, for example contributed by the camera [77]. The depolarization and scattering by the (very few) particles in the sample plane might also contribute. The increase of c with decreasing beam area A_b is attributed

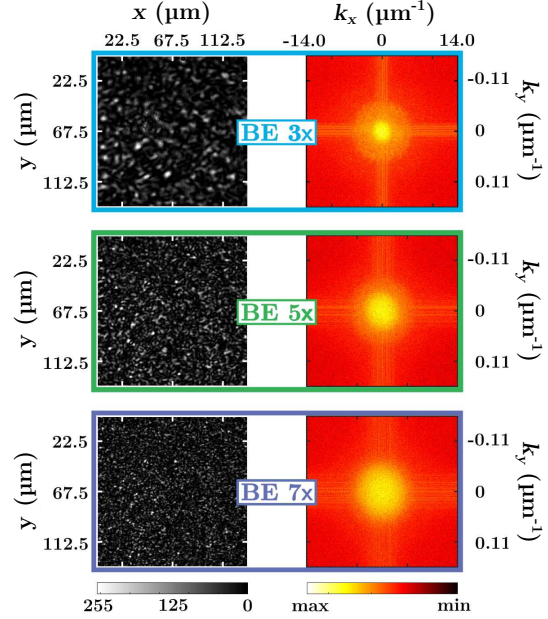


FIG. 4. (Color online) (left) Speckle patterns $I_D^{\blacksquare}(\mathbf{r})$ created with different beam areas A_b due to different magnifications of the beam expander (as indicated, Tab. I). Intensities are represented as grey levels (scale at bottom). (right) Corresponding power spectral densities with their values represented by colors (logarithmic scale in arbitrary units at bottom). For clarity the lowest frequencies are shifted to the center. The spurious high values in x and y direction through the origin are caused by boundary effects in the Fourier transform.

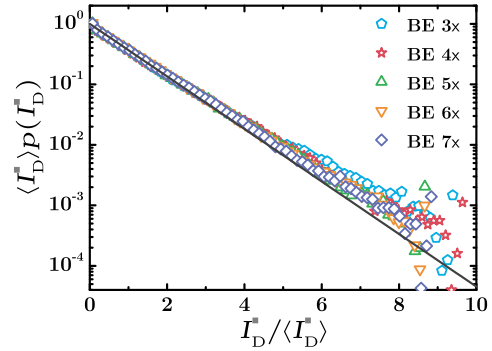


FIG. 5. (Color online) Normalized intensity distributions $\langle I_D^{\blacksquare} \rangle p(I_D^{\blacksquare})$ as observed in experiments with different beam areas A_b due to different magnifications of the beam expander (as indicated, Tab. I). Each symbol is the average of four data points. The line represents an exponential distribution (Eq. 1).

TABLE I. Experimental conditions with different magnifications of the beam expander, where the nominal magnifications serve as labels. Parameters characterizing the speckle patterns, namely the ratio of the beam area to the mean microlens area, A_b/A_1 where $A_1 \approx 2000 \mu\text{m}^2$, speckle contrast c (Eq. 2), and speckle area A_S^\blacksquare (Eq. 4). Parameters characterizing the speckle patterns convolved with the weight function $D^\circ(r)$ of a particle with radius $R = 1.4 \mu\text{m}$ and thus $A_m^\circ = 5.5 \mu\text{m}^2$, i.e. parameters characterizing the rPEL, namely the ratio of the effective particle area to the speckle size, $A_m^\circ/A_S^\blacksquare$, the parameter M , the correlation area A_S^U , the effective correlation area of the weight function $A_S^\circ = A_S^U - A_S^\blacksquare$. Furthermore, the corresponding symbols used in the figures are indicated.

experiment	A_b/A_1	c	$A_S^\blacksquare (\mu\text{m}^2)$	convolution with $D^\circ(r)$	$A_m^\circ/A_S^\blacksquare$	M	$A_S^U (\mu\text{m}^2)$	$A_S^\circ (\mu\text{m}^2)$
◊ BE 3×	15876	1.05	14.9	◆	0.37	1.3	20.6	5.7
★ BE 4×	28224	1.05	8.3	★	0.66	1.8	14.9	6.6
△ BE 5×	44100	1.05	5.1	▲	1.07	2.6	11.8	6.7
▽ BE 6×	63504	1.04	3.5	▼	1.57	3.1	10.2	6.7
◇ BE 7×	86436	1.04	2.6	◆	2.08	3.7	9.4	6.7

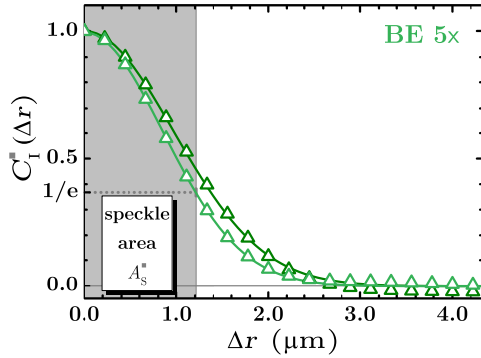


FIG. 6. (Color online) Intensity correlation function C_I^\blacksquare as a function of Δr in x (light green triangle, left) and y (dark green triangle, right) directions as observed in the experiment BE 5 \times (Tab. I). Predictions for a Gaussian beam detected by square pixels $C_I^\blacksquare(\Delta r)$ (Eq. 12) are fitted to the two data sets (solid lines). The length at which C_I^\blacksquare decays to $1/e$ (indicated for the x direction) is related to the speckle area A_S^\blacksquare .

to slight changes in the divergence of the beam that has not been corrected in this series.

To quantify the characteristic length scale of the fluctuations, i.e. the speckle area A_S^\blacksquare (Eq. 4), the spatial intensity correlation function $C_I^\blacksquare(\Delta \mathbf{r})$ (Eq. 3) is determined from the intensity $I_D^\blacksquare(\mathbf{r})$. It is separately calculated in x and y direction (Fig. 6) to account for the slightly elliptical beam (Sec. II B). The prediction for a Gaussian beam detected by a square pixel $C_I^\blacksquare(\Delta \mathbf{r})$ (Eq. 12) is fitted to the experimental data sets. Despite the approximation of the top-hat beam by a Gaussian beam, it describes the data very well. The small deviations at large $\Delta \mathbf{r}$ indicate some non-Rayleigh statistics. This is also suggested by the slightly too large contrast c (Tab. I) and small deviations of the intensity probability distribution $p(I_D^\blacksquare)$ from the ideal exponential case, and has been observed already previously [78]. Furthermore, there are

small fluctuations at large Δr which are attributed to the circular apertures. The lengths at which $C_I^\blacksquare(\Delta \mathbf{r})$ decays to $1/e$, Δr_x and Δr_y (Fig. 6), provide a measure of the speckle sizes in x and y directions, respectively, and the speckle area $A_S^\blacksquare = \pi(\Delta r_x^2 + \Delta r_y^2)$. They indicate slightly elliptical speckles with an axial ratio of about 1.1, consistent with the elliptical beam (Sec. II B).

For an effective measurement area much smaller than the speckle area ($A_m^\blacksquare \ll A_S^\blacksquare$), hence well above the Nyquist limit $A_S^\blacksquare \approx 2A_m^\blacksquare = 2 \text{ px}$, equivalent information can be obtained from the width of the power spectral density (Fig. 4, right), which is inversely proportional to the width of the spatial correlation function [79, 80]. With decreasing speckle area A_S^\blacksquare , indeed the peak at low frequencies becomes smaller and broader (Fig. 4, top to bottom), consistent with the findings based on $C_I^\blacksquare(\Delta \mathbf{r})$.

2. Time-varying Speckle Pattern

Our set-up offers the possibility to rotate the diffuser around the optical axis. While a rotation does not change the intensity statistics, the actual speckle pattern is changed and represents another realization, provided the rotation angle $\Delta \phi$ was large enough. The correlation between two speckle patterns, $I_D^\blacksquare(\phi, \mathbf{r})$ and $I_D^\blacksquare(\phi + \Delta \phi, \mathbf{r})$ is quantified by the angular correlation function, namely

$$C_I^\blacksquare(\Delta \phi) = \frac{\langle I_D^\blacksquare(\phi, \mathbf{r}) I_D^\blacksquare(\phi + \Delta \phi, \mathbf{r}) \rangle}{\langle I_D^\blacksquare \rangle^2} - 1, \quad (17)$$

where $\langle I_D^\blacksquare \rangle$ is independent of the angle ϕ and $\langle \rangle$ represents an average over all pixels, i.e. all \mathbf{r} , and realizations. As expected, $C_I^\blacksquare(\Delta \phi)$ decreases with increasing $\Delta \phi$ (Fig. 7). Only very small correlations, say 10%, are observed beyond $\Delta \phi_c \approx 2^\circ$. Thus, rotations with $\Delta \phi \gg \Delta \phi_c$ are expected to result in essentially uncorrelated realizations of the speckle pattern.

The definition of $C_I^\blacksquare(\Delta \phi)$ is analogous to the spatial intensity correlation function $C_I^\blacksquare(\Delta \mathbf{r})$ (Eq. 3), which can

3.1 Paper I: Experimental creation and characterization of random potential-energy landscapes exploiting speckle patterns

8

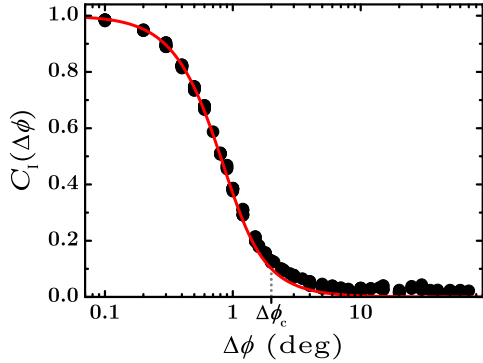


FIG. 7. (Color online) Angular intensity correlation function $C_I^{\blacksquare}(\Delta\phi)$ based on speckle patterns obtained with orientations of the diffuser that differ by $\Delta\phi$ (Eq. 17). The red line represents the calculation based on Eq. 18. Experimental conditions BE 5 \times , which implies a speckle area $A_S^{\blacksquare} = 5.1 \mu\text{m}$ (Tab. 1), a square field of view with lateral length $L_v = 202.2 \mu\text{m}$ and an exposure time of 1.1ms.

be used to calculate $C_I^{\blacksquare}(\Delta\phi)$. A rotation of the diffuser by $\Delta\phi$ implies a displacement of the speckle pattern by $\Delta\phi \times \mathbf{r}$, which depends on the distance $r = |\mathbf{r}|$ from the optical axis around which the speckle pattern is rotated. Thus, $I_D^{\blacksquare}(\phi, \mathbf{r})I_D^{\blacksquare}(\phi + \Delta\phi, \mathbf{r}) = I_D^{\blacksquare}(\phi, \mathbf{r})I_D^{\blacksquare}(\phi, \mathbf{r} - \Delta\phi \times \mathbf{r})$, which relates $C_I^{\blacksquare}(\Delta\phi)$ to $C_I^{\blacksquare}(\Delta\mathbf{r})$. Averaging over a circular field of view with radius R_v and square pixels, and using the correlation function for a Gaussian beam detected by square pixels, $C_I^{\blacksquare}(\Delta r)$ (Eq. 12), yields

$$\begin{aligned} C_I^{\blacksquare}(\Delta\phi) &= \frac{1}{\pi R_v^2} \int_0^{R_v} C_I^{\blacksquare}(r\Delta\phi) 2\pi r dr \\ &= \frac{A_s}{\pi R_v^2} \frac{1}{\Delta\phi^2} \left\{ 1 - \exp\left(-\frac{\pi R_v^2}{A_s} \Delta\phi^2\right) \right\}. \end{aligned} \quad (18)$$

For a square field of view with size L_v^2 and square pixels, the corresponding relation involves the error function. However, it can be approximated by a circular field of view, i.e. Eq. (18), with an effective radius $R_v \approx 0.57 L_v$, which corresponds to a slightly larger effective area. This prediction is confirmed by the experimental data (Fig. 7).

To fully characterize time-varying speckle patterns, the angular velocity has to be considered. This is similar to the situation in speckle contrast analysis, imaging applications and light scattering [81–84]. If the diffuser is rotated, and hence the speckle pattern changed, faster than the particles can follow, i.e. than their relaxation time, the colloidal particles effectively experience a temporally averaged and hence microscopically flat intensity pattern instead of a speckle pattern (Fig. 2). Then, only time-averaged intensities are of interest. Both, averages over many images with short exposure times as well as individual images with long exposure times, are considered. With appropriate camera parameters, both procedures

yield equivalent time-averaged intensities [83]. The average over many realizations indeed shows significantly reduced fluctuations compared to the static speckle pattern (Fig. 2A,B). Nevertheless, a small modulation remains, even in the azimuthal average (Fig. 2C).

B. Random Potential Energy Landscape

Having investigated the speckle patterns, we now consider their effect on spherical colloidal particles that are characterized by the weight function $D^{\circ}(\mathbf{r})$ (Eq. 15, Sec. III B 2). The effect of a speckle pattern can be described by an external potential $U(\mathbf{r})$, the rPEL (as the one shown in Fig. 3C). We will now determine the properties of $U(\mathbf{r})$.

1. Time-averaged local particle density

The speckle pattern affects the distribution of particles. It is quantified by the time-averaged local particle density $\rho(\mathbf{r})$ which is determined from the particle locations [85]. The density $\rho(\mathbf{r})$ for a (quasi) two-dimensional layer of particles with a mean surface fraction $\langle \rho \rangle = 0.25$, i.e. about 1200 particles in a field of view of $171 \times 171 \mu\text{m}^2$, is shown in figure 8. A qualitative inspection reveals that $\rho(\mathbf{r})$ resembles some of the characteristics of the rPEL $U(\mathbf{r})$ (Fig. 3C). It exhibits random fluctuations with a comparable characteristic length scale, but also longer-ranged correlations. Furthermore, the maxima of $\rho(\mathbf{r})$ are more pronounced while the saddle points and minima are blurred. Within reasonable measurement times, the low $\langle \rho \rangle$ and the strongly disordered potential hence do not provide sufficient statistics to obtain space-resolved information on $\rho(\mathbf{r})$ and thus the potential $U(\mathbf{r})$. This suggests to investigate samples with larger $\langle \rho \rangle$. However, a straight-forward determination of $U(\mathbf{r})$ from $\rho(\mathbf{r})$ through the Boltzmann distribution requires that particle–particle interactions can be neglected and thus that the sample is dilute. In more concentrated systems, the determination of $U(\mathbf{r})$ requires to apply more involved methods, e.g., liquid-state theory [29] or Inverse Monte Carlo Simulations [86]. This is beyond the scope of the present work.

2. Convolution with the Weight Function of a Spherical Particle

To avoid this complication, we investigate the convolution of the speckle pattern with the weight function of a spherical particle, $D^{\circ}(\mathbf{r})$, and, instead of the full $U(\mathbf{r})$, determine the statistics of $U(\mathbf{r})$, namely the distribution of its values, the magnitude of its fluctuations and its correlation area. In the case of a particle exposed to a light field, $D^{\circ}(\mathbf{r})$ describes the susceptibility of the particle to

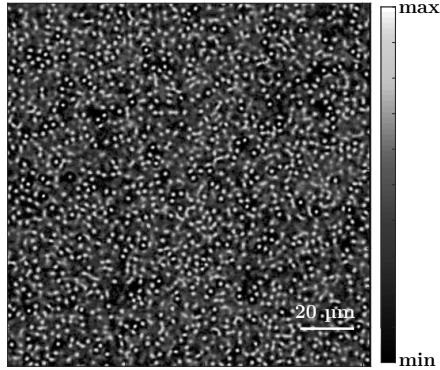


FIG. 8. Time-averaged local particle density $\rho(\mathbf{r})$ of a (quasi) two-dimensional layer of spherical polystyrene particles with sulfonated chain ends with radius $R = 1.4 \mu\text{m}$, polydispersity 3.2 % and mean surface density $\langle \rho \rangle = 0.25$ in a speckle pattern (BE 5 \times , Tab. I) created using a moderate laser power ($P_L = 1640 \text{ mW}$). About 37 000 images at 3.75 fps (AVT, Pike F032B) were recorded and averaged. Densities are represented as grey levels (logarithmic scale in arbitrary units).

light (Eq. 15), but is formally identical to a detector efficiency. The convolution of $D^\circ(\mathbf{r})$ with the intensity pattern $I(\mathbf{r})$ yields the total intensity $I_D^\circ(\mathbf{r})$ that is ‘detected’ by a particle at position \mathbf{r} (Eq. 8). Due to the light-matter interaction [34, 35, 68, 87–89], $I_D^\circ(\mathbf{r})$ represents an external potential $U(\mathbf{r}) = I_D^\circ(\mathbf{r})$ imposed on the particle, that is the rPEL. Since $D^\circ(\mathbf{r})$ takes into account the volume of the particle, the extended colloidal particle at position \mathbf{r} in the speckle pattern $I(\mathbf{r})$ can be regarded as a point-like particle in the potential $U(\mathbf{r}) = I_D^\circ(\mathbf{r})$. This procedure and a typical $U(\mathbf{r})$ are illustrated in Fig. 3. It has already successfully been applied to micron-sized colloidal particles in a one-dimensional rPEL; experiments and simulations yielded consistent results [40].

Potentials $U(\mathbf{r})$ obtained by convolving experimental speckle patterns $I_D^\circ(\mathbf{r})$ with the weight function $D^\circ(\mathbf{r})$ (Eqs. 8, 15) [40, 67, 68, 90] are quantitatively investigated in the following. This allows us to test whether $p(I_D^\circ) = p(U)$ can be described by a Gamma distribution (Eq. 9) and to find an approximation for the parameter M .

On a qualitative level, $U(\mathbf{r})$ appears washed out compared to the speckle pattern (Fig. 3) due to the convolution with $D^\circ(\mathbf{r})$. The magnitude of the fluctuations is reduced and their characteristic length scale is increased, in particular if the particle is large. This is consistent with experimental observations (Fig. 8).

The distribution of potential values $p(U)$ depends on the speckle area A_S^\square (Eq. 4) and the effective particle area $A_m^\circ = (8\pi/9)R^2$ (Eq. 16). If A_S^\square is kept constant, the effect of the particle area A_m° on $p(U)$ can be studied (Fig. 9A). We consider particles with radii in the range $0.3 \mu\text{m} \leq R \leq 5.0 \mu\text{m}$, which are large enough to be observed with the microscope. A small R or A_m° leads to an

almost exponential distribution and develops into an approximately Gaussian distribution as A_m° increases. Correspondingly, for constant A_m° but decreasing A_S^\square , a similar transition from an exponential to an approximately Gaussian distribution is observed (Fig. 9B). More general, similar distributions are obtained for comparable A_m°/A_S^\square (Fig. 9C) and thus $p(U)$ appears to only depend on this ratio with its shape changing from an almost exponential distribution to an approximately Gaussian distribution upon increasing A_m°/A_S^\square .

For all A_m° and A_S^\square , a Gamma distribution (Eq. 9) is fitted to the data. The Gamma distribution describes the distribution of potential values $p(U)$ well and only depends on A_m°/A_S^\square . Only small deviations are observed, similar to those reported before [91]. They are attributed to the approximations leading to the Gamma distribution [54], e.g. a Gaussian instead of a top-hat beam and the presence of finite optical components and detector pixels, and a possible effect of the (very few) particles on the speckle pattern (Sec. IV A).

The fit of the Gamma distribution to the data yields the parameter M (Eq. 9, Fig. 9), which is related to the contrast c and standard deviation σ . In the case of the potential, σ represents the magnitude of the fluctuations or ‘roughness’ of the random potential $U(\mathbf{r})$. Thus we consider $M^{-1} \sim \sigma^2$. Independent of the specific particle and speckle sizes, M^{-1} only depends on A_m°/A_S^\square and decreases with increasing A_m°/A_S^\square (Fig. 10). Thus, the magnitude of the fluctuations only depends on the number of speckles that interact with a particle.

The correlation area A_S^U of the potential $U(\mathbf{r})$ is obtained from the length at which the correlation function $C_U(\Delta r)$ decays to $1/e$ (Fig. 11, Tab. I). The correlation area of the intensity or speckle area A_S^\square decreases with increasing beam size and hence also A_S^U . The difference between both values is the effective correlation area of the weight function; $A_S^\circ = A_S^U - A_S^\square$ (Tab. I). The value of A_S° only depends on the weight function $D^\circ(\mathbf{r})$ as long as the effective particle area A_m° is larger than the speckle area A_S^\square , consistent with the data (Tab. I).

3. Convolution with Other Weight Functions

Instead of convolving the intensity $I_D^\circ(\mathbf{r})$ with the weight function of spherical particles, $D^\circ(\mathbf{r})$, it is convolved with the weight function of cubic particles, $D^\square(\mathbf{r})$, with different effective particle areas A_m^\square . A similar $M^{-1}(A_m^\square/A_S^\square)$ is obtained (Fig. 10, magenta \times). This indicates that the precise shape of the particle is not crucial, as long as it has the same effective particle area A_m .

Furthermore, the effect of smoothing is investigated. The intensity $I_D^\circ(\mathbf{r})$ is smoothed using a filter before it is convolved with $D^\circ(\mathbf{r})$. The filter replaces each pixel’s intensity $I_D^\circ(\mathbf{r})$ by the average intensity of the $n \times n$ pixels surrounding the pixel, $I_D^\circ(\mathbf{r})$. Smoothing is equivalent to the convolution of the intensity with $D^\square(\mathbf{r})$ described above, but $I_D^\circ(\mathbf{r})$ in addition is sub-

3.1 Paper I: Experimental creation and characterization of random potential-energy landscapes exploiting speckle patterns

10

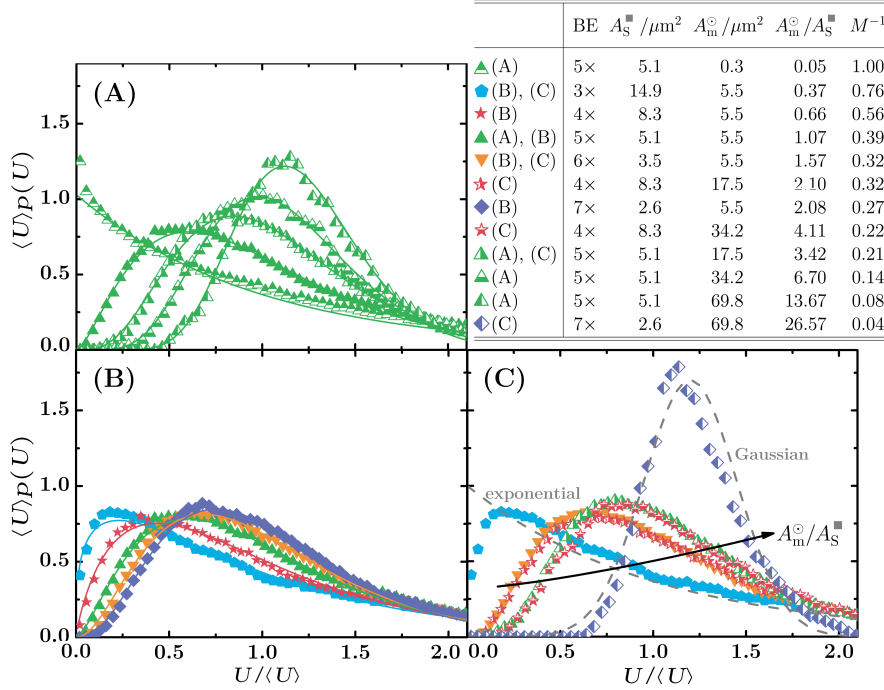


FIG. 9. Normalized distribution of potential values $\langle U \rangle p(U)$ calculated by the convolution of an experimentally-determined speckle pattern $I_D^\square(\mathbf{r})$ with the weight function $D^\circ(\mathbf{r})$ of a colloidal particle for (A) different effective particle areas A_m^\square and constant speckle area $A_S^\square = 5.1 \mu\text{m}^2$ (BE 5×, Tab. I), (B) different A_S^\square and constant $A_m^\square = 5.5 \mu\text{m}^2$ and (C) different A_m^\square/A_S^\square . The different conditions and the inverse of the fit parameter M are summarized in the table. The solid lines represent fits by Gamma distributions (Eq. 9) and dashed lines in (C) fits by an exponential and a Gaussian distribution as indicated.

sequently convolved with $D^\circ(\mathbf{r})$. Both yield virtually identical results (Fig. 10, red +, green +), as long as the smoothing is taken into account in the calculation of A_S^U , i.e. $A_S^U = A_S^\square + A_S^\square + A_S^\square$. This becomes increasingly more significant as smoothing extends over larger areas.

Finally, $I_D^\square(\mathbf{r})$ is binned into larger ‘meta pixels’ resulting in a larger effective measurement area A_m^\square , but smaller number of (meta) pixels. This is in contrast to smoothing, where the number of pixels is maintained. The corresponding intensity $I_D^\square(\mathbf{r})$ mimicks a camera with larger but less pixels. Hence, the number of speckles in the effective measurement area is increased, $A_m^\square/A_S^\square > A_m^\square/A_S^\square$. Nevertheless, for a sufficient number of meta pixels (above about 20), $p(I_D^\square)$ can be described in good approximation by a Gamma distribution (Eq. 9, data not shown) and $M^{-1}(A_m^\square/A_S^\square)$ shows the same dependence on A_m^\square/A_S^\square (Fig. 10, blue asterisk).

These findings suggest that the dependence of M^{-1} on A_m/A_S does not strongly depend on the experimental conditions as long as they are properly taken into account through A_m and A_S . Thus, our experimental situation, namely a top-hat beam and a particle as ‘de-

detector’, appears well approximated by a Gaussian beam and a square or circular detector. Indeed, M as given by Eqs. 13 or 14, which both only depend on the ratio A_m/A_S , reproduces our findings very well (Fig. 10, lines). This confirms previous experimental results for similar, but not identical, speckle patterns and optical geometries [70, 75]. We hence established an appropriate description of the statistics of the rPEL, $U(\mathbf{r})$, imposed on the colloidal particles. In particular, the distribution of potential values can be characterized by a Gamma distribution (Eq. 9) and the parameter M^{-1} , quantifying the magnitude of its fluctuations, by Eq. 13 or 14.

V. CONCLUSIONS

We experimentally realize random potential energy landscapes exploiting the interaction of matter with light. Colloidal particles are investigated which act as ‘detectors’ in a random intensity pattern, that is laser speckles. The speckle pattern is produced using an optical set-up which is based on a special diffuser. The diffuser creates a top-hat beam containing a speckle pattern. This

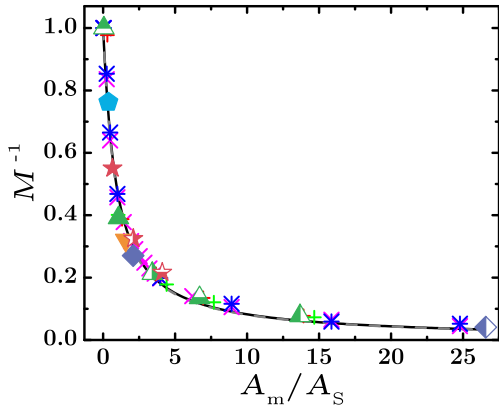


FIG. 10. (Color online) Parameter M^{-1} , which quantifies the fluctuations of the potential $U(\mathbf{r})$, as a function of the ratio of the effective particle area A_m and the speckle area A_s , for different conditions (as indicated in Fig. 9) as well as (magenta \times) cubic (instead of spherical) particles with different sizes, i.e. effective particle areas A_m^{\square} , in the experimental condition BE 5 \times , (red +, green +) spherical particles in an intensity pattern which has been smoothed over 5×5 and 10×10 pixels, respectively, and (blue asterisk) a point-like particle, i.e. no convolution, in an intensity pattern which has been binned over different numbers of pixels (1×1 to 50×50). The dashed grey and solid black lines represent predictions for a Gaussian beam and a square (Eq. 13) and circular (Eq. 14) detector, respectively.

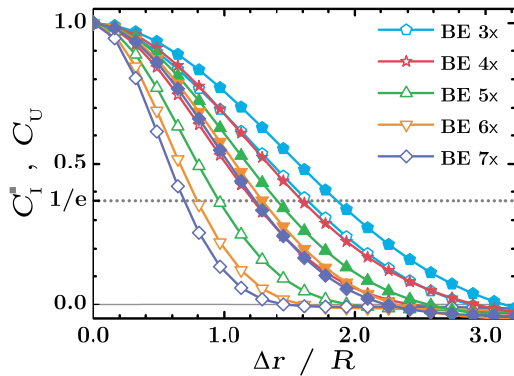


FIG. 11. (Color online) Intensity, $C_I^{\square}(\Delta r)$ (connected open symbols), and potential, $C_U(\Delta r)$ (connected filled symbols), correlation functions as a function of Δr , which are based on the intensity $I_D^{\square}(\mathbf{r})$ and its convolution with the weight function $D^{\circ}(\mathbf{r})$ of a particle with radius $R = 1.4 \mu\text{m}$, respectively (Tab. I). The lengths at which the correlation functions decay to $1/e$ are related to the speckle areas A_s^{\square} and the correlation areas of the potential, A_s° , respectively, and hence to the effective correlation area of the weight function A_s° .

speckle pattern is quantitatively characterized. In the standard experimental conditions, the intensity distribution is found to follow an exponential distribution with the normalized standard deviation or contrast being close to one, which indicates that fully developed speckles are formed. Their size can be controlled through the size of the illuminating laser beam.

The interaction of the particle with the speckle pattern is described analogous to a detector recording the intensity. However, the intensity that is ‘detected’ by the particle represents an external potential that is imposed on the particle, the rPEL. It is found that the distribution of energy values of the rPEL can be described by a Gamma distribution and approximations for the standard deviation of the distribution are identified. Using these approximations, thus, the statistics of the rPEL can quantitatively be described. These relations together with the set-up, can be exploited to produce rPELs with the desired distribution of energy values and correlation lengths, where the shape of the distribution can be varied in a broad range, from exponential to Gaussian.

When colloidal particles are exposed to such an intensity pattern, that is an rPEL, their spatial arrangement and dynamics will be affected as demonstrated previously [38, 40, 42, 43] and in agreement with theoretical predictions [1, 27–33]. In these previous studies, the speckle patterns have been created using a spatial light modulator [39]. Compared to this method, the present set-up offers a much larger field of view and thus the possibility to simultaneously observe a much larger number of particles. The distribution of potential energy values and their spatial correlation furthermore are tunable. In addition, the diffuser can be rotated and hence the speckle pattern varied. If this is faster than the particle dynamics, the particles experience a time-averaged and hence flat effective potential. Radiation pressure still pushes them towards the wall and the increased hydrodynamic interactions slow them down. Therefore, the effect of hydrodynamic wall-particle interactions can be determined independently.

ACKNOWLEDGMENTS

We thank R. Capellmann, M. Escobedo-Sanchez, S. Glöckner, F. Platten, D. Wagner and C. Zünke for very helpful discussions and suggestions, and the Deutsche Forschungsgemeinschaft (DFG) for financial support within the SFB-TR6.

3.1 Paper I: Experimental creation and characterization of random potential-energy landscapes exploiting speckle patterns

12

- [1] D. J. Wales, *Energy Landscapes* (Cambridge University Press, England, 2004).
- [2] A. Heuer, *J. Phys.: Condens. Matter* **20**, 373101 (2008).
- [3] P. G. Debenedetti and F. H. Stillinger, *Nature* **410**, 259 (2001).
- [4] C. A. Angell, *Science* **267**, 1924 (1995).
- [5] F. H. Stillinger, *Science* **267**, 5206 (1995).
- [6] A. P. Jardine, S. Dworski, P. Fouquet, G. Alexandrowicz, D. J. Riley, G. Y. H. Lee, J. Ellis, and W. Allison, *Science* **304**, 1790 (2004).
- [7] F. Córdoba-Valdés, R. Castañeda-Priego, J. Timmer, and C. Fleck, *Soft Matter* **10**, 8475 (2014).
- [8] C.-L. Hsieh, S. Spindler, J. Ehring, and V. Sandoghdar, *J. Phys. Chem. B* **118**, 1545 (2014).
- [9] P. Tierno, P. Reimann, T. H. Johansen, and F. Sagués, *Phys. Rev. Lett.* **105**, 230602 (2010).
- [10] L. Chen, M. Falcioni, and M. W. Deem, *J. Phys. Chem. B* **104**, 6033 (2000).
- [11] M. Weiss, M. Elsner, F. Kartberg, and T. Nilsson, *Biophys. J.* **87**, 3518 (2004).
- [12] F. Höfling and T. Franosch, *Rep. Prog. Phys.* **76**, 046602 (2013).
- [13] I. M. Tolić-Nørrelykke, E.-L. Munteanu, G. Thon, L. Oddershede, and K. Berg-Sørensen, *Phys. Rev. Lett.* **93**, 078102 (2004).
- [14] M. White, M. Pasienski, D. McKay, S. Q. Zhou, D. Ceperley, and B. DeMarco, *Phys. Rev. Lett.* **102**, 055301 (2009).
- [15] M. Robert-de Saint-Vincent, J.-P. Brantut, B. Allard, T. Plisson, L. Pezzé, L. Sanchez-Palencia, A. Aspect, T. Bourdel, and P. Bouyer, *Phys. Rev. Lett.* **104**, 220602 (2010).
- [16] P. Bouyer, *Rep. Progr. Phys.* **73**, 062401 (2010).
- [17] J. E. Lye, L. Fallani, M. Modugno, D. S. Wiersma, C. Fort, and M. Inguscio, *Phys. Rev. Lett.* **95**, 070401 (2005).
- [18] C. Fort, L. Fallani, V. Guarrera, J. E. Lye, M. Modugno, D. S. Wiersma, and M. Inguscio, *Phys. Rev. Lett.* **95**, 170410 (2005).
- [19] D. Clément, A. F. Varón, M. Hugbart, J. A. Retter, P. Bouyer, L. Sanchez-Palencia, D. M. Gangardt, G. V. Shlyapnikov, and A. Aspect, *Phys. Rev. Lett.* **95**, 170409 (2005).
- [20] D. Clément, A. F. Varón, J. A. Retter, L. Sanchez-Palencia, A. Aspect, and P. Bouyer, *New J. Phys.* **8**, 165 (2006).
- [21] P. Horak, J.-Y. Courtois, and G. Grynberg, *Phys. Rev. A* **58**, 3953 (1998).
- [22] R. L. Baldwin, *Nature* **369**, 183 (1994).
- [23] K. A. Dill and H. S. Chan, *Nat. Struct. Mol. Biol.* **4**, 10 (1997).
- [24] S. D. Durbin and G. Feher, *Annu. Rev. Phys. Chem.* **47**, 171 (1996).
- [25] H. Frauenfelder, S. G. Sligar, and P. G. Wolynes, *Science* **254**, 1598 (1991).
- [26] H. Janovjak, H. Knaus, and D. J. Muller, *J. Am. Chem. Soc.* **129**, 246 (2007).
- [27] J.-P. Bouchaud and A. Georges, *Phys. Rep.* **195**, 127 (1990).
- [28] D. S. Dean, I. T. Drummond, and R. R. Horgan, *J. Stat. Mech.: Theory Exp.*, P07013 (2007).
- [29] A. Sengupta, S. Sengupta, and G. I. Menon, *Europhys. Lett.* **70**, 635 (2005).
- [30] M. B. Isichenko, *Rev. Mod. Phys.* **64**, 961 (1992).
- [31] I. Goychuk and V. O. Kharченко, *Phys. Rev. Lett.* **113**, 100601 (2014).
- [32] S. Banerjee, R. Biswas, K. Seki, and B. Bagchi, *J. Chem. Phys.* **141**, 124105 (2014).
- [33] R. Zwanzig, *Proc. Natl. Acad. Sci. USA* **85**, 2029 (1988).
- [34] A. Ashkin, J. M. Dziedzic, J. E. Bjorkholm, and S. Chu, *Opt. Lett.* **11**, 288 (1986).
- [35] A. Ashkin, *Biophys. J.* **61**, 569 (1992).
- [36] D. G. Grier, *Nature* **424**, 810 (2003).
- [37] K. Dholakia, P. Reece, and M. Gu, *Chem. Soc. Rev.* **37**, 42 (2008).
- [38] F. Evers, R. D. L. Hanes, C. Zunke, R. F. Capellmann, J. Beverunge, C. Dalle-Ferrier, M. C. Jenkins, I. Ladadwa, A. Heuer, R. Castañeda-Priego, and S. U. Egelhaaf, *Eur. Phys. J. - Special Topics* **222**, 2995 (2013).
- [39] R. D. L. Hanes, M. C. Jenkins, and S. U. Egelhaaf, *Rev. Sci. Instrum.* **80**, 083703 (2009).
- [40] R. D. L. Hanes, C. Dalle-Ferrier, M. Schmiedeberg, M. C. Jenkins, and S. U. Egelhaaf, *Soft Matter* **8**, 2714 (2012).
- [41] R. D. L. Hanes and S. U. Egelhaaf, *J. Phys.: Condens. Matter* **24**, 464116 (2012).
- [42] R. D. L. Hanes, M. Schmiedeberg, and S. U. Egelhaaf, *Phys. Rev. E* **88**, 062133 (2013).
- [43] F. Evers, C. Zunke, R. D. L. Hanes, J. Beverunge, I. Ladadwa, A. Heuer, and S. U. Egelhaaf, *Phys. Rev. E* **88**, 022125 (2013).
- [44] R. W. Bowman and M. J. Padgett, *Rep. Prog. Phys.* **76**, 28 (2013).
- [45] K. C. Neuman and S. M. Block, *Rev. Sci. Instrum.* **75**, 2787 (2004).
- [46] M. P. N. Juniper, R. Besseling, D. G. A. L. Aarts, and R. P. A. Dullens, *Opt. Expr.* **20**, 28707 (2012).
- [47] B. J. Ackerson and A. H. Chowdhury, *Faraday Discuss. Chem. Soc.* **83**, 309 (1987).
- [48] M. C. Jenkins and S. U. Egelhaaf, *J. Phys.: Condens. Matter* **20**, 404220 (2008).
- [49] C. Dalle-Ferrier, M. Krüger, R. D. L. Hanes, S. Walta, M. C. Jenkins, and S. U. Egelhaaf, *Soft Matter* **7**, 2064 (2011).
- [50] C. Bechinger, M. Brunner, and P. Leiderer, *Phys. Rev. Lett.* **86**, 930 (2001).
- [51] J. Mikhael, J. Roth, L. Helden, and C. Bechinger, *Nature* **454**, 501 (2008).
- [52] J. Mikhael, M. Schmiedeberg, S. Rausch, J. Roth, H. Stark, and C. Bechinger, *Proc. Natl. Acad. Sci. USA* **107**, 7214 (2010).
- [53] J. C. Dainty, in *Progress in Optics XIV*, edited by E. Wolf (North-Holland, 1976).
- [54] J. W. Goodman, *Speckle Phenomena in Optics: Theory and Applications* (Roberts & Co., Englewood, Colorado, 2007).
- [55] A. P. Mosk, A. Lagendijk, G. Leroosey, and M. Fink, *Nat. Phot.* **6**, 283 (2012).
- [56] G. Volpe, L. Kurz, A. Callegari, G. Volpe, and S. Gigan, *Opt. Expr.* **22**, 18159 (2014).
- [57] D. Boiron, C. Mennerat-Robilliard, J.-M. Forunier, L. Guidoni, C. Salomon, and G. Grynberg, *Eur. Phys. J. D* **7**, 373 (1999).

- [58] G. Brügger, L. S. Froufe-Pérez, F. Scheffold, and J. J. Sáenz, *Nat. Comm.* **6**, 7460 (2015).
- [59] V. G. Shvedov, A. V. Rode, Y. V. Izdebskaya, D. Leykam, A. S. Desyatnikov, W. Krolikowski, and Y. S. Kivshar, *J. Opt.* **12**, 124003 (2010).
- [60] S. S. Kondov, W. R. McGehee, J. J. Zirbel, and B. DeMarco, *Science* **334**, 66 (2011).
- [61] K. M. Douglass, S. Sukhov, and A. Dogariu, *Nat. Phot.* **6**, 834 (2012).
- [62] T. R. M. Sales, *Opt. Eng.* **42**, 3084 (2003).
- [63] G. M. Morris, T. R. M. Sales, S. Chakmakjian, and D. J. Schertler, *Engineered Diffusers for Display and Illumination Systems: Design, Fabrication, and Applications.*, Tech. Rep. (RPC Photonics, 2007).
- [64] T. R. M. Sales, *Adv. Opt. Techn.* **1**, 127 (2012).
- [65] F. M. Dickey, ed., *Laser Beam Shaping: Theory and Techniques, Second Edition* (CRC Press Inc., 2014).
- [66] A. H. Chowdhury, F. K. Wood, and B. J. Ackerson, *Optics Communications* **86**, 547 (1991).
- [67] K. Loudiyi and B. J. Ackerson, *Phys. A* **184**, 1 (1992).
- [68] M. Pelton, K. Ladavac, and D. G. Grier, *Phys. Rev. E* **70**, 031108 (2004).
- [69] O. Korotkova, *Random Light Beams: Theory and Applications* (CRC Press Inc., 2013).
- [70] D. Li, D. P. Kelly, R. Kirner, and J. T. Sheridan, *Appl. Opt.* **51**, A1 (2012).
- [71] D. Li, D. P. Kelly, and J. T. Sheridan, *J. Opt. Soc. Am. A* **28**, 1896 (2011).
- [72] D. Li, D. P. Kelly, and J. T. Sheridan, *J. Opt. Soc. Am. A* **28**, 1904 (2011).
- [73] J. W. Goodman, in *Laser Speckle and Related Phenomena*, edited by J. C. Dainty (Springer, New York, 1984).
- [74] I. M. Lifshits, S. A. Gredeskul, and L. A. Pastur, *Introduction to the Theory of Disordered Systems* (Wiley, New York, 1988).
- [75] S. E. Skipetrov, J. Peuser, R. Cerbino, P. Zakharov, B. Weber, and F. Scheffold, *Opt. Expr.* **18**, 14519 (2010).
- [76] Y. Baykal, *Opt. Laser Techn.* **45**, 593 (2013).
- [77] L. Song and D. S. Elson, *Biomed. Opt. Expr.* **4**, 89 (2013).
- [78] Y. Bromberg and H. Cao, *Phys. Rev. Lett.* **112**, 213904 (2014).
- [79] S. J. Kirkpatrick, D. D. Duncan, R. K. Wang, and M. T. Hinds, *J. Opt. Soc. Am. A* **24**, 3728 (2007).
- [80] S. J. Kirkpatrick, D. D. Duncan, and E. M. Wells-Gray, *Opt. Lett.* **33**, 2886 (2008).
- [81] J. D. Briers and S. Webster, *J. Biomed. Opt.* **1**, 174 (1996).
- [82] D. D. Duncan, S. J. Kirkpatrick, and R. K. Wang, *J. Opt. Soc. Am. A* **25**, 9 (2008).
- [83] F. Scheffold and I. D. Block, *Opt. Expr.* **20**, 192 (2012).
- [84] D. Briers, D. D. Duncan, E. Hirst, S. J. Kirkpatrick, M. Larsson, W. Steenbergen, T. Stromberg, and O. B. Thompson, *J. Biomed. Opt.* **18**, 066018 (2013).
- [85] J. C. Crocker and D. G. Grier, *J. Coll. Interf. Sci.* **179**, 298 (1996).
- [86] P. Bahukudumbi and M. A. Bevan, *J. Chem. Phys.* **126**, 244702 (2007).
- [87] C. F. Bohren and D. R. Huffman, *Absorption and Scattering of Light by Small Particles* (Wiley-VCH, New York, 2004).
- [88] A. Rohrbach, *Phys. Rev. Lett.* **95**, 168102 (2005).
- [89] D. Bonessi, K. Bonin, and T. Walker, *J. Opt. A: Pure Appl. Opt.* **9**, 228 (2007).
- [90] M. C. Jenkins and S. U. Egelhaaf, *Adv. Coll. Interf. Sci.* **136**, 65 (2008).
- [91] A. D. Ducharme, *Opt. Expr.* **15**, 14573 (2007).

3.1 Paper I: Experimental creation and characterization of random potential-energy landscapes exploiting speckle patterns

This page has been left intentionally blank.

3.2 Paper II: Colloids Exposed to Random Potential Energy Landscapes: from Particle Number Density to Particle-Potential and Particle-Particle Interactions

Journal: Journal of Chemical Physics (JCP)

Reference: Accepted

Impact factor: 3.017

Authors: **Jörg Bewerunge**, Ankush Sengupta, Ronja Capellmann, Florian Platten, Surajit Sengupta and Stefan U. Egelhaaf

1st author

JB performed the measurements and analysed the data. AS and SS performed theoretical calculations. JB and SUE conceived, designed and discussed the experiments. All authors discussed the results, contributed to their interpretation and the writing of the manuscript.

75% contribution of JB

3.2 Paper II: Colloids Exposed to Random Potential Energy Landscapes: from Particle Number Density to Particle-Potential and Particle-Particle Interactions

This page has been left intentionally blank.

Colloids Exposed to Random Potential Energy Landscapes: from Particle Number Density to Particle-Potential and Particle-Particle Interactions

Jörg Bewerunge,¹ Ankush Sengupta,² Ronja F. Capellmann,¹ Florian Platten,¹ Surajit Sengupta,³ and Stefan U. Egelhaaf¹

¹⁾ *Condensed Matter Physics Laboratory, Heinrich Heine University, 40225 Düsseldorf, Germany*

²⁾ *Department of Chemical Physics, Weizmann Institute of Science, 234 Herzl St., Rehovot 7610001, Israel*

³⁾ *TIFR Centre for Interdisciplinary Sciences, Hyderabad 500075, India*

(Dated: 8 July 2016)

Colloidal particles were exposed to a random potential energy landscape (rPEL) that has been created optically via a speckle pattern. The mean particle density as well as the potential roughness, i.e. the disorder strength, were varied. The local probability density of the particles as well as its main characteristics were determined. For the first time, the disorder-averaged pair density correlation function $g^{(1)}(r)$ and an analogue of the Edwards-Anderson order parameter $g^{(2)}(r)$, which quantifies the correlation of the mean local density among disorder realisations, were measured experimentally and shown to be consistent with replica liquid state theory results.

PACS numbers: 05.20.Jj, 47.57.-s, 64.70.pv, 82.70.Dd

I. INTRODUCTION

The potential energy landscape (PEL) of a system depends on the coordinates and/or other parameters of its constituents.¹ The concept of a PEL is successfully used in many fields of science to determine the properties and behavior of systems ranging from small, large and polymeric molecules, proteins and other biomolecules to clusters, glasses and biological cells.¹ It is also applied to describe the transport over atomic surfaces,²⁻⁴ in materials with defects (e.g., ions in zeolites⁵ or charge carriers in conductors with impurities⁶), in inhomogeneous media^{7,8} (e.g., porous gels,⁹ cell membranes¹⁰ or cells¹¹⁻¹⁴) or in the presence of fixed obstacles as in a Lorentz gas.¹⁵ They are also used to determine the rates of (bio)chemical reactions,^{1,16} the folding of proteins and DNA,¹⁷⁻²³ as well as the particle dynamics in dense suspensions close to freezing,²⁴ in glasses^{4,25-35} or, more general, in crowded systems.¹²

We focus on random potential energy landscapes (rPEL), which have been used in the interpretation of several experimental observations. For example, rPEL with a Gaussian distribution of energy values with a width of about the thermal energy have been used to describe the behavior of RNA, proteins and transmembrane helices.^{19,36,37} Although a rPEL might only represent a crude approximation for many experimental situations, it often provides a very useful initial description of the effect of disorder on the dynamics.^{5,35,38}

The PEL is experimentally realised by exploiting the interaction of light with colloidal particles,^{39,40} which was already applied to realise, e.g., sinusoidal⁴¹⁻⁴⁵ or random landscapes.⁴⁶⁻⁵¹ (See 49 for a review.) Here we investigate how a rPEL modifies the spatial arrangement of ensembles of colloidal particles.^{1,7,52} Local density variations occur, which are related to the distribution of

energy levels $p(U)$ and the spatial correlation function $C_U(r)$ of the underlying potential. For various disorder strengths, controlled through the laser power P , and particle concentrations, i.e. mean particle number densities ρ_0 , we track particle positions and calculate the local density $\rho(\mathbf{r}, t)$ at each time t , based on which different correlation functions are obtained: the disorder-averaged pair distribution function or pair density correlation function $g^{(1)}(r)$,⁵³ and, to characterize the quenched disorder, the density correlation $g^{(2)}(r)$,^{52,54} similar to the Edwards-Anderson order parameter,⁵⁵⁻⁵⁷ which is intensively used in the context of spin glasses and has been proposed in the context of pinned vortex liquids⁵⁴ and calculated in computer simulations.^{52,58} However, as yet it has never been measured in an experiment. In this paper, we proceed to do precisely that. This analysis provides the main characteristics of the effect of the disorder, i.e. the rPEL, with respect to particle-potential as well as pair and higher order inter-particle interactions and can easily be extended to other systems, such as magnetic bubble arrays in a disordered potential,⁵⁹⁻⁶¹ particles on patterned surfaces⁶² and vortex liquids as well as glasses in the presence of random pinning.^{58,63}

II. MATERIALS AND METHODS

A. Optical Set-up

A random intensity distribution, i.e. a speckle pattern, was created by directing an expanded laser beam (Laser Quantum, Opus 532, wavelength 532 nm, maximum intensity $P_{\max} = 2.6$ W) onto a microlens array (RPC Photonics, Engineered Diffuser™ EDC-1-A-1r, diameter 25.4 mm)^{64,65} and subsequently focussing the modified beam into the sample plane of an inverted microscope.

3.2 Paper II: Colloids Exposed to Random Potential Energy Landscapes: from Particle Number Density to Particle-Potential and Particle-Particle Interactions

2

This results in a macroscopically uniform beam with a so called top-hat intensity distribution. However, the wavefronts from the randomly-distributed microlenses interfere in the sample plane. This leads to microscopic intensity variations, so-called laser speckles, to which the particles were exposed. The interaction of the particles with the speckle pattern can be described by a rPEL. The particle size roughly matches the speckle size, but is much larger than the laser wavelength. Moreover, the laser intensity is spread over a large field of view. Thus, we neither expect nor observe optical binding effects^{66,67} or light field-induced dispersion forces.⁶⁸ The colloidal particles were observed using the inverted microscope (Nikon, Eclipse Ti-U) with a 20 \times objective (Nikon, CFI S Plan Fluor ELWD, numerical aperture 0.45). A detailed description of the optical set-up and a statistical analysis of both the intensity pattern and the resulting rPEL can be found in ref. 51, where the present conditions correspond to ‘BE 5 \times ’.

B. Samples

Samples consisted of spherical polystyrene particles with sulfonated chain ends (Invitrogen, diameter $D = 2.8 \mu\text{m}$, polydispersity 3.2 %) dispersed in purified water (ELGA purelab flex, electrical resistivity $18.2 \times 10^4 \Omega\text{m}$). Three glass cover slips (#1.5) and a microscope slide (all from VWR) were assembled to form a small capillary.⁶⁹ After the capillary was filled with the dispersion, it was sealed with UV-glue (Norland, NOA61). Due to the density difference between particles and water, the particles sedimented and formed a quasi two-dimensional layer at the bottom of the sample cell.

C. Data Acquisition

Each measurement consisted of $K \approx 27,000$ images, which were recorded at 3.75 frames per second using an 8-bit camera (AVT, Pike F-032B with 640×480 pixels and pixel pitch of $0.372 \mu\text{m}$). Particle positions were determined using standard procedures.⁷⁰ Because the system evolves from a quenched random distribution towards its equilibrium distribution, care was taken that the correlation functions are not affected by the relaxation process, i.e. do not show a time dependence.⁷¹

Based on the particle positions, we determined the number of particles $\mathcal{N}(x_m, y_n, t, l)$ in each region at $\mathbf{r} = \mathbf{r}_{mn} = (x_m, y_n)$ at each time t for a particular realisation of the potential l (out of L different realisations), and calculated the local particle density as

$$\rho(x_m, y_n, t, l) = \frac{\mathcal{N}(x_m, y_n, t, l)}{\Delta x \Delta y}, \quad (1)$$

where $\Delta x = x_m - x_{m-1}$ and $\Delta y = y_n - y_{n-1}$, with $\Delta x = \Delta y$ for all $m = 1 \dots M$, $n = 1 \dots N$. Hence the quadratic regions all have the same size of $0.186 \mu\text{m}$, which is well

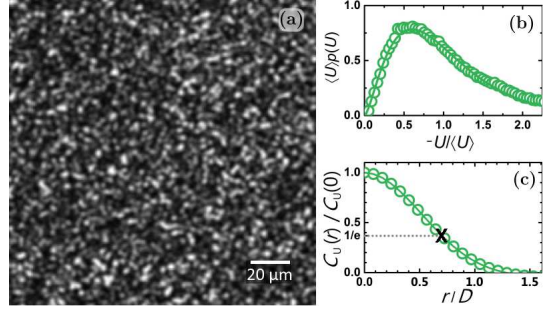


FIG. 1. (a) Random potential energy landscape (rPEL), i.e. $U(\mathbf{r})$, as calculated by convolving the measured intensity pattern $I(\mathbf{r})$ with the projected volume of a particle of diameter $D = 2.8 \mu\text{m}$, (b) its normalized probability density of energy values $p(U)$ and (c) its normalized spatial correlation function $C_U(r)/C_U(0)$ with $1/e$ -width $0.69D$ indicated by a cross.

above the uncertainty of the particle positions, about $0.05 \mu\text{m}$.⁷⁰ It is noteworthy that these regions do not coincide with pixels of the camera. The distance r between two regions at \mathbf{r} and \mathbf{r}' is $r = |\mathbf{r} - \mathbf{r}'|$, which depends on the location of both regions and thus on m, m', n and n' . It was divided into bins of $\Delta r = 0.2\Delta x$, which represents a compromise between good statistics and high resolution.

III. RESULTS AND DISCUSSION

A. Random Potential Energy Landscape (rPEL)

The colloidal particles were exposed to a rPEL by exploiting the interaction of light with particles having a refractive index different from the one of the dispersing liquid. Their interaction usually is described by two forces:^{39,40} a scattering force, which pushes the particles along the beam, and a gradient force, which pulls particles with a larger refractive index than the one of the solvent towards regions of high intensity. This effect is typically applied in optical tweezers which are used to trap or manipulate colloidal particles.^{39,40,72,73} Rather than single focused beams, an extended light field can be used to create a PEL.⁴⁹ To predict not only the shape of the PEL but also its amplitude, the particles' susceptibility or polarizability needs to be known, which typically is not the case. Nevertheless, it is possible to calculate the typical characteristics of the PEL by integrating the local intensity $I(\mathbf{r})$ over the particle's projected volume, thus taking the particle volume traversed by the light beam into account.⁷⁴ This results in an estimate of the potential $U(\mathbf{r})$ imposed on a particle, which then is considered to be point-like.⁵¹

Fig. 1 (a) shows one realisation of the rPEL, i.e. $U(\mathbf{r})$, as a grey scale image which was obtained by convolv-

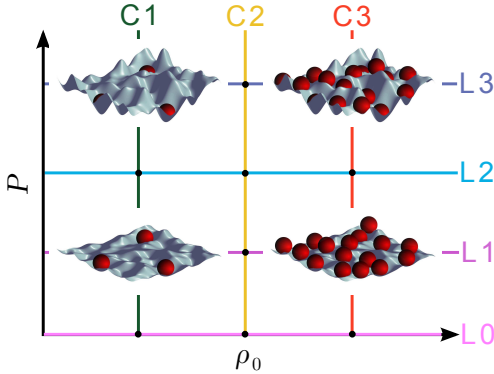


FIG. 2. Different laser powers P (L0 to L3), corresponding to different mean potential values $\langle U \rangle$ or disorder strengths, and mean particle densities ρ_0 (C1 to C3) are investigated. For four conditions sketches showing particles in a rPEL are shown.

ing a recorded intensity pattern with the projected volume of a particle. The rPEL was characterized by the distribution of energy values $p(U)$, which follows a Gamma distribution⁷⁵ with shape parameter $M = 2.6$ (Fig. 1 (b), for details see condition BE5 \times in Tab. II of ref. 51). The length scale of the fluctuations was described by the normalized spatial covariance function $C_U(\mathbf{r}) = \langle U(\mathbf{r}')U(\mathbf{r}' + \mathbf{r}) \rangle_{\mathbf{r}'} / \langle U(\mathbf{r}') \rangle_{\mathbf{r}'}^2 - 1$, whose azimuthal average can be described by a Gaussian distribution $C_U(r) = \exp(-(r/\xi)^2)$ with $\xi = 0.69D$ (Fig. 1 (c)).

B. Particles in the rPEL

In the experiments, the particle concentration, i.e. the mean particle number density ρ_0 or the particle area fraction $\phi_A = \pi(D/2)^2\rho_0$, as well as the laser power P , and hence the mean potential value $\langle U \rangle$ and the disorder strength, were varied, whereas the shape of the distribution, $p(U)$, and the spatial correlation function, $C_U(r)$, remain unchanged (Fig. 2). We consider three different ρ_0 (C1: $\rho_0 = 0.007 \mu\text{m}^{-2}$, C2: $\rho_0 = 0.041 \mu\text{m}^{-2}$, C3: $\rho_0 = 0.072 \mu\text{m}^{-2}$, corresponding to area fractions $\phi_A = 0.045, 0.25$ and 0.45 , respectively) as well as four different P (L0: 0 mW, L1: 917 mW, L2: 1640 mW, L3: 2600 mW), and indicate conditions by CiLj.

Fig. 3 shows images of colloidal particles (top) and their trajectories (bottom) for two different mean particle densities ρ_0 (C1, C3) and increasing laser power P and hence disorder strength (L0, L1, L3), where L0 corresponds to the absence of a laser field and hence free diffusion. (For images at other combinations of mean particle density and laser power see Fig. 12 in the appendix.) Neither for the low nor for the high mean particle density an effect of the potential is immediately visible in the im-

ages. However, there is a clear effect of the rPEL on the trajectories. For the low mean particle density C1, as the disorder strength is increased, the motion of the particles is restricted to small areas and a few particles even stay in one potential minimum for the entire measurement time. At high mean particle density C3 and low laser power L1 (Fig. 3 (f)) almost the whole field of view is sampled by the particles. This indicates that the particles are very mobile and exchange positions. In contrast, for high potential roughness L3 (Fig. 3 (j)) some particles appear stuck in potential minima. This prevents other particles from exploring their neighbourhood and leads to regions depleted of particle centres.

The dynamic behaviour has important consequences on how particles sample a PEL. Since experiments have a limited measurement time, sampling can be incomplete and hence local information only be partially accessible. The completeness of sampling determines whether time-averaged quantities might hold reliable local information and describe all points in a PEL, or whether only spatially-averaged quantities might provide reliable information. Very low mean particle densities result in only limited information on some locations of the PEL. Upon increasing the mean particle density, sampling can become more complete (e.g. C3L1). However, higher mean particle densities also enhance particle-particle interactions, which hence might dominate particle-potential interactions. This reduces correlations with the underlying potential. Moreover, a strongly varying potential can also result in an ‘undersampling’ of energetically unfavourable areas, i.e. potential maxima, since they are avoided by the particles. The unexplored areas might depend on the initial positions of the particles, due to the quenched disorder of the potential. An average over different disorder realisations might help, but excludes the determination of local quantities, which lose their relevance.

C. Time-Averaged Particle Density

First, we consider the time-averaged (or thermal-averaged) local particle density

$$\langle \rho(\mathbf{r}, t, l) \rangle_t = \frac{1}{K} \sum_{k=1}^K \rho(x_m, x_n, t, l). \quad (2)$$

Its ensemble and disorder average gives the mean particle density $\rho_0 = [\langle \rho(\mathbf{r}, t, l) \rangle_{t, \mathbf{r}}]_l$, where $\langle \dots \rangle_t$, $\langle \dots \rangle_{\mathbf{r}}$ and $[\dots]_l$ denote time, ensemble and disorder averages, respectively. In the experiments presented here, the large field of view provides a sufficient disorder average within a single rPEL realisation. Thus here the total number of disorder realisations $L = 1$ and the sample average implies an ensemble and disorder average.

Fig. 4 shows the time-averaged local particle density $\langle \rho(\mathbf{r}, t) \rangle_t$, for large laser power L3 and high mean particle density C3 (cf. Fig. 3 (i) and (j)). (For further examples see Fig. 11 in the appendix.) For dilute samples in

3.2 Paper II: Colloids Exposed to Random Potential Energy Landscapes: from Particle Number Density to Particle-Potential and Particle-Particle Interactions

4

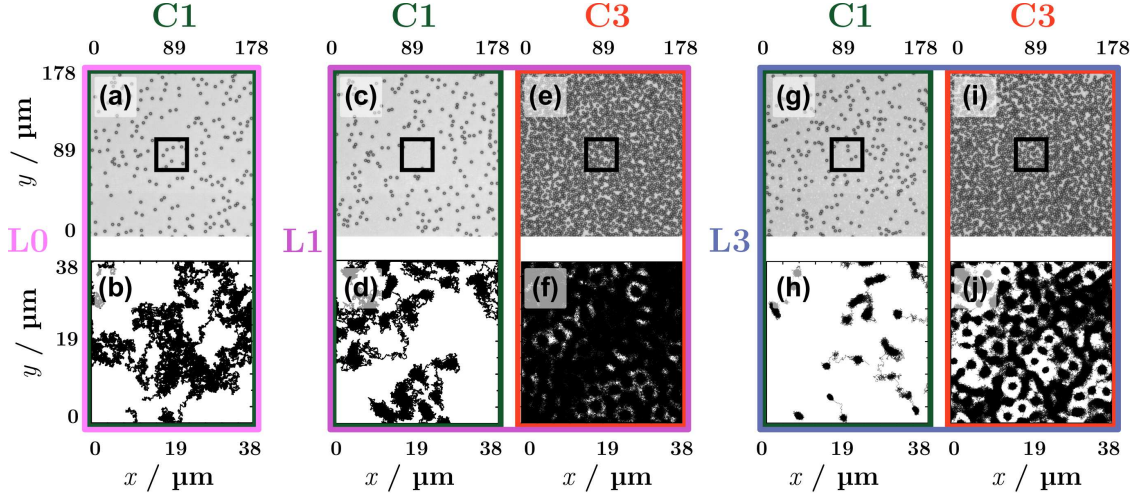


FIG. 3. (top) Micrographs of parts of the samples ($178 \times 178 \mu\text{m}^2$) and (bottom) particle trajectories in a central region ($38 \times 38 \mu\text{m}^2$, indicated in the micrographs) during a time $\Delta t = 7200$ s after the micrograph has been taken, for different laser powers L0, L1, L3 (left to right) and mean particle densities C1, C3.

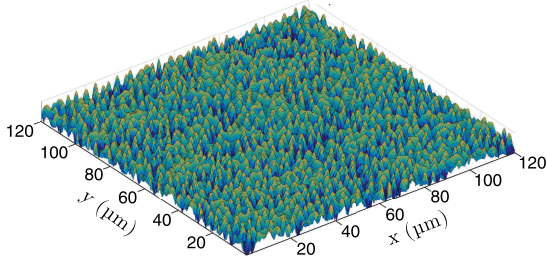


FIG. 4. Time-averaged local particle density $\langle \rho(\mathbf{r}, t) \rangle_t$ for high laser power L3 and large mean particle density C3. The logarithmic colour scale indicates low ($\rho_0 = 1 \times 10^{-4} \mu\text{m}^{-2}$) to high ($\rho_0 = 0.63 \mu\text{m}^{-2}$) local densities by dark blue to red colours.

equilibrium, $\langle \rho(\mathbf{r}, t) \rangle_t$ is related to $U(\mathbf{r})$ (Fig. 1 (a)) by the Boltzmann distribution. At mean particle densities which result in reasonable statistics, however, $\langle \rho(\mathbf{r}, t) \rangle_t$ is affected by both, $U(\mathbf{r})$ and particle-particle interactions.

The local time-averaged particle density $\langle \rho(\mathbf{r}, t) \rangle_t$ is characterized by the two-dimensional density autocovariance function $C(\mathbf{r})$, i.e. the density autocorrelation function of $\langle \rho(\mathbf{r}, t) \rangle_t$ around the mean ρ_0 , which is, making use of the Wiener-Khinchin theorem,⁷⁶ given by

$$C(\mathbf{r}) = \left[\langle \langle \rho(\mathbf{r}', t) \rangle_t \langle \rho(\mathbf{r}' + \mathbf{r}, t) \rangle_t \rangle_{\mathbf{r}'} \right]_l - \rho_0^2 = \left[\mathcal{F}^{-1} \left(\mathcal{F} \{ \langle \rho(\mathbf{r}, t) \rangle_t - \rho_0 \} \mathcal{F}^* \{ \langle \rho(\mathbf{r}, t) \rangle_t - \rho_0 \} \right) \right]_l \quad (3)$$

where \mathcal{F} , \mathcal{F}^{-1} , and $*$ indicate the Fourier transformation, inverse Fourier transformation, and complex con-

jugation, respectively. Since isotropic samples are considered, an azimuthal average is carried out; $C(r) = (1/2\pi) \int_0^{2\pi} C(r, \Theta) d\Theta$.

In Fig. 5, the azimuthally-averaged density autocovariance function $C(r)$ is shown for different laser powers. It shows similar behaviour for all investigated experimental conditions since varying the laser power only changes the disorder strength but not the shape or statistics of the rPEL. A pronounced peak is located at the origin which is well described by a Gaussian distribution $C(r) = \sigma^2 \exp(-(r/l_c)^2)$ (Fig. 5 inset). Its amplitude $\sigma^2 = C(0) = \langle \langle \rho(\mathbf{r}, t) \rangle_t^2 \rangle_{\mathbf{r}} - \rho_0^2$ is the variance of the local particle density and describes the probability to find a, not necessarily the same, particle in a specific region for the entire measurement time. Thus the amplitude σ^2 characterizes the mean depth of the potential minima as sampled by the particles. It increases with potential strength about linearly and also increases with ρ_0 (Fig. 6(a)). With increasing ρ_0 , the particles occupy increasingly higher potential values thus broadening the range of occupied values and increasing σ . The correlation length l_c (Fig. 6(b)) characterizes the width of the potential minimum as sampled by the particles. It decreases with laser power P , i.e. disorder strength, reflecting the tighter pinning. It also depends on the mean particle density ρ_0 . For low ρ_0 , particle-potential interactions dominate, whereas with increasing ρ_0 , the particles occupy increasingly higher potential values within the same minimum and hence l_c increases. In contrast, for high ρ_0 , particle-particle interactions dominate and the area fraction occupied by particles becomes important. Then l_c is mostly determined by the particle diameter D rather than the speckle size and hence slightly decreases

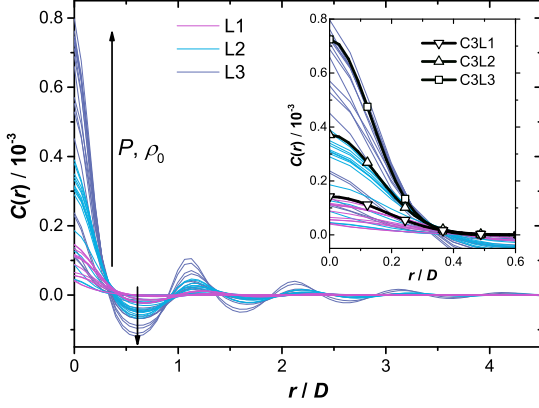


FIG. 5. Azimuthally averaged autocovariance or spatial autocorrelation function $C(r)$ of the time-averaged particle density $\langle \rho(\mathbf{r}, t) \rangle_t$ as a function of normalized distance r/D for different laser powers P (L1-L3, indicated by colours) and increasing mean particle density ρ_0 (indicated by arrows). Inset: Same data with Gaussian fits to data corresponding to mean particle density C3 as black lines with symbols representing different laser powers (as indicated).

before reaching a constant level. The height of this level decreases with potential strength, since the smaller the particles' excursions the smaller l_c .

The primary peak of $C(r)$ is followed by a minimum, which is more pronounced as the laser power increases (Fig. 5, indicated by arrow). It occurs at a distance comparable to the correlation length of the potential, $0.69D$ (Fig. 1), independent of both, P and ρ_0 . In contrast, the minimum becomes more pronounced with P and ρ_0 . It is caused by particles pinned in potential minima, which exclude particles from their vicinity (Fig. 3 (f) and (j)). The higher order minima (and maxima) are roughly spaced by multiples of the particle diameter D . These oscillations are caused by either particle-potential or, in the case of high ρ_0 , multiple-particle interactions and thus reflect spatial arrangements of neighbouring particles, such as, e.g., caused by depletion and caging.

D. Correlation Functions

To characterize the particle-potential and particle-particle interactions, based on the measured time-averaged local particle density $\langle \rho(\mathbf{r}, t) \rangle_t$ we determine the pair distribution or pair density correlation function $g^{(1)}(r)$, the off-diagonal density correlation function $g^{(2)}(r)$ and the total correlation or Ursell function $h(r)$ which all are normalized by ρ_0^2 .

The off-diagonal density correlation function $g^{(2)}(r)$ is an analogue of the Edwards-Anderson order param-

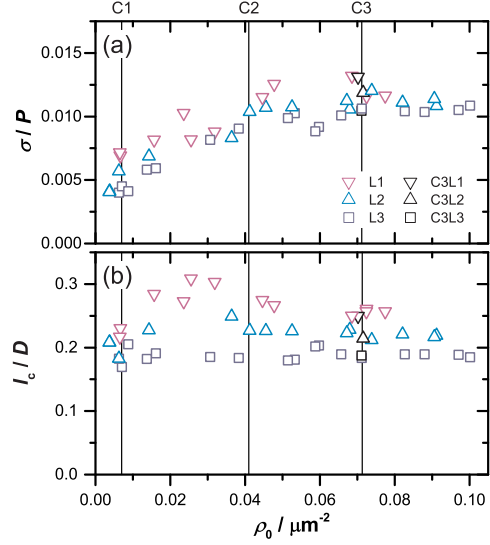


FIG. 6. (a) Standard deviation σ and (b) correlation length l_c of the time-averaged particle density $\langle \rho(\mathbf{r}, t) \rangle_t$ as a function of mean particle density ρ_0 shown for different laser powers P (L1-L3, as indicated).

eter.^{52,77} It is defined by

$$g^{(2)}(\mathbf{r}) = \frac{1}{\rho_0^2} [\langle \langle \rho(\mathbf{r}', t, l) \rangle_t \langle \rho(\mathbf{r}' + \mathbf{r}, t, l) \rangle_t \rangle_{\mathbf{r}'}]_l \quad (4)$$

and hence is the normalized spatial correlation function of the mean local density among disorder realisations. It quantifies the probability for a particle to be pinned by the rPEL, i.e. it quantifies whether a certain location is still occupied by a particle after an arbitrarily long time period.⁷⁷ Therefore it describes a coupling between spatial disorder of pinning sites and particle positional ordering in time as well as multiple-particle interactions. Without an external potential, i.e. vanishing disorder strength, and for low enough mean particle densities, where particle-particle interactions are not important, $g^{(2)}(\mathbf{r}) = 1$. Application of an external quenched disorder, here in the form of the speckle pattern of the external laser field, disrupts this conservation law locally and thereby breaks the corresponding symmetry. This phenomenon is directly observed in the form of the real space inhomogeneities introduced in the density profile. The off-diagonal density correlation function $g^{(2)}(\mathbf{r})$ characterizes the order parameter of this symmetry-broken disordered state. Furthermore, for a large field of view and hence disorder averaging in one single realisation of the rPEL, $g^{(2)}(\mathbf{r}) = C(\mathbf{r})/\rho_0^2 + 1$. We consider the azimuthal average $g^{(2)}(r)$. It is calculated from the exper-

3.2 Paper II: Colloids Exposed to Random Potential Energy Landscapes: from Particle Number Density to Particle-Potential and Particle-Particle Interactions

6

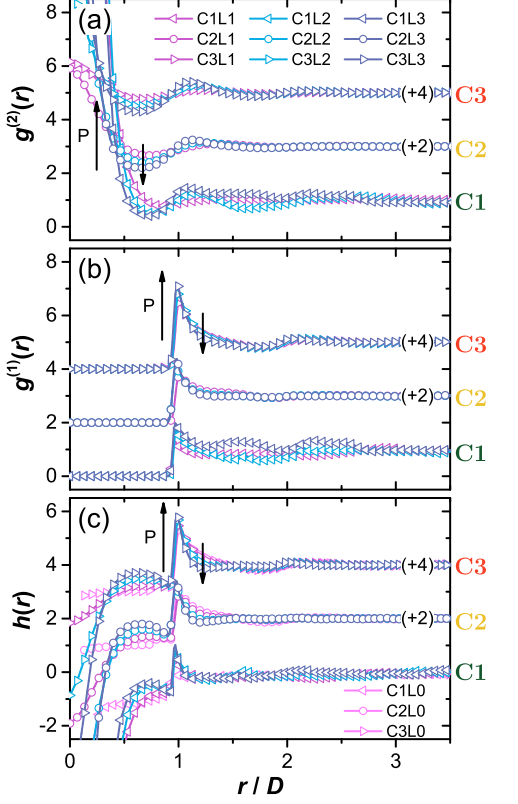


FIG. 7. (a) Azimuthally averaged off-diagonal density correlation function $g^{(2)}(r)$, (b) pair density correlation function $g^{(1)}(r)$, and (c) total correlation function $h(r)$ as a function of the normalized distance r/D for different laser powers P (L1-L3, indicated by arrows) and mean particle densities ρ_0 (C1-C3, as indicated). The data corresponding to C2 and C3 were shifted along the y-axis by +2 and +4, respectively.

imental data by

$$g^{(2)}(r) = \frac{1}{\rho_0^2} \frac{1}{L} \sum_{l=1}^L \frac{1}{MN} \sum_{m', n'=1}^{MN} \times \frac{1}{N_r} \sum_{m, n} \left[\left\{ \frac{1}{K} \sum_{k=1}^K \rho(x_{m'}, y_{n'}, t, l) \right\} \times \left\{ \frac{1}{K} \sum_{k=1}^K \rho(x_{m'+m}, y_{n'+n}, t, l) \right\} \right] \quad (5)$$

where m and n are chosen such that regions with their centres in an annulus between radii $r - \Delta r/2$ and $r + \Delta r/2$ are included with N_r the number of such regions.

Fig. 7 (a) shows $g^{(2)}(r)$ for different mean particle densities ρ_0 (C1-C3) and laser powers P (L1-L3, indicated by arrows). (Further conditions are shown in Fig. 13 in the

appendix.) For large distances r the time-averaged particle density is uncorrelated and thus $g^{(2)}(r \rightarrow \infty) = 1$. By contrast, correlations between high local densities, reflecting potential minima, lead to deviations from unity. For small distances $r \rightarrow 0$ a pronounced peak is observed, consistent with the observations in connection with the density autocovariance function $C(r)$ (cf. Fig. 5). For distances larger than the minimal particle-particle distance $r > D$, no clear r dependence of the fluctuations is visible for the lowest ρ_0 (C1). This is attributed to the irregular distribution of the small number of particles in the random potential, in particular the potential minima, and hence the limited sampling (see Sec. III B). For medium and high ρ_0 (C2, C3) maxima occur around multiple integers of D . In the absence of a rPEL no such fluctuations are present in $g^{(2)}(r)$ (Fig. 13 in the appendix). This indicates the interplay of particle-particle and particle-potential interactions.

The correlation function $g^{(1)}(\mathbf{r})$, which is the disorder-averaged analogue of the pair distribution function or pair density correlation function, is defined by⁵²

$$g^{(1)}(\mathbf{r}, l) = \frac{1}{\rho_0^2} \left[\langle \rho(\mathbf{r}', t, l) \rho(\mathbf{r}' + \mathbf{r}, t, l) \rangle_{t, \mathbf{r}'} \right]_l - \frac{1}{\rho_0} \delta(\mathbf{r}, l) \quad (6)$$

where $\delta(\mathbf{r}, l)$ is the Dirac delta function and the time average for the disordered system has to be taken prior to the disorder average. Note that the time-average of the product of the densities is taken in Eq. (6), whereas the product of the time-averaged densities is considered in Eq. (4). In the canonical ensemble the last term vanishes. The azimuthal average can be determined from the experimental data by

$$g^{(1)}(r) = \frac{1}{\rho_0^2} \frac{1}{L} \sum_{l=1}^L \frac{1}{MN} \sum_{m', n'=1}^{MN} \frac{1}{N_r} \sum_{m, n} \times \frac{1}{K} \sum_{k=1}^K \rho(x_{m'}, y_{n'}, t, l) \rho(x_{m'+m}, y_{n'+n}, t, l) \quad (7)$$

where, again, m and n are chosen to include regions with their centres in an annulus between radii $r - \Delta r/2$ and $r + \Delta r/2$. It describes the spatial variance in the time-averaged local particle density.⁵³

For $r < D$, $g^{(1)}(r) = 0$ whereas $g^{(1)}(r) = 1$ for $r \gg D$ for all conditions (Fig. 7 (b)), which resembles a hard sphere system. At intermediate r , oscillations similar to the ones found for $g^{(2)}(r)$ are observed. For large ρ_0 they hardly depend on the laser power P . At low ρ_0 the fluctuations are more pronounced but appear at random distances. This is attributed to the limited sampling of the rPEL due to the small number of particles (see Sec. III B).

The peak at $r = D$, the contact value $g^{(1)}(D)$, is linked to the compressibility and thus the equation of state⁷⁸⁻⁸⁰ (Fig. 8). The contact value $g^{(1)}(D)$ increases with ρ_0 and P . The experimentally determined $g^{(1)}(D)$ is very sensitive to the number of particles and their localization errors as well as the histogram parameters, i.e.

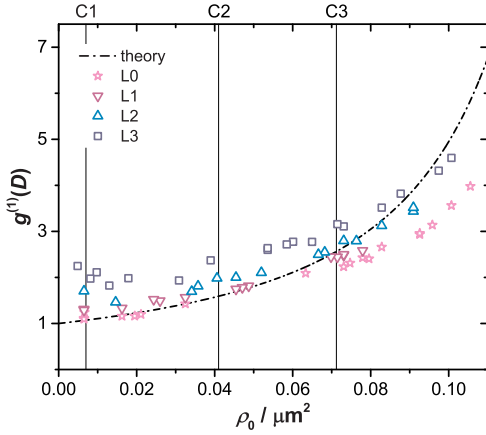


FIG. 8. Contact value of the pair density correlation function $g^{(1)}(D)$ as a function of the mean particle density ρ_0 for different laser powers P (L0-L3, as indicated). The dashed line represents the prediction by the Henderson equation of state.⁷⁹

bin positions and size. In particular at higher densities ($\rho_0 > 0.06 \mu\text{m}^{-2}$), the peak of $g^{(1)}(r)$ at $r \approx D$ is very sharp compared to the bin size and the uncertainty of our tracking procedure and therefore $g^{(1)}(D)$ is expected to be underestimated. A theoretical prediction for hard spheres,^{79,80} $g^{(1)}(D) = (1 - 7\phi_A/16) / (1 - \phi_A)^2$ (Fig. 8) agrees with the experimental data obtained in the absence of a rPEL (L0, indicated by pink stars) for low densities ($\rho_0 \lesssim 0.06 \mu\text{m}^{-2}$) but differs at higher densities. This is possibly caused by the above mentioned uncertainties involved in the determination of $g^{(1)}(D)$.

The total correlation or Ursell function $h(r)$ is given by

$$h(r) = g^{(1)}(r) - g^{(2)}(r). \quad (8)$$

The contributions of particle-potential interactions to $g^{(1)}(r)$ are taken into account by $g^{(2)}(r)$ and hence $h(r)$ mainly describes the disorder-, ensemble- and time-averaged density fluctuations caused by particle-particle and multiple-particle interactions. Therefore, $h(r)$ appears as a pair distribution function which hardly contains correlations due to the potential, in particular for $r > D$. For a homogeneous, isotropic fluid in the absence of an external potential, and hence $g^{(2)}(r) = 1$, it becomes $h(r) = g^{(1)}(r) - 1$, resembling the pair correlation function.

The total correlation function $h(r)$ is shown in Fig. 7 (c) for different mean potential densities ρ_0 (C1-C3) and laser powers P (L0-L3). In the absence of a rPEL (L0), $h(r)$ is approximately -1 for $r < D$, shows a peak at $r \approx D$ and is about zero beyond the peak for $r \gg D$. In the presence of a rPEL, the behaviour for $r < D$ differs due to the strongly increasing $g^{(2)}(r)$. The height

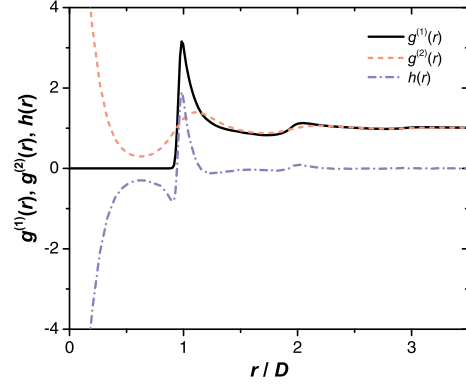


FIG. 9. Comparison of the azimuthally averaged pair density correlation function $g^{(1)}(r)$, off-diagonal density correlation function $g^{(2)}(r)$, and total correlation or Ursell function $h(r)$ as a function of normalized distance r/D for high laser power L3 and mean particle density C3.

of the peak at $r \approx D$ increases with increasing mean particle density and its width decreases with increasing laser power. Remarkably, beyond this peak $h(r)$ is almost constant and takes a value of about zero for all investigated mean particle densities and laser powers. This is due to the balance between $g^{(1)}(r)$ and $g^{(2)}(r)$ which is illustrated in Fig. 9 by a direct comparison of all three functions. The above-mentioned concurrence of the oscillations of $g^{(1)}(r)$ and $g^{(2)}(r)$ results in an almost flat $h(r)$ beyond the first peak. The remaining maximum of $h(r)$ at $r \approx 2D$ is rather attributed to particle-particle and multiple-particle interactions than particle-potential interactions. (For a comparison of $g^{(1)}(r)$ and $g^{(2)}(r)$ at all measured combinations of mean particle density ρ_0 and laser power P see Fig. 13 in the appendix.)

E. Replica Liquid State Theory

For a deeper understanding of our results, we compare the experimentally obtained correlation functions $g^{(1)}(r)$ and $g^{(2)}(r)$ to predictions of liquid state theory,⁵³ generalised to include the effects of an external rPEL, i.e. quenched disorder. While the details of this theory have been described previously,^{52,54} they are briefly mentioned for completeness.

The colloidal particles are assumed to interact with each other through a hard sphere pair potential $V(r)$ and are exposed to a random potential $U(\mathbf{r})$ with the distribution of energy values $p(U)$ being Gaussian and the short ranged spatial correlations quantified by $C_U(r)$ as in the experiments. To obtain the free energy of this system, the disorder-average of the logarithm of the partition func-

3.2 Paper II: Colloids Exposed to Random Potential Energy Landscapes: from Particle Number Density to Particle-Potential and Particle-Particle Interactions

8

tion, $[\ln Z]_l$, is calculated using the replica trick,⁵⁵

$$[\ln Z]_l = \lim_{q \rightarrow 0} \int dU p(U) \frac{Z^q - 1}{q},$$

where Z^q is the partition function of a set of q non-interacting realisations of the same system, i.e. ‘replicas’. The partition function of \mathcal{N} particles replicated q times and averaged over the disorder distribution $p(U)$ is identical to the partition function of $\mathcal{N} \times q$ particles interacting with the potential $V^{\alpha\beta}(r) = V(r)\delta_{\alpha\beta} + C_U(r)$.⁵⁴ The liquid state theory for such a system is now constructed assuming replica symmetry where all liquid state correlation functions, such as the pair correlation function, share the symmetry $g^{\alpha\beta}(r) = g^{\beta\alpha}(r) = g^{(1)}(r)\delta_{\alpha\beta} + g^{(2)}(r)(1 - \delta_{\alpha\beta})$. In the $q \rightarrow 0$ limit, the Ornstein-Zernike relation is⁵³

$$\begin{aligned} h^{(1)}(k) &= \frac{c^{(1)}(k) - (c^{(1)}(k) - c^{(2)}(k))^2}{(1 - c^{(1)}(k) + c^{(2)}(k))^2} \\ h^{(2)}(k) &= \frac{c^{(2)}(k)}{(1 - c^{(1)}(k) + c^{(2)}(k))^2}, \end{aligned} \quad (9)$$

where $h^{(1)}(k)$ is the Fourier transform of the (diagonal) pair correlation function $h^{(1)}(r) = g^{(1)}(r) - 1$ and $c^{(1)}(r)$ the corresponding direct correlation function. The off-diagonal correlations, with superscript (2), are defined analogously. The Ornstein-Zernike relation needs to be complemented with a closure relation in order to solve for the correlation functions. We have used two sets of closure relations to try to reproduce the measured correlation functions. Firstly, the analogue of the Percus-Yevick (PY) equation modified for the replicated case,

$$\begin{aligned} c^{(1)}(r) &= \left(e^{-\beta(V(r)+C_U(r))} - 1 \right) \left(1 + y^{(1)}(r) \right) \\ c^{(2)}(r) &= \left(e^{-\beta C_U(r)} - 1 \right) \left(1 + y^{(2)}(r) \right), \end{aligned} \quad (10)$$

where $y^{(1)}(r) = h^{(1)}(r) - c^{(1)}(r)$ and similarly $y^{(2)}(r)$ are the indirect correlation functions. These relations are solved using the method of Gillan.⁸¹

The results from the replicated PY liquid state theory are compared to the experimental results for C3L1, i.e. a mean particle density $\rho_0 = 0.56 D^{-2}$ (Fig. 10). Fitting yielded for the strength of the disorder $\langle U^2 \rangle^{1/2} = 1.8 k_B T$ with the thermal energy $k_B T$, consistent with experimental expectations, and for the correlation length $\xi = 0.43 D$, which is somewhat lower than the experimental value $\xi = 0.69 D$. While the $g^{(2)}(r)$ agree remarkably well, the PY approximation overestimates correlations in $g^{(1)}(r)$. This is a well known feature of the PY closure. To correct for this, we propose and solve a hybrid set of closure relations where the first equation of the set in Eq. (10) is replaced with

$$c^{(1)}(r) = e^{-\beta(V(r)+C_U(r))+y^{(1)}(r)} - 1 - y^{(1)}(r) \quad (11)$$

and the second equation is kept the same. This results in much better agreement of the $g^{(1)}(r)$ while the $g^{(2)}(r)$ is

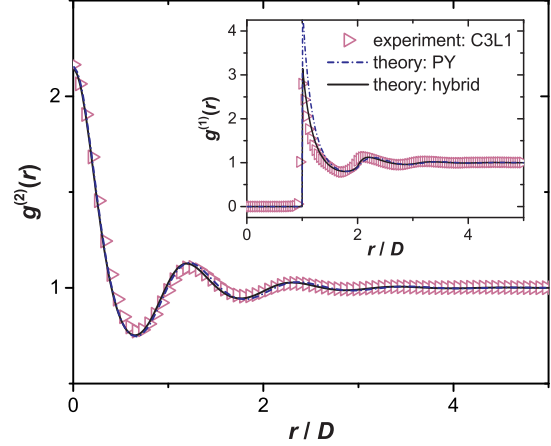


FIG. 10. Comparison of the experimentally determined azimuthally averaged off-diagonal density correlation function $g^{(2)}(r)$ and the pair density correlation function $g^{(1)}(r)$ (inset) with results obtained from liquid state theory, as a function of normalized distance r/D for low laser power L1 and high mean particle density C3.

almost unchanged. Thus, with the hybrid set of closure relations quantitative agreement between experimental data and replica liquid state theory predictions are obtained.

For experiments with the same laser power P , also the strength of the disorder $\langle U^2 \rangle^{1/2}$ and the correlation length ξ remain constant, independent of the mean particle density ρ_0 . Ideally, the results from our replica liquid state theory should follow these expectations. However, at large laser powers Eqs. (10) and (11) begin to give unphysical results. Also the fitted values, especially for ξ , depend on ρ_0 . This indicates that the validity of the simple closure relations used in our theory is limited if the disorder is strong. Moreover, it is important to ensure that the whole landscape is sampled by the particles, which is particularly difficult for dilute systems within a reasonable measurement time. This can only be resolved by further experiments on a larger set of densities ρ_0 and laser powers P and/or by a better liquid state theory.⁸²

Finally, the time-averaged local particle density in the presence of the rPEL is given by:^{52,53}

$$\langle \rho(\mathbf{r}, t, l) \rangle_t = \rho_0 - \frac{\rho_0^2}{k_B T} \int d\mathbf{r}' h(|\mathbf{r} - \mathbf{r}'|) U(\mathbf{r}') + \dots \quad (12)$$

which links the time-averaged local particle density $\langle \rho(\mathbf{r}, t, l) \rangle_t$ to the disorder potential $U(\mathbf{r})$. This analytical relationship can be used to determine $U(\mathbf{r})$ from a measurement of $\langle \rho(\mathbf{r}, t, l) \rangle_t$ or to predict $\langle \rho(\mathbf{r}, t, l) \rangle_t$ from $U(\mathbf{r})$ and $h(r)$.⁵²

IV. CONCLUSIONS

We investigated colloidal particles in a random potential energy landscape (rPEL) with energy values distributed according to a Gamma distribution. It was imposed by a laser speckle pattern. The rPEL affects the distribution of particles which, at higher mean particle densities, is also modified by particle-particle interactions. Therefore, local particle density variations occur, which are correlated in time and space. The time-averaged local particle density was determined and analysed as a function of mean particle density ρ_0 and laser power P , i.e. disorder strength. The off-diagonal density correlation function $g^{(2)}(r)$ not only reflects the potential roughness, but also spatial correlations in the local density caused by pinned particles. Thus it reflects particle-potential and particle-particle interactions. The pair density correlation function $g^{(1)}(r)$ is also influenced by spatial correlations of the rPEL. As a result, the total correlation or Ursell function $h(r) = g^{(1)}(r) - g^{(2)}(r)$ hardly reflects particle-potential interactions, but characterizes particle-particle and multiple-particle interactions. To our knowledge, this is the first time these correlation functions have experimentally been determined in the presence of disorder. Furthermore, they have successfully been compared to results from replica liquid state theory. This results in quantitative agreement, but also points towards deficits in the existing liquid state theory and calls for further experiments.

ACKNOWLEDGMENTS

We thank Manuel Escobedo-Sanchez, Jürgen Horbach, Hartmut Löwen, Gautam Menon, and Christoph Zunke for very helpful discussions and suggestions. We acknowledge funding by the Deutsche Forschungsgemeinschaft (DFG) (grant EG269/6-1) and the FP7-PEOPLE-2013-IRSES (grant no: 612707, DIONICOS).

- ¹D. J. Wales, *Energy Landscapes* (Cambridge University Press, England, 2004).
- ²J. Barth, *Surf. Sci. Rep.* **40**, 75 (2000).
- ³A. P. Jardine, S. Dworski, P. Fouquet, G. Alexandrowicz, D. J. Riley, G. Y. H. Lee, J. Ellis, and W. Allison, *Science* **304**, 1790 (2004).
- ⁴D. Nguyen, J. Mallek, A. N. Cloud, J. R. Abelson, G. S. Girolami, J. Lyding, and M. Gruebele, *J. Chem. Phys.* **141**, 204501 (2014).
- ⁵L. Chen, M. Falcioni, and M. W. Deem, *J. Phys. Chem. B* **104**, 6033 (2000).
- ⁶A. Heuer, S. Murugavel, and B. Roling, *Phys. Rev. B* **72**, 174304 (2005).
- ⁷M. B. Isichenko, *Rev. Mod. Phys.* **64**, 961 (1992).
- ⁸H. Scher and M. Lax, *Phys. Rev. B* **7**, 4491 (1973).
- ⁹R. M. Dickson, D. J. Norris, Y.-L. Tzeng, and W. E. Moerner, *Science* **274**, 966 (1996).
- ¹⁰C.-L. Hsieh, S. Spindler, J. Ehring, and V. Sandoghdar, *J. Phys. Chem. B* **118**, 1545 (2014).
- ¹¹M. Weiss, M. Elsner, F. Kartberg, and T. Nilsson, *Biophys. J.* **87**, 3518 (2004).
- ¹²F. Höfling and T. Franosch, *Rep. Prog. Phys.* **76**, 046602 (2013).
- ¹³I. M. Tolić-Nørrelykke, E.-L. Munteanu, G. Thon, L. Oddershede, and K. Berg-Sørensen, *Phys. Rev. Lett.* **93**, 078102 (2004).
- ¹⁴P. C. Blainey, G. B. Luo, S. C. Kou, W. F. Mangel, G. L. Verdine, B. Bagchi, and X. S. Xie, *Nat. Struct. Mol. Biol.* **16**, 1224 (2009).
- ¹⁵F. Höfling, T. Franosch, and E. Frey, *Phys. Rev. Lett.* **96**, 165901 (2006).
- ¹⁶W. Min, X. S. Xie, and B. Bagchi, *J. Chem. Phys.* **131**, 065104 (2009).
- ¹⁷R. L. Baldwin, *Nature* **369**, 183 (1994).
- ¹⁸S. D. Durbin and G. Feher, *Annu. Rev. Phys. Chem.* **47**, 171 (1996).
- ¹⁹H. Janovjak, H. Knaus, and D. J. Müller, *J. Am. Chem. Soc.* **129**, 246 (2007).
- ²⁰A. Arcella, G. Portelly, R. Collepardo-Guevara, D. Chakraborty, D. J. Wales, and M. Orozco, *J. Phys. Chem. B* **118**, 8540 (2014).
- ²¹H. Frauenfelder, S. G. Sligar, and P. G. Wolynes, *Science* **254**, 1598 (1991).
- ²²K. A. Dill, *Biochem.* **24**, 1501 (1985).
- ²³J. D. Bryngelson and P. G. Wolynes, *J. Phys. Chem.* **93**, 6902 (1989).
- ²⁴A. V. Indrani and S. Ramaswamy, *Phys. Rev. Lett.* **73**, 360 (1994).
- ²⁵T. R. Kirkpatrick, D. Thirumalai, and P. G. Wolynes, *Phys. Rev. A* **40**, 1045 (1989).
- ²⁶A. Heuer, *J. Phys.: Condens. Matter* **20**, 373101 (2008).
- ²⁷W. Götz, *J. Phys.: Condens. Matter* **11**, A1 (1999).
- ²⁸C. A. Angell, *Science* **267**, 1924 (1995).
- ²⁹F. Sciortino, *J. Stat. Mech.*, P05015 (2005).
- ³⁰M. Goldstein, *J. Chem. Phys.* **51**, 3728 (1969).
- ³¹S. Sastry and P. G. Debenedetti, *Nature* **393**, 554 (1998).
- ³²P. Charbonneau, J. Kurchan, G. Parisi, P. Urbani, and F. Zamponi, *Nat. Comm.* **5**, 3725 (2014).
- ³³M. D. Ediger, C. A. Angell, and S. R. Nagel, *J. Phys. Chem.* **100**, 13200 (1996).
- ³⁴F. H. Stillinger, *Science* **267**, 5206 (1995).
- ³⁵C. P. Royall and S. R. Williams, *Phys. Rep.* **560**, 1 (2015).
- ³⁶C. Hyeon and D. Thirumalai, *Proc. Natl. Acad. Sci. USA* **100**, 10249 (2003).
- ³⁷I. Goychuk and V. O. Kharченко, *Phys. Rev. Lett.* **113**, 100601 (2014).
- ³⁸P. G. Wolynes, *Acc. Chem. Res.* **25**, 513 (1992).
- ³⁹A. Ashkin, J. M. Dziedzic, J. E. Bjorkholm, and S. Chu, *Opt. Lett.* **11**, 288 (1986).
- ⁴⁰A. Ashkin, *Biophys. J.* **61**, 569 (1992).
- ⁴¹B. J. Ackerson and A. H. Chowdhury, *Faraday Discuss.* **83**, 309 (1987).
- ⁴²C. Bechinger, M. Brunner, and P. Leiderer, *Phys. Rev. Lett.* **86**, 930 (2001).
- ⁴³M. C. Jenkins and S. U. Egelhaaf, *J. Phys.: Condens. Matter* **20**, 404220 (2008).
- ⁴⁴C. Dalle-Ferrier, M. Krüger, R. D. L. Hanes, S. Walta, M. C. Jenkins, and S. U. Egelhaaf, *Soft Matter* **7**, 2064 (2011).
- ⁴⁵M. P. N. Juniper, R. Besseling, D. G. A. L. Aarts, and R. P. A. Dullens, *Opt. Expr.* **20**, 28707 (2012).
- ⁴⁶K. M. Douglass, S. Sukhov, and A. Dogariu, *Nat. Photon.* **6**, 834 (2012).
- ⁴⁷R. D. L. Hanes, C. Dalle-Ferrier, M. Schmiedeberg, M. C. Jenkins, and S. U. Egelhaaf, *Soft Matter* **8**, 2714 (2012).
- ⁴⁸R. D. L. Hanes and S. U. Egelhaaf, *J. Phys.: Condens. Matter* **24**, 464116 (2012).
- ⁴⁹F. Evers, R. D. L. Hanes, C. Zunke, R. F. Capellmann, J. Beverunge, C. Dalle-Ferrier, M. C. Jenkins, I. Ladadwa, A. Heuer, R. Castañeda Priego, and S. U. Egelhaaf, *Eur. Phys. J. Special Topics* **222**, 2995 (2013).
- ⁵⁰G. Volpe, L. Kurz, A. Callegari, G. Volpe, and S. Gigan, *Opt. Express* **22**, 18159 (2014).
- ⁵¹J. Beverunge and S. U. Egelhaaf, *Phys. Rev. A* **93**, 013806 (2016).

3.2 Paper II: Colloids Exposed to Random Potential Energy Landscapes: from Particle Number Density to Particle-Potential and Particle-Particle Interactions

10

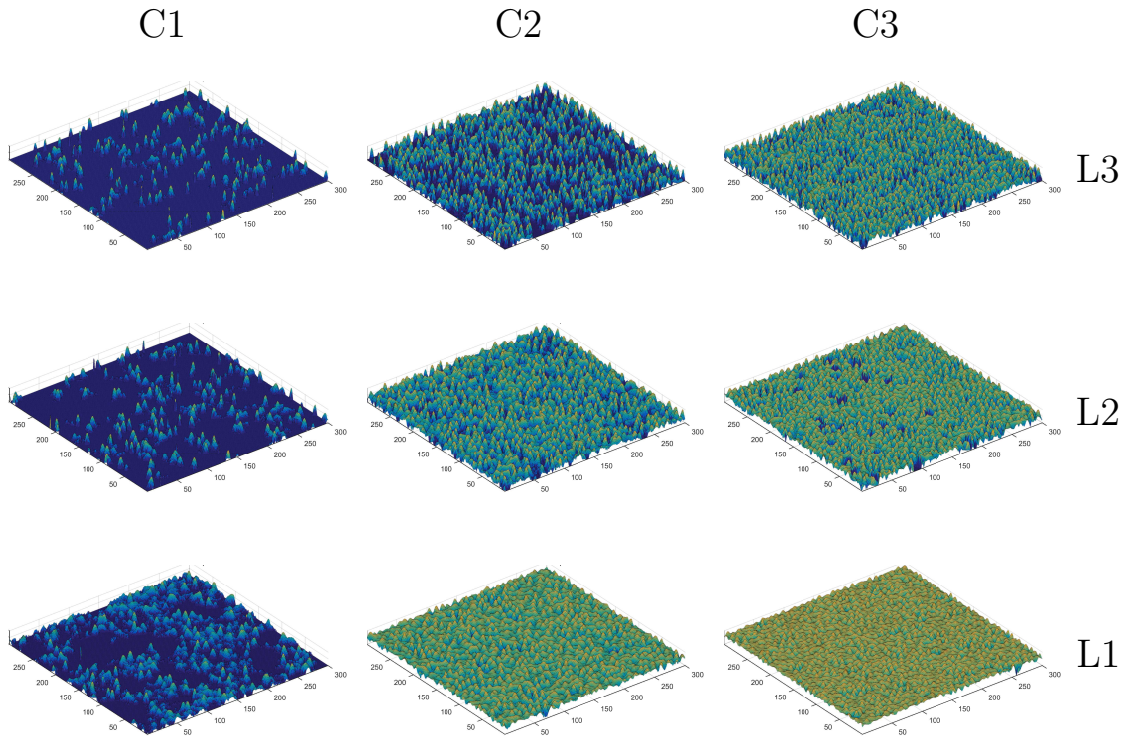


FIG. 11. Time-averaged local particle density $\langle \rho(\mathbf{r}, t) \rangle_t$ for increasing laser power (L1-L3) and mean particle density (C1-C3, as indicated). Colour scale indicates low to high densities by blue to red colours, where different scales are used for the different conditions.

- ⁵²A. Sengupta, S. Sengupta, and G. I. Menon, *Europhys. Lett.* **70**, 635 (2005).
- ⁵³J.-P. Hansen and I. R. McDonald, *Theory of Simple Liquids*, 3rd ed. (Academic, London, 2006).
- ⁵⁴G. I. Menon and C. Dasgupta, *Phys. Rev. Lett.* **73**, 1023 (1994).
- ⁵⁵S. F. Edwards and P. W. Anderson, *J. Phys. F* **5**, 965 (1975).
- ⁵⁶H.-J. Sommers, *J. Physique Lett.* **43**, 719 (1982).
- ⁵⁷G. Parisi, "An introduction to the statistical mechanics of amorphous systems," in *Field Theory, Disorder and Simulations* (World Scientific, 2012) Chap. 12, pp. 195–244.
- ⁵⁸C. Dasgupta and O. T. Valls, *Phys. Rev. B* **74**, 184513 (2006).
- ⁵⁹R. Seshadri and R. M. Westervelt, *Phys. Rev. Lett.* **70**, 234 (1993).
- ⁶⁰R. Seshadri and R. Westervelt, *Physica D* **66**, 223 (1993).
- ⁶¹R. Seshadri and R. M. Westervelt, *Phys. Rev. B* **47**, 8620 (1993).
- ⁶²H.-J. Wu, W. N. Everett, S. G. Anekal, and M. A. Bevan, *Langmuir* **22**, 6826 (2006).
- ⁶³C. Dasgupta and D. Feinberg, *Phys. Rev. B* **57**, 11730 (1998).
- ⁶⁴T. R. M. Sales, *Opt. Eng.* **42**, 3084 (2003).
- ⁶⁵F. M. Dickey, ed., *Laser Beam Shaping: Theory and Techniques, Second Edition* (CRC Press Inc., 2014).
- ⁶⁶M. M. Burns, J.-M. Fournier, and J. A. Golovchenko, *Phys. Rev. Lett.* **63**, 1233 (1989).
- ⁶⁷R. W. Bowman and M. J. Padgett, *Rep. Prog. Phys.* **76**, 28 (2013).
- ⁶⁸G. Brügger, L. S. Froufe-Pérez, F. Scheffold, and J. J. Sáenz, *Nat. Comm.* **6**, 7460 (2015).
- ⁶⁹M. C. Jenkins and S. U. Egelhaaf, *Adv. Colloid Interface Sci.* **136**, 65 (2008).
- ⁷⁰J. C. Crocker and D. G. Grier, *J. Colloid Interface Sci.* **179**, 298 (1996).
- ⁷¹J. Bewerunge, I. Ladadwa, F. Platten, C. Zunke, A. Heuer, and S. U. Egelhaaf, "Time- and ensemble-averages in evolving systems: the case of brownian particles in random potentials," (2016), submitted to *Phys. Chem. Chem. Phys.*
- ⁷²D. G. Grier, *Nature* **424**, 810 (2003).
- ⁷³K. Dholakia, P. Reece, and M. Gu, *Chem. Soc. Rev.* **37**, 42 (2008).
- ⁷⁴F. Evers, C. Zunke, R. D. L. Hanes, J. Bewerunge, I. Ladadwa, A. Heuer, and S. U. Egelhaaf, *Phys. Rev. E* **88**, 022125 (2013).
- ⁷⁵J. W. Goodman, *Speckle Phenomena in Optics: Theory and Applications* (Roberts & Co., Englewood, Colorado, 2007).
- ⁷⁶E. G. Steward, *Fourier optics: an introduction* (Courier Corporation, 2004).
- ⁷⁷D. L. Stein and C. M. Newman, *Spin Glasses and Complexity* (Princeton University Press, 2013).
- ⁷⁸E. Helfand, H. L. Frisch, and J. L. Lebowitz, *J. Chem. Phys.* **34**, 1037 (1961).
- ⁷⁹D. Henderson, *Mol. Phys.* **30**, 971 (1975).
- ⁸⁰X. Guo and U. Riebel, *J. Chem. Phys.* **125**, 144504 (2006).
- ⁸¹M. J. Gillan, *Mol. Phys.* **38**, 1781 (1979).
- ⁸²F. J. Rogers and D. A. Young, *Phys. Rev. A* **30**, 999 (1984).

APPENDIX

1. Particle Arrangements

Fig. 12 shows micrographs of colloidal particles for three different mean particle densities ρ_0 (C1-C3) and increasing laser power P , i.e. disorder strength, (L1-L3). Neither for low nor for high mean particle density and/or laser power an effect of the potential is immediately visible in the images.

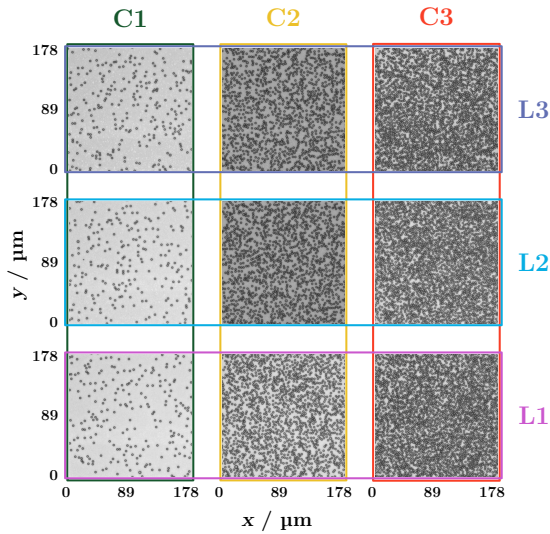


FIG. 12. Micrographs of parts of the samples ($178 \times 178 \mu\text{m}^2$) for increasing laser power (L1-L3) and mean particle density (C1-C3, as indicated).

2. Time-Averaged Local Particle Density

The time-averaged local particle density $\langle \rho(\mathbf{r}, t) \rangle_t$ for three different laser powers P , i.e. disorder strengths, (L1-L3) and mean particle densities ρ_0 (C1-C3) is shown in Fig. 11. For dilute samples trapping of particles in deep potential minima during the entire measurement time leads to a discretisation of the density landscape. This becomes stronger with increasing laser power. At higher mean particle densities, $\langle \rho(\mathbf{r}, t) \rangle_t$ is affected by both particle-potential and particle-particle interactions, resulting in a smoothed density landscape. This becomes more apparent with a decrease in the laser power.

3. Correlation Functions

The azimuthally-averaged pair density correlation function $g^{(1)}(r)$ and off-diagonal density correlation func-

tion $g^{(2)}(r)$ at all measured combinations of mean particle density ρ_0 and laser power P (L0-L3) are shown in Fig. 13. For very large distances r the time-averaged local particle density is uncorrelated, and thus $g^{(1)}(r \rightarrow \infty) = 1$ and $g^{(2)}(r \rightarrow \infty) = 1$ independent of the mean particle density ρ_0 and the laser power P , i.e. disorder strength. By contrast, correlations at finite distances r between high local density values reflect pinning sites, i.e. particle cages or potential minima, and can be identified by deviations from this value. In the absence of a rPEL (L0), $g^{(1)}(r)$ shows a strong dependence on the mean particle density whereas $g^{(2)}(r) \approx 1$ for all mean particle densities, except for very few low mean particle densities ρ_0 which is attributed to insufficient statistics. However, in the presence of a rPEL (L1-L3) and for medium to high mean particle densities ρ_0 , for both correlation functions maxima are observed around integer multiples of D , which increase with mean particle density ρ_0 and laser power P and indicate the interplay of particle-particle and particle-potential interactions.

3.2 Paper II: Colloids Exposed to Random Potential Energy Landscapes: from Particle Number Density to Particle-Potential and Particle-Particle Interactions

12

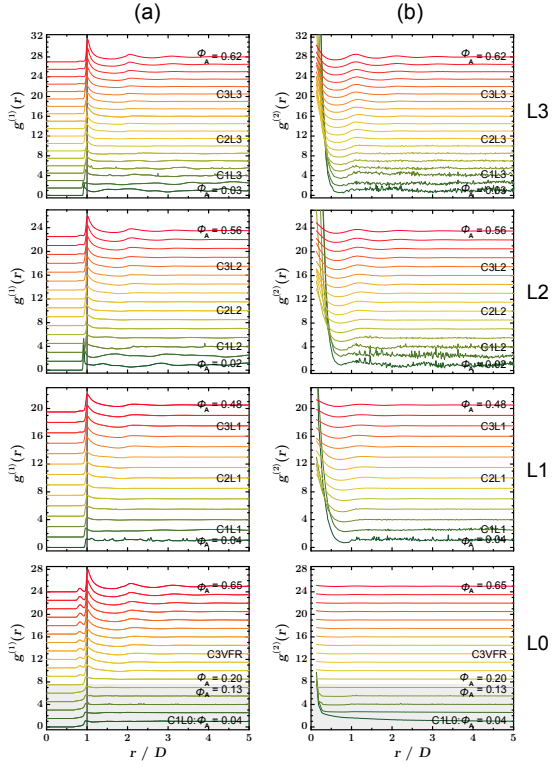


FIG. 13. (a) Azimuthally-averaged pair density correlation function $g^{(1)}(r)$ and (b) off-diagonal density correlation function $g^{(2)}(r)$ for increasing laser power (L0-L3) and mean surface fraction ϕ_A or particle density (C1-C3, as indicated by colour gradient from green to red). Data are shifted vertically for clarity.

3.3 Paper III: Particle dynamics in two-dimensional random-energy landscapes: Experiments and simulations

Journal: Physical Review E

Reference: *Phys. Rev. E*, **88**, 022125 (2013)

Impact factor: 2.288

Authors: Florian Evers, Christoph Zunke, Richard D. L. Hanes, **Jörg Bewerunge**, Imad Ladadwa, Andreas Heuer, and Stefan U. Egelhaaf

4th author

10% contribution of JB

3.3 Paper III: Particle dynamics in two-dimensional random-energy landscapes: Experiments and simulations

This page has been left intentionally blank.

Particle dynamics in two-dimensional random energy landscapes – experiments and simulations

Florian Evers,^{1,*} Christoph Zunke,¹ Richard D. L. Hanes,¹ Jörg
Bewerunge,¹ Imad Ladadwa,^{2,3} Andreas Heuer,² and Stefan U. Egelhaaf¹

¹*Condensed Matter Physics Laboratory, Heinrich-Heine-University,
Universitätsstraße 1, 40225 Düsseldorf, Germany*

²*Institut für Physikalische Chemie, Universität Münster, 48149 Münster, Germany*

³*Fahad Bin Sultan University, 71454 Tabuk, Saudi-Arabia*

(Dated: July 8, 2016)

The dynamics of individual colloidal particles in random potential energy landscapes were investigated experimentally and by Monte Carlo simulations. The value of the potential at each point in the two-dimensional energy landscape follows a Gaussian distribution. The width of the distribution, and hence the degree of roughness of the energy landscape, was varied and its effect on the particle dynamics studied. This situation represents an example of Brownian dynamics in the presence of disorder. In the experiments, the energy landscapes were generated optically using a holographic set-up with a spatial light modulator, and the particle trajectories were followed by video microscopy. The dynamics are characterized using, e.g., the time-dependent diffusion coefficient, the mean squared displacement, the van Hove function and the non-Gaussian parameter. In both, experiments and simulations, the dynamics are initially diffusive, show an extended subdiffusive regime at intermediate times before diffusive motion is recovered at very long times. The dependence of the long-time diffusion coefficient on the width of the Gaussian distribution agrees with theoretical predictions. Compared to the dynamics in a one-dimensional potential energy landscape, the localization at intermediate times is weaker and the diffusive regime at long times reached earlier, which is due to the possibility to avoid local maxima in two-dimensional energy landscapes.

PACS numbers: 05.40.Fb (Random walks and Levy flights), 82.70.Dd (Colloids)

I. INTRODUCTION

The Brownian motion of colloidal particles is one of the classical phenomena in statistical physics [1–4]. In real situations, the particles often do not move freely, but their dynamics are modified by an external potential [5–7]. Especially a random potential, and thus Brownian motion in the presence of disorder, leads to interesting transport phenomena [8, 9]. Up to now, the dynamics in random potentials have been studied mainly by theory and computer simulations [10–19]. Theoretical models include the random barrier model [13], the random trap model [14], the random walk with barriers [15] and the continuous time random walk [16] as well as studies of diffusion in a rough potential [20] and in materials with defects like zeolites [21]. In particular, the long-time limit has been investigated for different realizations of random potentials [8, 9]. In contrast, less is known on the intermediate regime and the time needed to reach the long-time limit. To our knowledge, only very few systematic experimental tests of theoretical and simulation predictions have been performed [22–24]. Nevertheless, the theoretical predictions have been applied successfully to experimental data and the concept of particles diffusing through an energy landscape has proven to be very useful in understanding very different

phenomena. This includes particle diffusion in inhomogeneous media (e.g. single molecule dynamics in porous gels [25] or in cells [26–28]), the dynamics on rough surfaces [29, 30], the dynamics of particles moving along the walls between magnetic domains [22, 31], the dynamics of independent charge carriers in a conductor with impurities (in the parameter range where conduction can be modeled as a classical process) [32, 33]. In particular, random potentials with a Gaussian distribution of energy levels have been suggested for different systems [9, 22, 34]. Furthermore, some processes can be represented by a trajectory in the systems’ configuration space, for example vitrification leading to glassy systems [35–41] or protein folding [42–47]. Often diffusion in a random potential energy landscape represents a crude approximation only, but it can nevertheless provide a useful first description of the effect of disorder on the dynamics [8, 48]. Disorder may modify the value of the diffusion coefficient or it may alter Brownian motion leading to anomalous diffusion. Which effect dominates depends not only on the specific process, but also on the time scale of interest.

An external potential can be imposed on a polarizable colloidal particle by exposing it to a light field [49–52]. Light exerts different forces on particles, if their refractive index differs from (typically exceeds) that of the solvent: a scattering force or ‘radiation pressure’, which pushes particles along the laser beam, and a gradient force, which attracts particles toward regions of high light intensity [50–52]. A classical application of this effect are optical tweezers which are used to trap

* florian.evers@hhu.de

3.3 Paper III: Particle dynamics in two-dimensional random-energy landscapes: Experiments and simulations

2

individual particles by a tightly focused laser beam [50–55]. Furthermore, above a certain light intensity, a periodic light field can induce a disorder-order transition in a two-dimensional charged colloidal system, known as light-induced freezing. If the intensity is increased further, the induced crystal melts into a modulated liquid; this process is called light-induced melting [56–58]. In addition to the particle arrangement, the particle dynamics can be affected by periodic [59] and random [23] light fields, resulting in anomalous diffusion. Light fields hence provide a means to manipulate the spatial arrangement and dynamics of colloidal particles.

Recently, we experimentally realized one-dimensional random energy landscapes [23, 53] and periodic potentials [49, 59] using laser light fields and studied the dynamics of individual particles in these potentials. Here, this is extended to the dynamics of individual colloidal particles in two-dimensional random potentials. In our experiments and simulations, the values of the two-dimensional random potential were drawn from a Gaussian distribution, whose width ε represents the degree of roughness of the potential and, in the experiments, was controlled by the laser power P . The static properties of the potential were determined quantitatively. Furthermore, the trajectories of individual particles in this potential were followed using video microscopy [60–62] and compared to our simulation results. The dynamics were characterized by, e.g., the time-dependent diffusion coefficient, the mean squared displacement (MSD), the non-Gaussian parameter, and the van Hove function. The dynamics are initially diffusive but then, at intermediate times, show an extended subdiffusive regime before diffusive behaviour is reestablished at very long times. Our findings are compared to the particle dynamics in one-dimensional random potentials [23, 24] and periodic potentials [59]. In two-dimensional potential energy landscapes, particles can bypass large barriers. Therefore, the particle dynamics are controlled by minima and saddle points instead of minima and maxima. Moreover, compared to periodic potentials, the barriers have different heights, which significantly affects the particle dynamics.

II. MATERIALS AND METHODS

A. Sample preparation

Each sample consisted of surfactant-free sulfonated polystyrene particles with a radius $R = 1.4 \mu\text{m}$ and polydispersity 3.2 % (Interfacial Dynamics Microspheres & Nanospheres) suspended in heavy water (D_2O), so that the particles cream rather than sediment. Stock solutions of the particles were diluted to result in an area fraction of the creamed sample, $\sigma < 0.10$, which represents a compromise between negligible particle-particle interactions and reasonable statistics. Area fractions were estimated from micrographs according to $\sigma = \pi R^2 N/A$ with N and A being the number of particles and the area covered by

the light field, respectively.

The heavy water (D_2O) was de-ionised by stirring with ion exchange resin to increase the particle-glass repulsion and thus reduce the fraction of particles sticking to the glass surface. To further reduce sticking, all glassware was sonicated in 2% Helmanex II solution at about 60°C and then rinsed with Millipore water and dried in air prior to use. Each sample cell was constructed from a microscope slide and three cover slips, two used as spacers (number 0 with thickness $0.085 - 0.13 \text{ mm}$, supplied by VWR) with a gap between them and the third on top to create a narrow capillary (number 1 with thickness $0.13 - 0.16 \text{ mm}$, supplied by VWR) [63]. Thin cover glasses were used as spacers to allow imaging of the creamed particles using a high resolution objective with a working distance of 0.13 mm . The sample chamber was filled using capillary action and subsequently sealed with UV glue.

B. Light field generation

The set-up contains a laser with a wavelength of 532 nm (Ventus 532-1500, Laser Quantum). Its beam is expanded and then reflected from a spatial light modulator (Holoeye 2500-LCR). Subsequently, it is directed through two telescopes to reduce its diameter and reflected off three mirrors to steer it through an inverted microscope (Nikon Eclipse 2000-U) into the sample [23, 53, 64]. One of the mirrors is a dichroic mirror to introduce the beam into the microscope beam path and to use the microscope objective ($60\times$ oil immersion, numerical aperture NA 1.4, Nikon) to image the light field into the sample plane. The beam passes upwards through the sample and hence, due to radiation pressure, pushes the particles against the top of the cell, which reinforces the creaming of the particles. A notch filter in the imaging path prevents laser light from reaching the ocular or camera. To aid alignment, the notch filter can be removed and the sample replaced by a mirror, so that the light intensity distribution in the sample plane can be imaged using the microscope.

A kinoform (phase hologram) was calculated using the Gerchberg-Saxton iterative algorithm [65] (Fig. 1A) and displayed in the centre of the spatial light modulator. The kinoform corresponds to a homogeneous disc surrounded by a ring to prevent particle movements into and out of the disc. The Fourier transform of the kinoform is, as expected, a homogeneous disc surrounded by a ring (Fig. 1B). In order to account for the angle at which the laser impinges on the spatial light modulator (22.5°), the disc and ring are a factor $1/\cos(22.5^\circ) = 1.08$ taller than they are wide [23, 53]. The observed light field intensity $I(x, y)$ (Fig. 1C) corresponds to the disc of the Fourier transformed kinoform. Indeed, the illumination is overall flat but, crucially, has some fluctuations due to the finite size and pixelation of the light modulator [23]. These fluctuations are exploited in the following. Furthermore,

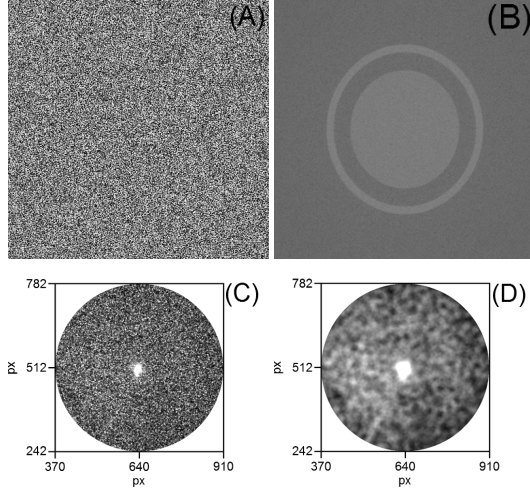


FIG. 1. (A) Kinoform calculated by applying the Gerchberg-Saxton algorithm to a homogeneous disc surrounded by a ring and (B) its Fourier transform. (C) Micrograph of the observed intensity $I(x, y)$ of the disc taken at very low laser power $P \leq 0.2$ mW. (D) Potential $U(x, y)$ as experienced by a point-like test particle obtained by convoluting $I(x, y)$ with the volume of a spherical particle with radius $R = 1.4 \mu\text{m} \hat{=} 12.7$ px.

there is a bright 0th-order peak in the centre. Using this peak, a particle was trapped and used to monitor any drift of the set-up [23]. Global drifts were found to be negligible during individual measurements (up to 4 h).

C. Video microscopy and particle tracking

The samples were observed using the inverted microscope. Micrographs were recorded using a CMOS camera (PL-B742F, Pixelink). Particle coordinates were extracted from the time series of micrographs and the trajectories determined using IDL routines [60]. To allow for an unambiguous reconstruction of the trajectories, the distance particles move between two images was required to be much smaller than the average interparticle distance and thus limited to $1.2R$. Furthermore, care was taken that particles do not approach each other or the boundary closely such that particle–particle and particle–boundary interactions can be neglected. Typical measurement times were 2 to 3 h. Particles which were stuck to the glass were identified by comparing the particles’ short-time friction coefficient ξ_i , i.e. the inverse mobility, determined from the mean squared displacement, to the expected bulk value $\xi_0 = 6\pi\eta R$ with the solvent viscosity $\eta = 1.19 \times 10^{-3}$ Pas at room temperature. Particles with $\xi_i > 20\xi_0$ were declared stuck and removed from the analysis. Typically, one particle was stuck to the glass in the field of view, which contained about 20 particles.

For identical conditions, measurements at different positions in the sample yielded very similar results, despite slightly different particle area fractions σ . This reproducibility allowed us to average several independent measurements of equal recording time T_{exp} to improve statistics.

D. Monte Carlo simulations

The Monte Carlo simulations were performed on a 4096×4096 square lattice with the lattice points separated by a distance Δs in both directions, where we have set $\Delta s = 1$. The potential values at the lattice points, $\tilde{U}(x, y)$, were produced using a Box-Muller algorithm generating numbers which are Gaussian distributed with zero mean and standard deviation $\tilde{\epsilon}$. The potential $\tilde{U}(x, y)$ was convoluted with the particle volume to obtain the potential $U(x, y)$ felt by a point-like test particle

$$U(x, y) = \frac{\sum_k \sum_l \tilde{U}(x - k\Delta s, y - l\Delta s) a(k, l)}{\sqrt{\sum_k \sum_l a^2(k, l)}} \quad (1)$$

where the double sum runs over the projected particle, i.e. $k^2 + l^2 \leq m^2$ with $k\Delta s$ and $l\Delta s$ the distances from the particle centre in the two directions and $R = m\Delta s$ the radius of the particle. The volume of the particle is represented by

$$a(k, l) = 2\sqrt{(m^2 - k^2 - l^2)}. \quad (2)$$

As a compromise between negligible discretization effects and viable computation time, we have chosen $m = 32$ and thus $-32 \leq k, l \leq 32$.

The convolution leads to a potential $U(x, y)$ (Fig. 2), which is smoother than $\tilde{U}(x, y)$. Its values follow the same Gaussian distribution, albeit with a spatial correlation decaying on the length scale of the particle size. It is supposed to resemble the potential energy landscape experienced by a colloidal particle in the light field (Sec. III A).

Once the potential energy landscape $U(x, y)$ was fixed, a particle was positioned on a randomly chosen lattice point. During the simulation, a direction is chosen randomly and, depending on the energy difference ΔU to the neighbouring lattice point, the particle is moved in any case if $\Delta U \leq 0$, or moved with a finite probability $\exp(-\Delta U/k_B T)$ if $\Delta U > 0$ (where $k_B T$ is the thermal energy). By averaging over 1024 different initial positions of the particle, representative averages can be determined. For each Monte Carlo run, the short-time diffusion coefficient D_0 and the related Brownian time $t_B = R^2/4D_0$ were calculated by a linear fit to the MSD at short times. In analogy to the experiment, data were acquired up to $T_{\text{sim}} = 1000 t_B$. This yielded particle trajectories as in the experiments. Thus, the different parameters, such as

3.3 Paper III: Particle dynamics in two-dimensional random-energy landscapes: Experiments and simulations

4

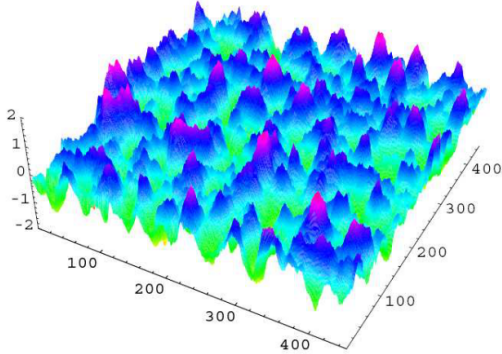


FIG. 2. (Color online) Some region of the spatially correlated Gaussian potential energy landscape $U(x, y)/k_B T$ obtained by convolution of a spatially uncorrelated Gaussian energy landscape with the particle volume. It thus reflects the potential felt by a particle (Fig. 1D) and is used in the Monte Carlo simulations.

the mean squared displacement, were determined as in the experiments, including averaging over waiting times (see below). It turned out that within statistical uncertainty the results for different realizations of the potential energy landscape $U(x, y)$ are identical. As in the experiments, separate simulations were performed for different values of the degree of roughness $0 < \varepsilon \leq 3 k_B T$ to investigate its effect on the dynamics.

III. RESULTS AND DISCUSSION

We studied the behaviour of individual colloidal particles in two-dimensional random potential energy landscapes. At first, the properties of the experimentally created energy landscapes are presented. Then, the particle dynamics in these energy landscapes are discussed and compared to the results of our Monte Carlo simulations and theoretical predictions. Finally, our experimental and simulation results are contrasted with the dynamics in one-dimensional random and periodic potentials.

A. Properties of the optically generated random potential

A realization of the light field at very low laser power is displayed in Fig. 1C. The light field interacts with polarizable particles [50–52]. The polarizable particle volume is taken into account by convolving the local light intensity $I(x, y)$ with the particle volume. The effect of the light field on the particle is then represented by an external potential $U(x, y)$ as felt by a point-like test particle (Fig. 1D).

To determine the characteristic length scales of the

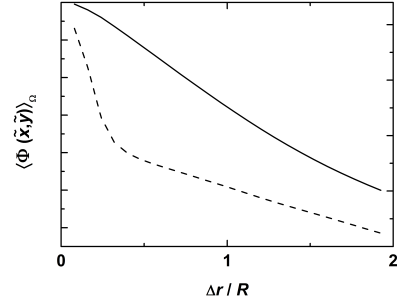


FIG. 3. Azimuthally averaged spatial correlation function $\langle \Phi(\vec{x}, \vec{y}) \rangle_\Omega$ of the laser intensity $I(x, y)$ (dashed line) and of the potential energy landscape felt by a point-like test particle $U(x, y)$ (solid line) vs. the distance Δr as determined from Fig. 1C and D, respectively.

light field intensity $I(x, y)$ and of the potential felt by a point-like test particle $U(x, y)$, the spatial correlation functions were determined and their azimuthal average $\langle \Phi(\vec{x}, \vec{y}) \rangle_\Omega$ calculated. The spatial correlation of the light field intensity $I(x, y)$ decays on a short length scale compared to the particle size. However, the convolution with the particle volume introduces a length scale, namely the particle diameter $2R$. The spatial correlation of the potential $U(x, y)$, which was similarly determined, indeed decays on a characteristic length of $2R$ (Fig. 3).

Based on the observed light intensity $I(x, y)$ and potential energy landscape $U(x, y)$ (Fig. 1C,D), the distributions of the light intensity values $p(I)$ and potential values $p(U)$ were determined (Fig. 4). The distribution $p(I)$ follows the probability density function of a Gamma distribution [66]

$$f_\Gamma(I) = \frac{b^k}{\Gamma(k)} I^{k-1} e^{-bI}, \quad (3)$$

where $I \geq 0$, $\Gamma(k)$ is the Gamma function and b the scale parameter. A fit to the experimental $p(I)$ yielded a shape parameter $k = 3.1 \pm 0.1$ (Fig. 4A), corresponding to a 3D speckle pattern [66, 67]. The distribution $p(U)$ can be described by a Gaussian distribution

$$f_G(U) = \frac{1}{\sqrt{2\pi\varepsilon^2}} e^{-\frac{(U-\langle U \rangle)^2}{2\varepsilon^2}} \quad (4)$$

with the average $\langle U \rangle$ and width or standard deviation ε (Fig. 4B). Due to the convolution with the particle volume, $U(x, y)$ represents a weighted average of several independent (random) values of $I(x, y)$ and thus $p(U)$ has a significantly reduced width compared to $p(I)$. The width ε characterizes the degree of roughness of the random potential $U(x, y)$, which is controlled by the laser power P , but cannot easily be determined experimentally. Thus, to establish a quantitative relation between the roughness

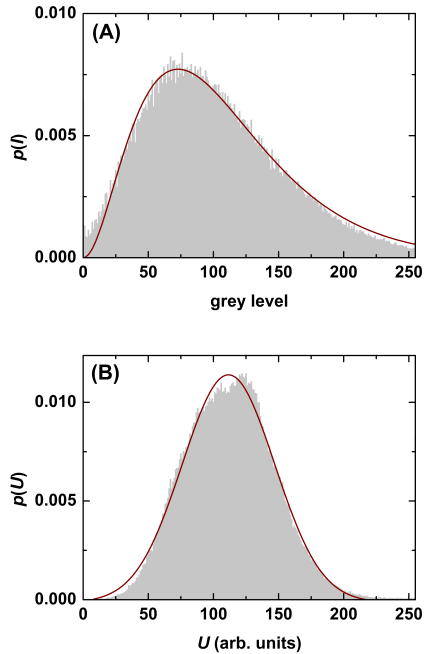


FIG. 4. (Color online) Distribution of (A) values of the intensity of the light field, $p(I)$, and (B) values of the potential as felt by a point-like test particle, $p(U)$, based on the observed intensity $I(x, y)$ and potential $U(x, y)$ shown in Fig. 1C and D, respectively. Dark lines are fits based on a Gamma and Gaussian distribution, respectively.

ε , used in the simulations, and the laser power P , applied in experiments, the experimental potential energy landscape was calibrated. This was achieved by a direct comparison of the experimental and simulation results, namely of the time-dependent diffusion coefficient $D(t)$ at very short and long times (Sec. III C). The calibration resulted in an approximately linear relation between ε and P , which might saturate for large P (Fig. 5).

B. Dynamics in the random potential – experiments

The effect of two-dimensional random energy landscapes on the particle dynamics is qualitatively illustrated in Fig. 6. Outside the light field (white background), particles undergo free diffusion, exploring a large area. This region is separated by a large barrier (white/green rings) from the two-dimensional random light field (green disc). Within the random potential, the excursions of the particles are limited and hence the particle dynamics are slowed down. The particles remain longer at some positions, which correspond to local min-

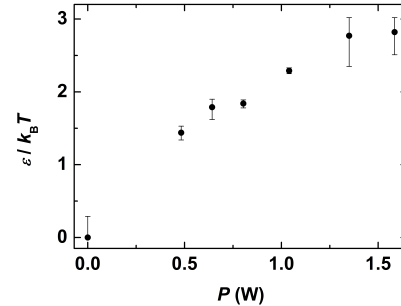


FIG. 5. Standard deviation ε of the distribution of potential energy values, $p(U)$, as a function of laser power P .

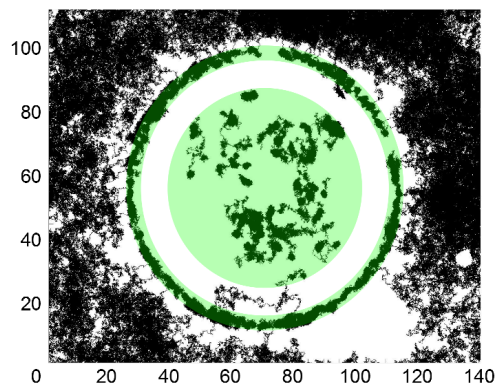


FIG. 6. (Color online) Trajectories of particles undergoing diffusion in a two-dimensional plane, part of which contains a random potential (green background) which is separated by a barrier (white/green rings) from the surroundings (white background). Particle radius $R = 1.4 \mu\text{m}$, particle surface fraction $\sigma = 0.04$, laser power $P = 1.32 \text{ W}$ corresponding to a standard deviation $\varepsilon = 2.8 k_B T$, and a recording time $T_{\text{exp}} = 3.8 \text{ h}$. Coordinates are given in μm .

ima of the potential. For a potential with a larger degree of roughness ε , i.e. a larger width of $p(U)$, this effect is more pronounced with particles being more efficiently trapped and hence exploring a smaller region.

Based on the particle trajectories, different statistical properties were computed to characterize the particle dynamics. We found identical behaviour along the x - and y -directions as expected for an isotropic system. The dynamical properties were hence determined as a function of the distance, $\Delta r = [(\Delta x)^2 + (\Delta y)^2]^{1/2}$, where distances are scaled by the particle radius $R = 1.4 \mu\text{m}$ and times by the Brownian time $t_B = R^2/(4D_0) = (6.4 \pm 0.1) \text{ s}$ with D_0 experimentally determined in the absence of a random potential, i.e. $\varepsilon = 0$, but in the vicinity of the water-glass interface. This renders the data independent

3.3 Paper III: Particle dynamics in two-dimensional random-energy landscapes: Experiments and simulations

6

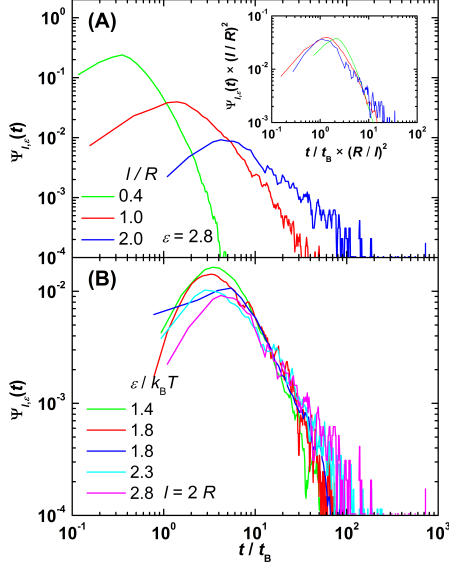


FIG. 7. (Color online) Particle residence time distribution $\Psi_{l,\varepsilon}(t)$ representing the probability that it takes a particle a time t to travel at least a distance l in a random potential with standard deviation ε . All curves are smoothed by a moving five-points average. (A) $\Psi_{l,\varepsilon}(t)$ for different length l/R (as indicated, increasing left to right) and $\varepsilon = 2.8 k_B T$, scaled plot as inset. (B) $\Psi_{l,\varepsilon}(t)$ for $l/R = 2$ and different ε (as indicated, decreasing from top at maxima).

of the specific experimental conditions, except for a radiation pressure effect (Sec. III C). Moreover, the statistical properties were obtained by averaging over different particles, which are well separated and thus non-interacting, and over waiting times t_0 to improve statistics. Since, initially, the occupancy of energy levels was homogeneous but tended toward a Boltzmann distribution in the course of the experiment, the average over waiting times depends on the total measurement time T_{exp} , which was $T_{\text{exp}} \approx 1000 t_B$.

Depending on the particle positions, the particles experience various potential values $U(x, y)$ and are trapped for different times, reflecting the different heights of the saddle points to the neighbouring minima. The time t required to explore at least a distance l in a potential with roughness ε has been determined and the particle residence time distribution $\Psi_{l,\varepsilon}(t)$ calculated. To explore a distance l by free diffusion with diffusion coefficient D_0 , on average the time $t = l^2/(4D_0)$ is required. To explore larger distances l and/or in the presence of a random potential, on average larger times are required. For short distances $l < 2R$, i.e. within a minimum, $\Psi_{l,\varepsilon}(t)$ does not significantly depend on ε but depends on the distance l (Fig. 7A). The l dependence is mainly governed

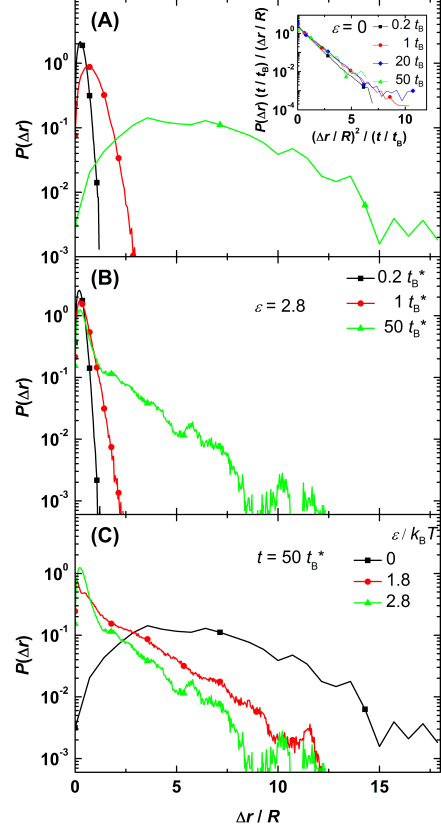


FIG. 8. (Color online) Distribution of particle displacements Δr within time t , $P(\Delta r, t)$ (A) in the absence of a potential ($\varepsilon = 0$), i.e. for free diffusion, with the scaled $P(\Delta r, t)$ as an inset, (B) in the presence of a random potential with roughness $\varepsilon = 2.8 k_B T$ for different times t (as indicated, increasing left to right) and (C) with different roughnesses ε (as indicated, increasing right to left) for time $t = 50 t_B$.

by the longer time required to diffuse a larger distance l as shown by a rescaling assuming diffusive motion (Fig. 7A, inset). In contrast, to travel a distance of at least $2R$, which corresponds to the typical minimum-minimum separation (Fig. 3), in general requires to cross a barrier or saddle point, whose average height depends on ε . Accordingly, $\Psi_{l,\varepsilon}(t)$ depends on the roughness ε (Fig. 7B) and the mean residence time exceeds the average time $t = 4t_B$ required to diffuse $2R$ in the absence of a potential.

The probability distribution of particle displacements Δr , i.e. the self part of the van Hove function, $P(\Delta r, t)$, at different delay times t is calculated based on the trajec-

tories by averaging over all waiting times t_0 and particles i :

$$P(\Delta r, t) = \langle \delta(\Delta r - [r_i(t_0+t) - r_i(t_0)]) \rangle_{t_0, i}, \quad (5)$$

where $r_i(t)$ is the position of particle i at time t and the average is taken over particles i and waiting times t_0 to improve statistics. In the case of free two-dimensional diffusion, i.e. without any external potential, $P(\Delta r, t)$ follows a Rayleigh distribution, $P(\Delta r, t) \sim \Delta r / (2D_0 t) \exp(-\Delta r^2 / 4D_0 t)$, whose width increases linearly with time t (Fig. 8A). In the presence of a random potential, $P(\Delta r, t)$ changes qualitatively (Fig. 8B). The potential tends to trap the particle so that it explores less space and the distributions $P(\Delta r, t)$ get much narrower. This is more pronounced for longer times, when the dynamics include barrier crossing. Accordingly, at long delay times, the roughness of the potential significantly affects $P(\Delta r, t)$, which becomes narrower with increasing ε (Fig. 8C).

The width of the distribution of particle displacements, $P(\Delta r, t)$, can be characterized by the mean squared displacement (MSD)

$$\langle \Delta r^2(t) \rangle = \langle \Delta x^2(t) \rangle + \langle \Delta y^2(t) \rangle, \quad (6)$$

which is calculated from the particle trajectories according to

$$\begin{aligned} \langle \Delta x^2(t) \rangle &= \left\langle [x_i(t_0+t) - x_i(t_0)]^2 \right\rangle_{t_0, i} \\ &\quad - \langle [x_i(t_0+t) - x_i(t_0)] \rangle_{t_0, i}^2 \end{aligned} \quad (7)$$

and $\langle \Delta y^2(t) \rangle$ correspondingly, with the second term correcting for possible drifts. In the absence of a potential ($\varepsilon = 0$), $\langle \Delta r^2(t) \rangle$ increases linearly with time, as expected for free diffusion (Fig. 9A). In the presence of a random potential, the particle dynamics exhibit three distinct regimes. Both, at short times ($t/t_B \lesssim 0.1$) and long times ($t/t_B \gtrsim 30$), the particle dynamics are diffusive. At small t , the diffusive behaviour reflects small excursions within local minima and is thus essentially independent of the roughness ε . Nevertheless, diffusion is reduced compared to free diffusion ($\varepsilon = 0$) because laser pressure pushes the particles closer to the water-glass interface and thus reduces their mobility [68–70], with only a weak dependence on laser power $P > 0$ and hence $\varepsilon > 0$. Furthermore, the averaging over waiting times t_0 (Eqs. 6,7) leads to a reduction of the MSD, especially at short times. This is due to the evolution of the system towards an equilibrium (Boltzmann) distribution which leads to an increasing occupation of deep minima. (Both effects are discussed in more detail in Sec. III C.) For large enough t , hopping between minima becomes important and constitutes a random walk. Thus, diffusive behaviour is reestablished at long times, although with a strongly reduced diffusion coefficient. At intermediate t , the MSDs exhibit an inflection point, which becomes increasingly pronounced as ε increases. This subdiffusive behaviour is caused by the particle being trapped in local

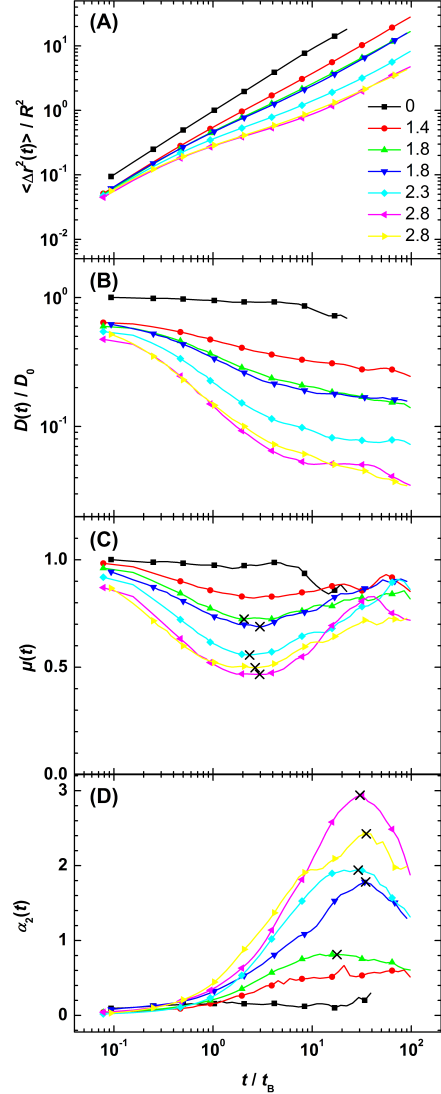


FIG. 9. (Color online) (A) Normalized mean squared displacement $\langle \Delta r^2(t) \rangle / R^2$, (B) normalized diffusion coefficient $D(t)/D_0$, (C) exponent $\mu(t)$ in the relation $\langle \Delta r^2(t) \rangle \sim t^{\mu(t)}$ and (D) non-Gaussian parameter $\alpha_2(t)$ as a function of delay time t normalized by the Brownian time t_B in the presence of a two-dimensional random potential with roughness ε (as indicated, increasing from top (A-C) and bottom (D), respectively). For clarity, only every fifth data point is plotted as a symbol. Black crosses indicate minima and maxima of $\mu(t)$ and $\alpha_2(t)$, respectively.

3.3 Paper III: Particle dynamics in two-dimensional random-energy landscapes: Experiments and simulations

8

minima for prolonged times before it escapes to a neighbouring minima. Since there is a wide range of residence times (Fig. 7), reflecting barriers of different heights, the subdiffusive regime extends over a broad range of times.

From the two-dimensional MSD $\langle \Delta r^2(t) \rangle$, the time-dependent diffusion coefficient $D(t)$ can be calculated according to

$$D(t) = \frac{1}{2d} \frac{\partial}{\partial t} \langle \Delta r^2(t) \rangle, \quad (8)$$

where in the present case the dimension $d = 2$. The three regimes discussed above are also reflected in the normalized time-dependent diffusion coefficient $D(t)/D_0$ (Fig. 9B). Toward very short times, $D(t)/D_0$ tends toward one (actually slightly below one due to the radiation pressure and the averaging mentioned above and discussed in Sec. III C). It strongly decreases at intermediate times to reach a much smaller value D_∞ at long times, where hopping between minima dominates and diffusion is reestablished, reflected in the plateau of $D(t)$ at long times. The asymptotic diffusion coefficient D_∞ was determined experimentally and will be discussed together with the simulation results in Sec. III C.

In order to characterize deviations from diffusive behaviour, in particular the subdiffusion at intermediate times, the exponent μ in the relation $\langle \Delta r^2(t) \rangle \sim t^{\mu(t)}$ is determined from the slope of the MSD in double-logarithmic representation:

$$\mu(t) = \frac{\partial \log \langle \Delta r^2(t) \rangle}{\partial \log(t)}. \quad (9)$$

For free diffusion $\mu = 1$, while $\mu < 1$ in the case of subdiffusion. The subdiffusive dynamics at intermediate times results in a minimum in $\mu(t)$. It becomes more pronounced with increasing ε , but remains at about the same time (Fig. 9C, crosses). In contrast, the diffusive behaviour at short and long times is reflected in the trend of $\mu(t)$ toward one in these two limits.

While the exponent $\mu(t)$ characterizes deviations from diffusive behaviour, the non-Gaussian parameter $\alpha_2(t)$ quantifies, in the case of one dimension, the deviation of the distribution of particle displacements from a Gaussian distribution. It corresponds to the first non-Gaussian correction [40]. In two dimensions, it quantifies deviations from a Rayleigh distribution (Fig. 8). Following a previous definition [71]:

$$\alpha_2(t) = \frac{\langle \Delta r^4(t) \rangle}{(1 + 2/d) \langle \Delta r^2(t) \rangle^2} - 1, \quad (10)$$

where $\langle \Delta r^4(t) \rangle = \langle \Delta x^4(t) \rangle + \langle \Delta y^4(t) \rangle + 2 \langle \Delta x^2(t) \rangle \langle \Delta y^2(t) \rangle$ and $\langle \Delta x^4(t) \rangle$ and $\langle \Delta y^4(t) \rangle$ are defined in analogy to $\langle \Delta x^2(t) \rangle$. The time-dependence of $\alpha_2(t)$ also shows three different dynamic regimes (Fig. 9D). At very short and very long times, when the particle dynamics are diffusive, $\alpha_2(t) \approx 0$, while at intermediate times $\alpha_2(t)$ develops a peak which becomes more pronounced and moves to larger times

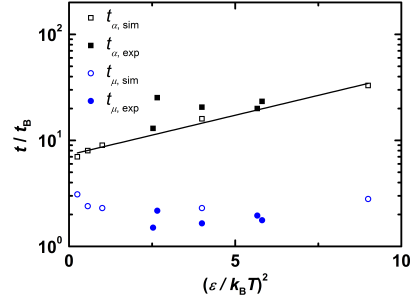


FIG. 10. (Color online) Characteristic times, namely of the minimum in the exponent $\mu(t)$, i.e. t_μ , and the maximum in the non-Gaussian parameter $\alpha_2(t)$, i.e. t_α , as a function of the degree of roughness ε of the potential from experiments (filled symbols, corresponding to the crosses in Fig. 9C,D but taking the radiation pressure effect, as quantified in the inset of Fig. 11, into account) and simulations (open symbols). The solid line is a guide to the eye.

with increasing ε . This reflects the broader distribution of barrier heights and hence residence times $\Psi_{l,\varepsilon}(t)$ at larger ε (Fig. 7).

All parameters indicate an intermediate time regime characterized by subdiffusive dynamics. In particular, a minimum in the exponent $\mu(t)$ at t_μ and, at a later time t_α , a maximum in the non-Gaussian parameter $\alpha_2(t)$ are observed (Fig. 9C,D). While the time t_μ hardly depends on ε , the maximum in $\alpha_2(t)$ shifts to significantly larger times t_α with increasing ε (Fig. 10). The minimum of $\mu(t)$ is reached when diffusion is most efficiently suppressed. This occurs just before a significant fraction of the particles start to escape the minima. This implies relatively shallow minima, which have a similar depth for essentially all ε . Thus the dependence of t_μ on ε is very small. On the other hand, the maximum of $\alpha_2(t)$ occurs when the dynamics is maximally heterogeneous, i.e. some minima have long been left, others only recently and some not yet. This spread increases with ε and hence does the maximum of $\alpha_2(t)$. Accordingly, to reach this maximally heterogeneous state takes longer and thus t_α increases with ε .

C. Dynamics in the random potential – simulations

The simulations also show three regimes: initially diffusion followed by subdiffusive behaviour and finally again diffusion with a considerably reduced diffusion coefficient D_∞ (Fig. 11), consistent with our experimental findings (Fig. 9).

Already at short times, the diffusion coefficient $D(t)$ is noticeably reduced. The reduction, caused by the random potential, is considerably enhanced by the averaging

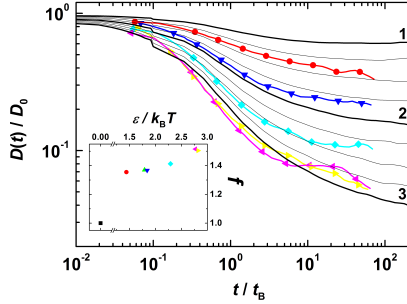


FIG. 11. (Color online) Normalized diffusion coefficient $D(t)/D_0$ as a function of delay time t/t_B for different roughnesses ε from simulations (black solid lines, for $\varepsilon/k_B T = 1, 1.25, 1.5, 1.75, 2, 2.25, 2.5, 2.75, 3$) and experiments (coloured lines with symbols as in Fig. 9 and sequence top to bottom). Here, the experimental data are scaled with an effective diffusion coefficient and effective Brownian time to account for the effect of radiation pressure (see text for details). The dependence of the scaling factor f on radiation pressure, which is proportional to the laser power P and hence the degree of roughness ε (Fig. 5), is shown as inset.

over waiting times t_0 (Eqs. 6,7). As time progresses, the initially homogeneous particle distribution develops into the equilibrium distribution with the energy levels occupied according to the Boltzmann distribution. This implies a growing occupation of deep minima, in which the particles reside for a long time, and hence slower dynamics. With increasing simulation time T_{sim} (or measurement time T_{exp}), and hence an increasing range of waiting times $0 \leq t_0 \leq T_{\text{sim}} - t$ included in the average, the weight of near-equilibrium distributions with a large fraction of less-mobile particles increases. Hence, the averaging over t_0 leads to a smaller mean diffusion coefficient $D(t)$ with the decrease becoming more pronounced as T_{sim} increases and t decreases. The decrease of $D(t)$ is thus particularly noticeable at short times t . Furthermore, the simulation time has to be matched to the measurement time, $T_{\text{sim}} \approx T_{\text{exp}}$, to allow for a meaningful comparison.

At long times, diffusion is reestablished although with a significantly smaller diffusion coefficient $D_\infty(\varepsilon)$, which is estimated by the value at $t = 80 t_B$, i.e. $D_\infty \approx D(80 t_B)$ (Fig. 12). The diffusion coefficient at long times, $D_\infty(\varepsilon)$, has been linked to the free diffusion coefficient D_0 [9, 72–74]:

$$\frac{D_\infty(\varepsilon)}{D_0} = e^{-\frac{1}{2} \left(\frac{\varepsilon}{k_B T} \right)^2} \quad (11)$$

The most dominant feature of this equation is the dependence on $-(\varepsilon/k_B T)^2$ which is just the ratio of the equilibrium energy of a Gaussian distribution $-\varepsilon^2/k_B T$ and $k_B T$. This first term dominates the temperature-dependence of the barrier, because the typical energies

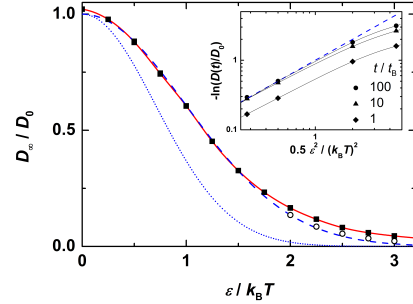


FIG. 12. (Color online) Ratio of the long-time diffusion coefficient $D_\infty \approx D(80 t_B)$ and the diffusion coefficient D_0 in the absence of a potential as a function of the degree of roughness ε as obtained from simulations. Solid symbols: total simulation time similar to the experimental recording time, $T_{\text{sim}} \approx T_{\text{exp}}$, open symbols: one order of magnitude longer simulation time, $T_{\text{sim}} \approx 10 T_{\text{exp}}$, $D_\infty \approx D(1000 t_B)$. The red solid line represents a spline interpolation of the simulation data and the blue dashed and dotted lines the theoretical predictions for a two-dimensional [9] and one-dimensional [20] random potential, respectively. The inset shows the ratio $D(t)/D_0$ at different times $t = t_B, 10 t_B$ and $100 t_B$. The black lines are guides to the eye.

to be crossed for transitions between different regions are essentially temperature-independent, as suggested by a percolation picture (cf. [19]). The simulation findings and theoretical prediction show very good agreement at small ε and deviations at large $\varepsilon \gtrsim 2 k_B T$ (Fig. 12). These deviations are due to the increasingly longer times required to reach the asymptotic long-time value D_∞ which, for $\varepsilon \gtrsim 2 k_B T$, is beyond the simulation time T_{sim} (Fig. 11). This is illustrated by the approach of $D(t, \varepsilon)$ toward $D_\infty(\varepsilon)$ for different ε , which is particularly slow and eventually beyond the simulation time T_{sim} for large ε (Fig. 12, inset). Note that the simulation time was matched to the experimental recording time, $T_{\text{sim}} \approx T_{\text{exp}}$, in order to obtain equivalent averaging. If the simulation time is increased by an order of magnitude, $T_{\text{sim}} \approx 10 T_{\text{exp}}$, a significantly better agreement with the theoretical prediction is observed (Fig. 12).

At intermediate times, the dynamics are dominated by the slow transition from the initial to the long-time diffusion. This transition can be characterized by the times discussed above: t_μ and t_α at which the minimum of $\mu(t)$ and the maximum of $\alpha_2(t)$ occur, respectively. These times have been extracted from the simulation data and quantitatively agree with the experimental results (Fig. 10). Based on the Stokes-Einstein equation, the α -relaxation time is expected to be inversely proportional to the long-time diffusion coefficient D_∞ [75]. Furthermore, the maximum of the non-Gaussian parameter, i.e. t_α , is typically close to the α -relaxation time. Together with Eq. 11, this suggests $\ln t_\alpha \sim (\varepsilon/k_B T)^2$. This

3.3 Paper III: Particle dynamics in two-dimensional random-energy landscapes: Experiments and simulations

10

is indeed observed (Fig. 10). The range of ε is, however, too small to unambiguously confirm this relation.

We now quantitatively compare our experimental and simulation results. This requires to determine the relationship between ε and the experimentally applied laser power P as well as the friction coefficient of the particles, ξ_0^* , which implicitly also depends on the laser power P . Due to hydrodynamic effects, the friction coefficient varies with the particles' distance from the water-glass interface [68–70]. The distance is controlled by a balance between the repulsive particle-wall interaction [76–79] and the radiation pressure (and gravity) [50–52], which pushes the particles toward the glass slide and depends on P [64]. Both, $\varepsilon(P)$ and $\xi_0^*(P)$, are together determined in an iterative procedure which is based on a comparison of the experimental and simulation results and is described in the following.

Although the degree of roughness ε of the optically-generated potential $U(x, y)$ can be tuned via the laser power P and we expect a linear relationship $\varepsilon \sim P$, $\varepsilon(P)$ cannot easily be determined experimentally. Therefore, in a first step, this relation has been estimated using D_∞ , which depends on ε (in the simulations, Figs. 11, 12) and P (in the experiments, Fig. 9). Since the asymptotic limit D_∞ is not accessible, we use $D_\infty/D_0 \approx D(80t_B)/D_0$ for the simulation results and $D_\infty/D_0 \approx D(80t_B)/D(0.2t_B)$ for the experimental results since the short time limit of the diffusion coefficient is not accessible experimentally (and affected by radiation pressure as described below). An interpolation of $D_\infty(\varepsilon)/D_0$ determined in simulations (Fig. 12, red line) was used to assign an ε to the $D_\infty(P)/D(0.2t_B)$ from experiments with different P . This yields a first approximation for $\varepsilon(P)$.

The friction coefficient of the particles implicitly also depends on the laser power P . A finite $P > 0$ will lead to radiation pressure pushing the particles closer to the water-glass interface and hence increases the friction coefficient $\xi_0^* > \xi_0$ and reduces the diffusion coefficient $D_0^* < D_0$. At short times, the diffusion coefficient tends to a value, D_s , which can be used to guide the correction. Although the short-time dynamics are hardly affected by the random potential, the averaging over waiting times t_0 (Eq. 8) affects D_s [24], as mentioned above. Thus, the experimental value $D_s = D(t_s)$, where $t_s \approx 0.2t_B$, was fitted to the corresponding simulation value, which is equally affected by the averaging. The choice of D_s affects t_B and in turn t_s and hence $D(t_s)$. Therefore, the procedure was iterated until consistent relations were obtained.

This procedure yielded a relation $\varepsilon(P)$ (Fig. 5), which appears linear up to large P where ε starts to saturate. The slope is consistent with a previous calibration of a one-dimensional random potential when taking the different illuminated areas into account [23]. Furthermore, the iterative procedure provides the friction coefficient; $\xi_0^* \approx 1.4\xi_0$ for $P > 0$ and $\xi_0^* = \xi_0$ for $P = 0$ and the simulations (Fig 11, inset). This implies a scaling factor $f = \xi_0^*/\xi_0$, leading to an effective diffusion coefficient

$D_0^* = D_0/f$ and an effective Brownian time $t_B^* = ft_B$ in the experiments with $P > 0$, while in the simulations and experiments with $P = 0$, $D_0^* = D_0$ and $t_B^* = t_B$. Also other procedures have been followed to determine $\varepsilon(P)$ and $\xi_0^*(P)$; they all resulted in a linear relation $\varepsilon(P) \sim P$ with slopes within 20% and also very similar $\xi_0^*(P)$.

Having determined $\varepsilon(P)$ and corrected the experimental data for radiation pressure effects, we can compare the experimental and simulation results (Fig. 11). While the dynamics at short and long times have been exploited to obtain $\varepsilon(P)$ and ξ_0^* , a comparison of the intermediate subdiffusive behaviour with the transition from short to long-time diffusion and the corresponding time scales is meaningful. The dynamics at intermediate times indeed quantitatively agree. In addition, the quantitative agreements of the time scales, t_μ and t_α , determined from the experimental and simulation data (Fig. 10) have already been discussed.

D. Comparison to particle dynamics in one-dimensional random and periodic potentials

As in two-dimensional random potentials, in one-dimensional random potentials the particle dynamics also show three distinct regimes: diffusion at short and long times and subdiffusion at intermediate times (Fig. 13) [23, 24]. The dynamics are much slower in the one-dimensional case. In particular, it takes a much longer time to approach the asymptotic long-time limit. In general, the characteristic times, for example t_μ and t_α , are considerably longer and show a stronger dependence on ε . Furthermore, the long-time diffusion coefficient D_∞ is smaller (Fig. 12, blue dotted line) [20]:

$$\frac{D_\infty(\varepsilon)}{D_0} = e^{-\left(\frac{\varepsilon}{k_B T}\right)^2} \quad (12)$$

In two dimensions, D_∞ is larger because large barriers can be avoided, but the exponential dependence on $(\varepsilon/k_B T)^2$ remains, consistent with the percolation argument.

In addition to random potentials, colloidal particles have also been investigated in periodic potentials [56–59, 80, 81]. In a sinusoidal potential [59], only one barrier height exists and thus the distribution of escape times is narrower. The dynamics at intermediate times exhibit a smaller slope at the inflection point of the mean squared displacement, corresponding to a more pronounced subdiffusive behaviour with a deeper minimum of the exponent $\mu(t)$. On the other hand, long-time diffusion is established earlier as very deep minima are absent.

IV. CONCLUSIONS

We investigated the dynamics of individual colloidal particles in two-dimensional random potential energy landscapes, whose values follow a Gaussian distribution

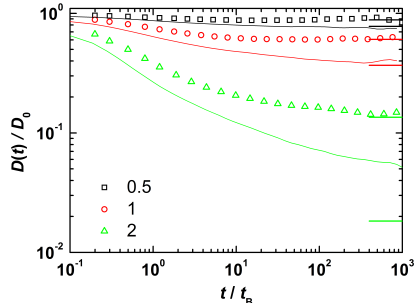


FIG. 13. (Color online) Normalized diffusion coefficient $D(t)/D_0$ as a function of normalized delay time t/t_B for particles in a one-dimensional (lines) and two-dimensional (symbols) random potential with different standard deviations ε (as indicated) as observed in simulations. Solid horizontal lines at large t/t_B correspond to theoretical predictions [9, 20].

with a standard deviation ε , which characterizes the degree of roughness of the potential. In the experiments, the potential was created using an optical set-up and the roughness ε was controlled via the laser power P . The experimentally observed dynamics agree with our Monte Carlo simulation results. Three distinct regimes have been observed. At short times, the particles exhibit diffusive behaviour within their local minima, in which they remain until they cross a barrier, i.e. a saddle point, to a neighbouring minima. The wide distribution of barrier heights leads to a significant spread in residence times. In the mean squared displacement this is

reflected as a broad subdiffusive region with a relatively large slope at the inflection point at intermediate times. At long times, the hopping between minima resembles a random walk and diffusive dynamics are recovered although with a significantly reduced diffusion coefficient. The long-time diffusion coefficient decreases with increasing degree of roughness ε in agreement with theoretical predictions [9]. This decrease is less pronounced than in one-dimensional potential energy landscapes [20]. This is attributed to the possibility to bypass large barriers in two-dimensions.

The system presented here can also serve as a well-controlled, tunable and easily observable model for other systems, which either explore space or configuration space, i.e. a potential energy landscape. These systems include crowded systems, such as concentrated colloidal suspensions, supercooled liquids, glasses [33, 35–40], or living cells [26–28], but also complex potential energy landscapes, such as those suggested in protein folding [42–44, 46, 47].

ACKNOWLEDGEMENT

We thank Jürgen Horbach (University Düsseldorf), Anand Yethiraj (Memorial University, Newfoundland), Wilson C. K. Poon (The University of Edinburgh) and David Dean (University Bordeaux) for very helpful discussions and comments. Financial support from the International Helmholtz Research School of Biophysics and Soft Matter (IHRS BioSoft) and the German Science Foundation (DFG) through the German-Dutch Collaborative Research Centre SFB-TR6 (Project Section C7) and the Research Unit FOR1394 (Projects P2, P4) is gratefully acknowledged.

-
- [1] M. D. Haw, *J. Phys.: Condens. Matter* **14**, 7769 (2002).
 - [2] E. Frey and K. Kroy, *Annalen der Physik* **14**, 20 (2005).
 - [3] D. Babić, C. Schmitt, and C. Bechinger, *Chaos* **15**, 026114 (2005).
 - [4] P. Hänggi and F. Marchesoni, *Chaos* **15**, 026101 (2005).
 - [5] I. M. Sokolov, *Soft Matter* **8**, 9043 (2012).
 - [6] H. Löwen, *J. Phys.: Condens. Matter* **20**, 404201 (2008).
 - [7] A. van Blaaderen, *MRS Bulletin* **29**, 85 (2004).
 - [8] J.-P. Bouchaud and A. Georges, *Phys. Rep.* **195**, 127 (1990).
 - [9] D. S. Dean, I. T. Drummond, and R. R. Horgan, *J. Stat. Mech.*, P07013 (2007).
 - [10] S. Havlin and D. Ben-Avraham, *Adv. Phys.* **36**, 695 (1987).
 - [11] M. B. Isichenko, *Rev. Mod. Phys.* **64**, 961 (1992).
 - [12] R. L. Jack and P. Sollich, *J. Stat. Mech.* **2009**, P11011 (2009).
 - [13] J. Bernasconi, H. U. Beyeler, S. Strässler, and S. Alexander, *Phys. Rev. Lett.* **42**, 819 (1979).
 - [14] J. W. Haus, K. W. Kehr, and J. W. Lyklema, *Phys. Rev. B* **25**, 2905 (1982).
 - [15] D. S. Novikov, E. Fieremans, J. H. Jensen, and J. A. Helpert, *Nat. Phys.* **7**, 508 (2011).
 - [16] H. Scher and M. Lax, *Phys. Rev. B* **7**, 4491 (1973).
 - [17] M. Schmiedeberg, J. Roth, and H. Stark, *Eur. Phys. J. E* **24**, 367 (2007).
 - [18] A. M. Lacasta, J. M. Sancho, A. H. Romero, I. M. Sokolov, and K. Lindenberg, *Phys. Rev. E* **70**, 051104 (2004).
 - [19] J. C. Dyre, *Phys. Rev. B* **51**, 12276 (1995).
 - [20] R. Zwanzig, *Proc. Natl. Acad. Sci.* **85**, 2029 (1988).
 - [21] L. Chen, M. Falcioni, and M. W. Deem, *J. Phys. Chem. B* **104**, 6033 (2000).
 - [22] F. Sciortino, *J. Stat. Mech.*, P05015 (2005).
 - [23] R. D. L. Hanes, C. Dalle-Ferrier, M. Schmiedeberg, M. C. Jenkins, and S. U. Egelhaaf, *Soft Matter* **8**, 2714 (2012).
 - [24] R. D. L. Hanes and S. U. Egelhaaf, *J. Phys.: Condens. Matter* **24**, 464116 (2012).
 - [25] R. M. Dickson, D. J. Norris, Y.-L. Tzeng, and W. E. Moerner, *Science* **274**, 966 (1996).
 - [26] M. Weiss, M. Elsner, F. Kartberg, and T. Nilsson, *Biophys. J.* **87**, 3518 (2004).

3.3 Paper III: Particle dynamics in two-dimensional random-energy landscapes: Experiments and simulations

12

- [27] I. M. Tolić-Nørrelykke, E.-L. Munteanu, G. Thon, L. Oddershede, and K. Berg-Sørensen, *Phys. Rev. Lett.* **93**, 078102 (2004).
- [28] D. S. Banks and C. Fradin, *Biophys. J.* **89**, 2960 (2005).
- [29] A. Naumovets, *Physica A* **357**, 189 (2005).
- [30] J. Barth, *Surf. Sci. Rep.* **40**, 75 (2000).
- [31] P. Tierno, P. Reimann, T. H. Johansen, and F. Sagués, *Phys. Rev. Lett.* **105**, 230602 (2010).
- [32] A. Byström and A. M. Byström, *Acta Crystallogr.* **3**, 146 (1950).
- [33] A. Heuer, S. Murugavel, and B. Roling, *Phys. Rev. B* **72**, 174304 (2005).
- [34] A. Sengupta, S. Sengupta, and G. I. Menon, *EPL (Europhysics Letters)* **70**, 635 (2005).
- [35] A. Heuer, *J. Phys.: Condens. Matter* **20**, 373101 (2008).
- [36] P. G. Debenedetti and F. H. Stillinger, *Nature* **410**, 259 (2001).
- [37] V. Lubchenko and P. G. Wolynes, *Annu. Rev. Phys. Chem.* **58**, 235 (2007).
- [38] C. A. Angell, *Science* **267**, 1924 (1995).
- [39] W. C. K. Poon, *J. Phys.: Condens. Matter* **14**, R859 (2002).
- [40] W. van Meegen, T. C. Mortensen, S. R. Williams, and J. Müller, *Phys. Rev. E* **58**, 6073 (1998).
- [41] A. Heuer, B. Doliwa, and A. Saksengwijit, *Phys. Rev. E* **72**, 021503 (2005).
- [42] R. B. Best and G. Hummer, *Phys. Chem. Chem. Phys.* **13**, 16902 (2011).
- [43] C. M. Dobson, A. Sali, and M. Karplus, *Angew. Chem. Int. Ed.* **37**, 868 (1998).
- [44] J. D. Bryngelson, J. N. Onuchic, N. D. Socci, and P. G. Wolynes, *Proteins* **21**, 167 (1995).
- [45] S. D. Durbin and G. Feher, *Annu. Rev. Phys. Chem.* **47**, 171 (1996).
- [46] K. A. Dill and H. S. Chan, *Nat. Struct. Mol. Biol.* **4**, 10 (1997).
- [47] R. Winter, D. Lopes, S. Grudzielanek, and K. Vogtt, *J. Non-Equilib. Thermodyn.* **32**, 41 (2007).
- [48] P. G. Wolynes, *Acc. Chem. Res.* **25**, 513 (1992).
- [49] M. C. Jenkins and S. U. Egelhaaf, *J. Phys.: Condens. Matter* **20**, 404220 (2008).
- [50] A. Ashkin, *Proc. Natl. Acad. Sci.* **94**, 4853 (1997).
- [51] J. E. Molloy and M. J. Padgett, *Contemp. Phys.* **43**, 241 (2002).
- [52] R. W. Bowman and M. J. Padgett, *Rep. Prog. Phys.* **76**, 026401 (2013).
- [53] R. D. L. Hanes, M. C. Jenkins, and S. U. Egelhaaf, *Rev. Sci. Instrum.* **80**, 083703 (2009).
- [54] D. G. Grier, *Nature* **424**, 810 (2003).
- [55] K. Dholakia and W. Lee, in *Advances in Atomic, Molecular, and Optical Physics*, Vol. 56 (Academic Press, 2008) pp. 261–337.
- [56] K. Loudiyi and B. J. Ackerson, *Physica A* **184**, 1 (1992).
- [57] Q.-H. Wei, C. Bechinger, D. Rudhardt, and P. Leiderer, *Phys. Rev. Lett.* **81**, 2606 (1998).
- [58] C. Bechinger, Q. H. Wei, and P. Leiderer, *J. Phys.: Condens. Matter* **12**, A425 (2000).
- [59] C. Dalle-Ferrier, M. Krüger, R. D. L. Hanes, S. Walta, M. C. Jenkins, and S. U. Egelhaaf, *Soft Matter* **7**, 2064 (2011).
- [60] J. C. Crocker and D. G. Grier, *J. Coll. Interf. Sci.* **179**, 298 (1996).
- [61] P. Habdas and E. R. Weeks, *Curr. Opin. Coll. Interf. Sci.* **7**, 196 (2002).
- [62] C. Kreuter, P. Leiderer, and A. Erbe, *Coll. Polym. Sci.* **290**, 575 (2012).
- [63] M. C. Jenkins and S. U. Egelhaaf, *Adv. Coll. Interf. Sci.* **136**, 65 (2008).
- [64] C. Zunke, R. D. L. Hanes, F. Evers, and S. U. Egelhaaf, in preparation.
- [65] R. W. Gerchberg and W. O. Saxton, *Optik* **35**, 237 (1972).
- [66] J. W. Goodman, *Speckle Phenomena in Optics: Theory and Applications* (Roberts & Co Publ., 2010).
- [67] K. M. Douglass, S. Sukhov, and A. Dogariu, *Nat. Photonics* **6**, 833 (2012).
- [68] E. S. Pagac, R. D. Tilton, and D. C. Prieve, *Chem. Eng. Comm.* **148–150**, 105 (1996).
- [69] J. Leach, H. Mushfique, S. Keen, R. Di Leonardo, G. Ruocco, J. M. Cooper, and M. J. Padgett, *Phys. Rev. E* **79**, 026301 (2009).
- [70] P. Sharma, S. Ghosh, and S. Bhattacharya, *Appl. Phys. Lett.* **97**, 104101 (2010).
- [71] B. Vorselaars, A. V. Lyulin, K. Karatasos, and M. A. J. Michels, *Phys. Rev. E* **75**, 011504 (2007).
- [72] D. S. Dean, I. T. Drummond, and R. R. Horgan, *J. Phys. A: Math. Gen.* **30**, 385 (1997).
- [73] D. S. Dean, I. T. Drummond, and R. R. Horgan, *J. Phys. A: Math. Gen.* **37**, 2039 (2004).
- [74] C. Touya and D. S. Dean, *J. Phys. A: Math. Theor.* **40**, 919 (2007).
- [75] K. S. Schweizer, *Curr. Opin. Coll. Interf. Sci.* **12**, 297 (2007).
- [76] W. A. Ducker, T. J. Senden, and R. M. Pashley, *Nature* **353**, 239 (1991).
- [77] S. G. Flicker, J. L. Tipa, and S. G. Bike, *J. Coll. Interf. Sci.* **158**, 317 (1993).
- [78] J. Y. Walz, *Curr. Opin. Coll. Interf. Sci.* **2**, 600 (1997).
- [79] H. H. von Grünberg, L. Helden, P. Leiderer, and C. Bechinger, *J. Chem. Phys.* **114**, 10094 (2001).
- [80] C. Emary, R. Gernert, and S. H. L. Klapp, *Phys. Rev. E* **86**, 061135 (2012).
- [81] K. Lichtner, A. Pototsky, and S. H. L. Klapp, *Phys. Rev. E* **86**, 051405 (2012).

3.4 Paper IV: Particle Dynamics in Rough Potentials with Spatial Correlations

Journal: Physical Review E

Reference: To be submitted

Impact factor: 2.288

Authors: Sebastian Horstmann, **Jörg Bewerunge**, Christoph Zunke, Florian Platten, and Stefan U. Egelhaaf

2nd author

SH performed the measurements and SH and JB analysed the data. JB, CZ, FP and SUE conceived, designed and discussed the experiments. All authors discussed the results and contributed to their interpretation and the writing of the manuscript.

40% contribution of JB

3.4 Paper IV: Particle Dynamics in Rough Potentials with Spatial Correlations

This page has been left intentionally blank.

Particle Dynamics in Rough Potentials with Spatial Correlations

Sebastian Horstmann,¹ Jörg Bewerunge,¹ Christoph Zunke,¹ Florian Platten,¹ and Stefan U. Egelhaaf¹

¹*Condensed Matter Physics Laboratory, Heinrich Heine University, 40225 Düsseldorf, Germany*

(Dated: July 8, 2016)

PACS numbers: 05.20.Jj, 05.40.*, 42.30.Ms, 47.57.J-, 64.70.pv, 82.70.Dd

I. INTRODUCTION

Recently dynamics in rough potentials with (spatial) correlations, where the correlations can either be within particle arrangement/dynamics or only the ones from the potential itself, got into the centre of interest [1]. We investigate the diffusion of colloidal particles, which were exposed to a rough potential energy landscape (rPEL) with Gamma-distributed potential energy levels $p(U)$ and a Gaussian-distributed spatial correlation function C_U , and analyse their dynamics as a function of the particle radius R with regard to particle-potential interactions. The radius R and the correlation length are of similar size. The rPEL originates in the potential felt by spherical particles which were exposed to a random laser intensity pattern, so called laser speckles, and thus exploiting optical forces and hence both the potential energy distribution and the correlation function depend on the particle radius due to the gradient forces of the laser field. But also radiation pressure acts on the sedimented particles, pushes them onto the glass wall of the sample cell and thus particle-wall interactions have to be considered. These are corrected for in the description of hydrodynamic interactions (HI) near a surface by Faxén.

Theoretical predictions by Stokes-Einstein for diffusion in bulk and for a constant particle centre-wall separation h by Faxén exist. The particles with different radii have different buoyancy forces and hence sedimentation is a function of the particle volume. Eventually, in equilibrium the net force is zero so that the gravitational force counteracts the buoyancy force. Thus we can calculate the sedimentation length l_g and show that the particles sediment down to a separation h that is exactly their own radius R plus l_g . In addition, the laser pressure forces the particles to lower their height even more to exactly $h = R$ independent of the particle size. This limit is caused by the normal force, which has to be considered as soon as the particles are settled on the bottom glass slide. However, the influence of an interface, i.e. the wall, on the diffusive behaviour of a colloidal particle was already predicted by Faxén, who described the slow down of dynamics near the surface due to hydrodynamic interactions (HI) as a function of the particle-wall separation. In this work we show that this model can be used to describe the hindered diffusion of sedimented colloidal particles near a glass interface both in the absence and in the presence of an optical force, i.e. radiation pressure. Since short time dynamics are independent of the potential roughness but solely influenced by HIs,

all experiments can be normalized with the experimental short-term diffusion coefficient D_S , which corresponds to Faxén's model for the case of totally sedimented particles ($h = R$) and thus is proportional to the particle radius, and the corresponding time t_s .

The normalized long-term diffusion coefficient D_L/D_S shows a clear dependence on the radius R ; a strong decrease for $R < 2 \mu\text{m}$ followed by a plateau at $R \geq 2 \mu\text{m}$. The particle volume and thus the over the particle integrated intensity increases with the radius and hence the influence of the rPEL gets stronger. However, spatial correlations of the potential have to be considered since it shows a dependence on the average speckle size which was calculated to be of the order of $R = 2 \mu\text{m}$ [2]. The behaviour for smaller particles can be explained by the different initial speed of the particles and thus different sampling of the potential landscape, the one for larger particles by the smoothing out of the potential correlations.

So far, little was published about intermediate dynamics referring to correlations. Here, we show the minimum of the diffusive exponent μ_{\min} and the non-Gaussian parameter (NGP) α_2 . On the one hand, μ_{\min} behaves similar to the long-term diffusion limit D_L . The NGP, on the other hand, shows different, heterogeneous dynamics, which can again be separated into two regimes of the particle radius for $R < 2$ and $R > 2 \mu\text{m}$. Furthermore the time of the minimum in the diffusive exponent t_{\min} and the value of the MSD at this time MSD_{\min} are of interest. The later is related to $1/R$ via the potential trap stiffness.

II. MATERIALS AND METHODS

A. Sample Preparation

Samples consist of spherical polystyrene particles (Interfacial Dynamics Corporation) dispersed in purified water (ELGA purelab flex, electrical resistivity $\rho = 18.2 \times 10^4 \Omega\text{m}$) and are prepared in home-made glass microscopy cells [3]. Monodisperse samples with particle radii $R = 0.8 - 4.2 \mu\text{m}$ were used. Three glass cover slips and a microscope slide (VWR) are assembled to form a small capillary and closed with uv-glue (Norland). Due to the density difference between particles and the surrounding medium, particles are forced to sediment building a (quasi) two-dimensional layer. In this case, instead of using the bulk concentration as an indicator for

3.4 Paper IV: Particle Dynamics in Rough Potentials with Spatial Correlations

2

particle-particle interactions, it is sensible to look at the particle area fraction $\phi_A = \pi NR^2/A$, which is hereinafter also referred to as concentration (of the two-dimensional system), with number of particles N in the field of view with area A . For all measurements $\phi_A < 0.04$.

B. Data Acquisition

The particle positions and their movements are examined with an inverted microscope (Nikon, Eclipse Ti-U) and a 20 \times objective (Nikon, CFI S Plan Fluor ELWD, numerical aperture $NA = 0.45$) while images of time-series were recorded by a CCD camera (AVT, Pike F-032B with 640×480 pixels and pixel pitch $pp_x = pp_y = 0.372 \mu\text{m px}^{-1}$). Typical images have a quadratic field of view of $460 \times 460 \text{ px}^2 = 171 \times 171 \mu\text{m}^2$. For every measurement about 59600 images at a frame rate of 7.5 fps are recorded. Furthermore, position determination and subsequent trajectory analysis were carried out using particle tracking routines in IDL [4]. Subsequently, the short time dynamics, which are only influenced by the laser pressure (and HIs) but not by the roughness of the rPEL, were analyzed and time- and ensemble-averaged parameters describing the diffusion, e.g., the mean-squared displacement (MSD) and the short time diffusion coefficient D_S , calculated. Since the particles are initially quenched in the rPEL, the system still relaxes within the time of the measurement and thus, since time-averaged data is considered, the long time dynamical behaviour of the system, in contrast to short time dynamics, depends on the analysis time. Furthermore, the relaxation time of the system strongly depends on the mobility of the particles and thus on particle radius R . This was corrected by cutting the trajectories (for every measurement) at a maximal time of $t = 40t_s$, where $t_s = R^2/4D_S$ is the time a particle needs to move a distance equal to its own radius with its initial diffusion coefficient D_S .

C. Random Potential Energy Landscape

The particles were exposed to a random potential energy landscape (rPEL), which was realized with an optical set-up based on laser light (Laser Quantum, Opus 532, wavelength $\lambda = 532 \text{ nm}$, maximum laser power $P_{L,\text{max}} = 2.6 \text{ W}$) shaped with a special diffuser (RPC Photonics, Engineered Diffuser EDC- 1-A-1r,) [2, 5]. In this way, it is possible to imprint a macroscopically flat (top-hat intensity distribution) but microscopically rough (laser speckles on the particle length scale) intensity landscape on the sample plane. The experiments described in this work were performed at fixed conditions of the optical set-up ('BE 5 \times ' in [2]) resulting in a speckle area $A_S = 5.1 \mu\text{m}^2$. Further parameters characterizing the speckle patterns convolved with the weight function of a spherical particle with radius R and thus effective

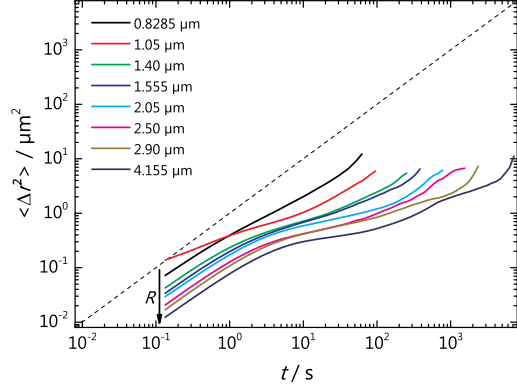


FIG. 1. MSD vs time t (both not scaled) for different radii R .

particle area $A_m = \frac{8}{9}\pi R^2$ are, here for $R = 1.4 \mu\text{m}$, the ratio of the effective particle area to the speckle area $A_m/A_S = 1.07$ and the correlation parameter $M = 2.6$. It results in a rPEL felt by the diffusing particles with the spatial correlations and energy level distribution mainly determined by the properties of the underlying intensity landscape and the particle radius. So far, much work focussed on Gaussian roughness ($M \gg 1$), while rugged energy landscapes are much more common. Here, the correlations of the potential, i.e. M , were tuned by changing the particle radius R while holding the speckle size A_S constant.

III. RESULTS AND DISCUSSION

We investigate colloidal particles exposed to a rPEL with Gamma-distributed potential energy levels and analyse their dynamics as a function of the particle radius with regard to particle-potential interactions. A typical measure to analyse particle dynamics is the mean-squared displacement (MSD), $\langle \Delta r^2 \rangle$, which corresponds to the variance of the displacement probability distribution and is given by

$$\langle \Delta r^2(t) \rangle = \langle [\mathbf{r}_i(t_w + t) - \mathbf{r}_i(t_w)]^2 \rangle_{t_w, i} \quad (1)$$

$$= 4D_0 t \quad (2)$$

where $\langle \dots \rangle$ denotes time- and ensemble averaging and the proportionality constant D_0 is called the self-diffusion coefficient. The MSD is proportional to the time t for freely diffusing particles [6]. If the particles' motion is influenced by the particle concentration or an external potential, 'anomalous' diffusion emerges, and eq. (2) becomes

$$\langle \Delta r^2(t) \rangle \propto t^\mu \quad (3)$$

with the diffusive exponent μ .

Figure 1 shows the MSD for different particle radii R . As expected, the particles show diffusive behaviour at short times, sub-diffusive behaviour ($\mu < 1$) at intermediate times and tend to become diffusive again (but with a smaller diffusion coefficient D_L) at large time scales, independent of the particle's radius. Furthermore, the influence of the radius is clearly visible as a shift to smaller MSD values for increasing values of the particle radius at all time scales, i.e. the particles' motion is increasingly restricted the bigger the particles are.

A. Hindered Short-Time Diffusion Near the Wall

In this work the particles are sedimented to a quasi two-dimensional layer at the bottom of the sample cell and hence particle-wall interactions have to be considered for their influence on the particle dynamics [7–9]. The distance to the bottom cover slip can be estimated by the gravitational length l_g which is given by

$$l_g(R) = \frac{k_B T}{g \Delta \rho V_p} \quad (4)$$

with the Boltzmann constant k_B , temperature T , the standard acceleration due to gravity $g = 9.80665 \text{ m/s}^2$, the difference between the density of the polystyrene particle $\rho_p = 1.05 \times 10^3 \text{ kg/m}^3$ and the dispersion medium $\rho_m = 1.000 \times 10^3 \text{ kg/m}^3$ (water), $\Delta \rho$, and the particle volume $V_p = 4\pi R^3/3$.

The Stokes-Einstein diffusion coefficient D_0^{SE} , which describes free particle diffusion in bulk, is given by

$$D_0^{\text{SE}}(R) = \frac{k_B T}{6\pi\eta R} \quad (5)$$

with the viscosity of the dispersion medium η ($\eta = 1.002 \times 10^{-3} \text{ Pas}$ for water at $T = 20 \text{ C}$). If a particle approaches a surface its lateral motion depends on the particle centre-surface distance h and is generally slowed down due to hydrodynamic interactions (HI). Faxén [10] suggested a correction term to describe the dynamics near a wall, which includes the dependence on h normalized by the particle radius R . The corrected short-term diffusion coefficient D_0^{F} is given by

$$D_0^{\text{F}}(h, R) = \left(1 - \frac{9}{16} \frac{R}{h} + \mathcal{O}\left(\frac{R^3}{h^3}\right)\right) D_0^{\text{SE}}(R) \quad (6)$$

with the particle centre-wall separation h . It has been shown to match with experimental results of particles moving parallel and close to a surface, even with only the first order term of the expansion [7]. For the case of $R = h$ it becomes

$$D_0^{\text{F}}(h = R) \approx \frac{7}{16} D_0^{\text{SE}}. \quad (7)$$

The experimental short-time diffusion coefficient for sedimented particles D_0 is shown in fig. 2 as a function

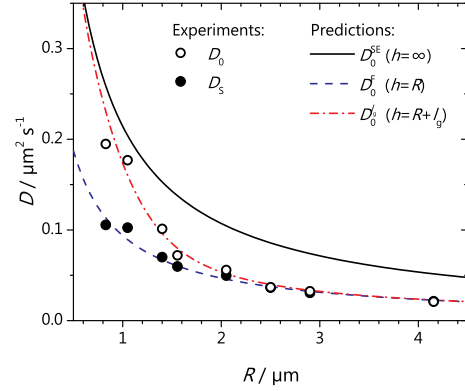


FIG. 2. Experimental short time diffusion coefficient in the absence of a laser field, D_0 (open symbols), and for the case with a rPEL and high laser power $P_L = 2600 \text{ mW}$, D_S (closed symbols), in comparison with theoretical predictions for bulk diffusion, i.e. Stokes-Einstein, D_0^{SE} (eq. (5), black solid line), in a distance $h = R$, D_0^{F} (eq. (6), blue dashed line), and a distance $h = R + l_g$ from the wall, D_0^{F} (red dash-dotted line), based on Faxén's prediction with the gravitation length l_g .

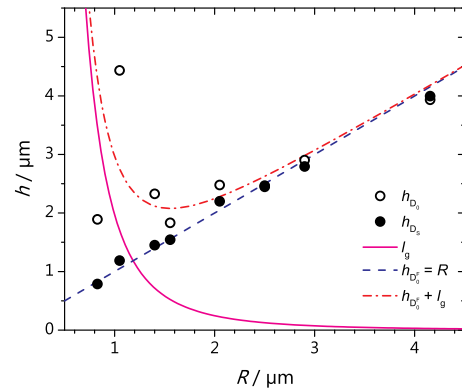


FIG. 3. Experimental particle centre-wall separation h for the case without (h_{D_0} , open symbols) and with a rPEL (h_{D_S} , closed symbols). Calculated gravitational length l_g (eq. (4), pink solid line), particle size R (blue dashed line) and a combination of both ($R + l_g$, red dash-dotted line).

of the particle radius R (open symbols). It was determined by calculating the time-dependent diffusion coefficient $D(t)$ as

$$D(t) = \frac{1}{2} \frac{\partial}{\partial t} \langle \Delta r^2(t) \rangle \quad (8)$$

and subsequently evaluating $D_0 = \lim_{t \rightarrow 0} D(t)$. The short-time diffusion is well described by Faxén's correction with $h = R + l_g$ (fig. 2, red dash-dotted line), i.e. the particles are sedimented to an equilibrium position above

3.4 Paper IV: Particle Dynamics in Rough Potentials with Spatial Correlations

4

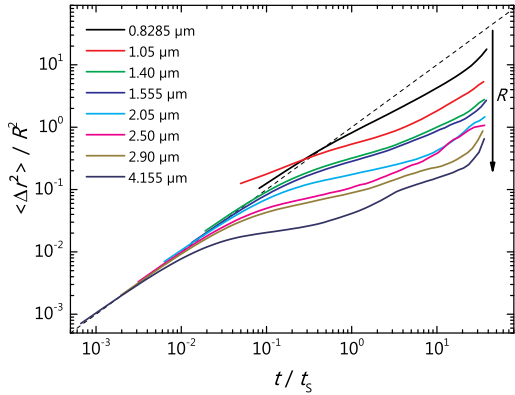


FIG. 4. The MSD normalized with the particle radius R as a function of the time normalized with t_s , i.e. the MSD corrected for the influence of HIs due to sedimentation and laser pressure. All curves (aside from the one for $R = 1 \mu\text{m}$) show a short-term diffusion which is scalable with R , $D/D_S \approx 1$, and a size dependent decrease of intermediate and long-term dynamics.

the bottom sample wall which depends on the particle's sedimentation length l_g (eq. (4)) as shown in fig. 3. Exposing the particles to an optical field leads to radiation pressure, which pushes the particles closer to the wall, since it points in the same direction as the gravitational force. This effect is independent of the shape of the optical landscape, i.e. the optical gradient forces, and thus shows no further influence of the rPEL. However, it pushes the particles closer to the wall (fig. 3, filled symbols) and thus their short-time diffusion coefficient D_S (fig. 2, filled symbols) is further reduced in comparison to the diffusion of just sedimented particles D_0 (open symbols), especially for the case of small particles ($R \leq 2 \mu\text{m}$). Moreover, comparing the resulting particle-wall separation in the presence of radiation pressure h_{D_S} (fig. 3, filled symbols) with the particle radius R (blue dashed line) shows, within experimental errors, a perfect match, i.e. the particles are more or less in contact with the wall, and hence the short-time dynamics can be shown to be well described by Faxén's correction with particle-wall separation $h = R$, $D_0^F(h = R)$ (eq. (7), cf. fig. 2). Thus, since short time dynamics are independent of the potential roughness but solely influenced by HIs, all experiments can be normalized with the experimental short-term diffusion coefficient D_S , which corresponds to Faxén's model for the case of totally sedimented particles ($h = R$) and thus is proportional to the particle radius (fig. 2), and the corresponding time t_s . Figure 4 shows the MSD normalized with the particle radius R as a function of the time normalized with t_s . At short times $D/D_S \approx 1$ independent of the particle radius R .

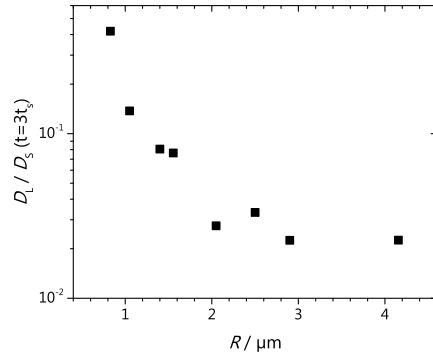


FIG. 5. Normalized long-term diffusion coefficient D_L/D_S , with $D_L = D(t = 3t_s)$, as a function of the particle radius R , shown on a logarithmic scale.

B. Anomalous Diffusion as a Function of the Particle Size

In contrast to the short-term dynamics, the intermediate and long-term dynamics are strongly influenced by the rPEL. The normalized long-term diffusion coefficient D_L/D_S , with $D_L = D(t = 3t_s)$, as a function of the particle radius R is shown on a logarithmic scale in fig. 5. Although it is steadily decreasing for all R , the slow down of D_L/D_S with increasing R is the strongest for small particle radii ($R < 2 \mu\text{m}$) and shows a saturation at values of $R \geq 2 \mu\text{m}$. Here we show results for particle sizes between a radius less than half of the average intensity speckle size, which is $s = 1.98 \mu\text{m}$, ($R_{\min} = 0.8 \mu\text{m}$) and up to roughly two times larger than the speckle size ($R_{\max} = 4.155 \mu\text{m}$). Since D_L was corrected for influences of short-time dynamics and thus HIs, these results can solely be explained by the interaction of the particles with the rough potential. The particle-potential interactions are mainly influenced by two effects. On the one hand, the particle volume directly effects the strength of the optical trapping by influencing its trap stiffness κ [11]. This effect shows ambiguous behaviour with increasing particle volume and can, depending on the wavelength of the laser light and the particle volume, either increase or decrease the effect of the potential. On the other hand, integrating more local intensities over a larger effective area of the particles leads to a smoothing of the potential correlations. Hence, D_L saturates to a plateau for values of the radius that are larger than the speckle size.

At intermediate time scales anomalous diffusion is observed. A good measure to describe anomalous diffusion is the time dependent diffusive exponent $\mu(t)$, which can be calculated from

$$\mu(t) = \frac{\partial}{\partial \log(t)} \log(\langle \Delta r^2(t) \rangle). \quad (9)$$

If particles are hindered in their motion, one speaks of sub-diffusion which is indicated by $\mu(t) < 1$. As already

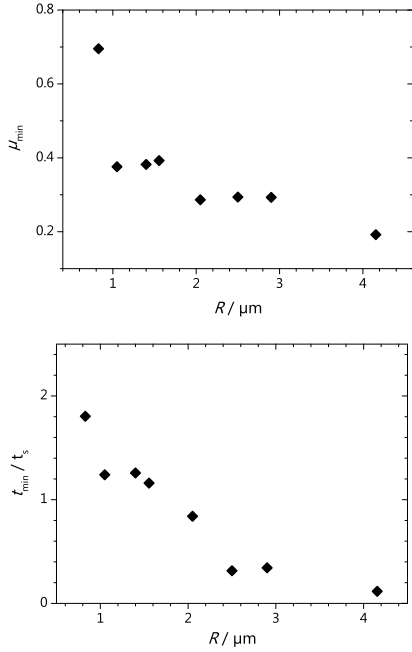


FIG. 6. The minimum of the diffusive exponent μ_{\min} (a) and the time t_{\min} at which $\mu(t)$ becomes minimal normalized by t_s (b), both as a function of the particle radius R .

seen by the analysis of the MSD (cf. fig. 1), sub-diffusion is apparent at intermediate times for all investigated particle radii. It is useful to further quantify this reduction in the diffusivity by determining the minimum of the diffusive exponent μ_{\min} as a function of the particle radius R (fig. 6). μ_{\min} shows comparable behaviour to the one of the long time diffusion coefficient D_L , that is decreasing values with increasing radius R . Although the statistics at intermediate times are better due to the time-averaging, the trends of μ_{\min} are less pronounced than for longer times. This is presumably caused by ongoing relaxation of the system while the measurements were performed.

As a link to sub-diffusive behaviour at intermediate times, where $\mu(t)$ shows a minimum, the square-root of the plateau value of the MSD, $\sqrt{\text{MSD}_{\min}}$, was determined as a function of particle radius R . $\sqrt{\text{MSD}_{\min}}$ can be seen as a measure for the average displacement of particles trapped in the laser potential. Thus a proportionality of $\sqrt{\text{MSD}_{\min}}$ with the stiffness of the single optical traps κ is suggested [11, 12]. Although the trap stiffness κ usually shows ambiguous behaviour as a function of the particle radius R normalized with the laser wavelength λ , here, only particles larger than the wavelength ($2\pi R/\lambda \gtrsim 3$ [11]) are considered and thus the geometrical optics regime is valid for all investigated particle sizes. Hence a monotone decrease of the trap stiffness with in-

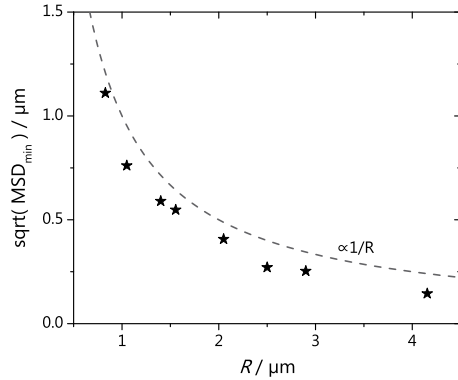


FIG. 7. The square-root of the plateau value of the MSD, $\sqrt{\text{MSD}_{\min}}$, as a function of particle radius R . The dashed line indicates $1/R$.

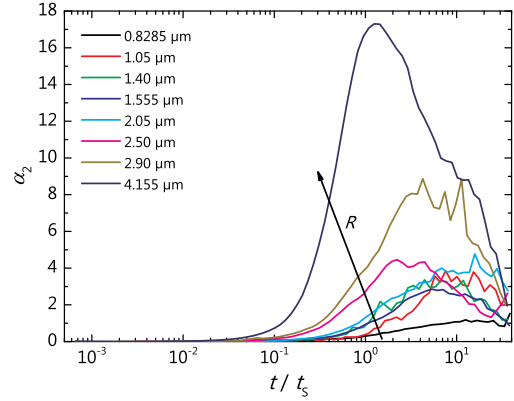


FIG. 8. The non-Gaussian parameter α_2 as a function of the normalized time t/t_s for different particle radii R .

creasing particle radius, i.e. $\kappa \propto \sqrt{\text{MSD}_{\min}} \propto 1/R$, is expected [11].

In the absence of a drift one can also calculate the so called non-Gaussian parameter (NGP) α_2 as

$$\alpha_2(t) = \frac{\langle \Delta r^4(t) \rangle}{3 \langle \Delta r^2(t) \rangle^2} - 1, \quad (10)$$

where $\langle \Delta r^4(t) \rangle$ is the next higher non-zero moment of the displacement distribution, which is calculated accordingly to $\langle \Delta r^2(t) \rangle$. The non-Gaussian parameter α_2 is the excess kurtosis of the displacement distribution and thus indicates deviations of the shape of the measured distribution from a perfect Gaussian. It is shown in fig. 8 as a function of the normalized time t/t_s for different particle radii R . Again, two regimes can be identified which are roughly separated by the average speckle size $s = 1.98 \mu\text{m}$. Although large particles seem to be less

influenced by the rPEL, as seen in the long-term diffusion coefficient D_L , their motion is very heterogeneous in comparison to smaller particles with $R \leq s$. This can be explained by large particles seeing several laser speckles at once and thus correlations between adjacent speckles have to be included. Since the rPEL of this work has potential energy levels which are Gamma-distributed, it is, in comparison to Gaussian rPELs, more likely that the diffusion of the particles is strongly influenced by few very deep potential wells. The larger a particle is, the higher is the probability to be initially quenched to a position in the rPEL at which such a deep potential well is present and hence some of the larger particles are longer pinned in potential traps although the overall correlations are less pronounced and hence most particles show normal diffusive behavior, as without a rPEL.

IV. CONCLUSIONS

We investigated the diffusion of colloidal particles, which were exposed to a rough potential energy landscape, and analysed their dynamics as a function of the particle radius R with regard to the particle-potential interactions and potential correlations. The short-term diffusion coefficient D_S in presence of a laser field, which

pushes the particles to the bottom slide of the sample cell, was determined. Taking the gravitational length l_g and the particle centre-wall separation into account, it was used to normalize the experimental long-term diffusion coefficient D_L for hydrodynamic interactions. At intermediate and long times, particle dynamics is strongly influenced by the rPEL resulting in anomalous diffusion, which is indicated by a small diffusive exponent, $\mu < 1$, and a large NGP, $\alpha_2 > 1$. Furthermore, these parameters were analysed as a function of the particle radius R . With increasing R both D_L and the minimum in the diffusive exponent μ_{\min} monotonically decrease with a trend to saturate for large particles. A proportionality of $\sqrt{\text{MSD}_{\min}}$, which can be seen as a measure for the average displacement of particles trapped in the laser potential, with the stiffness of single optical traps κ was suggested.

ACKNOWLEDGMENTS

We thank David Dean, Thomas Franosch, Andreas Heuer, Jürgen Horbach, Imad Ladadwa, and Hartmut Löwen for very helpful discussions and suggestions, and the Deutsche Forschungsgemeinschaft (DFG) for financial support (grant EG269/6-1).

-
- [1] I. Goychuk and V. O. Kharchenko, *Phys. Rev. Lett.* **113**, 100601 (2014).
 - [2] J. Beverunge and S. U. Egelhaaf, *Phys. Rev. A* **93**, 013806 (2016).
 - [3] M. C. Jenkins and S. U. Egelhaaf, *Adv. Colloid Interface Sci.* **136**, 65 (2008).
 - [4] J. C. Crocker and D. G. Grier, *J. Colloid Interface Sci.* **179**, 298 (1996).
 - [5] T. R. M. Sales, *Opt. Eng.* **42**, 3084 (2003).
 - [6] A. Einstein, *Annalen der Physik* **322**, 549 (1905).
 - [7] B. Lin, J. Yu, and S. Rice, *Phys. Rev. E* **62**, 3909 (2000).
 - [8] P. Sharma, S. Ghosh, and S. Bhattacharya, *Appl. Phys. Lett.* **97**, 104101 (2010).
 - [9] A. Sonn-Segev, J. Blainey, P. C. awdziewicz, E. Wajnryb, M. L. Ekiel-Blzewska, H. Diamant, and Y. Roichman, *J. Chem. Phys.* **143**, 074704 (2015).
 - [10] H. Faxén, *Annalen der Physik* **373**, 89 (1922).
 - [11] A. Mazolli, P. A. Maia Neto, and H. M. Nussenzveig, *Proc. R. Soc. Lond. A* **459**, 3021 (2003).
 - [12] T. A. Nieminen, N. du Preez-Wilkinson, A. B. Stilgoe, V. L. Loke, A. A. Bui, and H. Rubinsztein-Dunlop, *J. Quant. Spectrosc. Radiat. Transfer* **146**, 59 (2014).

3.5 Paper V: Time- and ensemble-averages in evolving systems: the case of Brownian particles in random potentials

Journal: Physical Chemistry Chemical Physics (PCCP)

Reference: In press

Impact factor: 4.493

Authors: **Jörg Bewerunge**, Imad Ladadwa, Florian Platten, Christoph Zunke, Andreas Heuer, and Stefan U. Egelhaaf

1st author

JB and IL performed experiments and simulations, respectively. JB and FP analysed the data. All authors conceived, designed and discussed the experiments and simulations and contributed to the writing of the manuscript.

40% contribution of JB

3.5 Paper V: Time- and ensemble-averages in evolving systems: the case of Brownian particles in random potentials

This page has been left intentionally blank.

Time- and ensemble-averages in evolving systems: the case of Brownian particles in random potentials

Jörg Bewerunge,¹ Imad Ladadwa,² Florian Platten,¹ Christoph Zunke,¹ Andreas Heuer,³ and Stefan U. Egelhaaf¹

¹*Condensed Matter Physics Laboratory, Heinrich Heine University, 40225 Düsseldorf, Germany*

²*Fahad Bin Sultan University, SA-71454 Tabuk, Saudi-Arabia*

³*Institut für Physikalische Chemie, Universität Münster, D-48149 Münster, Germany*

(Dated: 8 July 2016)

Anomalous diffusion is a ubiquitous phenomenon in complex systems. It is often quantified using time- and ensemble-averages to improve statistics, although time averages represent a non-local measure in time and hence can be difficult to interpret. We present a detailed analysis of the influence of time- and ensemble-averages on dynamical quantities by investigating Brownian particles in a rough potential energy landscape (PEL). Initially, the particle ensemble is randomly distributed, but the occupancy of energy values evolves towards the equilibrium distribution. This relaxation manifests itself in the time evolution of time- and ensemble-averaged dynamical measures. We use Monte Carlo simulations to study particle dynamics in a potential with a Gaussian distribution of energy values, where the long-time limit of the diffusion coefficient is known from theory. In our experiments, individual colloidal particles are exposed to a laser speckle pattern inducing a non-Gaussian roughness and are followed by optical microscopy. The relaxation depends on the kind and degree of roughness of the PEL. It can be followed and quantified by the time- and ensemble-averaged mean squared displacement. Moreover, the heterogeneity of the dynamics is characterized using single-trajectory analysis. The results of this work are relevant for the correct interpretation of single-particle tracking experiments in general.

PACS numbers: 05.20.Jj, 47.57.-s, 64.70.pv, 82.70.Dd

I. INTRODUCTION

The mean-squared displacement (MSD), $\langle \delta r^2(t) \rangle$, is often used to characterize the dynamics of Brownian particles. In many situations, the dependence of the MSD on lag time t follows a power law, according to

$$\langle \delta r^2(t) \rangle \propto t^\mu. \quad (1)$$

For normal diffusion, the MSD increases linearly with time and one obtains $\mu = 1$. However, in recent years, interest moved to anomalous diffusion, i.e. $\mu \neq 1$.¹⁻³ Systems with $\mu < 1$ and $\mu > 1$ are called sub- and superdiffusive, respectively. We focus on subdiffusive behavior, which occurs, e.g., in many-particle systems, such as crowded biological cells,⁴⁻⁶ dense colloidal suspensions,^{7,8} and other glassy samples.⁹ Moreover, individual particles might undergo subdiffusion due to confinement,^{5,10} e.g. in disordered or porous media,¹¹⁻¹⁴ or external potentials.¹⁵ Due to the advances in single molecule experiments and particle tracking algorithms,¹⁶⁻¹⁹ an increasing number of such studies are performed and quantitative data sets become available.

The average on the left-hand side of Eq. (1) can be understood in different ways. First, as an ensemble average (EAMSD) $\langle \delta r_i^2(t) \rangle_i$ over the trajectories of N particles i

$$\langle \delta r_i^2(t) \rangle_i = \frac{1}{N} \sum_{i=1}^N [r_i(t) - r_i(0)]^2. \quad (2)$$

Second, as a time average (TAMSD) over a very long single trajectory of particle i , which extends up to a maxi-

mum time $t_{\max} \gg t$, i.e. an average over waiting times t_0 :

$$\langle \delta r_i^2(t) \rangle_{t_0} = \frac{1}{t_{\max} - t} \int_{t_{\text{start}}}^{t_{\text{start}} + t_{\max} - t} [r_i(t_0 + t) - r_i(t_0)]^2 dt_0, \quad (3)$$

where the start time, t_{start} , of the measurement might not coincide with the start of the experiment. Furthermore, a combination of both is possible and yields the time- and ensemble-averaged mean-squared displacement (TEAMSD):

$$\langle \delta r^2(t) \rangle_{t_0, i} = \left\langle \langle \delta r_i^2(t) \rangle_{t_0} \right\rangle_i. \quad (4)$$

Thus, the question arises whether the ensemble or the time-average or both should be applied.²⁰

In an ergodic system,

$$\lim_{t_{\max} \rightarrow \infty} \langle \delta r_i^2(t) \rangle_{t_0} = \langle \delta r_i^2(t) \rangle_i, \quad (5)$$

whereas, in a non-ergodic system, the TAMSD represents a stochastic variable. Recently, the dependence of TAMSDs on the duration t_{\max} of the trajectory, has been related to the long-term relaxation behavior or ageing of ergodic and non-ergodic systems.^{21,22} Moreover, differences between TAMSDs and EAMSDs have been used to identify the type or mechanism underlying anomalous diffusion in complex fluids.²³⁻²⁵

3.5 Paper V: Time- and ensemble-averages in evolving systems: the case of Brownian particles in random potentials

2

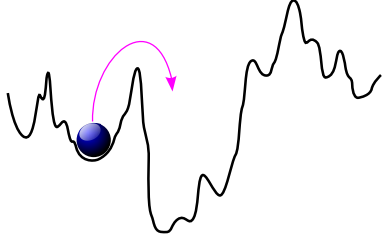


FIG. 1. Generic situation studied in this work: a single particle exploring a random potential energy landscape (PEL).

The dynamics of individual Brownian particles exposed to a stationary random potential energy landscape (PEL), as illustrated in Fig. 1, provides a useful description for many diffusion and transport processes in disordered or porous media. Colloidal model systems can be used to systematically and quantitatively study particle dynamics in experiments²⁶⁻³¹ and simulations.³²⁻³⁷ In particular, almost any external potential can be imposed on colloidal particles using laser light fields.^{15,38} Recently, we experimentally realized one- and two-dimensional random PEL and studied their effect on particle dynamics.^{39,40} Initially, particles were positioned randomly in the PEL (Fig. 1) and first explored the landscape in their vicinity, diffusing within local minima. At intermediate times, particle motion was constrained to the minima, leading to a pronounced subdiffusive regime, whereas, at long times, particle hopping between minima could be described by normal diffusion with, however, a significantly reduced long-time diffusion coefficient D_∞ . The transition from intermediate subdiffusion to the long-time asymptotic limit is expected to occur on a time scale τ , the effective relaxation time,

$$\tau \approx \frac{l^2}{D_\infty}, \quad (6)$$

where l is the characteristic length scale of the PEL.^{14,41,42} In particular, for $t_{\max} \gg \tau$, TAMSDs and EAMSDs are found to be identical, reflecting the ergodicity of the system.

In this work, we studied the dynamics of individual Brownian particles in random PELs with Gaussian and non-Gaussian (i.e. here Gamma) distributions of energy values (or “roughness”) by experiments and Monte Carlo (MC) simulations, where, for a Gaussian distribution, D_∞ is known from theory.¹⁴ In our experiments, the particles were exposed to a laser speckle pattern, which leads to a Gamma distribution of energy values, and their dynamics was followed by optical video microscopy and single-particle trajectories were extracted⁴³ and analyzed. Initially the particles were randomly distributed in the PEL and hence were in a non-equilibrium situation. During the experiments and simulations, they developed towards the equilibrium distribution. Due to this evolution of the system, the time- and ensemble-averaged

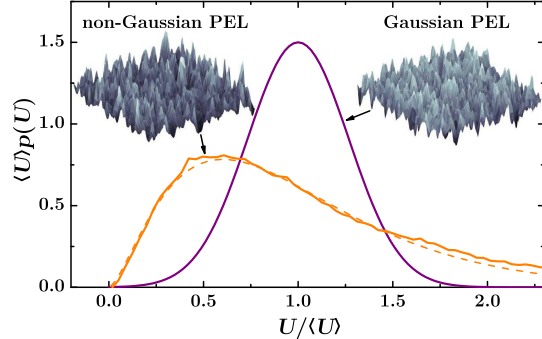


FIG. 2. Distribution $p(U)$ of energy values U of random PELs used in the experiments (Gamma distributed with $M = 2.6$, i.e. non-Gaussian, $p_\Gamma(U)$; calculation and fit shown as solid and dashed line, respectively) and simulations (Gaussian distributed, $p_G(U)$) and schematic sketches of the corresponding PELs (insets).

dynamical properties depend on the maximum duration t_{\max} of the investigated particle trajectories. Time- and ensemble-averaged MSDs (TEAMSDs) can be used to follow the equilibration of the systems, especially, in combination with the spread of the MSDs of single particles.

II. MATERIALS & METHODS

A. Sample Preparation

Samples consisted of an aqueous suspension of polystyrene spheres with sulfonated chain ends (Interfacial Dynamics Corporation, radius $R = 1.4 \mu\text{m}$, polydispersity 3.2%). Suspensions were filled into sample cells by capillary action. Sample cells were constructed from thoroughly cleaned glass cover slips and a microscope slide (VWR) glued together with Norland Optical Adhesive 61 to result in a small capillary.⁴⁴ Once the particles had sedimented into a (quasi) two-dimensional layer on the cover slip, we determined the particle area fraction $\phi_A = \pi R^2 N/A$ with the particle number N in the investigated area A of the light field. The samples were dilute ($\phi_A \leq 0.06$) and hence particle-particle interactions negligible.

B. Light Field Generation

A solid-state laser (Laser Quantum, Opus 532, wavelength $\lambda = 532 \text{ nm}$) with a maximum intensity $P_L = 2.6 \text{ W}$ provided a linearly-polarized Gaussian beam. The central optical element was a special diffuser (RPC Photonics, Engineered Diffuser™ EDC-1-A-1r).⁴⁵ If the diffuser is illuminated by an expanded Gaussian laser beam,

a macroscopically flat top-hat intensity pattern with fluctuations on a microscopic scale, i.e. a speckle pattern, is produced. The characteristic speckle size is controlled by the diameter of the illuminating laser beam; in our experiments, the particle–speckle size ratio was about 1. Details of the optical set-up are described in ref.⁴⁶

The effect of this speckle pattern on a colloidal particle can be described by a random PEL (Fig. 2 left inset).⁴⁶ The distribution of energy values $p(U)$ follows a Gamma distribution

$$p_{\Gamma}(U) = \frac{1}{\Gamma(M)} \left(\frac{M}{\langle U \rangle} \right)^M U^{M-1} e^{-MU/\langle U \rangle} \quad (7)$$

with the mean of the distribution $\langle U \rangle$, i.e. the average of the energy values, the Gamma function $\Gamma(M)$, and the shape parameter $M = 2.6$ (Fig. 2, for details see condition BE5× in Tab. II of ref.⁴⁶). The standard deviation of the distribution, $\varepsilon = \langle U \rangle / \sqrt{M}$, i.e. the degree of roughness of the potential, is controlled by the laser power $P_L \propto \varepsilon$.^{40,46} Moreover, for large values of M , $p_{\Gamma}(U)$ tends to a Gaussian distribution of energy values (Fig. 2):

$$p_G(U) = \frac{1}{\sqrt{2\pi\varepsilon^2}} \exp\left(-\frac{(U - \langle U \rangle)^2}{2\varepsilon^2}\right). \quad (8)$$

For the same standard deviation the Gamma distributed PEL has a large fraction of very high maxima than the Gaussian distributed PEL.

The colloidal particles were followed using a commercial inverted microscope (Nikon Eclipse Ti-U) with a 20× objective (Nikon CFI S Plan Fluor ELWD, numerical aperture 0.45). In most experiments, a CMOS camera (PixeLINK, PL-B741F) with a maximum field of view of 1280×1024 pixels ($431 \times 345 \mu\text{m}^2$) was used to record about 10 200 images at a frame rate of 2 frames per second for a complete measurement run. For each image, the particle locations were determined in an area of 1000×1000 pixels.⁴³ Few particles had short-time diffusion coefficients less than two percent of the mean diffusion coefficient and hence were considered stuck to the cover slip and disregarded. Particle locations were connected to yield particle trajectories.⁴³ We only considered trajectories which extended over at least 10 frames. Then the number of trajectories (typically 250) was approximately constant (± 5) over time.

C. Monte Carlo Simulations

The Monte Carlo simulations were performed on a 4096×4096 square lattice with the lattice points separated by a distance Δs in both directions, where we have set $\Delta s = 1$. The potential values at the lattice points, $\tilde{U}(x, y)$, were produced using a Box-Muller algorithm generating numbers which are Gaussian distributed with standard deviation $\tilde{\varepsilon}$. To mimick the experimental situation, the potential $\tilde{U}(x, y)$ was convoluted with the particle volume to obtain the potential $U(x, y)$ which can

then be thought to be imposed onto a point-like test particle. The potential $U(x, y)$ is smoother than $\tilde{U}(x, y)$. Its values follow a Gaussian distribution with a standard deviation ε . The spatial correlation l of $U(x, y)$ decays on the length scale of the particle size; $l \approx 2R$.⁴⁰ The spatial correlation is similar to the Gamma-distributed random PEL experienced by a colloidal particle in the light field.⁴⁶

Once $U(x, y)$ was determined, a particle was positioned on a randomly chosen lattice point. During the simulation, a direction was chosen randomly and, depending on the energy difference ΔU to the neighbouring lattice point, the move was always accepted if $\Delta U \leq 0$ or otherwise accepted with probability $\exp(-\Delta U/k_B T)$ if $\Delta U > 0$ (where $k_B T$ is the thermal energy). For each Monte Carlo run, the short-time diffusion coefficient D_0 and the related Brownian time $t_B = R^2/(4D_0)$ were calculated. Data were acquired up to $t_{\max} = 10000 t_B$. Averages based on 1024 runs with different initial particle positions appeared reliable. It turned out that, within statistical uncertainty, the results for different realizations of the potential energy landscape $U(x, y)$ are identical. Separate simulations were performed for different values of the standard deviation $0 k_B T \leq \varepsilon \leq 5 k_B T$ to investigate its effect on the dynamics. Details of the simulations are given in ref.⁴⁰

D. Data analysis

Based on the particle trajectories, different statistical properties were computed to characterize the particle dynamics. The dynamical properties were determined as a function of the distance, $\Delta r = [(\Delta x)^2 + (\Delta y)^2]^{1/2}$, where distances are scaled by the particle radius R and times by the Brownian time t_B . In our experiments, we had $R = 1.4 \mu\text{m}$ and $t_B = 5.5 \text{ s}$ based on the experimentally determined short-time diffusion coefficient D_0 . This renders the data independent of the specific experimental conditions. Initially, the occupancy of energy values was homogeneous but tended towards its equilibrium distribution in the course of the experiment. Therefore, the average over waiting times t_0 depends on the total measurement time t_{\max} .

The two-dimensional mean-squared displacement (MSD) is given by

$$\langle \Delta r^2(t) \rangle = \langle \Delta x^2(t) \rangle + \langle \Delta y^2(t) \rangle, \quad (9)$$

which is calculated from the particle trajectories according to

$$\langle \Delta x^2(t) \rangle = \langle \delta x^2 \rangle_{t_0, i} - \langle \delta x \rangle_{t_0, i}^2 \quad (10)$$

and $\langle \Delta y^2(t) \rangle$ correspondingly. The second term corrects for possible drifts. From the two-dimensional MSD, $\langle \Delta r^2(t) \rangle$, the time-dependent diffusion coefficient $D(t)$ was calculated according to

$$D(t) = \frac{1}{2d} \frac{\partial}{\partial t} \langle \Delta r^2(t) \rangle, \quad (11)$$

3.5 Paper V: Time- and ensemble-averages in evolving systems: the case of Brownian particles in random potentials

4

where in the present case the dimension $d = 2$. The exponent μ (Eq. 1) was determined from the slope of the MSD in double-logarithmic representation:

$$\mu(t) = \frac{\partial \log (\langle \Delta r^2(t) \rangle)}{\partial \log (t)}. \quad (12)$$

While the exponent $\mu(t)$ characterizes deviations from diffusive behaviour, the non-Gaussian parameter $\alpha_2(t)$ corresponds to the excess kurtosis and is given by:

$$\alpha_2(t) = \frac{\langle \Delta r^4(t) \rangle}{(1 + 2/d) \langle \Delta r^2(t) \rangle^2} - 1, \quad (13)$$

where $\langle \Delta r^4(t) \rangle$ is defined analogous to $\langle \Delta r^2(t) \rangle$ (Eqs. 8,9).⁴⁰

III. RESULTS AND DISCUSSION

We first discuss the effect of the maximum simulation time t_{\max} on the parameters describing the (evolving) particle dynamics in a random PEL with a Gaussian distribution of energy values (“Gaussian roughness”), where the long-time limit of the diffusion coefficient is known from theory. Then, we analyze how time- and ensemble-averaged dynamical properties reflect the relaxation behavior in PELs with Gaussian and non-Gaussian roughness. Moreover, we show how such quantities can be used to follow equilibration, here the evolution from an initially homogeneous distribution to its equilibrium distribution. This notion will be confirmed by the analysis of single particle trajectories.

Fig. 3 shows Monte Carlo simulation data for particle dynamics in a random PEL with a Gaussian distribution of energy values. Part (A) contains data on the mean-squared displacement averaged over different particles and waiting times (TEAMSD, eq. 4) for different values of the standard deviation of the PEL, ε (Eq. 8), and different maximum simulation times t_{\max} . In the absence of an external potential, the TEAMSD increases linearly with time for all values of t_{\max} (black solid line), as expected for free diffusion. In the presence of the random potential, the TEAMSD increases linearly with time at very short and very long times, but exhibits a pronounced slowing-down at intermediate times. Correspondingly, at very short and very long times, the diffusion coefficient (Fig. 3B) shows a plateau and, at intermediate times, an extended decrease. At very small t , the dynamics reflect diffusion within local minima and is thus essentially independent of ε . At small t , such that $\langle \Delta r^2 \rangle_{t_0, i} \lesssim R^2$, the TEAMSD depends on ε but only slightly on t_{\max} , reflecting small excursions within local minima. For large enough t , hopping between minima dominates and results in a random walk. Thus, diffusive behaviour is reestablished at long times, although with a strongly reduced diffusion coefficient D_∞ . At intermediate t , the TEAMSDs exhibit an inflection point, which becomes increasingly pronounced as ε increases. This subdiffusive behaviour

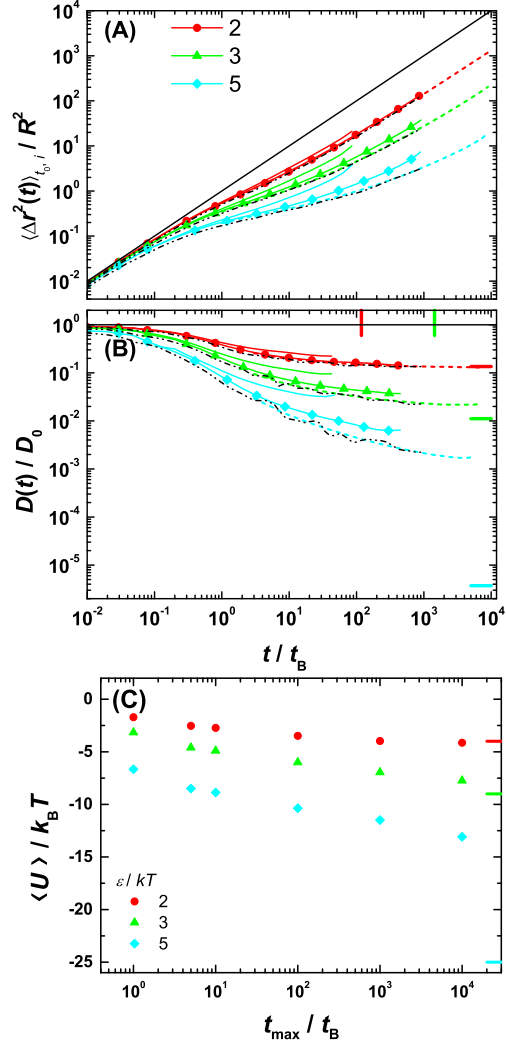


FIG. 3. (A) Time- and ensemble-averaged mean-squared displacement (TEAMSD), $\langle \Delta r^2(t) \rangle_{t_0, i}$, and (B) diffusion coefficient $D(t)$ as a function of lag time t of particles in a random PEL with a Gaussian distribution of energy values with different standard deviations ε (as indicated, in units of $k_B T$). The simulations extend over different times $t_{\max} = 10^2 t_B$, $10^3 t_B$ and $10^4 t_B$ (solid lines, connected symbols and dashed lines, respectively), whereas the start time $t_{\text{start}} = 0$ in all cases. In addition, the ensemble-averaged mean-squared displacement (EAMSD), $\langle \Delta r^2(t) \rangle_i$, is shown for a very large t_{start} when equilibrium is reached (black dash-dotted lines). The black solid lines indicate free diffusion. Solid horizontal lines at large t indicate theoretical predictions (Eq. 14)¹⁴ and solid vertical lines relaxation times (Eq. 6). (C) Mean occupied energy value $\langle U \rangle / k_B T$ as a function of t_{\max} . Solid horizontal lines indicate the long time limit $\langle U \rangle / k_B T = -(\varepsilon / k_B T)^2$.

is caused by particles being trapped in local minima for prolonged times before they can escape to neighbouring minima. Since there is a wide range of residence times, reflecting barriers of different heights, the subdiffusive regime extends over a broad range of times.

For a Gaussian distribution of energy values (Eq. 8), the long-time diffusion coefficient, D_∞ , is known from theory.^{14,47-49} It strongly depends on ε and is predicted to follow (Fig. 3B, solid horizontal lines):

$$\frac{D_\infty(\varepsilon)}{D_0} = \exp\left(-\frac{1}{2}\left(\frac{\varepsilon}{k_B T}\right)^2\right) \quad (14)$$

For $\varepsilon = 2 k_B T$ the long-time diffusive limit is reached within the time window investigated, whereas it is not reached in the cases of $\varepsilon = 3$ and $5 k_B T$, even for $t_{\max} = 10^4 t_B$ (dashed lines). According to Eq. (6), the relaxation time is expected to scale as $\tau \approx 16 t_B \exp(\frac{1}{2}(\varepsilon/k_B T)^2)$. Thus, $\tau = 118 t_B$, $1440 t_B$ and $4.3 \times 10^6 t_B$ for $\varepsilon = 2, 3$ and $5 k_B T$, respectively, consistent with the observed transition times for $\varepsilon = 2$ and $3 k_B T$ (Fig. 3B, solid vertical lines).

We also analyzed the dependence of the mean occupied energy value, $\langle U \rangle$, on the maximum simulation time t_{\max} , which corresponds to the maximum possible waiting time t_0 (Fig. 3C). $\langle U \rangle$ exhibits a continuous decrease from $\langle U \rangle = 0$ at $t_{\max} = 0$ to

$$\langle U \rangle = -\frac{\varepsilon^2}{k_B T} \quad (15)$$

in the long time limit (vertical lines). This decrease reflects the relaxation of the particle ensemble into deeper minima and is the main reason for the decrease of the MSD with increasing t_{\max} (Fig. 3A).

Fig. 3 reveals a strong effect of the maximum simulation time t_{\max} , i.e. the maximum possible waiting time t_0 , on the TEAMSDs and diffusion coefficients (solid lines, connected symbols and dashed lines of the same color), reflecting the relaxation of the initially homogeneously distributed particles to their equilibrium distribution. For $\varepsilon = 2k_B T$, the long-time limit is reached within the maximum simulation time considered here. The corresponding TEAMSDs with the two largest values of t_{\max} almost coincide at long lag times t , reflecting that the system is relaxed relatively quickly. Short lag times $t \ll t_{\max}$ imply larger maximum waiting times $t_0 = t_{\text{start}} + t_{\max} - t$ (Eq. 3) and hence also a large weight of slower dynamics even for the shorter t_{\max} , which implies only a small dependence on t_{\max} . Furthermore, for $t \ll t_B$, the particles only explore one minimum and therefore the local dynamics is basically independent of the height of the PEL. Hence, the TEAMSDs at short times coincide irrespective of t_{\max} . Similar applies to very large $t \gg \tau$, which implies $t_{\max} \gg \tau$, and hence the TEAMSDs also coincide at long times. At intermediate lag times t , larger t_{\max} lead to a larger weight of later times. Due to the evolution of the system towards its equilibrium distribution with an increasing occupation

of deep minima at longer absolute times (Fig. 3C), this imposes slower dynamics which results in a monotonic decrease of the TEAMSD and the diffusion coefficient with increasing t_{\max} . Consistent with this, the decrease is most pronounced for the largest ε with particles exploring the deepest minima. These results imply that the TEAMSDs can be used to characterize the relaxation behavior of the system.

While Fig. 3 is based on systems with Gaussian roughness, Fig. 4 compares data from systems with Gaussian (A1-A4) and non-Gaussian (Gamma) roughness (B1-B4), as obtained from Monte Carlo simulations and particle tracking experiments, respectively. Again, we analyze how the relaxation of the system is reflected in time- and ensemble-averaged dynamical quantities. For different values of the standard deviation ε , we study the effect of increasing measurement time t_{\max} , i.e. we truncate the trajectories after different times (see sketch C1).

As in Fig. 3, we observe a decrease of the TEAMSD and the diffusion coefficient with increasing effective measurement time t_{\max} and standard deviation ε , which is quantified by $D_{50} = D(t=50t_B)$ (Fig. 4). In addition, we have extracted the local slope of the MSD, $\mu(t)$. At short lag times t , $\mu(t)$ decreases, reaching a minimum, μ_{\min} , at about 2-3 t_B , which corresponds to the inflection point of $D(t)$. The μ_{\min} decreases with increasing t_{\max} (C3), until the equilibrium value of μ_{\min} is reached. Moreover, μ decreases with the standard deviation ε due to the deeper minima. At the minimum, the particles are most efficiently trapped. For larger times t , the particles succeed in escaping first the shallow and then also deeper minima and, correspondingly, $\mu(t)$ rises over some time range reflecting the distribution of the depths of the minima. Finally in the long-time diffusive limit, $\mu(t)$ is expected to reach a value of 1, but is observed to diverge due to the vanishing number of trajectories.

The non-Gaussian parameter $\alpha_2(t)$ quantifies the deviation from a Gaussian distribution of particle displacements. It is approximately zero at short and very long times, indicating that the distribution of particle displacements is well described by a Gaussian and consistent with diffusive dynamics. At intermediate times, $\alpha_2(t)$ exhibits a peak, α_{\max} , denoting the time at which the diffusion is maximally heterogeneous. This occurs after some particles have already escaped shallow minima while others are still caught in deeper minima and, therefore, the peak in $\alpha_2(t)$ occurs at later times than the minimum in $\mu(t)$. The maximum of $\alpha_2(t)$ strongly increases with t_{\max} , reflecting the increased heterogeneity, and with ε , due to the increasingly deeper minima (C4).

Qualitatively, the trends of particle dynamics in the non-Gaussian random PEL (B1-B4) resemble those in a Gaussian random PEL (A1-A4). However, quantitative differences are observed. For the two higher laser powers, the diffusion coefficient $D(t)$ (B2) roughly decreases to similar values as in the Gaussian cases (A2; see also comparison in C2), whereas the minimum of $\mu(t)$ and the maxima of $\alpha_2(t)$ are more pronounced in the non-

3.5 Paper V: Time- and ensemble-averages in evolving systems: the case of Brownian particles in random potentials

6

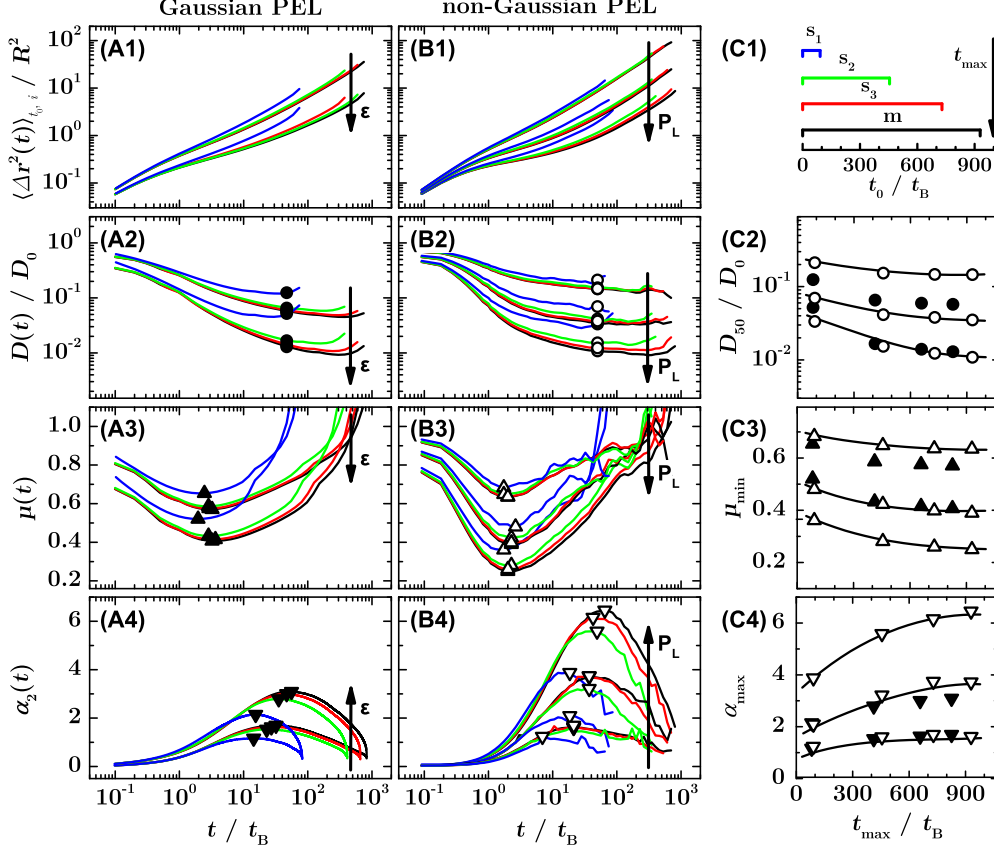


FIG. 4. Particle dynamics in random PEL with Gaussian (A1-A4, MC simulations for $\varepsilon = 3$ and $5 k_B T$) and non-Gaussian roughness (B1-B4, experiments with $P_L = 917, 1640,$ and 2600 mW) with different maximum times t_{\max} (as indicated schematically in C1), whereas the start time $t_{\text{start}} = 0$ in all cases. TEAMSD $\langle \Delta r^2(t) \rangle_{t_0, i}$ (A1, B1), diffusion coefficient $D(t)$ (A2, B2), characteristic slope of the MSD $\mu(t)$ (A3, B3), and non-Gaussian parameter $\alpha_2(t)$ (A4, B4) as a function of lag time t . Characteristic values (marked by symbols in parts A and B), namely the diffusion coefficient at $t/t_B = 50$ (C2), the minimum of $\mu(t)$ (C3), and the maximum of $\alpha_2(t)$ (C4), as a function of the maximum time t_{\max} .

Gaussian case (C3 and C4). These differences are due to the asymmetric distribution of energy values in the non-Gaussian case (Fig. 2) and thus the larger fraction of very high energy barriers which affect the relaxation process.

In Fig. 5, we show how the relaxation of the system affects the time- and ensemble-averaged dynamical properties. The time average is taken over a constant time interval t_{\max} that, however, starts at different times t_{start} after the particles have been exposed to the random PEL (C1). The general behavior is similar to the one described above. The TEAMSD (A1,B1) and the diffusion coefficient (A2,B2) at intermediate and long times decrease with t_{start} . Correspondingly, the values of $\mu(t)$ and $\alpha_2(t)$ decrease and increase with t_{start} , respectively (A3, B3

and A4, B4). The dependencies of D_{50} , μ_{\min} , and α_{\max} on t_{start} demonstrate the effect of the relaxation process. The longer the particles explored the random PEL, the deeper minima they found and, correspondingly, D_{50} and μ_{\min} decrease and α_{\max} increases with t_{start} . Once the system is completely relaxed, these properties level off at their equilibrium values. Due to the constant t_{\max} , this series (Fig. 5) reflects the evolution of the system with time, i.e. t_{start} , more directly than the previous series (Fig. 4). However, t_{\max} is at most equal but typically much smaller than in the previous section. This can have serious implications for the statistical uncertainties and is the reason that often a constant t_{start} and an increasing t_{\max} , as in the previous series (Fig. 4), is preferred despite the associated problems in data interpretation.

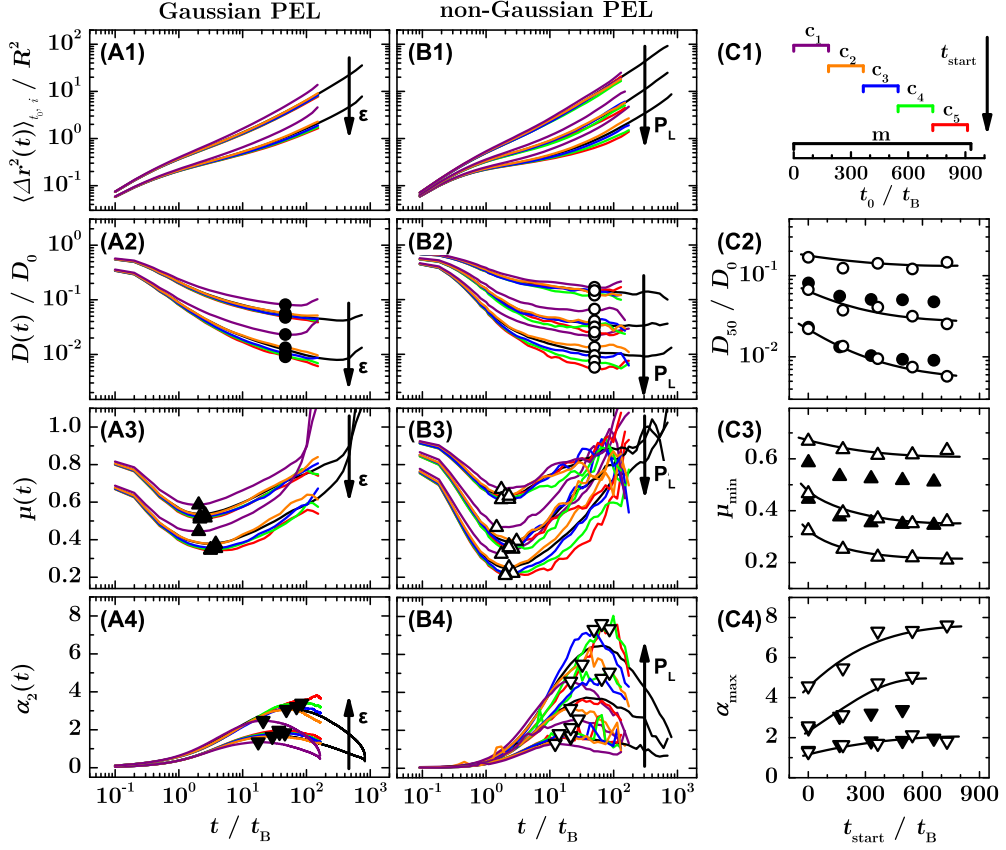


FIG. 5. Particle dynamics in random PEL with Gaussian (A1-A4, MC simulations for $\varepsilon = 3$ and $5 k_B T$) and non-Gaussian roughness (B1-B4, experiments with $P_L = 917, 1640$, and 2600 mW) averaged over the same time interval t_{\max} , but starting at different times t_{start} after the particles have been exposed to the random PEL (as indicated schematically in C1). TEAMSD $\langle \Delta r^2(t) \rangle_{t_0, i}$ (A1, B1), diffusion coefficient $D(t)$ (A2, B2), characteristic slope of the MSD $\mu(t)$ (A3, B3), and non-Gaussian parameter $\alpha_2(t)$ (A4, B4) as a function of lag time t . Characteristic values (marked by symbols in parts A and B), namely the diffusion coefficient at $t/t_B = 50$ (C2), the minimum of $\mu(t)$ (C3), and the maximum of $\alpha_2(t)$ (C4), as a function of the starting time t_{start} .

To illustrate the dynamics in equilibrium, Fig. 6 shows TEAMSDs of particles exposed to the PEL for long but different times t_{start} before the measurement was started, similar as in Fig. 5C1. Within their statistical errors, the TEAMSDs coincide at all times. This suggests that the times t_{start} were long enough for the system to be in or close to equilibrium. In particular, this analysis can serve as a predictor for equilibration in experiments.

To shed more light on how the time- and ensemble averages affect the MSDs, we have performed a single particle trajectory analysis (Fig. 7). Fig. 7A corresponds to the time series c_1 (Fig. 5C1), in which the measurements starts as soon as particles are exposed to the PEL. Time-averaged MSDs of single particle trajectories are

calculated (TAMSDs, thin black lines). The huge spread of TAMSDs indicates the dynamic heterogeneity of the ensemble of particles exploring minima with a biased distribution of depths. The TAMSDs initially increase with time, but those of particles in very deep minima very soon reach plateaux, which extend to the end of the measurement time with $\langle \Delta r^2(t) \rangle_{t_0} \approx 0.1R^2$. The TAMSDs of particles in shallower minima exhibit larger plateau values. Particles might even escape the minima, diffusing into the next ones, and hence the corresponding TAMSDs show diffusive behavior at late times. Particles only experiencing very shallow minima have TAMSDs which only slightly differ from free diffusion. The TAMSDs of the whole ensemble are averaged to yield the time and

3.5 Paper V: Time- and ensemble-averages in evolving systems: the case of Brownian particles in random potentials

8

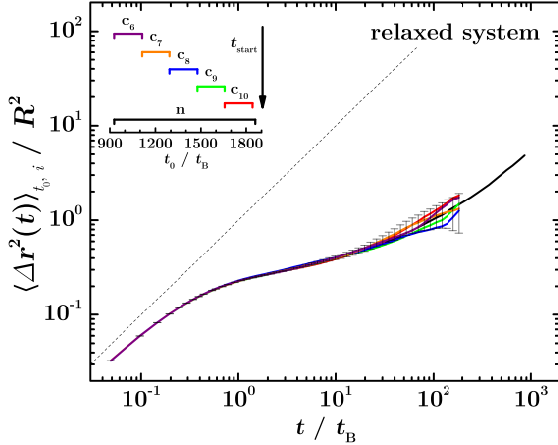


FIG. 6. TEAMSDs $\langle \Delta r^2(t) \rangle_{t_0, i}$ as a function of lag time t of particles in a random PEL with a non-Gaussian roughness (experiments with $P_L = 1640$ mW), averaged over the same time interval but starting at different times t_{start} that are all long compared to the relaxation time τ of the system (as indicated in the inset).

ensemble-averaged MSD (TEAMSD, thick magenta line)

In addition, we include the EAMSD $\langle \Delta r^2(t) \rangle_i$, which are not averaged over waiting times (thick yellow line). The EAMSD is much larger at intermediate times than the TEAMSD. While time-averaged MSDs are highly nonlocal in time, due to the contributions from different times during the temporal evolution of the system, the (only) EAMSD is local in time. Thus, the EAMSD is larger, because some particles are not (yet) trapped at a specific time. The observed difference between EAMSD ($t_0 = 0$) and TEAMSD indicates that the system is far from being equilibrated.

At a later time in the course of the experiment (Fig. 7B), which corresponds to time series c_5 (Fig. 5C1), more particles are trapped in local minima. Thus, their TAMSDs exhibit plateaux. EAMSD ($t_0 = 0$) and TEAMSD coincide at short and intermediate times and slightly deviate at long times. This indicates that the system is almost in equilibrium. If the whole measurement time is taken into account (Fig. 7C), which corresponds to time series m (Fig. 5C1), the impact of the relaxation is still strong, leading to a marked difference between EAMSD ($t_0 = 0$) and TEAMSD, similar to Fig. 7A. In Fig. 7D, trajectories of the relaxed system (Fig. 6, time series n) are shown. The dynamics of most particles is slowed down by local minima, leading to plateaux in their TAMSDs at intermediate and long times. Only few particles explore very shallow minima so that their TAMSDs are only slightly different from free diffusion. In particular, their dynamics becomes diffusive at long times, but with a reduced diffusion coefficient. For the relaxed system, EAMSD ($t_0 = 0$) and TEAMSD coin-

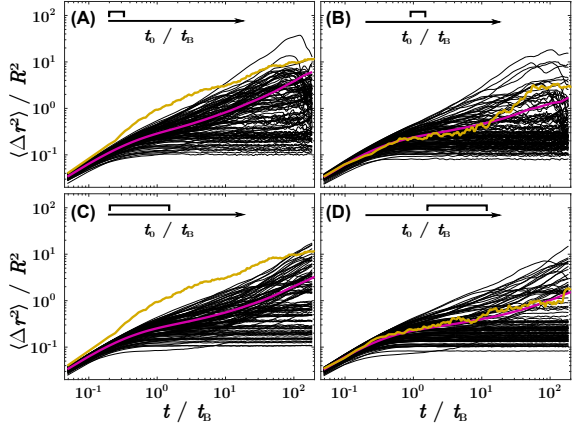


FIG. 7. Single particle dynamics in a random PEL with non-Gaussian roughness (experiments with $P_L = 1640$ mW) with different measurement periods (as indicated). TAMSDs $\langle \Delta r^2(t) \rangle_{t_0, i}$ (black lines), TEAMSDs $\langle \Delta r^2(t) \rangle_{t_0, i}$ (thick magenta lines), and EAMSDs $\langle \Delta r^2(t) \rangle_i$ with waiting time $t_0 = 0$ (thick yellow lines). Time series (A) c_1 (Fig. 5C1); (B) c_5 (Fig. 5C1); (C) m (Fig. 5C1); (D) n (Fig. 6).

cide at all times. If statistics allows for a good enough EAMSD, which is not averaged over waiting times, this can be compared to the TEAMSD. Their similarity then indicates the level of equilibration. Yet, at intermediate and large times, most single trajectory TAMSDs deviate from both the EAMSD and the TEAMSDs, reflecting the dynamic heterogeneity in the random PEL.

IV. CONCLUSION

We studied the effects of time- and ensemble-averaging on quantities characterizing the particle dynamics in random PELs. Initially the particles were homogeneously distributed, but the occupancy of energy values evolved towards its equilibrium distribution. The relaxation of the particle ensemble towards equilibrium becomes manifest in a reduction of the time-averaged MSD and diffusion coefficient with waiting time since deeper minima are increasingly populated. The effects are stronger in non-Gaussian random PELs and increase with the standard deviation of the potential, ε . Hence, the evolution of time-averaged quantities reflects the relaxation of the ensemble and can indicate the approach towards equilibrium and when it is reached. They correspond very well with the evolution of the mean occupied energy value. Moreover, single particle trajectory analysis reveals a marked spread, indicating dynamic heterogeneity due to the distribution of the depths of the potential minima. The results of this work are relevant for single particle tracking analysis and interpretation in general.

ACKNOWLEDGEMENT

We thank Michael Schmiedeberg (Erlangen, Germany), Hartmut Löwen (Düsseldorf, Germany) and Ralf Metzler (Potsdam, Germany) for very helpful discussions. We gratefully acknowledge support by the Deutsche Forschungsgemeinschaft (DFG) through the Research Unit FOR1394 (Projects P2, P4).

- ¹I. M. Sokolov, *Soft Matter* **8**, 9043 (2012).
- ²R. Metzler, J.-H. Jeon, A. G. Cherstvy, and E. Barkai, *Phys. Chem. Chem. Phys.* **16**, 24128 (2014).
- ³Y. Meroz and I. M. Sokolov, *Phys. Rep.* **573**, 1 (2015), a toolbox for determining subdiffusive mechanisms.
- ⁴M. Weiss, M. Elsner, F. Kartberg, and T. Nilsson, *Biophys. J.* **87**, 3518 (2004).
- ⁵F. Höfling and T. Franosch, *Rep. Prog. Phys.* **76**, 046602 (2013).
- ⁶M. Javanainen, H. Hammaren, L. Monticelli, J.-H. Jeon, M. S. Miettinen, H. Martinez-Seara, R. Metzler, and I. Vattulainen, *Faraday Discuss.* **161**, 397 (2013).
- ⁷K. S. Schweizer, *Curr. Opin. Coll. Interf. Sci.* **12**, 297 (2007).
- ⁸G. L. Hunter and E. R. Weeks, *Rep. Prog. Phys.* **75**, 066501 (2012).
- ⁹A. Heuer, *J. Phys.: Condens. Matter* **20**, 373101 (2008).
- ¹⁰F. Höfling, T. Franosch, and E. Frey, *Phys. Rev. Lett.* **96**, 165901 (2006).
- ¹¹J.-P. Bouchaud and A. Georges, *Phys. Rep.* **195**, 127 (1990).
- ¹²P. G. Wolynes, *Acc. Chem. Res.* **25**, 513 (1992).
- ¹³F. Sciortino, *J. Stat. Mech.: Theory Exp.*, P05015 (2005).
- ¹⁴D. S. Dean, I. T. Drummond, and R. R. Horgan, *J. Stat. Mech.: Theory Exp.*, P07013 (2007).
- ¹⁵F. Evers, R. D. L. Hanes, C. Zunke, R. F. Capellmann, J. Bewerunge, C. Dalle-Ferrier, M. C. Jenkins, I. Ladadwa, A. Heuer, R. Castañeda Priego, and S. U. Egelhaaf, *Eur. Phys. J. Special Topics* **222**, 2995 (2013).
- ¹⁶M. J. Saxton and K. Jacobson, *Annu. Rev. Biophys. Biomol. Struct.* **26**, 373 (1997).
- ¹⁷X. Michalet, *Phys. Rev. E* **82**, 041914 (2010).
- ¹⁸S. Burov, J.-H. Jeon, R. Metzler, and E. Barkai, *Phys. Chem. Chem. Phys.* **13**, 1800 (2011).
- ¹⁹D. Ernst and J. Köhler, *Phys. Chem. Chem. Phys.* **15**, 845 (2013).
- ²⁰A. Lubelski, I. M. Sokolov, and J. Klafter, *Phys. Rev. Lett.* **100**, 250602 (2008).
- ²¹R. E. Courtland and E. R. Weeks, *J. Phys.: Condens. Mat.* **15**, S359 (2003).
- ²²T. Uneyama, T. Miyaguchi, and T. Akimoto, *Phys. Rev. E* **92**, 032140 (2015).
- ²³D. Ernst, M. Hellmann, J. Köhler, and M. Weiss, *Soft Matter* **8**, 4886 (2012).
- ²⁴D. Ernst, J. Köhler, and M. Weiss, *Phys. Chem. Chem. Phys.* **16**, 7686 (2014).
- ²⁵C. Manzo, J. A. Torreno-Pina, P. Massignan, G. J. Lapeyre, M. Lewenstein, and M. F. Garcia Parajo, *Phys. Rev. X* **5**, 011021 (2015).
- ²⁶Q.-H. Wei, C. Bechinger, and P. Leiderer, *Science* **287**, 625 (2000).
- ²⁷C. Dalle-Ferrier, M. Krüger, R. D. L. Hanes, S. Walta, M. C. Jenkins, and S. U. Egelhaaf, *Soft Matter* **7**, 2064 (2011).
- ²⁸T. O. E. Skinner, S. K. Schnyder, D. G. A. L. Aarts, J. Horbach, and R. P. A. Dullens, *Phys. Rev. Lett.* **111**, 128301 (2013).
- ²⁹X.-g. Ma, P.-Y. Lai, and P. Tong, *Soft Matter* **9**, 8826 (2013).
- ³⁰G. Volpe, G. Volpe, and S. Gigan, *Sci. Rep.* **4**, 3936 (2014).
- ³¹X.-g. Ma, P.-Y. Lai, B. J. Ackerson, and P. Tong, *Soft Matter* **11**, 1182 (2015).
- ³²J. Sancho and A. Lacasta, *Eur. Phys. J. Special Topics* **187**, 49 (2010).
- ³³R. D. L. Hanes and S. U. Egelhaaf, *J. Phys.: Condens. Matter* **24**, 464116 (2012).
- ³⁴C. Emary, R. Gernert, and S. H. L. Klapp, *Phys. Rev. E* **86**, 061135 (2012).
- ³⁵E. C. Euán-Díaz, V. R. Misko, F. M. Peeters, S. Herrera-Velarde, and R. Castañeda Priego, *Phys. Rev. E* **86**, 031123 (2012).
- ³⁶M. Suñé Simon, J. M. Sancho, and K. Lindenberg, *Phys. Rev. E* **88**, 062105 (2013).
- ³⁷R. Gernert, C. Emary, and S. H. L. Klapp, *Phys. Rev. E* **90**, 062115 (2014).
- ³⁸M. C. Jenkins and S. U. Egelhaaf, *J. Phys.: Condens. Matter* **20**, 404220 (2008).
- ³⁹R. D. L. Hanes, C. Dalle-Ferrier, M. Schmiedeberg, M. C. Jenkins, and S. U. Egelhaaf, *Soft Matter* **109**, 2714 (2012).
- ⁴⁰F. Evers, C. Zunke, R. D. L. Hanes, J. Bewerunge, I. Ladadwa, A. Heuer, and S. U. Egelhaaf, *Phys. Rev. E* **88**, 022125 (2013).
- ⁴¹M. Schmiedeberg, J. Roth, and H. Stark, *Eur. Phys. J. E* **24**, 367 (2007).
- ⁴²R. D. L. Hanes, M. Schmiedeberg, and S. U. Egelhaaf, *Phys. Rev. E* **88**, 062133 (2013).
- ⁴³J. C. Crocker and D. G. Grier, *J. Colloid Interface Sci.* **179**, 298 (1996).
- ⁴⁴M. C. Jenkins and S. U. Egelhaaf, *Adv. Colloid Interface Sci.* **136**, 65 (2008).
- ⁴⁵T. R. M. Sales, *Adv. Opt. Techn.* **1**, 127 (2012).
- ⁴⁶J. Bewerunge and S. U. Egelhaaf, *Phys. Rev. A* **93**, 013806 (2016).
- ⁴⁷D. S. Dean, I. T. Drummond, and R. R. Horgan, *J. Phys. A: Math. Gen.* **30**, 385 (1997).
- ⁴⁸D. S. Dean, I. T. Drummond, and R. R. Horgan, *J. Phys. A: Math. Gen.* **37**, 2039 (2004).
- ⁴⁹C. Touya and D. S. Dean, *J. Phys. A: Math. Theor.* **40**, 919 (2007).

3.5 Paper V: Time- and ensemble-averages in evolving systems: the case of Brownian particles in random potentials

This page has been left intentionally blank.

3.6 Paper VI: Anomalous Colloidal Diffusion: Interplay of Crowding and an External Random Potential

Journal: Physical Review Letters / Physical Review E

Reference: To be submitted

Impact factor: 7.512 / 2.288

Authors: **Jörg Bewerunge**, Christoph Zunke, Stella Glöckner, Florian Platten and Stefan U. Egelhaaf

1st author

JB and SG carried out the measurements and JB analysed the data. JB, CZ, FP and SUE conceived the project, discussed the results and contributed to their interpretation. All authors contributed to the manuscript.

This manuscript is planned to be split up into two publications.

75% contribution of JB

3.6 Paper VI: Anomalous Colloidal Diffusion: Interplay of Crowding and an External Random Potential

This page has been left intentionally blank.

Anomalous Colloidal Diffusion: Interplay of Crowding and an External Random Potential

Jörg Bewerunge,¹ Christoph Zunke,¹ Stella Glöckner,¹ Florian Platten,¹ and Stefan U. Egelhaaf¹

¹*Condensed Matter Physics Laboratory, Heinrich Heine University, 40225 Düsseldorf, Germany*

(Dated: July 8, 2016)

Anomalous diffusion of colloidal particles can be observed studying disordered media or crowded environments, such as biological cells or cell membranes. It is often caused by interactions of the species under investigation with its (micro-)environment, for example adsorption sites or concentration gradients. The term anomalous diffusion usually is used to describe particle dynamics with a mean-squared displacement $\langle \Delta r^2 \rangle$ that is not proportional to the time t and/or non Gaussian statistics. With recent studies about the unexpected diffusive behaviour found in experiments, especially when applying single-molecule and single-particle tracking methods to biological samples, anomalous diffusion analysis gathered new interest. Yet, it is hard to analyse the mechanisms underlying species motion in crowded systems, e.g. biological cells, by simple diffusion models.

In this work, we investigate the dynamics of Brownian particles exposed to a random potential energy landscape (rPEL) as a function of particle concentration in order to shed light on the variety of diffusion phenomena occurring in crowded systems. We are thus able to study and disentangle the mutual effects of particle-particle and particle-potential interactions on the colloidal dynamics. The particle-potential interactions are caused by a random laser speckle intensity pattern that forces colloids to move to and stay in high intensity regions, which correspond to valleys in the resulting Gamma-distributed random potential energy landscape (rPEL). Particle-particle interactions are essentially determined by the particle concentration. As a result, obstacles, namely trapped particles, hinder the motion of diffusing ones, thus leading to a sub-diffusive regime, whereby the probability of obstacles becoming diffusive or particles trapped is mainly given by the characteristics of the potential energy landscape. Increasing laser power, that is potential strength, leads to a stronger trapping and therefore further immobilization of the trapped particle fraction. Furthermore, the likelihood of a particle to overcome the potential energy barrier, leaving a trap, and to get diffusive is decreased. In this work the short- and long-term colloidal dynamics are separately studied to reveal the mechanisms underlying the two counteracting effects. Thus, a critical concentration is identified, in which both effects cancel out each other, resulting in a re-entrant regime of the short-term diffusion coefficient D_s .

PACS numbers: 05.20.Jj, 05.40.*, 42.30.Ms, 47.57.J-, 64.70.pv, 82.70.Dd

I. INTRODUCTION

Recently anomalous diffusion, i.e. particle dynamics with a mean-squared displacement $\langle \Delta r^2 \rangle$ that is not proportional to the time t and/or non Gaussian statistics, has been gathered new interest [1–15]. This was initiated by the attempt to explain the unexpected diffusive behaviour found in experiments, especially when applying single-molecule and single-particle tracking methods to biological samples, such as cells and their membranes [6–8, 16, 17], biofilms [9] or prototypical crowded fluids, e.g. agarose [18] or dextran [10]. However, the sub-diffusive transport, e.g. through disordered media or in crowded environments, is generally of interest [11, 19–21]. The anomalous diffusion of tracer particles in crowded environments is a general scenario, encountered, e.g., by a single species in a biological cell diffusing in the presence of a zoo of different other species. The anomalous behavior is usually affected by a bunch of parameters, such as the concentrations of each species, the overall concentration within the cell, the size of the cell, its membrane stiffness and, very important, the inter-particle interactions [6–10, 13, 16–18]. The complex interplay of these parameters can even lead to counter-intuitive situations,

in which, e.g. intermediate diffusion in a crowded environment is speeded up (in contrast to the expected slowing down) [12]. Moreover, sub-diffusion can even decrease the time until a species finds one of its favourable spots or targets (e.g. special absorption or reaction sites in cells, on cell membranes or DNA) [22]. Anomalous diffusion has been intensively studied in experiments and in theory with special emphasis on dense [23, 24] or glassy systems [19, 25, 26] and disordered or porous media [2, 3, 27, 28]. In particular, theoretical approaches include Monte Carlo simulations [3, 27, 29] and lattice models [30], Brownian dynamics [14, 31], molecular dynamics simulations [2, 32, 33] and Mode-Coupling Theory [15, 25, 28]. As illustrated above, anomalous diffusion can occur in various situations. Therefore, many different models have been devised to analyze these scenarios [11, 13], including, among others, fractional Brownian motion [10], continuous-time random walk [11] and percolation models, such as obstructed diffusion [2–5, 30, 34]. The first, fractional Brownian motion, is basically a random walk model with a memory kernel, i.e. the increments of this process are anti-correlated in the case of sub-diffusion. Thus, this is a good model to characterize diffusion in viscoelastic media [10]. The continuous-time

3.6 Paper VI: Anomalous Colloidal Diffusion: Interplay of Crowding and an External Random Potential

2

random walk in turn consists of freely diffusing particles with power-law distributed waiting times between jumps, where ageing effects take place, such as weak-ergodicity breaking [11, 13], and hence differences between single particle- and ensemble-analysis should be considered. Moreover, the obstructed diffusion model is best characterized by randomly distributed (im)mobile obstacles hindering the particle diffusion. Depending on the obstacle concentration, particles can, above the percolation threshold, even be forced to diffuse in fractal-like sub-areas. Furthermore, non-Gaussian statistics seem to be relevant for understanding the mechanisms underlying anomalous diffusion [14].

So far, species motion in crowded systems, e.g. biological cells, can usually not be explained with single simple diffusion models, as e.g. excluded volume, and hence is not well understood. It is caused by various interactions of the species with its environment, e.g., amongst others, adsorption mechanisms, osmotic gradients and chemotaxis, and results in an underlying potential energy landscape (PEL) influencing the diffusion process. Thus, in this work, we shed light on the variety of diffusion phenomena occurring from the intersection of both crowding (high concentrations) and the amplitude of an underlying random potential with the help of our colloidal model system. Furthermore, we mimic both mobile obstacles and the diffusing species with identical colloidal particles. The particle-potential interactions are caused by a random laser speckle intensity pattern that forces colloids to move to and stay in high intensity regions, which correspond to valleys in the resulting Gamma-distributed random potential energy landscape (rPEL). Thus, each laser speckle can be approximated by a single optical trap with a random height distribution, while the characteristic width ϵ of the resulting potential distribution, i.e. the ‘(mean) potential strength’, is proportional to the laser power [35].

In order to systematically analyse particle dynamics in rPELs, we introduce a “state diagram”, in which particle concentration (area fraction ϕ_A) and mean roughness of the potential (laser power P_L) are used to characterize the different situations investigated (fig. 1). We focus on constant laser power P_L (indicated by lines L1-L3) or constant area fraction ϕ_A (indicated by lines C1-C3). At selected points of the state diagram, schematic illustrations of the rPELs are shown. Particle concentrations ($\phi_A \leq 0.65$) within the liquid phase are chosen to study the effects of particle-particle interactions on the dynamics.

This work is structured as follows. In section II we describe the sample preparation and experimental setup. Moreover, we introduce different measures, which are used to characterise anomalous diffusion in section III. We first investigate the influence of concentration and potential on ensemble- and time-averaged measures (section III A). Then, we analyse the underlying mechanisms via displacement distribution and single-trajectory analysis (section III B). Finally, the P_L - ϕ_A -dependence of the

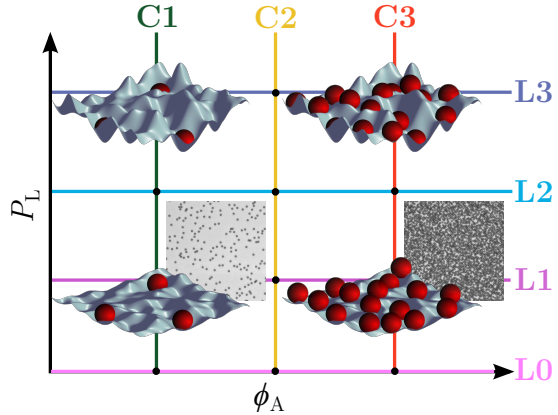


FIG. 1. ‘State diagram’, laser power P_L (mean of the rPEL roughness ϵ) vs. particle concentration ϕ_A , illustrating the different scenarios studied in this work. The effect of increasing particle concentration is studied at four different values of the laser power P_L (indicated by lines L0-L4). We focus on three different concentrations (lines C1-C3), but additional measurements viewing a broader range of concentrations have been performed at selected laser power (not indicated). Schematic illustrations are shown at selected positions in the state diagram. Furthermore, recorded images of typical samples at concentrations C1 and C3 are shown.

short-term and long-term diffusion coefficients are discussed in detail and possible interdependencies are identified.

II. MATERIALS AND METHODS

A. Sample Preparation

Samples consist of spherical polystyrene particles (Interfacial Dynamics Corporation radius $R = 1.4 \mu\text{m}$ and polydispersity 3.2%) dispersed in purified water (ELGA purelab flex, electrical resistivity $\rho = 18.2 \times 10^4 \Omega\text{m}$) and are prepared in self-made glass microscopy cells [36]. Three glass cover slips and a microscope slide (VWR) are assembled to form a small capillary and closed with uv-glue (Norland). Due to the density difference between particles and the surrounding medium, particles are forced to sediment building a (quasi) two-dimensional layer. The particle concentration of this layer is given by the particle area fraction $\phi_A = \pi N R^2 / A$ with the number of particles N in the field of view with area A .

B. Optical Microscopy

The particle positions and their movements are examined with an inverted microscope (Nikon, Eclipse Ti-U) and a 20 \times objective (Nikon, CFI S Plan Fluor ELWD,

numerical aperture $NA = 0.45$) while images of time-series were recorded by a CCD camera (AVT, Pike F-032B with 640×480 pixels and pixel pitch $pp_x = pp_y = 0.372 \mu\text{m px}^{-1}$). Figure 1 shows typical images with a quadratic field of view of $460 \times 460 \text{ px}^2 = 171 \times 171 \mu\text{m}^2$. For every measurement about 27000 images at a frame rate of 3.75 fps are recorded. Furthermore, position determination and subsequent trajectory analysis were carried out using particle tracking routines in IDL [37].

C. Random Potential Energy Landscape

The particles were exposed to a random potential energy landscape, which was realized with an optical set-up based on laser light (Laser Quantum, Opus 532, wavelength $\lambda = 532 \text{ nm}$, maximum laser power $P_{L,\text{max}} = 2.6 \text{ W}$) shaped with a special diffuser (RPC Photonics, Engineered Diffuser EDC- 1-A-1r.) [38, 39]. In this way, it is possible to imprint a macroscopically flat (top-hat intensity distribution) but microscopically rough (laser speckles on the particle length scale) intensity landscape on the sample plane. The experiments described in this work were performed at fixed conditions of the optical set-up ('BE 5x' in [39]): Parameters characterizing the speckle patterns are the ratio of the beam area to the mean microlens area, $A_b/A_l = 44100$ where $A_l \approx 2000 \mu\text{m}^2$, speckle contrast $c = 1.05$, and speckle area $A_S = 5.1 \mu\text{m}^2$. Parameters characterizing the speckle patterns convolved with the weight function of a spherical particle with radius $R = 1.4 \mu\text{m}$ and thus effective particle area $A_m = 5.5 \mu\text{m}^2$, i.e. parameters characterizing the rPEL, are the ratio of the effective particle area to the speckle area $A_m^{\text{eff}}/A_S = 1.07$, correlation parameter $M = 2.6$ and correlation area of the potential $A_S^U = 11.8 \mu\text{m}^2$.

Since the particles' refractive index is different from the one of the surrounding medium, the particles interact with the intensity speckle pattern via optical forces, namely the laser pressure and locally induced optical gradient forces [40–42]. It results in a potential energy landscape felt by the diffusing particles with the spatial correlations and energy level distribution mainly determined by the properties of the underlying intensity landscape and the particle radius. A detailed analysis of the experimental creation of rPELs is given in [39]. Consequently, the spatial correlation function C_U of the potential for particles with $R = 1.4 \mu\text{m}$ used here, is well-described by a Gaussian distribution with $1/e$ -width $\sigma_{C_U} = 1.38R$. It can be used as a measure for the spatial extent of the potential minima [39]. Furthermore, the intensity distribution of the speckle pattern $p(U)$ follows a Gamma distribution

$$p(U) = \frac{1}{\Gamma(M)} \left(\frac{M}{U}\right)^M I_D^{M-1} \exp\left(-\frac{M}{U}U\right),$$

where Γ is the Gamma function and $M = 2.6$. Thus, the

particles, which would freely diffuse in the absence of a laser speckle pattern, experience a rPEL. So far, much work focussed on Gaussian roughness ($M \gg 1$), while rugged energy landscapes are much more common.

D. Quantifying Anomalous Colloidal Diffusion

Particle diffusion is strongly affected by the presence of a rPEL and its statistical properties [35, 43]. The most direct approach of characterizing colloidal diffusion is to look at the first moment of the particle displacements $\langle \Delta x(t) \rangle_{t_0,i} = \langle [\mathbf{x}_i(t+t_0) - \mathbf{x}_i(t_0)] \rangle_{t_0,i}$ (or $\langle \Delta \mathbf{r}(t) \rangle_{t_0,i}$ in two dimensions), whereby the average $\langle \dots \rangle$ can be executed over either all particles i at positions \mathbf{x} (\mathbf{r} in $2d$) of the ensemble, all waiting times t_0 , or both. Ensemble averaged displacements represent a good measure for the analysis of direct temporal influences on, e.g., an ageing sample. Waiting time-averaged displacements correspond to single-trajectory analysis and, used in heterogeneous systems, therefore show scattering in the particle dynamics, i.e. deviations between single particle movements [6, 11]. However, for the case of a large field of view and long measurement times, ensemble and time average should be statistically equivalent if the sample is ergodic. Since experiments are often limited in either particle number or measurement time, both temporal and ensemble averaging is frequently preferred for the sake of good statistics. We use both ensemble and time averaging unless stated otherwise. Since $\langle \Delta \mathbf{r}(t) \rangle = \langle \Delta x(t) \rangle = \langle \Delta y(t) \rangle = 0$ for isotropic Brownian motion, particle dynamics is studied in terms of the displacement probability $G(\mathbf{r}, t)$, the so called van Hove function, and higher moments, e.g., the mean-squared displacement (MSD) $\langle \Delta r^2(t) \rangle$.

Analysis of the probability to find a particle at time t at the position \mathbf{r} , provided that there was a particle at the origin of the coordinate system at the time $t = 0$, leads to the so called van Hove correlation function [44–46]

$$\begin{aligned} G(\mathbf{r}, t) &= \left\langle \frac{1}{N} \sum_{i=1}^N \sum_{j=1}^N \delta[\mathbf{r} + \mathbf{r}_j(0) - \mathbf{r}_i(t)] \right\rangle \quad (1) \\ &= \frac{1}{N} \left\langle \sum_{i=1}^N \delta[\mathbf{r} + \mathbf{r}_i(0) - \mathbf{r}_i(t)] \right\rangle \\ &\quad + \frac{1}{N} \left\langle \sum_{i \neq j}^N \delta[\mathbf{r} + \mathbf{r}_j(0) - \mathbf{r}_i(t)] \right\rangle \\ &= G_s(\mathbf{r}, t) + G_d(\mathbf{r}, t), \quad (2) \end{aligned}$$

with the number of particles N , and the Dirac delta function $\delta[\dots]$. Here, G_s and G_d are the self- and distinct-part of the van Hove function, describing the mean distance a particle, starting at the origin at time $t = 0$, has moved at time t and the movements of the other particles, respectively. The self-part G_s describes the distance that a particle starting at the origin has moved at the time t .

3.6 Paper VI: Anomalous Colloidal Diffusion: Interplay of Crowding and an External Random Potential

4

G_s is also referred to as the probability density function of the mean displacements $p(\Delta r, t)$. For free diffusion in two dimensions, motions in x - and y -direction are independent from each other and hence $p(\Delta r, t)$ can be calculated from the van Hove self-part probability histogram via

$$p(\Delta r, t) = 2\pi\Delta r G_s(\Delta r, t) \quad (3)$$

$$= \frac{N(\Delta r, t)}{\left(\sum_{i=1}^N N(\Delta r, t)\right) w},$$

where $N(\Delta r, t)$ is the displacement counter, and w the histogram bin width. It is well characterised by a Rayleigh distribution

$$p(\Delta r, t) = \frac{\Delta r(t)}{R\sigma^2} \cdot e^{-(\Delta r(t))^2/2R^2\sigma^2}, \quad (4)$$

with the radius of the particles R and mode σ .

The mean-squared displacement (MSD) in two dimensions is given by

$$\langle \Delta r^2(t) \rangle = \langle \Delta x^2(t) \rangle + \langle \Delta y^2(t) \rangle = 4D_0t, \quad (5)$$

where D_0 is the self-diffusion coefficient for particles freely diffusing on a surface, resulting in the characteristic time $t_B = R^2/4D_0$. Furthermore, the relation $\langle \Delta x^2(t) \rangle = \langle [\mathbf{x}_i(t) - \mathbf{x}_i(0)]^2 \rangle - \langle [\mathbf{x}_i(t) - \mathbf{x}_i(0)] \rangle^2$ was used, where the second term corrects for possible drifts in the trajectories.

If the particle motion is influenced by the concentration and/or a potential landscape, one encounters ‘anomalous’ diffusion, and eq. (5) becomes

$$\langle \Delta r^2(t) \rangle \propto t^\mu \quad (6)$$

with the diffusive exponent μ . This implies the time dependence of μ can be calculated from

$$\mu(t) = \frac{\partial}{\partial \log(t)} \log(\langle \Delta r^2(t) \rangle), \quad (7)$$

and thus sub-diffusion, i.e. particles hindered in their motion, is indicated by $\mu(t) < 1$. In sections III A 1 and III A 2 the influence of particle concentration and potential depth on the diffusive exponent $\mu(t)$ are analysed in detail.

Moreover, following eq. (5) a time-dependent diffusion coefficient $D(t)$ can be calculated

$$D(t) = \frac{1}{2d} \frac{\partial}{\partial t} \langle \Delta r^2(t) \rangle \quad (8)$$

with dimension d . Furthermore, one can calculate the limits of very short $D_s = \lim_{t \rightarrow 0} D(t)/D_0$ and long times $D_{\text{long}} = \lim_{t \rightarrow \infty} D(t)/D_0$. However, caused by finite camera frame rate and measurement time T , these limits are not accessible in experiment. Therefore we estimate the

short-time diffusion coefficient by fitting a linear function to the experimentally measured mean-squared displacement with $t \leq 3$ s, so that its slope gives $D_s = D(t \leq 3 \text{ s})$. The chosen time is a compromise between looking at very short times, where particles presumably do not interact with the landscape, and a fit adequate number of measurement points (≥ 10), and mostly depends on the camera frame rate (usually 3.75 fps). The experimental long-time diffusion coefficient was defined as $D_{\text{long}} = (D_{\text{min}}(t))/D_0$. In the (sub-)diffusive regime $D(t)$ is, apart from by the time-averaging caused statistical uncertainties at $t \approx T$, a monotonically decreasing function for all lag times t until it reaches a plateau, when the diffusive regime is reached. Thus we can estimate the long-time diffusion coefficient as the minimal value $D_{\text{min}}(t)$. In particular, we study the limits of short times D_s and long times D_{long} in sections III A and III C.

We take the next higher non-zero moment of the displacement distribution $\langle \Delta r^4(t) \rangle$ into account to calculate the non-Gaussian parameter α_2 as

$$\alpha_2(t) = \frac{\langle \Delta r^4(t) \rangle}{\left(1 + \frac{2}{d}\right) \langle \Delta r^2(t) \rangle^2} - 1. \quad (9)$$

Therefore, the non-Gaussian parameter α_2 is related to the excess kurtosis of the displacement distribution, that is the deviation of the shape of the measured distribution from a perfect Gaussian. The mean-squared displacement $\langle \Delta r^2(t) \rangle$, that can be identified as the variance, and the non-Gaussian parameter $\alpha_2(t)$, thus describe the shape and alteration of the displacement distribution (eq. (3)) over time.

III. RESULTS AND DISCUSSION

First, the interplay of crowding and random potential is studied (section III A) by examination of the individual influences of both laser power (section III A 1) and particle concentration (section III A 2) on the dynamics. Subsequently, underlying mechanisms that govern particle dynamics are identified by analysis of the displacement distribution $p(\Delta r, t)$ (section III B 1) and single-particle trajectories (section III B 2). In the third part of the results (section III C), short- and long-term dynamics are further investigated with focus on the P_L - ϕ_A state diagram. We study the effect of particle concentration at fixed laser power (horizontal lines in fig. 1) and the effect of laser power at fixed particle concentration (vertical lines in fig. 1). In the following, L0, L1, L2 and L3 refer to different laser power P_L and C1, C2 and C3 refer to different area fractions ϕ_A , as further described in table I.

A. Interplay of Crowding and Random Potential

In this section, we will analyse the concurrent effects of crowding and random potential on particle dynamics.

TABLE I. Terms and colors used to indicate different laser power and particle concentration regimes (cf. fig. 1).

term	laser power P_L (mW)	area fraction ϕ_A	line/symbol color
L0	0		pink
L1	917		purple
L2	1640		light blue
L3	2600		dark blue
C1		0.05	green
C2		0.25	orange
C3		0.45	red

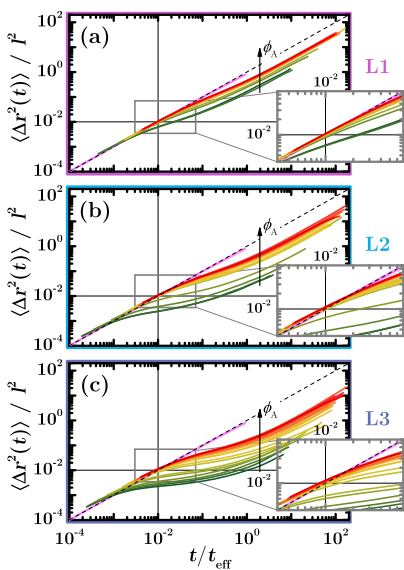


FIG. 2. Free volume scaling: Mean-squared displacement scaled with the particles' effective mean free path, $\langle \Delta r^2(t) \rangle / l^2$, as a function of the scaled time t/t_{eff} with $l^2 = \pi R^2 / \phi_A$ and $t_{\text{eff}} = \pi t_B / \phi_A$ at fixed laser power L1, L2 and L3, (a) to (c). Colored lines indicate low to high area fractions ϕ_A (from dark green to dark red). Black vertical and horizontal lines indicate the transition point $\sqrt{\langle \Delta r^2(t) \rangle} = 0.1l$ and its corresponding time, respectively.

Figure 2 shows the time-dependent mean-squared displacements $\langle \Delta r^2(t) \rangle$ for three laser powers L1-L3 and various concentrations. The MSD is scaled with the concentration dependent particles' effective mean free path $\langle \Delta r^2(t) \rangle / l^2$ as a function of the dimensionless time t/t_{eff} with $l^2 = \pi R^2 / \phi_A$ and $t_{\text{eff}} = \pi t_B / \phi_A$ [15]. We observe two general trends: First, as expected for Brownian motion, the mean-squared displacement for a dilute sample in the absence of an external potential (C1L0, pink line) is proportional to the time t . Second, all measurements that were done in a rough potential, independent of the potential strength or particle concentration, show

clear signs of sub-diffusive systems [1]: an initial short-term diffusive regime, followed by an intermediate sub-diffusive regime that again turns to diffusive behaviour for long times.

Considering the concentration influence on the dynamics, fig. 2 (a) shows that after scaling with l^2 , all mean-squared displacement lines, apart from the one showing the normal diffusion (C1L0, pink line) and the one for a rough potential but lowest concentration (dark green line), almost fall on top of each other. The scaling collapse indicates that, for the conditions studied, the short- and long-time diffusion coefficient are influenced by the available free volume accessible for the particles. Furthermore, we observe a transition from the diffusive to a sub-diffusive regime for displacements larger than about 10% of the mean free path l ($\sqrt{\langle \Delta r^2(t) \rangle} = 0.1l$, indicated by horizontal line in fig. 2). Thus it is consistent with a Lindemann-like criterion found in earlier studies of crowded colloidal systems [15, 47] and related to intra-cage dynamics in dense systems indicating cooperative dynamics. This can be interpreted as a clear signature of the dynamics being governed by the free volume. Short-term dynamics essentially depend on the particle area fraction via indirect hydrodynamic interactions, while long-time diffusion is better characterized by inter-particle interactions [48], which was also confirmed for the case of dense colloidal motion in a pore [49]. Therefore, hydrodynamic coupling between particles and the sample cell wall [50], possibly amplified by the particles being slightly pushed to the bottom glass slide by laser pressure, might have slight influence on the dynamics [15, 49, 51]. A closer look (inset fig. 2 (a)) reveals that in samples with a low concentration and a weak potential strong sub-diffusion occurs at intermediate and long times. The area fraction dependent scaling approach fails in the presence of a rPEL for the case of low concentrations, caused by the few particles all being trapped in the deepest potential minima. Therefore, the resulting mean-free path of the particles is mostly given by the particle movement within highly separated potential traps and independent of the particle concentration. Moreover, increasing the concentration leads to particles moving more freely (in between potential minima of different heights) and scaling with the area fraction becomes possible again.

In brief, depending on the potential roughness, three regimes can be identified (fig. 2): (a) Weak potentials L1: Scaling of the MSD with the mean free path is possible for all concentrations, but the lowest (dark green lines, correspond to points C1L1 and below in fig. 1); (b) Medium potential strength L2: Strong deviations in the intermediate and long-time diffusion regimes for low concentrations (green lines); (c) Strong potentials L3: Strong deviations in the intermediate and long-time diffusion regime for low to medium concentrations (green (inter alia C1L3) to dark yellow (C2L3) lines). Additionally, small deviations to the free diffusion case (pink, C1L0) occur at this laser power regardless of the concentration in the short-term regime.

3.6 Paper VI: Anomalous Colloidal Diffusion: Interplay of Crowding and an External Random Potential

6

We now scale all mean-squared displacements and times with the particle radius R and the Brownian time t_B , if not stated otherwise. Thus we are able to explore the different effects of crowding and the rPEL. We will first discuss the potential strength dependent dynamics (section III A 1) and afterwards the changes in dynamics when we increase the particle concentration (section III A 2).

1. Laser Power Dependent Dynamics

In fig. 3, the dynamics of a dilute solution C1 is studied in the absence of an external potential and as a function of laser power in terms of $\langle \Delta r^2(t) \rangle$ (a), $D(t)$ (b), $\mu(t)$ (c) and $\alpha_2(t)$ (d). Increasing the potential strength at constant concentration leads to sub-diffusive behaviour at intermediate times, which tends to become diffusive at late times. This becomes apparent in a steady decrease of the diffusion coefficient $D(t)$, which exhibits a plateau for long lag times (fig. 3 (b)). In addition, the diffusive exponent, which is a measure for non-Brownian dynamics, is smaller than one for all times ($\mu(t) < 1$) (fig. 3 (c)) and shows a laser power dependent minimum at times around t_B . An indicator for non-Gaussian dynamics is the appearance of a peak in the non-Gaussian parameter $\alpha_2(t)$ (fig. 3 (d)), which occurs in the presence of a rough potential and is most pronounced at the highest potential strength. Similar non-Gaussian sub-diffusive behaviour was already found for rough potential landscapes with a Gaussian potential energy distribution $p(U)$ [35, 43].

Figure 4 shows the normalized short-time diffusion coefficient D_s/D_0 (a), the normalized long-time diffusion coefficient D_{long}/D_0 (b), the minimum value of the diffusion exponent μ_{min} (c) and the maximum value of the non-Gaussian parameter α_{max} (d), as well as the times at which the minimum in μ and the maximum in α are reached, $t_{\mu_{\text{min}}}/t_B$ (e) and $t_{\alpha_{\text{max}}}/t_B$ (f), respectively. They are shown for concentrations C1, C2 and C3 (filled symbols, increasing area fraction accentuated by color gradient from green to red) as a function of the laser power P_L (corresponding to L0, L1, L2 and L3).

Both the short-time diffusion coefficient D_s and the long-time diffusion coefficient D_{long} are reduced with increasing laser power irrespective of the concentration (fig. 4 (a) and (b)). D_s describes the movement of particles for short times and distances (less than their own radius), e.g. the rattling in either potential traps or particle cages, whereas D_{long} is a measure for particles hopping between potential minima or inter-cage dynamics. Furthermore, the dip in the diffusive exponent deepens with laser power (fig. 4 (c)) and the non-Gaussian parameter peak grows with increasing laser power (fig. 4 (d)). A common feature exists in the variation of the last three measured variables. Increasing the concentration from C1 (green) to C3 (red) leads to a reduction of the differences between the values for the different potential strengths, i.e. the potential looses influence on the

particle dynamics.

Polanowski et al. [30] have simulated two-dimensional fluid dynamics in a crowded environment comprising static obstacles via a dynamic lattice liquid model, and thereby analysed anomalous diffusion and the cooperative phenomena occurring in such dense systems as a function of the obstacle concentration. Their simulation results for D_s/D_0 and D_{long}/D_0 , taken from ref. [30], are shown in parts in fig. 4 (a) and (b). They qualitatively resemble trends found in the experiments, at least for low to intermediate laser power. However, we have to emphasize, that we scaled the obstacle concentration to our laser potential arbitrarily (by a constant factor). Therefore, we only discuss basic similarities and discrepancies between the systems and their possible influence on the diffusion coefficients. In general, the dynamic lattice liquid model is based on liquids in which quasi-located particles that usually only vibrate on their lattice sites execute correlated motions with their neighbours, exchanging positions. In the case considered in the simulations, the number of particles is high and constant, while the concentration of pinned colloids (obstacles) is chosen to be between zero and the percolation transition. As a result two species of particles were found with the ‘slow’ particles being located near or in cages of obstacles and the ‘fast’ species far away from these. Comparing this to our experimental system, a similar picture can be found. In the absence of an external potential, all particles diffuse freely. In contrast, when a rough potential is applied, a few particles are trapped in deep potential wells. Their motion is restricted to $\langle \Delta r^2 \rangle \approx 0.1R^2$, and thus they act as quasi-static obstacles. However, most of the particles are not trapped and hence are still diffusing, but their motion is hindered by the (quasi-static) obstacles. Here, we took into account that, even though we usually use a picture of a higher dimensional potential landscape, the particles can only diffuse in two-dimensions, i.e. never overlap, and therefore appear as a barrier in the potential landscape for other particles at their present position. All data sets of both the short-term and the long-term diffusion coefficients D_s and D_{long} , shown in fig. 4 (a) and (b), respectively, decrease monotonically for increasing laser power. However, a difference between simulation and experiment is seen at high laser powers. The divergence of D_{long}/D_0 of the simulations is ascribed to a percolation transition at finite obstacle densities. This is not observed in experiments. Here, the number and spatial arrangement of the (quasi-static) obstacles largely depends on the potential strength and the potential energy distribution $p(U)$, which is static and independent of the laser power.

2. Concentration Dependent Dynamics

In this section, we analyse the effect of particle concentration on the dynamics at intermediate laser powers (fig. 5). Similar trends have been observed at

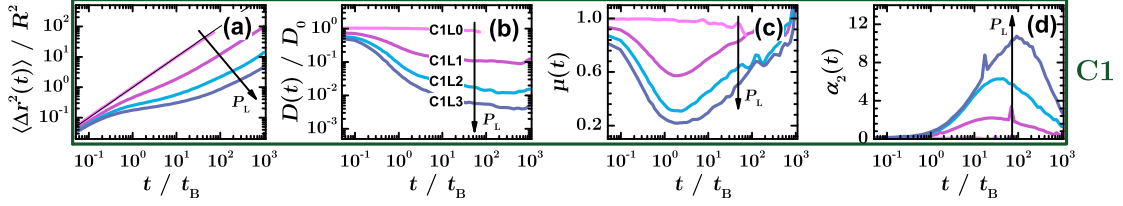


FIG. 3. Laser power dependent dynamics: (a) Time-dependent normalized mean-squared displacement $\langle \Delta r^2(t) \rangle / R^2$, (b) normalized diffusion coefficient $D(t) / D_0$, (c) diffusive exponent $\mu(t)$, and (d) Non-Gaussian parameter $\alpha_2(t)$ for concentration C1 and increasing laser power L0-L3 (colored lines, cf. fig. 1).

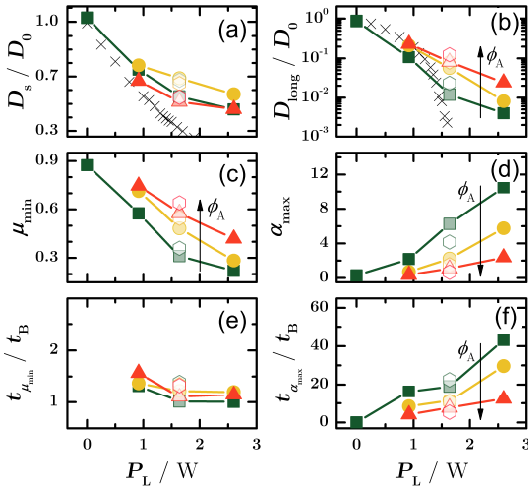


FIG. 4. Laser power dependent extreme values: (a) short-term diffusion coefficient D_s / D_0 , (b) long-term diffusion coefficient D_{long} / D_0 , (c) minimum in the diffusive exponent μ_{min} , (d) maximum in the non-Gaussian parameter α_{max} , (e) time of the minimum of the diffusive exponent $t_{\mu_{\text{min}}} / t_B$, and (f) time of the maximum of the non-Gaussian parameter $t_{\alpha_{\text{max}}} / t_B$ as a function of the laser power P_L , all for C1, C2 and C3, represented by different symbols and colors (dark green squares, dark yellow circles and red triangles, respectively) and for a variety of concentrations for laser power L2 as well. Values corresponding to fig. 6 are drawn as open and light shaded symbols. Lines are guides to the eye. In sub-figures (a) and (b) simulation data [30] is included (black crosses), corresponding to diffusion through a crowded environment as a function of obstacle concentration instead of the laser power (arbitrarily scaled with $P_L = \phi_{\text{obst}} \cdot 10 \text{ W}$).

lower/higher P_L (cf. fig. 6), but quantitative differences occur because both laser power and particle concentration affect the dynamics (see section III C for details). Figure 5 shows the time-dependent normalized mean-squared displacement $\langle \Delta r^2(t) \rangle / R^2$, normalized diffusion coefficient $D(t) / D_0$, diffusive exponent $\mu(t)$, and non-Gaussian parameter $\alpha_2(t)$ for increasing concentrations

at fixed medium laser power L2. Low to high concentrations are indicated by a color gradient dark green to dark red, respectively. The mean-squared displacement (fig. 5 (a)) and the diffusion coefficient (fig. 5 (b)) indicate sub-diffusive behaviour at all times. Furthermore, the diffusion coefficient $D(t) / D_0$ at intermediate to long times (fig. 5 (b), (f)) increases proportionally with the particle concentration. At intermediate times, it is preferable to analyse the logarithmic derivative of the mean-squared displacement, the diffusive exponent $\mu(t)$, and the excess kurtosis of the displacement distribution, the non-Gaussian parameter $\alpha_2(t)$, since they are more sensitive for dynamical behaviour going beyond normal Brownian diffusion. $\mu(t)$ (fig. 5 (c), (g)) shows a deep dip for low concentrations (C1L2, dark green) that is tailing off with increasing concentration. Since time- and ensemble-averaged measures are considered, the observed trends can be explained as follows. At low concentrations (and in equilibrium) all particles are trapped in the deepest potential wells, showing strong sub-diffusion. Upon adding particles, however, less pronounced potential minima are occupied, i.e. colloids are in average more mobile. At even higher concentrations, particle-particle interactions and collisions both prevent particles from occupying some of the deepest potential minima (excluded volume) and limit the average period for which particles get trapped, further smoothing out the influence of the potential. The minimum value μ_{min} is reached at times around t_B for all concentrations. This was expected, since $t_{\mu_{\text{min}}}$ only depends on the potential correlations, namely the average width of potential minima. It marks the time, when a majority out of the particle ensemble is trapped, as discussed in detail for diluted samples in rPELs with Gaussian roughness in [35, 43]. Then again, in $\alpha_2(t)$ (fig. 5 (d), (h)) a peak starts to appear at times around t_B with height and time of its maximum value α_{max} depending on the concentration. The short-term diffusion coefficient D_s (fig. 5 (e)), unlike the one for long lag times, shows an unsettled concentration dependence for medium potential strength L2 and hence does not provide enough information to draw conclusions concerning other potential depths. Therefore, a detailed analysis of the in section III A 1 introduced measurables D_s , D_{long} , μ_{min} , and α_{max} as a function of concentration was performed.

3.6 Paper VI: Anomalous Colloidal Diffusion: Interplay of Crowding and an External Random Potential

8

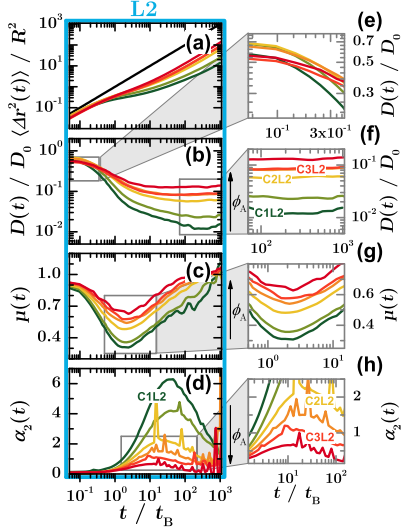


FIG. 5. Concentration dependent dynamics: (a) Time-dependent normalized mean-squared displacement $\langle \Delta r^2(t) \rangle / R^2$, (b) normalized diffusion coefficient $D(t)/D_0$, (c) diffusive exponent $\mu(t)$, and (d) non-Gaussian parameter $\alpha_2(t)$ for medium laser power L2 and increasing concentrations (coloured lines, from green (low concentration) to red (high concentration), according to line L2 in fig. 1). Sub-figures (e),(f),(g) and (h) constitute zoom into the time regimes matching with the appearance of D_s , D_{long} , μ_{min} and α_{max} , respectively.

Figure 6 shows the normalized short-time diffusion coefficient D_s/D_0 (a), the normalized long-time diffusion coefficient D_{long}/D_0 (b), the minimum value of the diffusion exponent μ_{min} (c) and the maximum value of the non-Gaussian parameter α_{max} (d), as well as the times at which the minimum in μ and the maximum in α are reached, $t_{\mu_{\text{min}}}/t_B$ (e) and $t_{\alpha_{\text{max}}}/t_B$ (f), respectively. Here, the long-time diffusion coefficient D_{long} and the minimum of the diffusive exponent μ_{min} continually increase, while the maximum of the non-Gaussian parameter α_{max} monotonically decreases the higher the concentration is. In contrast, the short-time diffusion coefficient D_s exhibits a maximum. Starting with the low concentration and following one of the lines drawn as guides to the eye D_s first increases for all investigated potential strengths L1-3, then decreases until it reaches a plateau at high concentrations. Additionally, a maximum in D_s at medium volume fractions ($\phi_A \approx 0.1 - 0.3$) is observed, but is not found in absence of a potential, where D_s monotonically decreases with increasing ϕ_A . Figures 6 (e) and (f) show the corresponding times $t_{\mu_{\text{min}}}/t_B$ and $t_{\alpha_{\text{max}}}/t_B$ at which the extreme values μ_{min} and α_{max} are reached, respectively. The time of the occurrence of the minimum in the diffusive exponent $t_{\mu_{\text{min}}}/t_B$ generally has a roughly constant value of about 1 for all concentra-

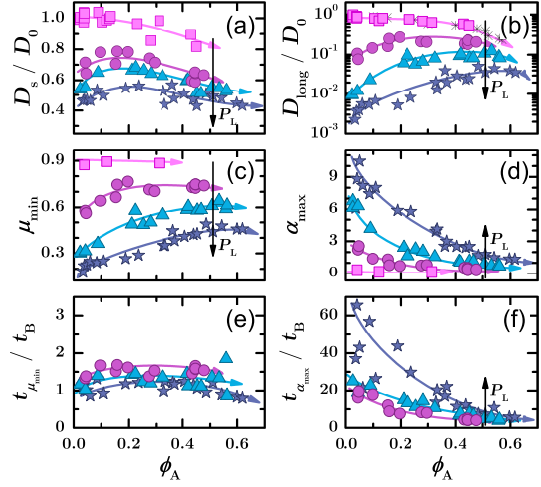


FIG. 6. Concentration dependent extreme values: normalized short-time diffusion coefficient D_s/D_0 (a), the normalized long-time diffusion coefficient D_{long}/D_0 (b), the minimum value of the diffusion exponent μ_{min} (c) and the maximum value of the non-Gaussian parameter α_{max} (d), as well as the times at which the minimum in μ and the maximum in α are reached, $t_{\mu_{\text{min}}}/t_B$ (e) and $t_{\alpha_{\text{max}}}/t_B$ (f), respectively. All are shown for L0, L1, L2 and L3 indicated by magenta squares, purple circles, light blue triangles and dark blue stars, respectively. In sub-figure (b) experimental data, corresponding to the case of no laser potential and taken from [51], is included as black crosses. Lines are guides to the eye.

tions and laser powers. Then again, $t_{\alpha_{\text{max}}}/t_B$ behaves almost identical to α_{max} . Increasing the concentration leads to decreasing peak values α_{max} and times $t_{\alpha_{\text{max}}}/t_B$, that is the displacement distribution behaves more Gaussian again. Together with the result that the minimum of the diffusive exponent μ_{min} is approaching a value of one (the value of normal diffusion) for high concentrations, this indicates the concentration to smooth out the sub-diffusive dynamics caused by the potential landscape. The scaling in fig. 2 (b-c) corroborates this conclusion. Concentration dependent scaling with l^2 works for medium and high laser power the better the higher the concentration is, since decreasing the particles' free accessible space counteracts the by the potential induced particle arrangement.

B. Identifying Mechanisms that Govern Particle Dynamics

So far, we have analysed the time- and ensemble-averaged measures of dynamics, which are well suited to discuss ensemble phenomena, especially at large time-scales. To get further inside into the underlying mechanisms, we study the behaviour of particles in time or

space individually [11]. In this section, we first analyse how the self-part of the van Hove correlation function, namely the normalized probability density of the particle displacements $p(\Delta r)$ depends on the time period, laser power and particle concentration. Second, we study the single trajectory time-averaged mean-squared displacements and, in particular, the corresponding population probability histograms.

1. van Hove Correlation Function

Since $\langle \Delta r^2(t) \rangle$ and $\alpha_2(t)$ only characterize its width and shape relative to a Gaussian distribution we analyse the self-part of the van Hove function $p(\Delta r, t)$ in more detail. Figure 7 shows the time dependence of $p(\Delta r, t)$ for three different scenarios: two-dimensional free diffusion L0 (a-d), a rough potential with constant concentration C2 (e-h) and various concentrations with constant intermediate laser power L2 (i-l), where grey dashed vertical lines indicate multiple integers of the width of the spatial correlation function of the potential landscape $\sigma_{C_V} = 1.38R$ [39]. Without an applied laser field (fig. 7 (a-d)), the peak of the probability function can be described by a Rayleigh distribution (eq. (4)) for all measured time scales. The maximal height of the distribution decreases with increasing times, whereas its width proportionally increases. Since the width corresponds to the ensemble-averaged mean-squared displacement particles undergo normal diffusion ($\mu = 1$) without deviations from Gaussian statistics ($\alpha_2 \approx 0$).

Now we focus on the influence of a rough potential on the dynamics (fig. 7 (e-l)). First, we look at the displacement probability distributions for rough potentials L1-L3 with constant concentration C2 (fig. 7 (e-h)). For small times ($t < t_B$, fig. 7 (e)), $p(\Delta r)$ can still be represented by a Rayleigh distribution (eq. (4)) with slightly different parameters than used in fig. 7 (a). The width of the probability peak decreases, whereas its height increases with increasing laser power. This indicates, that some of the particles move within limited regions, namely potential traps. The trend becomes stronger at later times (fig. 7 (f-h)). In addition, the point, at which the probability drops to zero, is in this case strongly affected by the mean potential strength. In fig. 7 (f), we observe for times $t \approx 2t_B$, that $p(\Delta r) = 0$ for $\Delta r \approx 1.38R$ at medium concentrations C2 and medium to large laser powers L2-L3. The probability function for low laser power L1 becomes zero for larger displacements, seemingly $\Delta r \approx 2R$. The first can be explained by the particles being trapped in the laser potential wells, whose average size is given by σ_{C_V} [39]. The latter, on the other hand, is presumably more affected by the inter-particle distance $2R$ than by the potential correlations, since the particle mobility is only slightly impaired in weak potentials. This statement is further confirmed by the analysis of even longer lag times and constant concentration C2 (fig. 7 (g-h)). Even for times $20t_B \leq t \leq 400t_B$ many particles are

still trapped, i.e. $p(\Delta r)$ is showing an increased probability of confined displacements $\Delta r \leq 1.38R$, for medium C2L2 and high laser powers C2L3, whereas for the case of low potential strength C2L1 most particles are diffusive again.

So far, we have focused on the pronounced peak at short spatial scales, which has been ascribed to particles being trapped only at short distances by either the potential wells, namely $\Delta r \leq 1.38R$, or other particles, leading to $\Delta r \leq 2R$, and being diffusive otherwise. Furthermore, we observe a distinctive feature at late time scales. In the insets of sub-figures 7 (g) and (h), it is shown that at late times ($t \geq 20t_B$, (g)) a second peak starts to form, which becomes more pronounced for long times ($t \approx 400t_B$, (h)). Since we are looking at ensemble averages, this can be explained by cooperative movements, i.e. all particles starting at the origin at $t = 0$ and getting trapped for short lag times have a non-vanishing probability to move about $2R$, the position of the second peak in $p(\Delta r)$. Trapped particles overcome surrounding potential energy barriers and hop to neighbouring potential minima, while other particles occupy the vacancies getting trapped. Although the concentration C2, $\phi_{A,C2} = 0.25$, is not very dense, the external potential causes dynamical behaviour which is well known from dense liquids, crowded environments or colloidal glasses as e.g. ‘particle cage hopping’ or other cooperative behaviour [2, 24, 32, 33, 47, 52, 53].

As a next step, we study the concentration dependence of these effects at constant laser power L2 (fig. 7 (i-l), low to high concentrations coloured in green to red, respectively). We find that not only the initial trapping at short times ($t \leq 2t_B$, (i-j)), but also the height and position of the second peak that evolves for medium to long times ($t \geq 20t_B$, (k-l)) are affected by the increase of the particle concentration. The higher the concentration of the particles, the lower is the main peak and the higher the second peak in $p(\Delta r)$. This can be explained by particle-particle collisions helping trapped particles to overcome the potential barrier of the initial potential wells, before possibly getting trapped again in another potential minimum, resulting in heterogeneous diffusion and a higher mean mobility. The self-part of the van Hove function $G_s(\Delta r)$ plotted logarithmically against the displacement Δr (SI, fig. 17) further corroborates this interpretation. In the presence of a rough potential and at intermediate to long times, an exponential tail (constant slope) is clearly visible, which is often found in crowded systems caused by a linear combination of several Gaussian G_s with different diffusion coefficients [14]. Moreover, the position of the second peak is studied (fig. 7 (k-l), inset). Despite of worse statistics at long time scales, the position changes continuously from the minimum inter-particle distance $\Delta r = 2R$ for medium times ($t \approx 20t_B$, (k)) and high concentrations (dark red line) to the position of the next potential well, namely two times the potential correlation length $\Delta r \approx 2.76R$, for late times ($t \geq 20t_B$, (l)) and low concentrations (dark green line). In addition, we do not expect effects due

3.6 Paper VI: Anomalous Colloidal Diffusion: Interplay of Crowding and an External Random Potential

10

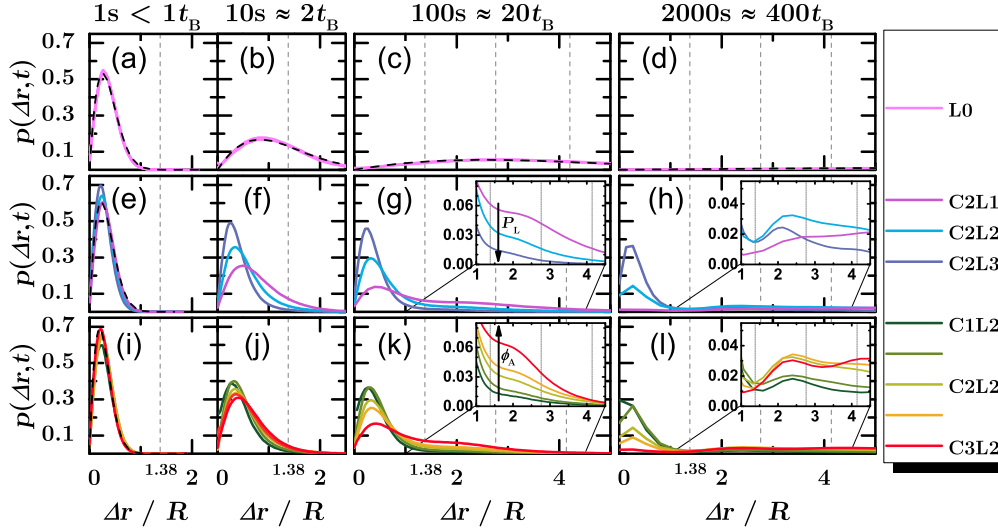


FIG. 7. Normalized probability density of the displacements $p(\Delta r)$ (self-part of the van Hove function) vs. the displacement Δr normalized by the particle radius R : different concentrations ϕ_A in the absence of an external potential (a-d), a rough potential and constant concentration C2 (e-h), and various concentrations in a rough potential L2 (i-l); for times $t = 1$ (a, e, i), 10 (b, f, j), 100 (c, g, k) and 2000 s (d, h, l). Black dashed lines correspond to Rayleigh probability density functions (fits). The grid of grey dashed vertical lines indicates the width of the spatial correlation function of the potential landscape $\sigma_{C_U} = 1.38 R$ [39].

to a liquid-hexatic transition, which could occur at even higher concentrations ($\phi_A \approx 0.70$) [29, 33], or due to a glass transition, which could occur at more polydisperse systems [19, 47, 54]. This is important to note, since the dynamical behaviour seen here, so far only known from glass or solid phases, can thus be assigned to the underlying potential. Therefore we conclude, particles diffusing through a random potential energy landscape with intermediate potential roughness get trapped in potential wells for short lag times, but also show a distinct second peak in their displacement probability distribution at longer time scales. Similar, presumably cooperative, behaviour has been observed in dense liquids [23, 24, 33], glass forming liquids [52, 53] or porous environments [2] and is interpreted as collective particle motions either in time or space inducing heterogeneous diffusion. For example, cooperative string-like behaviour found in dense quasi-two-dimensional liquids was explained with density fluctuations and temporal structural heterogeneity in the sample [23, 24]. Furthermore, Kim et al. [33] noted that, due to discretized dynamics, even in systems with seemingly Fickian dynamics ($\mu = 1$) various peaks in $p(\Delta r, t)$ can be found for several decades in time.

2. Single particle mean-squared displacements

To get deeper insight into the heterogeneity of the diffusive behaviour, we analyse single particle trajectories,

as exemplarily shown in fig. 8, at different lag times. For this purpose, time-averaged single particle mean-squared displacements are calculated and compared with the (time and) ensemble averages (fig. 10, see section IID for details of the averaging). Furthermore, time-averaged single-trajectory mean-squared displacement histograms are analysed (fig. 11). Based on this comprehensive analysis, we are able to disentangle contributions of single particle and ensemble effects.

Figure 8 shows snapshots of particle trajectories at high concentration C3 and laser power L3 for three different lag times $t = 2, 20, 200 t_B$. These lag times are characteristic, representing the times at which the time-regimes of the minimum in the diffusive exponent μ_{\min} , the maximum in the non-Gaussian parameter α_{\max} , and the transition to diffusive behaviour at long times occur. Particles are schematically shown at the start and end positions of their trajectories, as white and grey shaded circular areas, respectively, in accordance with their real size. Furthermore, a selection of particles and their trajectories are highlighted by different colors to emphasize particle movements and hence emerging trajectory overlaps. Figure 8 (a) represents particle movements within a lag time $t = 2 t_B$ at the beginning of the measurement. Particles can on average diffuse a distance of about their own radius before they feel the optical potential and eventually get trapped (dark grey particles). Hence, in this time range, the diffusion of the particles is strongly subdiffusive, leading to a minimum in the diffusive exponent

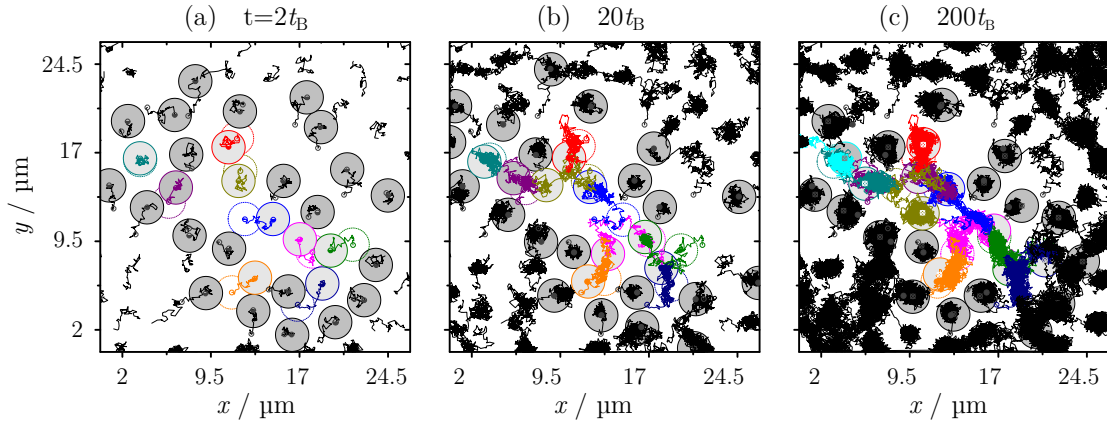


FIG. 8. Trajectories for high concentrations C3 and laser strength L3. Sub-figures (a), (b), and (c) show snapshots for different lag times $t = 2, 20, 200 t_B$, respectively. Some of the trajectories, which form a percolating cluster at long times, are highlighted by different colors to emphasize trajectory overlaps. Particles are schematically shown at the end positions of their trajectories, in accordance to their real size (radius $R = 1.4 \mu\text{m}$; as grey filled circular areas). Again, particles within the chosen cluster are indicated by colors, while surrounding, mostly trapped particles are drawn in dark grey. Furthermore, for the highlighted trajectories also the end position of the prior sub-figure, according to times $t = 0, 2, 20 t_B$ is indicated by 'particles', here drawn as white open circular areas with dashed borders.

μ . However, due to the high concentration, some particles (indicated by colors) can still move distances beyond the trap width ($\langle \Delta r^2 \rangle > \sigma = 1.38 R$), caused by their initial position and a limited number of deep potential wells. At later times (fig. 8 (b)), the particles' diffusion is more diversified. While some particles are strongly trapped, others already left potential minima and got diffusive again or vice versa. Particles indicated by colors start to form a percolating cluster, while exchanging their positions in weak potential minima. The diffusive heterogeneity is quantified by the maximum in the non-Gaussian parameter α_2 , which occurs in this time range. At even longer lag times the sample shows more diffusive behavior again. Most of the particles already left their initial traps, sampling more and more of the field of view. Still, there are differences between particles, that are strongly trapped (dark grey) and particles that are moving in a percolating cluster (colored), spanning for long times at least the length scale of the field of view.

The particle dynamics can be classified by three main diffusive processes, which are shown schematically in fig. 9 as differently colored trajectories. Besides strongly sub-diffusive (trapped, blue) and almost diffusive (percolating, red) behavior, a third process is identified (green). Since the mean distance between potential minima almost matches the particle diameter, a pronounced hopping motion of particles takes place. A particle can only move if one of its next-neighbours rearranges, which is similar to single file diffusion [55], but in this case strongly depends on the actual particle and potential minima arrangement. The green trajectories in fig. 9 form a connected line of five particles, each centred at

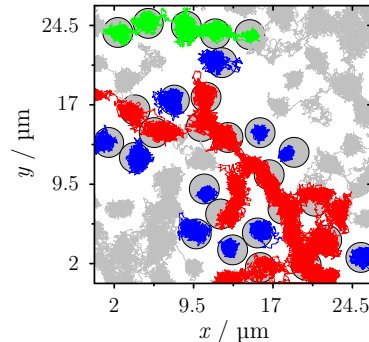


FIG. 9. Schematic overview of the main diffusive processes via a snapshot of trajectories at high concentrations C3 and laser power L3 with starting time $t_0 = 2 t_B$ and for lag time $t = 200 t_B$. Particles of interest are schematically drawn, in accordance to their size (radius $R = 1.4 \mu\text{m}$), as grey shaded circular areas at the end positions of the underlying trajectories. Trajectories showing strong trapping, percolating diffusion, and hopping motions, are colored blue, red, and green, respectively.

a potential minimum. For most of the time, particles are trapped within their initial potential valleys. However, if one of the particles is displaced by more than its own radius, the vacancy in the rPEL will very quickly be occupied by an adjacent particle. Therefore, string-like hopping motion with discretized step-sizes, which correspond to the average distance between two adjacent potential minima, occurs. Similar spatially re-

3.6 Paper VI: Anomalous Colloidal Diffusion: Interplay of Crowding and an External Random Potential

12

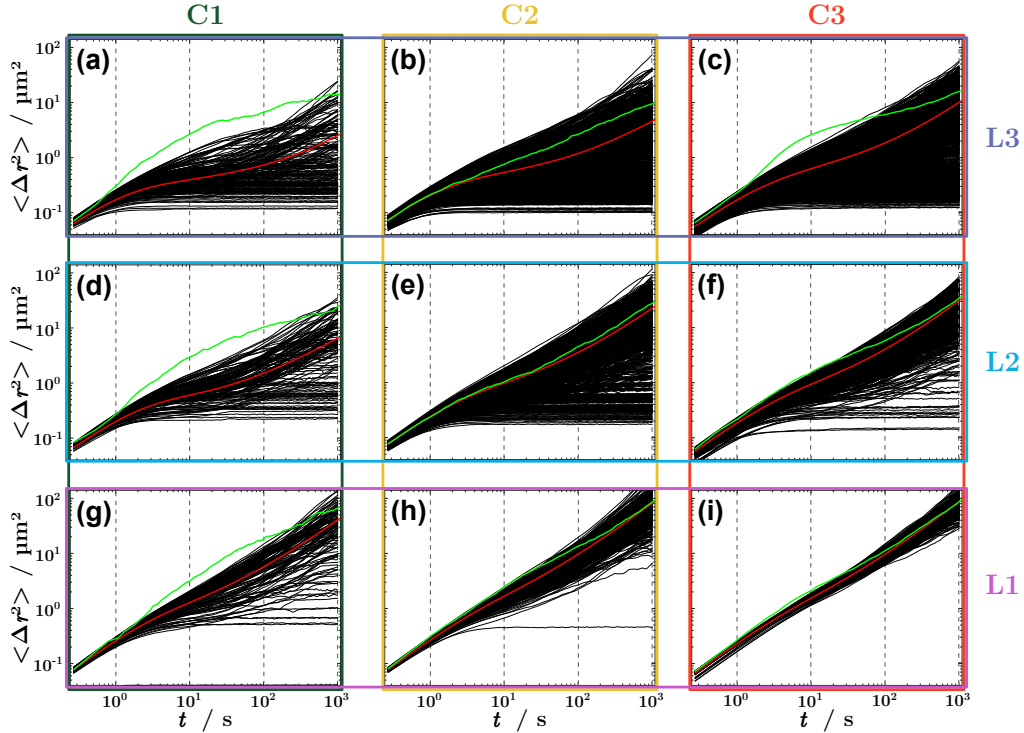


FIG. 10. Time-averaged single particle mean-squared displacements with ensemble and time averaged (red line) and only ensemble averaged mean-squared displacement (green line) for different laser powers L1-L3 (bottom to top) and concentrations C1-C3 (left to right), respectively. Times $t = 1, 10, 100, 1000$ s, for which the population probability histograms are calculated (fig. 11), are indicated by dashed vertical lines.

stricted, correlated dynamics were already observed in very dense two-dimensional systems [23] and are also expected to occur in more complex systems such as the dense Lorentz gas, porous media and crowded (cellular) environments [13, 27, 56–60].

Time-averaged single-particle squared displacements are analysed to characterize the heterogeneous dynamics. Figure 10 shows the time-averaged squared displacements for single trajectories corresponding to points C1L3 (a) to C3L1 (i) in the P_L - ϕ_A state diagram. Free, normal diffusion is characterized by a linear slope, no deviation between the time- and ensemble average (red line) and the ensemble-average (green line) and no scatter between single trajectories at short and intermediate times. Scatter between single trajectories at the end of the measurement time, in turn, is most probably caused by time-averaging, which leads to statistics that are worse at long times than at short lag times. For clarity, each second trajectory is shown, whereby we carefully checked that left out trajectories do not show different behaviour. For all concentrations and potential depths, deviations to the freely diffusing case are observed, the least at high concentrations and low laser power (C3L1, fig. 10 (i)). Single tra-

jectories that diverge at very short time scales are most probably caused by the slightly polydisperse samples and are therefore neglected in the following analysis. For low concentrations and/or high laser powers, roughly two different kinds of trajectories can be identified. First, trajectories that have an intermediate regime with only a slight sub-diffusive plateau becoming diffusive again within the measurement time. Second, trajectories of trapped particles forming a constant plateau that is prolonged beyond the time of measurement. It is important to note that, since the mean-squared displacement of the second group of particles is about two orders of magnitude lower at long times, the time- and ensemble-averaged value of $\langle \Delta r^2 \rangle_{i,t_0}$ is mainly determined by the faster particles that are already diffusive again. This is illustrated by the bending up of the red line, which, for all lag times, is located in the upper third of the single trajectories. As a consequence, the time- and ensemble-averaged measures are biased in direction of fast moving particles smoothing out effects of the slower species. The difference between the ensemble averaged $\langle \Delta r^2 \rangle_i$ (green line) and the ensemble- and time-averaged mean-squared displacement $\langle \Delta r^2 \rangle_{i,t_0}$, together with scattering of the trajectories for

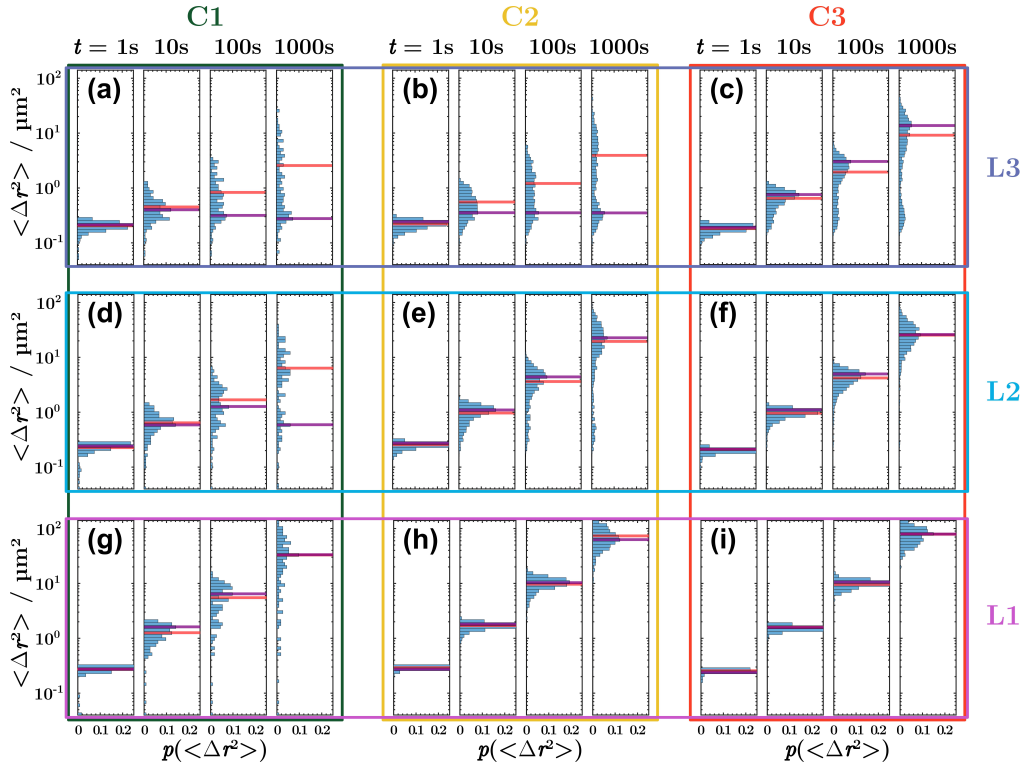


FIG. 11. Population probability histograms of the time-averaged single particle mean-squared displacements for times $t = 1, 10, 100, 1000$ s for different laser powers L1-L3 (bottom to top) and concentrations C1-C3 (left to right), respectively. Time- and ensemble averaged mean (red) and the maximum of the histogram (purple) are indicated by colored bars.

even intermediate times, indicates non-ergodic behaviour for at least the time of measurement and hints at weak-ergodicity breaking, which has been observed in many systems with anomalous diffusion [5, 6, 11, 61].

To better understand the single trajectory scattering, the probability density of single-particle mean-squared displacements $p(\langle \Delta r^2 \rangle_{t_0})$ is calculated for concentration-potential combinations of fig. 10 at lag times $t = 1, 10, 100, 1000$ s (indicated by vertical lines). The probability histograms are shown in fig. 11, where red and purple horizontal bars indicate the time- and ensemble-averaged mean and peak position, that is the highest probability to find a particle at this distance $p(\langle \Delta r^2 \rangle_{t_0})$ after time t , respectively. For high laser power L3 and low concentration C1 (fig. 11 (a)), the distribution at short times $t = 1$ s closely resembles Boltzmann statistics of free diffusion with the position of the mean being identical to the one of the distributions' peak. At later times $t \geq 10$ s the distribution splits up and a second peak evolves. Here, most of the particles are trapped for the whole measurement time giving rise to a strong second peak, which is even higher than the diffusive one. Furthermore, with

increasing time (fig. 11 (a), left to right), the position of the time- and ensemble-mean (red bar), which accounts for the diffusive particles, rises, while the distributions' peak position (purple bar) levels up at low mean-squared displacements. For the case of very rough landscapes L3 and low to medium concentration C1-2 (fig. 11 (a-b)), this phenomenon is most pronounced, whereas, for the highest investigated concentration (c), the peak and mean positions are almost identical for all times. Since the number of deep potential wells is constant and, at medium concentrations, all strong minima are occupied by particles, a further increase of the volume fraction leads to particles which are on average more mobile and the mean trapping time is decreased by particle-particle collisions. At constant laser power L2 with increasing concentration C1 to C3 (fig. 11 (d-f)), for all concentrations, less particles are strongly trapped, i.e. occupy the lowest potential energy values, for long times. For lower laser power L1, the same trend starting at even lower concentrations is observed (fig. 11 (g-i)). A time-averaged quantity which follows Boltzmann statistics implies that for low concentrations and long times only the deepest

3.6 Paper VI: Anomalous Colloidal Diffusion: Interplay of Crowding and an External Random Potential

14

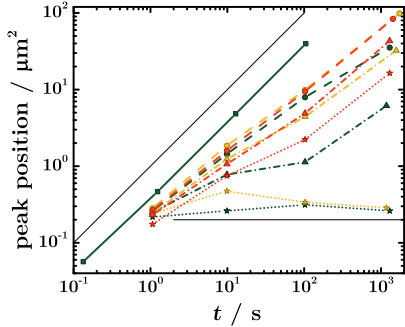


FIG. 12. Position of the highest peak in the single-trajectory mean-squared displacement probability distribution (indicated by green bars in fig. 11) plotted against the time for various concentrations and laser powers. Concentrations are indicated by a color gradient (green \equiv low to red \equiv high) and laser power L0, L1, L2 and L3 by different line types (and symbols) solid (squares), dashed (circles), dash-dotted (triangles up) and dotted (stars), respectively. Solid black lines are guides to the eye for slope 1 and a constant value $\langle \Delta r^2 \rangle = 0.2 \mu\text{m}$.

potential wells are filled. This is indeed observed in the experiments at low concentration C1 and intermediate to high laser powers L2-3 (fig. 11 (a),(d)) and at medium concentration C2 and high laser power L3 (b). The single trajectories (fig. 10 (a),(b),(d)) indicate that, at late times, most of the particles are trapped, i.e. occupy deep potential wells. At low laser power and/or higher concentrations, we observe a decreasing probability of particles to stay trapped over long times for increasing concentration due to particle-particle interactions and the onset of excluded volume effects. Hence, the free mean path of the particles is reduced and the probability of collisions raised. Furthermore, more particles undergoing Brownian motion are pinned in less deep traps for less time. Consequently, the particles' (trap-)residence time is decreased, since they either cannot find a (deep) potential minimum any more or are pushed out by other particles after short times already. This leads to a smoothing out of the underlying potential landscape, therefore inducing faster and more cooperative diffusive behaviour.

The position of the highest peak in the single-trajectory mean-squared displacement probability distribution (maxima in fig. 11) is separately plotted against the time as a function of concentration and potential strength in fig. 12. While the time-dependence of the peak's position is linear for L0 (solid green line), as expected for free diffusion, a more and more pronounced plateau can be identified for higher laser power (dash-dotted and dotted lines). It is most pronounced at low concentrations (green lines), in accordance with the analysis of the single-trajectory mean-squared displacements and their displacement probabilities above. The levelling up of the peak position is a clear sign that a large fraction

of the particles, which does not necessarily have to be the majority, is quasi-pinned in potential traps for at least the time of the plateau. However, a large number of the particles is still diffusive, so that a percolation transition is presumably not reached yet. The position of this maximum peak, e.g. $\langle \Delta r^2 \rangle \approx 0.2 \mu\text{m}$ for C1L3 (green dotted line in fig. 12), should correspond to the mean displacement of particles rattling around within traps and therefore scales with the average potential width and depth.

C. Are Short-Term Dynamics Indicative of the Long-Term Behaviour?

For ensemble-averaged measures the anomalous diffusion is most pronounced at intermediate time scales ($1 \leq t/t_B \leq 50$), with the strongest influence on both $D(t)$ and $\mu(t)$, as the results of section III A indicate, whereas for single particle measures strong deviations from normal diffusive behaviour are observed for short and large time scales (section III B). Thus, two counteracting influences, namely the particle-potential and particle-particle interactions, were identified. The first is most pronounced for low concentrations and high laser power, the latter for high concentrations and low laser power. To further characterize their interplay, we discuss the short-term diffusion coefficient D_s and the long-term diffusion coefficient D_{long} in the P_L - ϕ_A state diagram, followed by a comparison of both to identify possible connections.

1. Short-Term Diffusion

In fig. 13, the short-term diffusion coefficient D_s , introduced in section II D, is plotted in the form of the P_L - ϕ_A state diagram, where symbols represent measured concentrations and laser powers and D_s appears as colour scale. Furthermore, possible regions with similar values of D_s , referred to as iso-diffusivity areas, are indicated by colors as well, where the gradient from purple to dark red characterises increasing values. It has to be noted though, that these areas can be seen as an average over several iso-diffusivity lines with similar shape and, therefore, serve as guides to the eyes only. Furthermore, other similar D_s values could have been picked out, since D_s changes continuously and therefore no discrete transition between the indicated areas exists.

As already seen in fig. 4, D_s exhibits re-entrant behaviour with a maximum at $\phi_A = 0.1-0.3$ depending on the strength of the laser potential. For example, following line L2 with constant laser $P_{L,2}$ from low concentrations to high ones, the short time diffusion coefficient first increases until it reaches its maximum $D_{s,L2,\text{max}} \approx 0.06 \mu\text{m}^2\text{s}^{-1}$ at area fraction $\phi_A \approx 0.22$ and constantly decreases again afterwards and is true for all investigated, but especially pronounced for intermediate laser powers. To further explain this, we first identify possible iso-

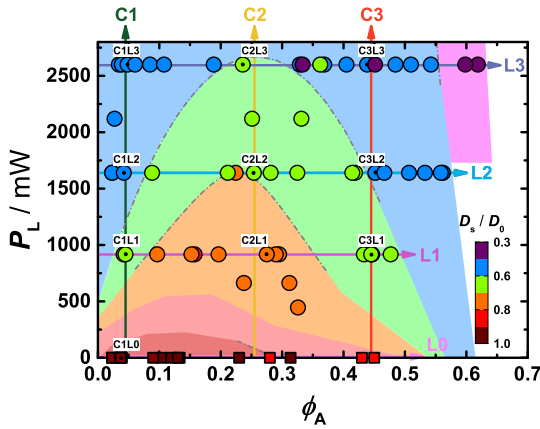


FIG. 13. Short-time diffusion coefficient D_s in the P_L - ϕ_A state diagram. Filled circles and squares are measured conditions with and without an external potential, respectively. Measurements that correspond to crossing points of the potential L0-L3 and concentration C1-C3 lines, following the diagram of fig. 1, are named and indicated by black dots. The value of the short-term diffusion coefficient D_s is represented by the colour scale, where the gradient from purple to dark red characterises increasing values. Grey dash-dotted lines indicate possible iso-diffusivity lines between suggested colored iso-diffusivity areas (see text for explanation).

diffusivity lines (grey dash-dotted lines in fig. 13) of short-term iso-diffusivity areas (indicated by colors), with the result, that measurement points with a similar short-time diffusion coefficient form a dome-shaped area. The width of the area increases with increasing laser power, since stronger potentials influence the particle interactions up to even higher concentrations. However, it is well known, that the particle interactions of dense samples ($\phi_A \geq 0.3$) are strongly dependent on the concentration, even without an impinged potential landscape. Therefore, the influence of the random potential energy landscape on the short-time particle dynamics is limited again at high concentrations. In addition, the peakedness of both the self-part of the van Hove function and the population probability histograms of the time-averaged single particle mean-squared displacements seem to be most pronounced at points coinciding with the most left points in the green iso-diffusivity area in fig. 13, corresponding to $D_s \approx 0.05 \mu\text{m}^2\text{s}^{-1}$.

2. Long-Term Diffusion

The long-term diffusion coefficient D_{long} was plotted in a P_L - ϕ_A diagram as well (fig. 14), but, in contrast to D_s , represented by a logarithmic color scale. In this case, long-term iso-diffusivity areas, featured again by uniform colors, are going somehow diagonal from points

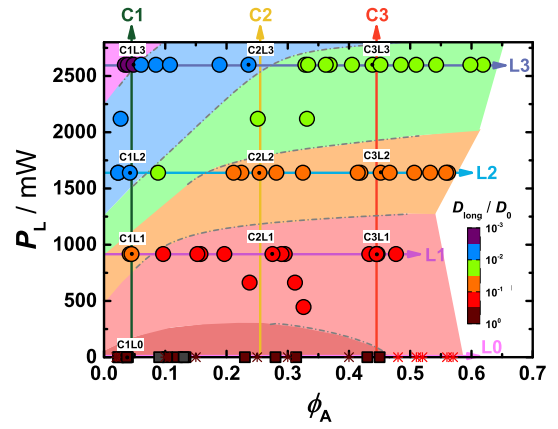


FIG. 14. Long-time diffusion coefficient D_{long} in the P_L - ϕ_A diagram. Filled circles and squares are measured points with and without an external potential, respectively. Furthermore, experimental data, corresponding to the absence of an external potential, taken from [51] is included as crosses. Measurements that correspond to crossing points of the potential L0-L3 and concentration C1-C3 lines, following the diagram of fig. 1, are named and indicated by black dots. The long-term diffusion coefficient D_{long} is represented by the log-colour scale, where the gradient from purple to dark red characterises increasing values. Grey dash-dotted lines indicate possible iso-diffusivity lines between suggested colored iso-diffusivity areas.

of low concentration and laser power to points of high ϕ_A and P_L . The iso-diffusivity lines show a tendency to saturate with increasing concentration. As described in section III A, D_{long} first continuously increases with increasing area fraction and afterwards levels up to a plateau for higher concentrations, provided that the potential strength is kept constant (cf. fig. 6). At even higher concentrations, the long-time diffusion coefficient is expected to decrease again, since particles become hindered in their motion by excluded volume effects. The concentrations at which the maximum is seemingly reached are $\phi_{A,\text{sat},1} \approx 0.1$, $\phi_{A,\text{sat},2} \approx 0.2$ and $\phi_{A,\text{sat},3} \approx 0.35$ for L1, L2 and L3, respectively. Furthermore these values coincide with starting points of long-term iso-diffusivity lines in fig. 14, corresponding to $D_{\text{long},1}/D_0 \approx 10^{-1}$, $D_{\text{long},2}/D_0 \approx 5 \cdot 10^{-2}$ and $D_{\text{long},3}/D_0 \approx 10^{-2}$ and therefore almost match the transition points identified for short-term diffusion (cf. fig. 13). It is interesting to note, that while further increasing the concentration at constant laser power, a re-entrant regime, as previously found for the short-term iso-diffusivity lines (cf. section III C 1), is expected to show up for all long-time diffusion coefficients as well, as suggested by the analysis of the long-term diffusion coefficient of measurements without an external potential (squares and asterisks in fig. 14, [48, 51]). Increasing the concentration leads to a monotonic decrease of D_{long}/D_0 , until a limit

3.6 Paper VI: Anomalous Colloidal Diffusion: Interplay of Crowding and an External Random Potential

16

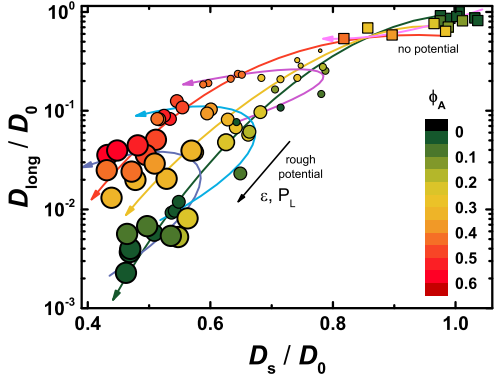


FIG. 15. Short-term diffusion coefficient D_s vs. long-term diffusion coefficient D_{long} . The symbol shape distinguishes between potential types: no potential (squares) and rough potential (circles). Color gradient (from dark green to dark red) and symbol size correspond to increasing area fraction ϕ_A and laser power P_L , respectively. Lines C1-C3 and L0-L3 are included as guides to the eye (cf. fig. 1).

of $D_{\text{long}}/D_0 \approx 0.1$ is reached, which was suggested for the two-dimensional freezing transition in the absence of hydrodynamic interactions [31].

3. D_s vs D_{long}

Due to their similarities, the dependence of both D_s and D_{long} on the area fraction as well as the potential is compared simultaneously. This is done in two ways, namely a D_s - D_{long} diagram with symbol size depending on P_L and color-coded by ϕ_A and the calculation of the difference $D_s - D_{\text{long}}$, as shown in figs. 15 and 16, respectively. Figure 15 provides an overview of both the short- and long-term diffusion coefficients, measured for all examined concentrations (symbol color) and laser powers (symbol size) in presence of a rough potential (circles), together with data measured in absence of a potential landscape (squares). Lines C1-C3 and L0-L3 are included as guides to the eye (cf. fig. 1). If no potential is applied, D_s is almost constant for low concentrations and decreases with increasing area fractions as D_{long} does as well. This behaviour was well described in literature [62] and is, for hard spheres, not expected to change until area fractions well above $\phi_A = 0.6$. Nonetheless, this is in strong contrast to the case of a rough potential, where D_s shows re-entrant behaviour (cf. fig. 13) while D_{long} even increases with increasing area fraction (cf. fig. 14), as indicated by lines L1-L3. Moreover, it was shown in section III A that the striking behaviour of D_s and D_{long} as a function of concentration is smoothed out by lowering the potential strength. Thus, the existence of a transition situated at low laser powers can be assumed, above which the long-term diffusion coefficient is de-

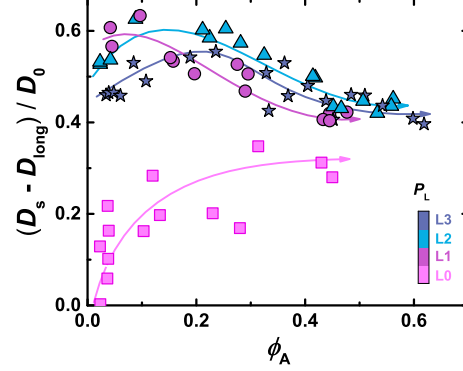


FIG. 16. Difference of short-term diffusion coefficient D_s and long-term diffusion coefficient D_{long} as a function of the area fraction ϕ_A . Symbols distinguish between potential type (shape) and strength (color) as follows: no potential (squares) and rough potential (circles). The color gradient from pink to dark blue corresponds to laser powers $P_{L,0}$ to $P_{L,3}$, respectively. Lines L0-L3 are included as guide to the eye.

ing with increasing concentration, as for the cases without a potential. Below this transition D_{long} behaves vice versa, as seen for all investigated laser powers (cf. fig. 14). The point of transition is indicated by a crossing of lines C1-C3 in fig. 15.

Furthermore, analysing the difference $D_s - D_{\text{long}}$ the suggested transition in dynamics is further clarified. Figure 16 shows the result of the normalized subtraction of short-term diffusion coefficient D_s and long-term diffusion coefficient D_{long} as a function of the area fraction ϕ_A with symbol shape and color indicating potential type (cf. fig. 15) and laser power, respectively. In the absence of an external potential and at low concentrations (pink line L0 and squares, fig. 16) $D_s - D_{\text{long}}$ increases monotonically with increasing ϕ_A , whereas in the presence of an rPEL a re-entrant behaviour with increasing area fraction, as indicated by lines L1-L3, is observed. However, at medium to high concentrations $D_s - D_{\text{long}}$ levels up irrespective of the potential, i.e. all lines L0 (from below), L1, L2 and L3 (from above) seem to continuously approach a constant value of $D_s - D_{\text{long}} \approx 0.35D_0$. For a certain range of low concentrations, that can reach up to $\phi_A \approx 0.3$ for the highest investigated potential strength L3, the short-term diffusion is mostly determined by trapped particles, thus particle-potential interactions. This is changing dramatically with higher area fractions, where concentration effects, i.e. particle-particle interactions, are dominating. As a result, in this concentration regime, only the mean free path of the particles l^2 is important, and mean-squared displacement data can be scaled as shown in fig. 2. As another consequence, both the short-term as well as the long-term diffusion coefficient decrease continuously, at least within the concentration range of our measurements.

IV. CONCLUSIONS

The dynamics of colloids probing a light-induced random potential energy landscape (rPEL) was investigated as a function of the sample concentration ϕ . On the one hand, Gauss-like random laser speckle intensity pattern forces the polarizable colloids to spend most time in high intensity regions, corresponding to valleys in the resulting rPEL. This leads to trapping of the particles and a sub-diffusive regime at intermediate lag times. Similarly, diffusion is slowed down if the particle concentration is high. However, at small and intermediate concentrations diffusion is accelerated. The concentration, on the other hand, acts as an opposing force. Collisions caused by particle-particle interactions increase the probability of previously trapped particles to overcome and cross an energy barrier, namely a saddle point in the landscape. To shed light on the mechanisms behind the counteracting effects of particle concentration and potential strength, we have analyzed short- and long-term colloidal dynamics in terms of D_s and D_{long} and studied ensemble and single trajectories. Thus, signs of cooperative particle behaviour depending on the potential strength and the concentration were found in both the displacement probability densities $p(\Delta r)$ (cf. fig. 7) and single-trajectory mean-squared displacements (cf. fig. 10), even though concentrations used in this experiments are well below the two-dimensional liquid-hexatic transition, for which this behaviour is well known [29, 32]. A critical concentration was identified, in which both effects cancel out each other, resulting in a re-entrant regime of D_s in the $P_L - \phi_A$ -state diagram (cf. fig. 13). Furthermore, similarities to a simulated system, i.e. Monte Carlo simulations of tracer diffusion through (im)mobile obstacles [3, 5], were observed. In particular, comparing the diffusion coefficients at short and intermediate times strengthens the assumption that our system is governed by two different behaviours of the particles, on the one hand within their traps mobile obstacles and on the other almost freely diffusing particles. Yet, the mobility of trapped particles is governed by the distribution of trap stiffnesses (given by the underlying potential landscape). Altogether, the results of this work provide further inside into the dynamics of tracer particles diffusing through an externally imposed random potential energy landscape as well as a crowded environment and thus the system introduced here could be used as a simplified model system to study, e.g., dynamics of several species in biological cells or diffusive transport on membranes. Moreover, in future experiments, we plan to quantitatively analyze the potential-particle interactions, i.e. trap sizes/stiffnesses

and waiting-time distributions, and the influence of both concentration and random potential on the ergodicity of the system to shed light on the heterogeneity of the dynamics [6, 11, 61].

ACKNOWLEDGMENTS

We thank David Dean, Thomas Franosch, Andreas Heuer, Jürgen Horbach, Imad Ladadwa, Thomas Konincks, Vincent Krakoviack, Hartmut Löwen, and Ralf Metzler for very helpful discussions and suggestions, and the Deutsche Forschungsgemeinschaft (DFG) for financial support (grant EG269/6-1).

APPENDIX

A. Self-part of the van Hove function $G_s(\Delta r, t)$

In the self-part of the van Hove function $G_s(\Delta r)$ for an external potential and at long times (SI, fig. 17 (f) and (i)) an exponential tail is visible (as linear behaviour with constant slope in the logarithmic representation). This is often found in crowded systems and possibly caused by a linear combination of several Gaussian G_s with different diffusion coefficients [14] indicating heterogeneous dynamics.

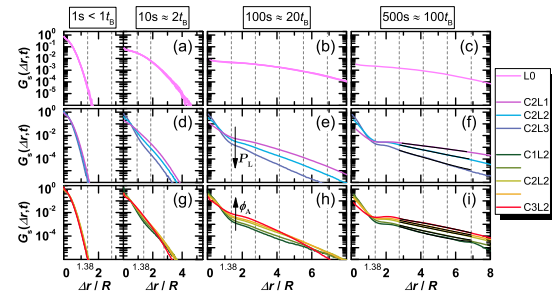


FIG. 17. Logarithmic plot of the self-part of the van Hove function $G_s(\Delta r)$ vs. the displacement Δr normalized by the particle radius R , for (a-c) no potential and different concentrations ϕ_A , (d-f) a rough potential and constant concentration (corresponding to C2) and (g-i) a rough potential and constant laser power L2; all for times $t = 1, 10, 100$ and 500 s. The grid of grey dashed vertical lines indicates the width of the spatial correlation function of the potential landscape $\sigma_{CV} = 1.38 R$ [39]. Black lines in sub-figures (f) and (i) correspond to exponential fits at long displacements ($\Delta r > 3R$).

[1] F. Evers, R. D. L. Hanes, C. Zunke, R. F. Capellmann, J. Beverunge, C. Dalle-Ferrier, M. C. Jenkins, I. Ladadwa, A. Heuer, R. Castañeda Priego, and S. U.

Egelhaaf, Eur. Phys. J. Special Topics **222**, 2995 (2013).
 [2] J. Kurzidim, D. Coslovich, and G. Kahl, J. Phys.: Condens. Matter **23**, 234122 (2011).

3.6 Paper VI: Anomalous Colloidal Diffusion: Interplay of Crowding and an External Random Potential

18

- [3] H. Berry and H. Chate, *Phys. Rev. E* **89**, 022708 (2014).
- [4] J. Guan, B. Wang, and S. Granick, *ACS Nano* **8**, 3331 (2014).
- [5] S. K. Ghosh, A. G. Cherstvy, and R. Metzler, *Phys. Chem. Chem. Phys.* **17**, 1847 (2015).
- [6] C. Manzo, T.-P. J. A., P. Massignan, G. J. Lapeyre Jr., M. Lewenstein, and F. G. Garcia Parajo, *Phys. Rev. X* **5**, 011021 (2015).
- [7] C.-L. Hsieh, S. Spindler, J. Ehring, and V. Sandoghdar, *J. Phys. Chem. B* **118**, 1545 (2014).
- [8] A. V. Weigel, B. Simon, M. M. Tamkun, and D. Krapf, *Proc. Natl. Acad. Sci. U. S. A.* **108**, 6438 (2011).
- [9] A. Birjiniuk, N. Billings, E. Nance, J. Hanes, K. Ribbeck, and P. S. Doyle, *New Journal of Physics* **16**, 085014 (2014).
- [10] D. Ernst, M. Hellmann, J. Köhler, and M. Weiss, *Soft Matter* **8**, 4886 (2012).
- [11] R. Metzler, J.-H. Jeon, A. G. Cherstvy, and E. Barkai, *Phys. Chem. Chem. Phys.* **16**, 24128 (2014).
- [12] I. Goychuk and V. O. Kharchenko, *Phys. Rev. Lett.* **113**, 100601 (2014).
- [13] F. Höfling and T. Franosch, *Rep. Prog. Phys.* **76**, 046602 (2013).
- [14] G. Kwon, B. J. Sung, and A. Yethiraj, *J. Phys. Chem. B* **118**, 8128 (2014).
- [15] M. J. Sanchez-Miranda, B. Bonilla-Capilla, E. Sarmiento-Gomez, E. Lazaro-Lazaro, A. Ramirez-Saito, M. Medina-Noyola, and J. L. Arauz-Lara, *Soft Matter* **11**, 655 (2015).
- [16] I. M. Tolić-Nørrelykke, E.-L. Munteanu, G. Thon, L. Oddershede, and K. Berg-Sørensen, *Phys. Rev. Lett.* **93**, 078102 (2004).
- [17] M. Weiss, M. Elsner, F. Kartberg, and T. Nilsson, *Biophys. J.* **87**, 3518 (2004).
- [18] M. T. Valentine, P. D. Kaplan, D. Thota, J. C. Crocker, T. Gisler, R. K. Prud'homme, M. Beck, and D. A. Weitz, *Phys. Rev. E* **64**, 061506 (2001).
- [19] A. Heuer, *J. Phys.: Condens. Matter* **20**, 373101 (2008).
- [20] L. Chen, M. Falcioni, and M. W. Deem, *J. Phys. Chem. B* **104**, 6033 (2000).
- [21] F. Córdoba-Valdés, R. Castañeda Priego, J. Timmer, and C. Fleck, *Soft Matter* **10**, 8475 (2014).
- [22] G. Guigas and M. Weiss, *Biophys. J.* **94**, 90 (2008).
- [23] A. H. Marcus, J. Schofield, and S. A. Rice, *Phys. Rev. E* **60**, 5725 (1999).
- [24] B. Cui, B. Lin, and S. A. Rice, *J. Chem. Phys.* **114**, 9142 (2001).
- [25] M. Bayer, J. M. Brader, F. Ebert, M. Fuchs, E. Lange, G. Maret, R. Schilling, M. Sperl, and J. P. Wittmer, *Phys. Rev. E* **76**, 011508 (2007).
- [26] R. Pastore, M. P. Ciamarra, G. Pesce, and A. Sasso, *Soft Matter* **11**, 622 (2015).
- [27] M. J. Saxton, *Biophys. J.* **66**, 394 (1994).
- [28] V. Krakoviack, *Phys. Rev. Lett.* **94**, 065703 (2005).
- [29] E. P. Bernard and W. Krauth, *Phys. Rev. Lett.* **107**, 155704 (2011).
- [30] P. Polanowski and A. Sikorski, *Soft Matter* **10**, 3597 (2014).
- [31] H. Löwen, *Phys. Rev. E* **53**, 53 (1996).
- [32] R. Zangi and S. A. Rice, *Phys. Rev. Lett.* **92**, 035502 (2004).
- [33] J. Kim, C. Kim, and B. J. Sung, *Phys. Rev. Lett.* **110**, 047801 (2013).
- [34] T. O. E. Skinner, S. K. Schnyder, D. G. A. L. Aarts, J. Horbach, and R. P. A. Dullens, *Phys. Rev. Lett.* **111**, 128301 (2013).
- [35] F. Evers, C. Zunke, R. D. L. Hanes, J. Bewerunge, I. Ladadwa, A. Heuer, and S. U. Egelhaaf, *Phys. Rev. E* **88**, 022125 (2013).
- [36] M. C. Jenkins and S. U. Egelhaaf, *J. Phys.: Condens. Matter* **20**, 404220 (2008).
- [37] J. C. Crocker and D. G. Grier, *J. Colloid Interface Sci.* **179**, 298 (1996).
- [38] T. R. M. Sales, *Opt. Eng.* **42**, 3084 (2003).
- [39] J. Bewerunge and S. U. Egelhaaf, *Phys. Rev. A* **93**, 013806 (2016).
- [40] A. Ashkin, *Phys. Rev. Lett.* **24**, 156 (1970).
- [41] A. Ashkin, *Biophys. J.* **61**, 569 (1992).
- [42] R. W. Bowman and M. J. Padgett, *Rep. Prog. Phys.* **76**, 28 (2013).
- [43] R. D. L. Hanes, C. Dalle-Ferrier, M. Schmiedeberg, M. C. Jenkins, and S. U. Egelhaaf, *Soft Matter* **8**, 2714 (2012).
- [44] L. van Hove, *Phys. Rev.* **95**, 249 (1954).
- [45] J.-P. Hansen and I. R. McDonald, *Theory of Simple Liquids*, 3rd ed. (Academic, London, 2006).
- [46] P. Hopkins, A. Fortini, A. J. Archer, and M. Schmidt, *The Journal of Chemical Physics* **133**, 224505 (2010).
- [47] J. N. Roux, J. L. Barrat, and J.-P. Hansen, *J. Phys.: Condens. Matter* **1**, 7171 (1989).
- [48] A. L. Thorneywork, R. E. Rozas, R. P. A. Dullens, and J. Horbach, *Phys. Rev. Lett.* **115**, 268301 (2015).
- [49] B. Bonilla-Capilla, A. Ramirez-Saito, M. A. Ojeda-Lopez, and J. L. Arauz-Lara, *J. Phys.: Condens. Matter* **24**, 464126 (2012).
- [50] M. A. Bevan and D. C. Prieve, *J. Chem. Phys.* **113**, 1228 (2000).
- [51] X. Ma, W. Chen, Z. Wang, Y. Peng, Y. Han, and P. Tong, *Phys. Rev. Lett.* **110**, 078302 (2013).
- [52] W. Kob, C. Donati, S. J. Plimpton, P. H. Poole, and S. C. Glotzer, *Phys. Rev. Lett.* **79**, 2827 (1997).
- [53] S. Sastry and P. G. Debenedetti, *Nature* **393**, 554 (1998).
- [54] L. J. Bonales, F. Martinez-Pedrero, M. A. Rubio, and F. Ortega, *Langmuir* **28**, 16555 (2012).
- [55] P. M. Richards, *Phys. Rev. B* **16**, 1393 (1977).
- [56] J.-P. Bouchaud and A. Georges, *Phys. Rep.* **195**, 127 (1990).
- [57] J. Kärger, M. Petzold, H. Pfeifer, S. Ernst, and J. Weitkamp, *Journal of Catalysis* **136**, 283 (1992).
- [58] F. Höfling, T. Franosch, and E. Frey, *Phys. Rev. Lett.* **96**, 165901 (2006).
- [59] J. Kärger, "Adsorption and diffusion," (Springer Berlin Heidelberg, Berlin, Heidelberg, 2008) Chap. Single-File Diffusion in Zeolites, pp. 329–366.
- [60] J. A. Dix and A. S. Verkman, *Annual Review of Biophysics Annual Review of Biophysics*, **37**, 247 (2008).
- [61] Y. Meroz and I. M. Sokolov, *Physics Reports* **573**, 1 (2015).
- [62] H. Löwen and G. Szamel, *J. Phys.: Condens. Matter* **5**, 2295 (1993).

3.7 Paper VII: Colloids in light fields: Particle dynamics in random and periodic energy landscapes

Journal: The European Physical Journal Special Topics

Reference: *Eur. Phys. J. Special Topics*, **222**, 2995 (2013)

Impact factor: 1.399

Authors: Florian Evers, Richard D. L. Hanes, Christoph Zunke, Ronja F. Capellmann, **Jörg Beyer**, Cecile Dalle-Ferrier, Matthew C. Jenkins, Imad Ladadwa, Andreas Heuer, Ramon Castañeda-Priego and Stefan U. Egelhaaf

5th author

5% contribution of JB

3.7 Paper VII: Colloids in light fields: Particle dynamics in random and periodic energy landscapes

This page has been left intentionally blank.

Colloids in light fields: particle dynamics in random and periodic energy landscapes

F. Evers,^{1,*} R.D.L. Hanes,¹ C. Zunke,¹ R.F. Capellmann,¹ J. Bewerunge,¹ C. Dalle-Ferrier,¹ M.C. Jenkins,¹ I. Ladadwa,^{2,3} A. Heuer,² R. Castañeda-Priego,⁴ and S.U. Egelhaaf^{1,†}

¹*Condensed Matter Physics Laboratory, Heinrich Heine University, 40225 Düsseldorf, Germany*

²*Institut für Physikalische Chemie, University Münster, 48149 Münster, Germany*

³*Fahad Bin Sultan University, 71454 Tabuk, Saudi-Arabia*

⁴*Division of Sciences and Engineering, University of Guanajuato, 37150 León, Mexico*

The dynamics of colloidal particles in potential energy landscapes have mainly been investigated theoretically. In contrast, here we discuss the experimental realization of potential energy landscapes with the help of light fields and the observation of the particle dynamics by video microscopy. The experimentally observed dynamics in periodic and random potentials are compared to simulation and theoretical results in terms of, e.g. the mean-squared displacement, the time-dependent diffusion coefficient or the non-Gaussian parameter. The dynamics are initially diffusive followed by intermediate subdiffusive behaviour which again becomes diffusive at long times. How pronounced and extended the different regimes are, depends on the specific conditions, in particular the shape of the potential as well as its roughness or amplitude but also the particle concentration. Here we focus on dilute systems, but the dynamics of interacting systems in external potentials, and thus the interplay between particle–particle and particle–potential interactions, is also mentioned briefly. Furthermore, the observed dynamics of dilute systems resemble the dynamics of concentrated systems close to their glass transition, with which it is compared. The effect of certain potential energy landscapes on the dynamics of individual particles appears similar to the effect of interparticle interactions in the absence of an external potential.

I. INTRODUCTION

The motion of colloidal particles in potential energy landscapes is a central process in statistical physics which is relevant for a variety of scientific and applied fields such as hard and soft condensed matter, nanotechnology, geophysics and biology [1–3]. Particle diffusion in periodic and random external fields is encountered in many situations [4–7], such as atoms, molecules, clusters or particles moving on a surface with a spatially varying topology or interaction [8], or moving through inhomogeneous bulk materials, e.g. porous media or gels [9], rocks [2], living cells or biological membranes [10–15]. It also includes the diffusion of charge carriers in a conductor with impurities [16, 17], particle diffusion on garnet films [18–20] or diffusion in optical lattices [21, 22], superdiffusion in active media [23], and vortex dynamics in superconductors [24]. Moreover, some processes are modelled by diffusion in the configuration space of the system, e.g. the glass transition [25–30] and protein folding [31–33].

Thermal energy drives the Brownian motion of colloidal particles [34, 35]. In free diffusion, their mean-squared displacement $\langle \Delta x^2(t) \rangle$ increases linearly with time t ; $\langle \Delta x^2(t) \rangle \propto t^\mu$ with $\mu = 1$. Particle–external potential (as well as particle–particle) interactions can modify the dynamics significantly leading to $\mu \neq 1$ [14, 36–42]. Often the dynamics slow down; on an intermediate time scale subdiffusion ($\mu < 1$) is observed, while at long times diffusion is reestablished with a reduced

(long-time) diffusion coefficient D_∞ . Different theoretical models have been developed to describe particle dynamics in external potentials, including the random barrier model [43], the random trap model [38, 44], the continuous time random walk [45], diffusion in rough and regular potentials [7, 46–48], the Lorentz gas model [49], and diffusion in quenched-annealed binary mixtures [50]. Typically, theories focus on the asymptotic long-time limit, which is often difficult to reach in experiments. In contrast, less is known about the behaviour at intermediate times, where the transitions between the different regimes occur. Furthermore, theoretical calculations have mainly been exploited to extract information from experimental data, while only recently have theoretical predictions been compared systematically with experiments [18–20, 51–58].

Here we thus focus on recent experimental results on the dynamics of colloidal particles in potential energy landscapes and their comparison to simulation and theoretical predictions. A prerequisite for systematic experiments is the controlled creation of external potential energy landscapes. This, for example, is possible due to the interaction of colloidal particles with light [59–66]. The effect of light on particles with a refractive index different (typically larger) from the one of the surrounding liquid is usually described by two forces: a scattering force or ‘radiation pressure’, which pushes the particles along the light beam, and a gradient force, which pulls particles toward regions of high light intensity. A classical application of this effect is optical tweezers which are used to trap and manipulate individual particles or ensembles of particles by a tightly focused laser beam or several laser beams, respectively [65–68]. Extended light fields rather than light beams can be used to create potential energy

* Florian.Evers@hhu.de

† Stefan.Egelhaaf@hhu.de

3.7 Paper VII: Colloids in light fields: Particle dynamics in random and periodic energy landscapes

2

landscapes. Arbitrary light fields can be generated using a spatial light modulator [61, 68] or an acousto-optic deflector [63, 64, 69], while crossed laser beams [60], diffrusers [70] and other optical devices can be used to create particular high-quality light fields (Sec. II).

Light fields can affect the arrangement and dynamics of colloidal particles within individual phases but can also induce phase changes. For example, upon increasing the amplitude of a periodic light field applied to a colloidal fluid, a disorder-order transition is induced in a two-dimensional charged colloidal system, known as light-induced freezing [41, 71–73]. A further increase of the amplitude results in the melting of the crystal into a modulated liquid; this process is called light-induced melting. Extended light fields can also be applied to direct heterogeneous crystallization and hence the structure and unit cell dimensions of the formed bulk crystals or quasi-crystals [74–78]. Using light fields, the effect of periodic as well as random potentials on the particle dynamics has been experimentally investigated [52–54] and compared to simulation and theoretical predictions [7, 38–40, 46, 54–56, 79, 80]. Most of the theoretical predictions only concern the asymptotic long-time behaviour. Possible links between the long-time behaviour and the intermediate dynamics, as observed in the experiments, are discussed [53, 56, 81]. Furthermore, the dynamics of individual particles in sinusoidal potentials are showing similarities with the dynamics in glasses [54, 82]. Inspired by this idea, in this review the dynamics of individual particles in different external potentials are compared to the dynamics of concentrated hard spheres [29, 83, 84]. Energy landscapes are not only considered in the context of glasses, but random energy landscapes with a Gaussian distribution of energy levels of width $\varepsilon \approx \mathcal{O}(k_B T)$, where $k_B T$ is the thermal energy, seem to be relevant for proteins, RNA and transmembrane helices [85, 86]. Moreover, the diffusion (or ‘permeation’) of rodlike viruses through smectic layers can be described by the diffusion in a sinusoidal potential of amplitude $\varepsilon \approx k_B T$ [87, 88].

II. COLLOIDS IN LIGHT FIELDS: CREATION OF POTENTIAL ENERGY LANDSCAPES

The optical force on a colloidal particle has been investigated extensively, in particular in the context of optical tweezers [62–67, 89–95]. We consider a transparent colloidal particle with a refractive index n_c suspended in a medium with a smaller refractive index n_m , that is $n_c > n_m$, and begin with the case of a particle much larger than the wavelength of light. In this case, the simple picture of ray optics applies. If light is incident on a particle, it will be scattered and reflected. While light arrives from only one direction, the scattered and reflected light travels in different directions. Hence the direction of the light and accordingly the momenta of the photons are changed. Due to conservation of momentum, an equal

but opposite momentum change will be imparted on the particle. The rate of momentum change determines the force on the particle, which acts in the direction of light propagation and might, e.g. due to the astigmatism of the objective, also have effects outside the main beam [96]. This is the so-called scattering force or, considering the photon ‘bombardment’, the radiation pressure.

When hitting the particle, the light beam will also be refracted, that is the particle acts as a (microscopic) lens. This, again, changes the direction of the beam and hence the momentum of the photons. The resulting force pushes the particle toward higher light intensities, mainly into the centre of the beam. This is the gradient force, which acts in lateral direction and gradients typically also exist in axial direction, e.g. toward a focus. This decomposition of the optical force into two components, the scattering and gradient forces, is done traditionally although both originate from the same physics.

If the particle with radius R is much smaller than the wavelength of light, λ , that is in the so-called Rayleigh regime, the particle’s polarizability is considered. The electric field of the light induces an oscillating dipole in the dielectric particle, which re-radiates light. This leads to the scattering force [91–94]

$$F_{\text{scatt}} = \frac{\sigma n_m}{c} I_0 \quad \text{with} \quad \sigma = \frac{128\pi^5 R^6}{3\lambda^4} \left(\frac{m^2 - 1}{m^2 + 2} \right)^2, \quad (1)$$

where I_0 is the incident light intensity, σ the scattering cross section of a spherical particle, c the speed of light and $m = n_c/n_m$.

The incident light intensity is typically inhomogeneous, $I_0(\vec{r})$, which leads to a further (component of the) force acting on the particle. An induced dipole in an inhomogeneous electric field experiences a force in the direction of the field gradient, the gradient force [93, 94]

$$F_{\text{grad}} = \frac{2\pi\alpha}{cn_m} \vec{\nabla} I_0(\vec{r}) \quad \text{with} \quad \alpha = n_m^2 R^3 \left(\frac{m^2 - 1}{m^2 + 2} \right), \quad (2)$$

where α characterises the polarizability of a sphere. The gradient force pushes particles with $n_c > n_m$ towards regions of higher intensity.

In the experiments described in the following, the particles are of comparable size to the wavelength of light. However, this case is much more difficult to model [63, 64, 97, 98] and will thus not be described here.

In optical tweezers, tightly focused laser light is used to trap particles. In contrast, exploiting the gradient force, here, extended spatially modulated light fields are applied to create potential energy landscapes [60]. The modulations in the potential are relatively weak such that typically particles are not trapped for long times, but only remain for some time in certain areas. Since the light field acts on the whole volume of the particle, its volume has to be convoluted with the light intensity to obtain the potential felt by the particle. Depending on the size of the particle and the modulation of the light field, the centre of the particle might thus be attracted to

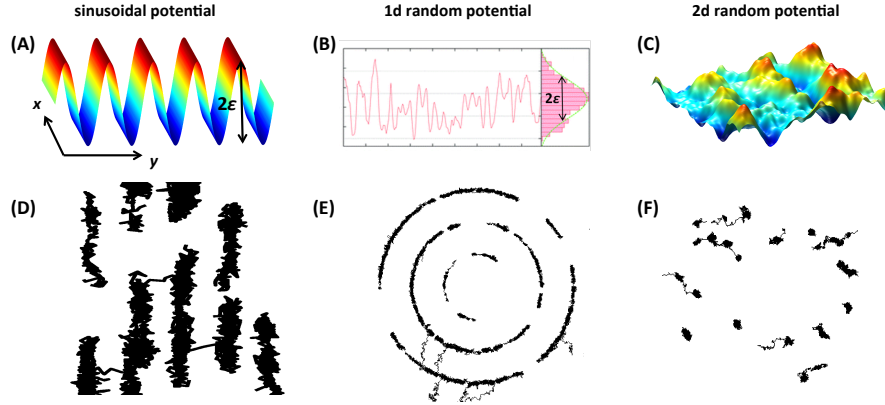


FIG. 1. (top) Schematic representations of the potential energy landscapes as felt by the particles and as reconstructed from experimental data (left to right): sinusoidally-varying periodic potential [54], one- and two-dimensional random potentials [52, 53]. For the one-dimensional random potential, the histogram of values of the potential, $p(U)$, is shown and compared to a Gaussian distribution (green line). (bottom) Representative particle trajectories in these potentials. The one-dimensional random potential was arranged in large circles to obtain ‘periodic boundary conditions’ and to improve the statistics by simultaneously investigating several circles.

bright or dark regions [60]. Furthermore, it is difficult to impose potentials with features smaller than the particle size.

Extended space- and also time-dependent light fields can be created using various optical devices, e.g. holographic instruments based on a spatial light modulator (SLM) [61, 67, 68] or an acoustic-optic deflector (AOD) [69]. Spatial light modulators use arrays of liquid-crystal pixels. Each pixel imposes a modulation of the phase, amplitude or polarization, which can be externally controlled. This allows creation of almost any light field, within the limits of the finite size, pixelation and modulation resolution of the SLM. The latter result in a noise component in the light field. This can be exploited to create random potentials. It can also be avoided by cycling different realizations of the same light field but with different phases, with a refresh rate beyond the structural relaxation rate of the sample [52, 53, 99]. Furthermore, the dynamic possibilities of a holographic instrument can be improved by combining it with galvanometer-driven mirrors [68].

A conceptually simple but more specialized set-up is based on a crossed-beam geometry, which yields a standing wave pattern, i.e. a sinusoidally-varying periodic light field, within an overlying Gaussian envelope due to the finite size of the beams [60, 72, 73, 100–102]. Moreover, optical devices, such as diffusors, can be used to generate special beam shapes like top-hat geometries or randomly-varying light fields [70].

While the gradient force is exploited to impose extended modulated potentials, whose amplitude is typically controlled by the laser power, the scattering force or radiation pressure will also affect the sample. The radiation pressure determines the distance of the particle

from the cover slip, which will thus depend on the laser power. Due to hydrodynamic interactions, the distance to the cover slip affects the diffusion of the particle, which typically is reduced compared to free diffusion [103–105]. The experimental data presented in the following are corrected for this effect.

III. DYNAMICS OF INDIVIDUAL COLLOIDS IN PERIODIC AND RANDOM POTENTIALS

Individual colloidal particles have been exposed to different potential energy landscapes (Fig. 1, top): sinusoidally-varying periodic potentials $U(y) = \varepsilon \sin(2\pi y/\lambda)$ with amplitude ε and wavelength λ (Fig. 1A), as well as one- and two-dimensional random potentials with a Gaussian distribution of potential values with (full) width 2ε (Fig. 1B,C). For the one-dimensional random potential, figure 1B shows the histogram of values of the potential, $p(U)$, which follows a Gaussian distribution $p(U) \propto \exp\{-(U - \langle U \rangle)^2/2\varepsilon^2\}$. In the experiments, the periodic potentials were generated using crossed laser beams [54, 60] and the random potentials using a spatial light modulator [52, 53, 68] (Sec. II).

The particle motions were monitored by video microscopy and the particle trajectories recovered by particle tracking algorithms [106, 107]. In the absence of a light field, i.e. without an external potential, colloidal particles undergo free diffusion, thus exploring large areas. However, in the presence of external potentials, the particle dynamics are modified (Fig. 1, bottom). The trajectories and hence the excursions of the particles were limited with the particles remaining for extended periods at positions that correspond to local minima of the

3.7 Paper VII: Colloids in light fields: Particle dynamics in random and periodic energy landscapes

4

potential. In the periodic potential, anisotropic trajectories were observed (Fig. 1D). Particle motion along the valleys (x direction) was unaffected, while their motion across the maxima (y direction) was hindered by barriers of height 2ε .

In the one-dimensional random potentials, the particles remained for different periods of time at different positions, reflecting the randomly-varying potential values along the circular path (Fig. 1E). (The circular paths provided ‘periodic boundary conditions’ and the use of several circles helped to improve statistics.) Similarly, in the two-dimensional random potentials, the motion of the particles was limited due to the presence of local potential minima and saddle points (Fig. 1F). Upon increasing the amplitude of the oscillations or the amplitude of the roughness, ε , the particles were more efficiently trapped and hence explored an even smaller region.

Based on the particle trajectories, different parameters were computed to characterize the particle dynamics quantitatively in the presence of external potentials. The mean-squared displacement (MSD) is calculated according to

$$\langle \Delta x^2(t) \rangle = \left\langle [x_i(t_0 + t) - x_i(t_0)]^2 \right\rangle_{t_0, i} - \langle [x_i(t_0 + t) - x_i(t_0)] \rangle_{t_0, i}^2, \quad (3)$$

where the second term corrects for possible drifts. For both, experiments and simulations, the average is taken over particles i and waiting time t_0 to improve statistics. The average over t_0 affects the results [55, 56], because initially the particles are randomly distributed while the distribution of occupied energy levels evolves toward a Boltzmann distribution. To render the data independent of the specific experimental conditions, $\langle \Delta x^2(t) \rangle$ was normalized by the square of the particle radius R^2 , and the time t by the Brownian time $t_B = R^2/(2dD_0)$ with the short-time diffusion coefficient D_0 and the dimension d .

From the MSD, the normalized time-dependent diffusion coefficient $D(t)/D_0$ is calculated according to

$$\frac{D(t)}{D_0} = \frac{\partial \langle \langle \Delta x^2(t) \rangle / R^2 \rangle}{\partial \log(t/t_B)}, \quad (4)$$

while the slope of the MSD in double-logarithmic representation

$$\mu(t) = \frac{\partial \log \langle \langle \Delta x^2(t) \rangle / R^2 \rangle}{\partial \log(t/t_B)} \quad (5)$$

corresponds to the exponent in the relation $\langle \Delta x^2(t) \rangle \sim t^{\mu(t)}$ and quantifies deviations from diffusive behaviour: for free diffusion $\mu = 1$, while $\mu < 1$ for subdiffusion and $\mu > 1$ for superdiffusion. In addition, the non-Gaussian parameter [82]

$$\alpha_2(t) = \frac{\langle \Delta x^4(t) \rangle}{(1 + 2/d) \langle \Delta x^2(t) \rangle^2} - 1 \quad (6)$$

characterizes the deviation of the distribution of particle displacements from a Gaussian distribution and represents the first non-Gaussian correction [108]. In the

two-dimensional case, the analogous equation based on $\langle \Delta r^2(t) \rangle$ and $\langle \Delta r^4(t) \rangle$ was calculated and has the corresponding meaning.

The effect of potential shape and amplitude on the particle dynamics was investigated in experiments [52–54], simulations [55, 56] and theory [54, 80], which all show consistent results (Fig. 2). Without an external potential ($\varepsilon = 0$), the MSD increases linearly with time and the diffusion coefficient $D(t)/D_0 \approx 1$, exponent $\mu(t) \approx 1$ and non-Gaussian parameter $\alpha_2(t) \approx 0$ are all independent of time, as expected for free diffusion. In contrast, in the presence of a periodic or random potential, the particle dynamics exhibit three distinct regimes which will be discussed in turn in the following. (Note that in the case of the sinusoidal potential, we only discuss the motion across the barriers, i.e. in y direction.)

At short times, the particle dynamics are diffusive and follow the potential-free case. This reflects small excursions within local minima and hence shows no significant dependence on the amplitude ε .

At intermediate times, the MSDs exhibit inflection points or plateaux, which become increasingly pronounced as ε increases. This corresponds to the decrease of the diffusion coefficients $D(t)/D_0$ from 1 to significantly lower values, the decrease of the exponent $\mu(t)$ and the increase of the non-Gaussian parameter $\alpha_2(t)$. The subdiffusive behaviour is caused by the particle being trapped in local minima for extended periods before it can escape to a neighbouring minimum.

In the case of the periodic potential, the barriers are all of equal height, 2ε , and thus the residence time distribution is relatively narrow. This is reflected in the reduced MSDs, the very pronounced and relatively quick decrease in $D(t)/D_0$ and $\mu(t)$ and increase in $\alpha_2(t)$. Thus, the minima in $\mu(t)$ and maxima in $\alpha_2(t)$ occur at relatively short times, $t_{\mu, \min}$ and $t_{\alpha, \max}$, respectively (Fig. 3, blue solid symbols). The minima in $\mu(t)$ occur earlier than the maxima in $\alpha_2(t)$. This is due to the fact that the minimum in $\mu(t)$ reflects the largest deviation from diffusive behaviour, i.e. when the probability to be (still) stuck in a minimum is largest and thus diffusion is most efficiently suppressed, whereas the maximum in $\alpha_2(t)$ indicates the largest deviation from the Gaussian distribution of displacements, i.e. the dynamics are maximally heterogeneous with some minima having been left a long time ago, some only recently, with others yet to be left. The maximum in $\alpha_2(t)$ thus only appears once jumps have occurred, which happens after the minimum in $\mu(t)$, and hence $t_{\mu, \min} < t_{\alpha, \max}$. This also implies a weak ε dependence of $t_{\mu, \min}$ and a significant ε dependence of $t_{\alpha, \max}$ since ε determines the height of the barrier which has to be crossed. Similarly, the intermediate regime ends once the particle escapes the minima and performs a random walk between different minima with the diffusion coefficient $D(t)/D_0$, $\mu(t)$ and $\alpha_2(t)$ reaching the plateau values, unity and zero, respectively. Again, since all barrier heights are identical, this occurs within a short period of time. Nevertheless, the time required to reach the end

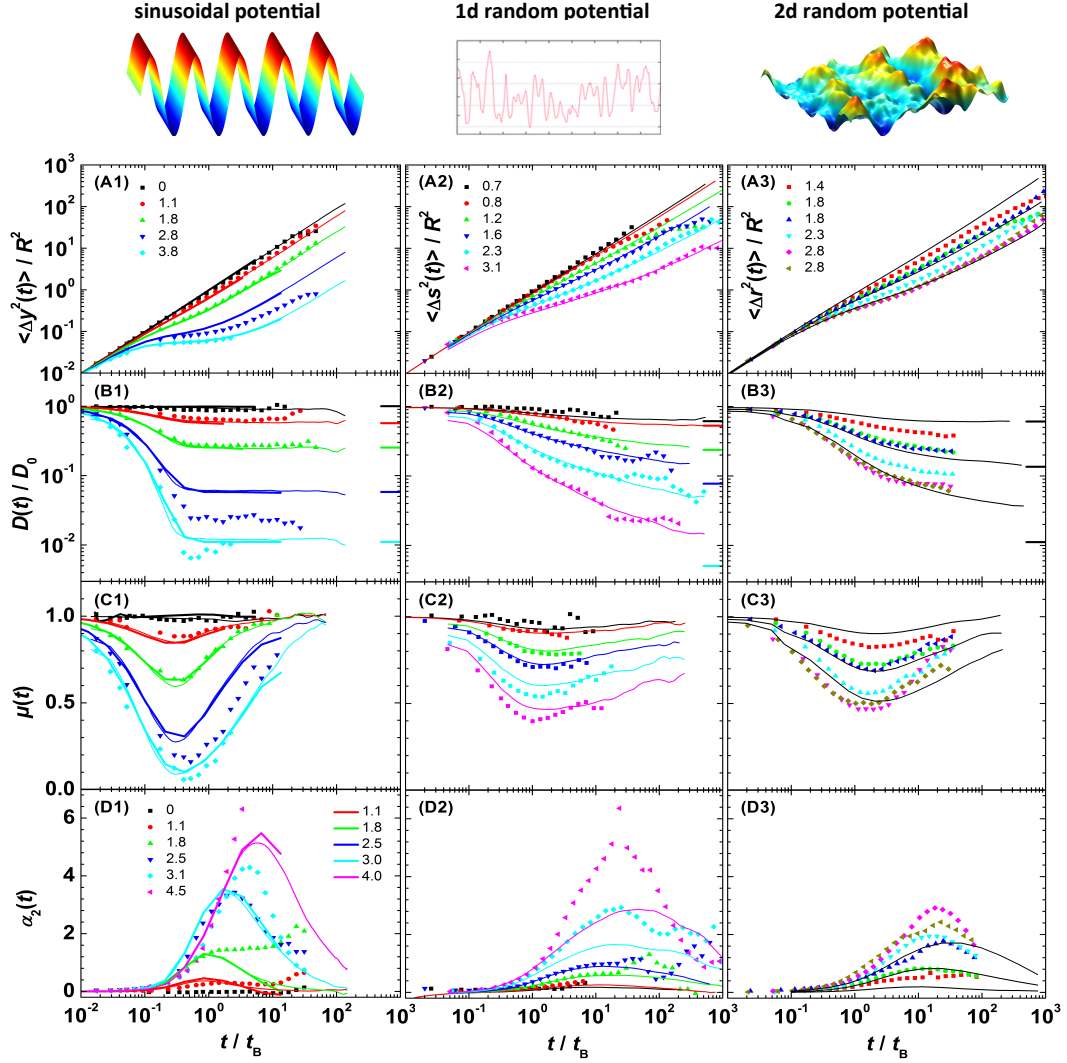


FIG. 2. Particle dynamics in (left to right) sinusoidally-varying periodic [54], one-dimensional random [52] and two-dimensional random potentials [53] as characterized by (top to bottom) the normalized mean-squared displacements (where the normalization has been done according to the specific potential shape), the normalized time-dependent diffusion coefficient $D(t)/D_0$, the exponent $\mu(t)$ in the relation $\langle \Delta x^2(t) \rangle \propto t^{\mu(t)}$, and the non-Gaussian parameter $\alpha_2(t)$ for different potential amplitudes and degrees of roughness ε (as indicated in the legends, in units of $k_B T$). Experimental data are represented by symbols, simulations by solid lines, theoretical predictions (for the periodic potential) by thick lines. Theoretical predictions for D_∞/D_0 are indicated by horizontal lines.

of the intermediate regime and hence the long-time diffusive limit, quantified either by $\mu \rightarrow 1$, i.e. $t_{\mu,\infty}$, or by $\alpha_2 \rightarrow 0$, i.e. $t_{\alpha,\infty}$, strongly depends on ε .

In the other case, i.e. in the presence of a random potential, there exists a wide range of barrier heights and thus residence times. This is reflected in the less pronounced plateaux or rather inflection points in the

MSDs, a very slow decrease of $D(t)/D_0$ with very slow approaches to the long-time plateaux as well as a slow decrease and increase of $\mu(t)$ and $\alpha_2(t)$, respectively, and in particular an extremely slow return of $\mu(t)$ and $\alpha_2(t)$ to 1 and 0, respectively. Therefore, the intermediate subdiffusive regime, as indicated by the range from $t_{\mu,\min}$ and $t_{\alpha,\max}$ to $t_{\mu,\infty}$ and $t_{\alpha,\infty}$, occurs relatively late and in par-

3.7 Paper VII: Colloids in light fields: Particle dynamics in random and periodic energy landscapes

6

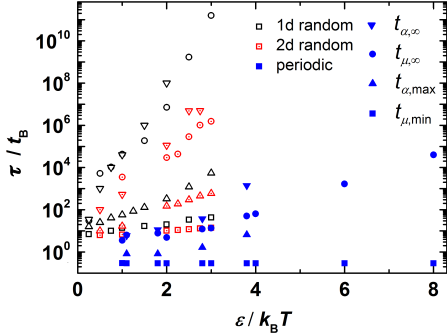


FIG. 3. Characteristic time scales τ in sinusoidally-varying periodic, one-dimensional and two-dimensional random potentials (as indicated and explained in the text). Data for the periodic potential are extracted from theoretical results. For the random potentials, data are retrieved from simulation data not averaged over waiting times t_0 [55, 56].

ticular extends over a broad range of times with a strong ε dependence (Fig. 3), where the particular ε dependence of $t_{\mu,\infty}$ and $t_{\alpha,\infty}$ is still under debate [53, 81]. For the one-dimensional random potential, subdiffusion is more pronounced than for the two-dimensional random potential, since in two dimensions maxima can be avoided and only saddle points need to be crossed. For the same reason, in one dimension, the ε dependence appears stronger and the intermediate regime extends to longer times. Thus, in the one-dimensional random potential the intermediate subdiffusive regime covers a longer time period than in the two-dimensional case, which in turn is longer and shows a stronger ε dependence than in the periodic potential. Moreover, increasing amplitude ε has similar effects for all potential shapes: First, the subdiffusive behaviour becomes more pronounced. Second, the intermediate regime extends to longer times, indicated by the slow returns of $\mu(t)$ and $\alpha_2(t)$ to 1 and 0, respectively. However, the beginning of the intermediate regime, characterized by the maxima in $\mu(t)$ and minima in $\alpha_2(t)$ and the corresponding times $t_{\mu,\min}$ and $t_{\alpha,\max}$, remains at about the same time with a weak ε dependence since no or only a few barrier crossings are involved. [109] Extrapolations of the characteristic times τ to vanishing potential amplitudes results in different values $\tau(\varepsilon \rightarrow 0)$ for the different potential shapes. Although unexpected, this might be related to the definitions of the amplitude ε for the periodic and random potentials, respectively, and to the fact that without an external potential, i.e. $\varepsilon = 0$, $\mu(t) = 1$ and $\alpha_2(t) = 0$ and thus no minimum in $\mu(t)$ and no maximum in $\alpha_2(t)$ exist and hence $\tau(\varepsilon=0)$ is not defined.

At very long times, again diffusive behaviour is observed with constant, but much smaller D_∞/D_0 and $\mu(t)$ returning to 1 and $\alpha_2(t)$ to 0. On long time scales, hop-

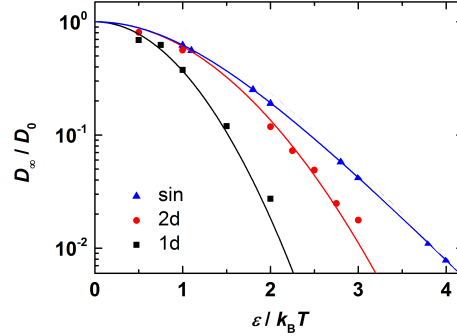


FIG. 4. Normalized long-time diffusion coefficient $D_\infty(\varepsilon)/D_0$ in one- and two-dimensional random potentials and sinusoidally-varying periodic potentials (left to right). Solid lines indicate theoretical predictions [7, 46, 80], symbols simulation results that have not been averaged over waiting times t_0 [54–56].

ping between minima becomes possible and, once more, the dominant process is a random walk, now between minima. The return to diffusion is fast in the case of the periodic potential, since very deep minima are absent, but slow in the two- and especially the one-dimensional random potential. With increasing amplitude ε , one notices increasingly long times to reach the asymptotic long-time limit (Fig. 3) and a decrease of the long-time diffusion coefficient $D_\infty(\varepsilon)$ (Fig. 4), which has been calculated for different potential shapes. For a periodic sinusoidal potential [54, 80]

$$\frac{D_\infty(\varepsilon)}{D_0} = J_0^{-2} \left(\frac{\varepsilon}{k_B T} \right) \approx 2\pi \left(\frac{\varepsilon}{k_B T} \right) e^{\left(\frac{-2\varepsilon}{k_B T} \right)}, \quad (7)$$

where J_0 is the Bessel function of the first kind of order 0 and the approximation holds for $\varepsilon \gg k_B T/2$ [54]. In the case of one- and two-dimensional random potentials one finds [7, 46, 110–112]

$$\frac{D_\infty(\varepsilon)}{D_0} = e^{-\frac{1}{d} \left(\frac{\varepsilon}{k_B T} \right)^2}. \quad (8)$$

In the case of a two-dimensional random potential, $D_\infty(\varepsilon)$ is larger because maxima can be avoided and only saddle points have to be crossed. Nevertheless, the exponential dependence on $-(\varepsilon/k_B T)^2$ remains, which is the ratio of the equilibrium energy of a Gaussian distribution, $-\varepsilon^2/k_B T$, and the thermal energy $k_B T$. The first term describes the equilibrium energy and dominates the dependence of the activation barriers on temperature, because the typical barrier energies to be overcome when moving between different regions are essentially independent of the thermal energy, as suggested by the percolation picture [113]. The theoretical predictions and simulation as well as experimental data agree (Fig. 4), except at large ε where deviations are noticeable. Figure 4

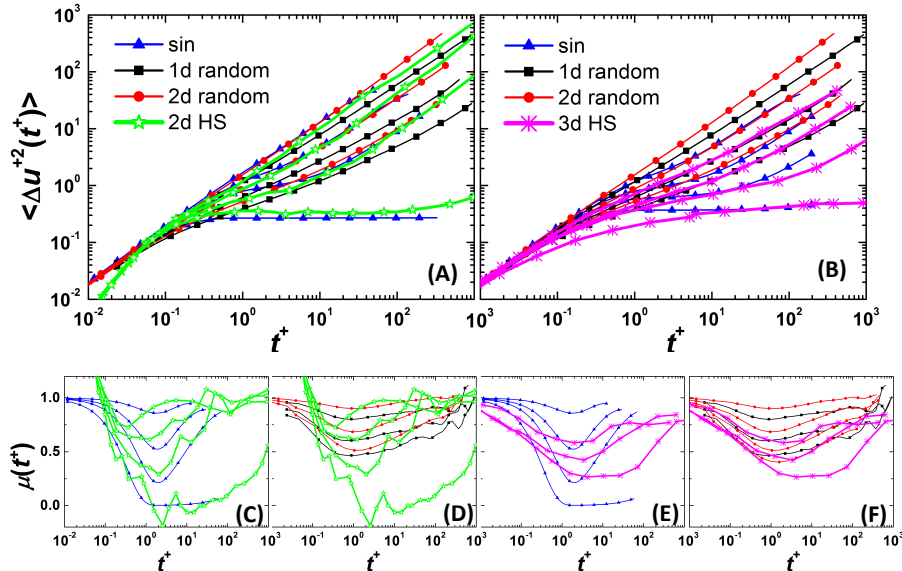


FIG. 5. Effect of particle-particle and particle-potential interactions on the particle dynamics. The dynamics of individual particles in sinusoidally-varying periodic and one- and two-dimensional random potentials (thin lines with symbols as indicated) [52–54] are compared to (A,C,D) (quasi) two-dimensional concentrated hard discs [83] and (B,E,F) three-dimensional concentrated hard spheres [29], the latter two in the absence of an external potential (thick lines as indicated). (A,B) Dimensionless mean squared displacements and (C–F) exponent $\mu(t)$ as function of dimensionless time. To allow for a comparison, both the mean squared displacement and the time have been normalized by typical length scales of the corresponding systems, indicated by the parameters $\langle \Delta u^{+2}(t^+) \rangle$ and t^+ . Shown are the theoretical predictions for individual particles in periodic potentials with amplitude (A,C) $\varepsilon/k_B T = 1, 2, 3, 8$ and (B,E) $2, 3, 4, 6$ [54], simulation results for individual particles in one-dimensional random potentials with amplitude $\varepsilon/k_B T = 1.2, 2.3, 3.1$ [56] and in two-dimensional random potentials with amplitude $\varepsilon/k_B T = 1.0, 2.0, 3.0$ [53, 55], simulation results for concentrated hard discs with surface fractions $\sigma = 0.68, 0.69, 0.70, 0.715$ in the absence of an external potential [83], experimental data for concentrated hard spheres with volume fractions $\Phi = 0.466, 0.519, 0.558, 0.583$ in the absence of an external potential [29] (all top to bottom).

shows the theoretical predictions and simulation results, the latter agreeing with the experimental data (Fig. 2). The slightly higher data are due to the fact that even for the longest investigated times the asymptotic long-time limit is not quite reached for the largest ε (Fig. 2). Moreover, the data suggest that the time to reach the long-time limit, characterised by $t_{\mu,\infty}(\varepsilon)$ or $t_{\alpha,\infty}(\varepsilon)$ (Fig. 3), is not related to $D_\infty(\varepsilon)^{-1}$ (Fig. 4).

The particle dynamics in periodic and random potentials as discussed above, resemble the dynamics of concentrated systems, whose subdiffusive behaviour has been associated with caging by neighbouring particles [114–116]. Thus particle-potential and particle-particle interactions seem to have similar effects on the particle dynamics. Their effects lead to characteristic signatures especially in the intermediate regime, which was described above. We hence can compare the dynamics of individual particles in external potentials and concentrated interacting particles without external potential (Fig. 5), namely experimental data from a three-dimensional bulk system containing hard spheres of different volume fractions [29] and experimental as well as simulation data

from (quasi) two-dimensional systems of hard discs with different surface fractions [83, 84]. The dynamics of the concentrated two-dimensional system and the individual particles in the periodic potential are strikingly similar (Fig. 5A,C), while the dynamics in the random potentials appear different (Fig. 5A,D). In contrast, the dynamics of the concentrated three-dimensional system seem different from the individual particles in the periodic potential, for example the intermediate MSD is broader (Fig. 5B,E), while it resembles the dynamics in the random potentials (Fig. 5B,F).

IV. DYNAMICS OF INTERACTING COLLOIDS IN PERIODIC AND RANDOM POTENTIALS

So far the dynamics of individual colloidal particles in periodic and random potentials were considered. It shows striking similarities with the dynamics of concentrated suspensions without external potentials [29, 83, 84]. The combined effect of particle-potential and particle-particle interactions is hence briefly discussed. An in-

3.7 Paper VII: Colloids in light fields: Particle dynamics in random and periodic energy landscapes

8

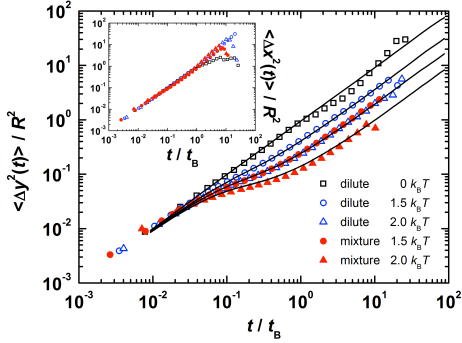


FIG. 6. Particle dynamics, namely MSD across the barriers, i.e. in y direction (main figure), and along the valleys, i.e. in x direction (inset), of an individual dilute large particle ($R_1 = 2.5 \mu\text{m}$, open symbols) and concentrated large particles in a binary mixture ($R_1 = 2.5 \mu\text{m}$, $R_2 = 1 \mu\text{m}$, total surface fraction $\sigma \approx 0.57$ with an about equal number of large and small spheres, filled symbols), both in sinusoidally-varying periodic potentials with wavelength $\lambda = 5.2 \mu\text{m}$ and different amplitudes (as indicated). Lines represent Brownian Dynamics simulations of individual particles in a periodic potential with $\varepsilon/k_B T = 0.0, 1.5, 2.0, 2.5$.

crease of the particle concentration in a one-dimensional channel leads to single file diffusion with $\langle \Delta x^2(t) \rangle \sim t^{0.5}$ [117], which becomes more complex if a periodic potential is present along the channel [42]. Also in two-dimensional potentials an interplay between the particle-potential and particle-particle interactions was observed [41], which, under the investigated conditions, may be linked to changes in the particle arrangement, caused by laser-induced freezing and melting [71–73]. More complex potential-induced disorder-order and disorder-disorder transitions have been theoretically investigated in mixtures, namely colloid-polymer mixtures and binary hard discs [118–120]. The dynamics of binary colloidal mixtures with large size disparity have been investigated without the presence of an external potential [121, 122]. Here, we focus on the dynamics of concentrated binary hard sphere mixtures in a periodic potential, with the mixture in the modulated liquid state. The MSDs of individual particles (similar to those in Sec. III) and of interacting particles in the presence of smaller particles in a periodic potential are determined (Fig. 6). No signature of single-file diffusion could be observed in the MSDs along the valleys, i.e. in x direction (Fig. 6, inset). Across the barriers, i.e. in y direction, the MSDs of the interacting large particles in the binary mixture (in a periodic potential with amplitude ε) resemble the MSDs of indi-

vidual large particles (in a periodic potential with a larger amplitude ε'). For the present conditions, in particular surface fraction $\sigma \approx 0.57$, we found $\varepsilon' \approx \varepsilon + 0.5 k_B T$. Moreover, the MSDs of the individual and interacting particles in a periodic potential agree with Brownian Dynamics simulations of an individual particle in a periodic potential (Fig. 6, lines). Similar observations have been made for interacting quasi-monodisperse particles in periodic and random potentials [79, 123].

V. CONCLUSION

Optical devices, such as spatial light modulators and acousto-optic deflectors, can be exploited to create a large variety of modulated light fields. Due to the polarizability of colloidal particles, this translates into potential energy landscapes of almost any shape. The large flexibility, together with the possibility to observe and track colloidal particles by video microscopy, provides an ideal experimental tool to systematically and quantitatively investigate fundamental questions in statistical physics. Here we focused on individual Brownian particles, but also briefly mentioned interacting particles, in periodic and random potentials. The experimental findings were compared to simulation results and theoretical predictions. While the latter mainly concerns the long-time asymptotic limit, the experiments and simulations also provide detailed quantitative information on the intermediate dynamics, which exhibit subdiffusive behaviour. This was compared to the distinct intermediate dynamics of concentrated colloidal suspensions, thus comparing particle-potential and particle-particle interactions. The interplay between these interactions was also illustrated using concentrated binary mixtures in external potentials. The dynamics of concentrated interacting particles in potential energy landscapes deserve further work, which will also be extended to time-dependent potentials.

ACKNOWLEDGEMENT

We gratefully acknowledge support by the Deutsche Forschungsgemeinschaft (DFG) through the SFB-Transregio TR6 “The Physics of Colloidal Dispersions in External Fields” (project C7), the Research Unit FOR 1394 “Nonlinear Response to Probe Vitrification” and the International Helmholtz Research School ‘BioSoft’. C. D.-F. thanks the Humboldt foundation for the award of a fellowship. We thank H.E. Hermes, J. Horbach, M. Laurati, H. Löwen, K.J. Mutch, P. Nielaba, K. Sandomirski, M. Schmiedeberg, D. Wagner, A. Yethiraj for very helpful discussions.

[1] J.-P. Bouchaud and A. Georges, Phys. Rep. **195**, 127 (1990).

[2] M. Sahimi, Rev. Mod. Phys. **65**, 1393 (1993).

- [3] J. Sancho and A. Lacasta, *Eur. Phys. J. Spec. Top.* **187**, 49 (2010).
- [4] J. Haus and K. Kehr, *Phys. Rep.* **150**, 263 (1987).
- [5] S. Havlin and D. Ben-Avraham, *Adv. Phys.* **36**, 695 (1987).
- [6] P. G. Wolynes, *Acc. Chem. Res.* **25**, 513 (1992).
- [7] D. S. Dean, I. T. Drummond, and R. R. Horgan, *J. Stat. Mech.*, P07013 (2007).
- [8] J. M. Sancho, A. M. Lacasta, K. Lindenberg, I. M. Sokolov, and A. H. Romero, *Phys. Rev. Lett.* **92**, 250601 (2004).
- [9] R. M. Dickson, D. J. Norris, Y.-L. Tzeng, and W. E. Moerner, *Science* **274**, 966 (1996).
- [10] G. Seisenberger, M. U. Ried, T. Endreß, H. Büning, M. Hallek, and C. Bräuchle, *Science* **294**, 1929 (2001).
- [11] M. Weiss, M. Elsner, F. Kartberg, and T. Nilsson, *Biophys. J.* **87**, 3518 (2004).
- [12] I. M. Tolić-Nørrelykke, E.-L. Munteanu, G. Thon, L. Oddershede, and K. Berg-Sørensen, *Phys. Rev. Lett.* **93**, 078102 (2004).
- [13] D. S. Banks and C. Fradin, *Biophys. J.* **89**, 2960 (2005).
- [14] F. Höfling and T. Franosch, *Rep. Prog. Phys.* **76**, 046602 (2013).
- [15] E. Barkai, Y. Garini, and R. Metzler, *Phys. Today* **65**, 29 (2012).
- [16] A. Byström and A. M. Byström, *Acta Crystallogr.* **3**, 146 (1950).
- [17] A. Heuer, S. Murugavel, and B. Roling, *Phys. Rev. B* **72**, 174304 (2005).
- [18] P. Tierno, P. Reimann, T. H. Johansen, and F. Sagués, *Phys. Rev. Lett.* **105**, 230602 (2010).
- [19] P. Tierno, F. Sagués, T. H. Johansen, and T. M. Fischer, *Phys. Chem. Chem. Phys.* **11**, 9615 (2009).
- [20] P. Tierno, F. Sagués, T. H. Johansen, and I. M. Sokolov, *Phys. Rev. Lett.* **109**, 070601 (2012).
- [21] F.-R. Carminati, M. Schiavoni, L. Sanchez-Palencia, F. Renzoni, and G. Grynberg, *Eur. Phys. J. D.* **17**, 249 (2001).
- [22] M. Šiler and P. Zemánek, *New J. Phys.* **12**, 083001 (2010).
- [23] K. M. Douglass, S. Sukhov, and A. Dogariu, *Nat. Phot.* **6**, 833 (2012).
- [24] K. Harada, O. Kamimura, H. Kasai, T. Matsuda, A. Tonomura, and V. V. Moshchalkov, *Science* **274**, 1167 (1996).
- [25] A. Heuer, *J. Phys.: Condens. Matter* **20**, 373101 (2008).
- [26] P. G. Debenedetti and F. H. Stillinger, *Nature* **410**, 259 (2001).
- [27] C. A. Angell, *Science* **267**, 1924 (1995).
- [28] W. C. K. Poon, *J. Phys.: Condens. Matter* **14**, R859 (2002).
- [29] W. van Meegen, T. C. Mortensen, S. R. Williams, and J. Müller, *Phys. Rev. E* **58**, 6073 (1998).
- [30] A. Heuer, B. Doliwa, and A. Saksangwijit, *Phys. Rev. E* **72**, 021503 (2005).
- [31] R. B. Best and G. Hummer, *Phys. Chem. Chem. Phys.* **13**, 16902 (2011).
- [32] C. M. Dobson, A. Sali, and M. Karplus, *Angew. Chem. Int. Ed.* **37**, 868 (1998).
- [33] J. D. Bryngelson, J. N. Onuchic, N. D. Socci, and P. G. Wolynes, *Proteins* **21**, 167 (1995).
- [34] M. D. Haw, *J. Phys.: Condens. Matter* **14**, 7769 (2002).
- [35] E. Frey and K. Kroy, *Ann. Phys.* **14**, 20 (2005).
- [36] J. Klafter and I. M. Sokolov, *Phys. World* **18**, 29 (2005).
- [37] I. M. Sokolov, *Soft Matter* **8**, 9043 (2012).
- [38] M. Schmiedeberg, J. Roth, and H. Stark, *Eur. Phys. J. E* **24**, 367 (2007).
- [39] C. Emary, R. Gernert, and S. H. L. Klapp, *Phys. Rev. E* **86**, 061135 (2012).
- [40] K. Lichtner, A. Pototsky, and S. H. L. Klapp, *Phys. Rev. E* **86**, 051405 (2012).
- [41] S. Herrera-Velarde and R. Castañeda-Priego, *Phys. Rev. E* **79**, 041407 (2009).
- [42] E. C. Euan-Diaz, V. R. Misko, F. M. Peeters, S. Herrera-Velarde, and R. Castañeda-Priego, *Phys. Rev. E* **86**, 031123 (2012).
- [43] J. Bernasconi, H. U. Beyeler, S. Strässler, and S. Alexander, *Phys. Rev. Lett.* **42**, 819 (1979).
- [44] J. W. Haus, K. W. Kehr, and J. W. Lyklema, *Phys. Rev. B* **25**, 2905 (1982).
- [45] H. Scher and M. Lax, *Phys. Rev. B* **7**, 4491 (1973).
- [46] R. Zwanzig, *Proc. Natl. Acad. Sci.* **85**, 2029 (1988).
- [47] W. Dieterich, I. Peschel, and W. Schneider, *Z. Phys. B Condens. Matter* **27**, 177 (1977).
- [48] P. Reimann, C. Van den Broeck, H. Linke, P. Hänggi, J. M. Rubi, and A. Pérez-Madrid, *Phys. Rev. E* **65**, 031104 (2002).
- [49] F. Höfling, T. Franosch, and E. Frey, *Phys. Rev. Lett.* **96**, 165901 (2006).
- [50] V. Krakoviack, *Phys. Rev. Lett.* **94**, 065703 (2005).
- [51] F. Sciortino, *J. Stat. Mech.*, P05015 (2005).
- [52] R. D. L. Hanes, C. Dalle-Ferrier, M. Schmiedeberg, M. C. Jenkins, and S. U. Egelhaaf, *Soft Matter* **8**, 2714 (2012).
- [53] F. Evers, C. Zunke, R. D. L. Hanes, J. Bewerunge, I. Ladadwa, A. Heuer, and S. U. Egelhaaf, *Phys. Rev. E* **88**, 022125 (2013).
- [54] C. Dalle-Ferrier, M. Krüger, R. D. L. Hanes, S. Walta, M. C. Jenkins, and S. U. Egelhaaf, *Soft Matter* **7**, 2064 (2011).
- [55] I. Ladadwa, F. Evers, A. Heuer, and S. U. Egelhaaf, in preparation (2013).
- [56] R. D. L. Hanes and S. U. Egelhaaf, *J. Phys.: Condens. Matter* **24**, 464116 (2012).
- [57] T. O. E. Skinner, S. K. Schnyder, D. G. A. L. Aarts, J. Horbach, and R. P. A. Dullens, *ArXiv e-prints*, 1302.2896 (2013).
- [58] X. Ma, P. Lai, and P. Tong, *Soft Matter*, DOI: 10.1039/C3SM51240A (2013).
- [59] A. Ashkin, *Science* **210**, 1081 (1980).
- [60] M. C. Jenkins and S. U. Egelhaaf, *J. Phys.: Condens. Matter* **20**, 404220 (2008).
- [61] K. Dholakia and T. Cizmar, *Nat. Phot.* **5**, 335 (2011).
- [62] K. Dholakia, P. Reece, and M. Gu, *Chem. Soc. Rev.* **37**, 42 (2008).
- [63] R. W. Bowman and M. J. Padgett, *Rep. Prog. Phys.* **76**, 026401 (2013).
- [64] K. C. Neumann and S. M. Block, *Rev. Sci. Instrum.* **75**, 2787 (2004).
- [65] J. E. Molloy and M. J. Padgett, *Contemp. Phys.* **43**, 241 (2002).
- [66] A. Ashkin, *Proc. Natl. Acad. Sci.* **94**, 4853 (1997).
- [67] D. G. Grier, *Nature* **424**, 810 (2003).
- [68] R. D. L. Hanes, M. C. Jenkins, and S. U. Egelhaaf, *Rev. Sci. Instrum.* **80**, 083703 (2009).
- [69] M. P. N. Juniper, R. Besseling, D. G. A. L. Aarts, and R. P. A. Dullens, *Opt. Express* **20**, 28707 (2012).

3.7 Paper VII: Colloids in light fields: Particle dynamics in random and periodic energy landscapes

10

- [70] J. Beverunge and S. U. Egelhaaf, in preparation (2013).
- [71] Q.-H. Wei, C. Bechinger, D. Rudhardt, and P. Leiderer, *Phys. Rev. Lett.* **81**, 2606 (1998).
- [72] K. Loudiyi and B. J. Ackerson, *Physica A* **184**, 1 (1992).
- [73] C. Bechinger, Q. H. Wei, and P. Leiderer, *J. Phys.: Condens. Matter* **12**, A425 (2000).
- [74] A. van Blaaderen, J. P. Hoogenboom, D. L. J. Vossen, A. Yethiraj, A. van der Horst, K. Visscher, and M. Dogterom, *Faraday Discuss.* **123**, 107 (2003).
- [75] M. Brunner and C. Bechinger, *Phys. Rev. Lett.* **88**, 248302 (2002).
- [76] B. V. R. Tata, R. G. Joshi, D. K. Gupta, J. Brijitta, and B. Raj, *Curr. Sci.* **103**, 1175 (2012).
- [77] E. Jaquay, L. J. Martínez, C. A. Mejia, and M. L. Povinelli, *Nano Lett.* **13**, 2290 (2013).
- [78] J. Mikhael, J. Roth, L. Helden, and C. Bechinger, *Nature* **454**, 501 (2008).
- [79] R. Castañeda-Priego, C. Dalle-Ferrier, S. Herrera-Velarde, and S. U. Egelhaaf, in preparation (2013).
- [80] R. Festa and E. d'Agliano, *Phys. A: Stat. Mech. Appl.* **90**, 229 (1978).
- [81] R. D. L. Hanes, M. Schmiedeberg, and S. U. Egelhaaf, in preparation (2013).
- [82] B. Vorselaars, A. V. Lyulin, K. Karatasos, and M. A. J. Michels, *Phys. Rev. E* **75**, 011504 (2007).
- [83] R. Zangi and S. A. Rice, *Phys. Rev. Lett.* **92**, 035502 (2004).
- [84] B. Cui, B. Lin, and S. A. Rice, *J. Chem. Phys.* **114**, 9142 (2001).
- [85] C. Hyeon and D. Thirumalai, *Proc. Nat. Acad. Sci.* **100**, 10249 (2003).
- [86] H. Janovjak, H. Knaus, and D. J. Muller, *J. Am. Chem. Soc.* **129**, 246 (2007).
- [87] M. P. Lettinga and E. Grelet, *Phys. Rev. Lett.* **99**, 197802 (2007).
- [88] E. Grelet, M. P. Lettinga, M. Bier, R. van Roij, and P. van der Schoot, *J. Phys.: Condens. Matter* **20**, 494213 (2008).
- [89] K. Dholakia and W. Lee, *Adv. Atom. Mol. Opt. Phys.* **56**, 261 (2008).
- [90] A. Ashkin, *Biophys. J.* **61**, 569 (1992).
- [91] A. Ashkin, J. M. Dziedzic, J. E. Bjorkholm, and S. Chu, *Opt. Lett.* **11**, 288 (1986).
- [92] M. Kerker, *The Scattering of Light and other Electromagnetic Radiation* (Academic Press, 1969).
- [93] Y. Harada and T. Asakura, *Opt. Comm.* **124**, 529 (1996).
- [94] K. Svoboda and S. M. Block, *Ann. Rev. Biophys. Biomol. Struct.* **23**, 247 (1994).
- [95] S. M. Barnett and R. London, *J. Phys. B.: At. Mol. Opt. Phys.* **39**, S671 (2006).
- [96] C. Zunke, R. D. L. Hanes, F. Evers, and S. U. Egelhaaf, in preparation (2013).
- [97] T. Thusty, A. Meller, and R. Bar-Ziv, *Phys. Rev. Lett.* **81**, 1738 (1998).
- [98] D. Bonessi, K. Bonin, and T. Walker, *J. Opt. A: Pure Appl. Opt.* **9**, S228 (2007).
- [99] M. Vieten, F. Evers, C. Zunke, and S. U. Egelhaaf, in preparation (2013).
- [100] A. Chowdhury, B. J. Ackerson, and N. A. Clark, *Phys. Rev. Lett.* **55**, 833 (1985).
- [101] W. Köhler and R. Schäfer, *Adv. Polym. Sci.* **151**, 1 (2000).
- [102] S. Wiegand, *J. Phys.: Condens. Matter* **16**, R357 (2004).
- [103] E. S. Pagac, R. D. Tilton, and D. C. Prieve, *Chem. Eng. Comm.* **148–150**, 105 (1996).
- [104] J. Leach, H. Mushfique, S. Keen, R. Di Leonardo, G. Ruocco, J. M. Cooper, and M. J. Padgett, *Phys. Rev. E* **79**, 026301 (2009).
- [105] P. Sharma, S. Ghosh, and S. Bhattacharya, *Appl. Phys. Lett.* **97**, 104101 (2010).
- [106] J. C. Crocker and D. G. Grier, *J. Coll. Interf. Sci.* **179**, 298 (1996).
- [107] M. C. Jenkins and S. U. Egelhaaf, *Adv. Coll. Interf. Sci.* **136**, 65 (2008).
- [108] W. van Meegen, T. C. Mortensen, S. R. Williams, and J. Müller, *Phys. Rev. E* **58**, 6073 (1998).
- [109] Note that the amplitude ϵ characterises the amplitude of the oscillations in the case of the periodic potential, while it represents the amplitude of the roughness, namely the width of the Gaussian distribution of values of the potential, in the case of the random potentials.
- [110] D. S. Dean, I. T. Drummond, and R. R. Horgan, *J. Phys. A: Math. Gen.* **30**, 385 (1997).
- [111] D. S. Dean, I. T. Drummond, and R. R. Horgan, *J. Phys. A: Math. Gen.* **37**, 2039 (2004).
- [112] C. Touya and D. S. Dean, *J. Phys. A: Math. Theor.* **40**, 919 (2007).
- [113] J. C. Dyre, *Phys. Rev. B* **51**, 12276 (1995).
- [114] P. N. Pusey and W. van Meegen, *Nature* **320**, 340 (1986).
- [115] K. S. Schweizer, *Curr. Opin. Coll. Interf. Sci.* **12**, 297 (2007).
- [116] K. S. Schweizer and E. J. Saltzman, *J. Chem. Phys.* **119**, 1181 (2003).
- [117] C. Lutz, M. Kollmann, and C. Bechinger, *Phys. Rev. Lett.* **93**, 026001 (2004).
- [118] I. O. Götze, J. M. Brader, M. Schmidt, and H. Löwen, *Mol. Phys.* **101**, 1651 (2003).
- [119] K. Franzrahe and P. Nielaba, *Phys. Rev. E* **76**, 061503 (2007).
- [120] K. Franzrahe and P. Nielaba, *Phys. Rev. E* **79**, 051505 (2009).
- [121] A. Imhof and J. K. G. Dhont, *Phys. Rev. E* **52**, 6344 (1995).
- [122] T. Voigtmann and J. Horbach, *Phys. Rev. Lett.* **103**, 205901 (2009).
- [123] C. Zunke, J. Beverunge, R. Capellmann, S. Glöckner, R. D. L. Hanes, F. Evers, and S. U. Egelhaaf, in preparation (2013).